BOUNDARY LAYER RECEPTIVITY OF FLOW OVER COMPLIANT SURFACES

Thesis submitted in accordance with the requirements of the University of Liverpool for the degree of Doctor in Philosophy by Jui-Che Huang

June 2006

ABSTRACT

The research described in this thesis is the first undertaken on the receptivity of boundary layers on compliant surfaces subjected to free stream turbulence. Both experimental and numerical work is presented.

An experimental investigation into boundary layer receptivity of flow over rigid and compliant surfaces was conducted. The near wall gain is a measure of the boundary layer receptivity and can be used to determine how boundary layer fluctuations respond to free stream turbulence. The effects of the interaction between the compliant surface and the boundary layer was determined through comparison of near wall gain measurements made on rigid and compliant surfaces. The measurements include the overall gain, the gain energy spectra and measurements in the transition zone. The results showed that a compliant surface is able to reduce the boundary layer receptivity and to delay transition. The largest transition delay was 3%. A correlation of the boundary layer receptivity and compliant surface properties was established using the parameters $\frac{\xi^2}{E\rho_{cs}L^2}$ and Reynolds number.

A receptivity prediction procedure that has already been used for rigid walls has been adapted for use with a compliant surface model. The model is a development of a volume-based visco-elastic compliant surface. Validation was taken with the experimental measurements and showed good agreement. Predictions were made with a range of wall compliances, coating thicknesses and damping factors to understand the individual effects of each on the boundary layer receptivity. The results demonstrated that the high compliance, low damping thin coating can prevent leading edge receptivity growth, and to reduce the development of receptivity a high damping is required.

Another aspect of the present research was to seek through numerical methods the best receptivity-suppression performance possible using compliant walls made from visco-elastic material. A genetic evolutionary algorithm was used for this purpose. The best material properties for suppressing boundary layer receptivity achieved a reduction in receptivity of 10%.

To

My Beloved

Parents

Acknowledgement

A special acknowledgement goes to my supervisor, Dr. Mark W. Johnson for making this work possible. His continuing guidance and support throughout this research is greatly appreciated.

I'd like to acknowledge Prof. M.P. Escudier my thesis advisor, for invaluable comments at the times when required, and his lectures on "Turbomachinery and Boundary layers" which were a great help to my experimental work.

John A. Redford, my colleague, has been a valuable source of assistance, encouragement and friendship, and I really appreciate all his help. It has been a great time working with him.

I am also grateful for the assistance of Derek Neary and Steve Bode. They provided valuable technical advice and organised the computer facilities and experimental equipment.

The biggest thanks of all go to my parents and my family, for their unending love and support, without their continuing support none of this would have been possible.

To all my friends in Taiwan or U.K., thank you for your company and spirit support.

CONTENT

NOMENCLATURE

Symbol		unit
a_1, a_2, a_3, a_4	arbitrary coefficient (equation 5.22)	
A_m	area over which the test mass is distributed	m^2
A	non-dimensional amplitude of perturbation (equation 5.20)	
A_0	non-dimensional amplitude of perturbation at turbulence grid (equation 5.20)	
B_1, B_2, B_3, B_4	complex constant (equation 5.57)	
B_L	$= \Omega_x \left(1 - \frac{c^2}{C_l^{\,2}}\right)^{\frac{1}{2}}$	
B_T	$= \Omega_x \left(1 - \frac{c^2}{C_t^{\,2}}\right)^{\frac{1}{2}}$	
c	non-dimensional fluctuation convection velocity (equation 5.16)	
C_f	$\frac{\mu\left(\frac{\partial u}{\partial y}\right)_w}{\frac{1}{2}\rho U^2}$, skin friction coefficient	
C_t	shear-wave speed of compliant surface	m/s
C_l	compression–wave speed of compliant surface	m/s
C_t^*	$= \frac{C_t}{U}$,non-dimensional shear-wave speed of compliant surface	
C_l^*	$= \frac{C_l}{U}$,non-dimensional compression–wave speed of compliant surface	
D	$\equiv \frac{d}{dY}$	
$e(f)$	energy spectral density in the near wall($y/\delta \approx 0.2$) boundary layer	m^2/s
$E(f)$	energy spectral density in the free stream	m^2/s
E	Young's modulus of compliant surface	N/m^2

E_s	$=\frac{E}{\rho U^2}$,non-dimensional Young's modulus	
$E_{dynamic}$	Young's modulus from dynamic measurement	N/m^2
E_{static}	Young's modulus from static measurement	N/m^2
$E_{voltage,0}$	voltage corresponding to zero flow velocity	V
$E_{voltage}$	measured voltage	V
f	fluctuation frequency in streamwise direction	s^{-1}
f_y, f_z	fluctuation frequency in normal, spanwise direction	s^{-1}
F	load force	N
F_c	non-dimensional frequency at which $Gain(f)=\frac{1}{2}G_o$	
G_0	$Gain(f)\, as\, f \to 0$, low frequency gain	
G_s	shear modulus of compliant surface	N/m^2
G_s *	$=\frac{G_s}{\rho U^2}$, non-dimensional shear modulus of compliant surface	
$Gain(f)$	$=\left(\frac{e(f)}{E(f)}\right)^{\frac{1}{2}}\frac{U}{u}$, near wall gain at $y/\delta \approx 0.2$	
$Gain_{overall}$	$=\frac{u_{rms}}{U_{rms}}\frac{U}{u}$, overall gain	
$Gain_z$	spanwise gain (gain averaged in streamwise and normal directions) (equation 5.29)	
H	boundary layer shape factor	
H_t	height increment for traverse gear	m
K_1	specimen calibration factor for compliant surface	m^{-1}
K_s	bulk modulus of compliant surface	N/m^2
K_s *	$=\frac{K_s}{\rho U^2}$,non-dimensional bulk modulus of compliant surface	
k_{static}	spring stiffness for static measurement	N/m
$k_{dynamic}$	spring stiffness for dynamic measurement	N/m

L	thickness of compliant surface	m
L_s	$=\frac{L}{\delta}$,non-dimensional thickness of compliant surface	
n	coefficient in King's Law (equation 3.2, 3.12)	
m	mass in spring damper system	kg
p'	fluctuating pressure	N/m^2
p_p	non-dimensional fluctuating pressure (equation 5.9)	
R^2	correlation coefficient	
Re	Reynolds number	
Re_x	$=\frac{\rho U x}{\mu}$, streamwise distance Reynolds number	
Re_{x_0}	$=\frac{\rho U x_0}{\mu}$, Reynolds number based on streamwise distance from turbulence grid	
Re_δ	$=\frac{\rho U \delta}{\mu}$, displacement thickness Reynolds number	
Re_{δ^*}	$=\frac{\rho U \delta^*}{\mu}$, displacement thickness Reynolds number	
Re_θ	$=\frac{\rho U \theta}{\mu}$, momentum thickness Reynolds number	
S	slope of the gain decay at high frequency	
S_1	force-displacement slope for compliant surface	N/m
Tu	$\frac{U_{rms}}{U}$,turbulence level	
t	time	s
T	$=\frac{Ut}{\delta}$, non-dimensional time	
T_o	ambient temperature	K
u, v, w	local mean streamwise, normal and spanwise velocities	m/s
u_p, v_p, w_p	Fourier components of non-dimensional streamwise, normal and spanwise velocities	
u'	local instantaneous perturbation velocity in the boundary layer	m/s
u_{rms}	local root mean square velocity	m/s

u_{y_0}	$= \left.\frac{\partial u}{\partial y}\right\|_W$, surface velocity gradient	s^{-1}
u_τ	$\left(\frac{\tau_W}{\rho}\right)^{1/2}$, friction velocity	m/s
U', V'	local instantaneous streamwise, normal perturbation velocity in the free stream	m/s
U	freestream time mean velocity	m/s
U_{eff}	effective cooling velocity	m/s
U_{rms}	freestream root mean square velocity	m/s
x_0	streamwise distance from turbulence grid (Ch.5)	m
x	streamwise distance from leading edge (Ch.4,Ch.5)	m
$x_0, x_1 \ldots, x_n$	amplitude of fluctuation for spring-damper system (Ch.3)	m
X, Y, Z	$= \frac{x}{\delta}, \frac{y}{\delta}, \frac{z}{\delta}$, non-dimensional streamwise, normal and spanwise coordinates	
y^+	$\frac{y u_\tau}{\nu}$	
Y_0, Y_1	position of compliant surface layer	
α	inclined angle of manometer(equation 3.10) misalignment angle of hot –wire (equation 3.14)	°
α_c	$\frac{\xi^2}{E\rho_{cs}L^2}$, non-dimensional compliant surface property	
$\alpha_{overheatratio}$	overheat ratio setup in the anemometer	
β	fluctuation decay coefficient	
β_w	spanwise wave number of streaks	
δ	boundary layer thickness	m
δ^*	$= \int_0^\infty \left(1 - \frac{u}{U_\infty}\right) dy$, boundary layer displacement thickness	m
Δh	the uncertainty of the height measurement for the manometer	m
$\Delta \ell$	measured displacement of compliant surface	m

ΔT	ambient temperature variation	K
Δu	velocity variation due to the ambient temperature change or system vibration	m/s
Δy	the displacement due to the system vibration	m
ΔZ_{min}	spanwise scale of the streaky structures	m
γ	intermittency	
Γ	system damping factor	N·s/m
η	displacement of compliant surface	m
$\eta_{Blasius}$	$y\sqrt{\frac{U}{\nu x}}$	
η_x	horizontal displacement of compliant surface	m
η_y	vertical displacement of compliant surface	m
η^*	$=\frac{\eta}{\delta}$,non-dimensional displacement of compliant surface	
$\eta_x{}^*$	$=\frac{\eta_x}{\delta}$,non-dimensional horizontal displacement of compliant surface	
$\eta_y{}^*$	$=\frac{\eta_y}{\delta}$,non-dimensional vertical displacement of compliant surface	
φ	scalar potential for displacement	
λ	$=\frac{\delta^2}{\nu}\frac{dU}{dx}$, Pohlhausen parameter (Ch.4), Lame's constant(Ch.5)	
λ_θ	$=\frac{\theta^2}{\nu}\frac{dU}{dx}$, Thwaites parameter	
λ_w	vortex wavelength (equation 5.30)	m
μ	dynamic fluid viscosity	kg/ms
ν	$=\frac{\mu}{\rho}$, kinematic viscosity, Poisson's ratio(Ch.5)	m^2/s
θ	$=\int_0^\infty \frac{u}{U_\infty}\left(1-\frac{u}{U_\infty}\right)dy$, boundary layer momentum thickness	m
ρ	fluid density	kg/m^3

ρ_{air}	air density	kg/m^3
ρ_{cs}	density of the compliant surface material	kg/m^3
ρ_{meths}	density of methylated spirit	kg/m^3
ρ_r	$=\frac{\rho_{cs}}{\rho}$, non-dimensional density ratio	
σ	normal stress within compliant surface	N/m^2
σ_W	fluid normal stress at wall	N/m^2
σ^*	$=\frac{\sigma}{\rho U^2}$,non-dimensional normal stress within compliant surface	
$\sigma_W{}^*$	$=\frac{\sigma_W}{\rho U^2}$, non-dimensional fluid normal stress at wall	
τ	shear stress within compliant surface	N/m^2
τ_W	fluid shear stress at wall	N/m^2
τ^*	$=\frac{\tau}{\rho U^2}$,non-dimensional shear stress within compliant surface	
$\tau_W{}^*$	$=\frac{\tau_W}{\rho U^2}$, non-dimensional fluid shear stress at wall	
ω_d	damped frequency of compliant surface	s^{-1}
ω_n	natural frequency of compliant surface	s^{-1}
$\Omega_X, \Omega_Y, \Omega_Z$	$=\frac{2\pi f\delta}{U}, \frac{2\pi f_y\delta}{U}, \frac{2\pi f_z\delta}{U}$, non-dimensional streamwise, normal ,spanwise frequencies	
ξ	material damping Narashimha non-dimensional distance(4.2.7)	N·s/m^2
ξ_s	$=\frac{\xi}{\rho UL}$,non-dimensional material damping	
$\vec{\psi}$	vector potential for displacement	
ς	damping ratio of compliant surface	
Subscripts		
e	end of transition	
s	start of transition	

t	derivatives in t	
W	at the wall	
x, y, z	streamwise, normal and spanwise direction	
X, Y, Z	non-dimensional streamwise, normal and spanwise direction	

CHAPTER ONE

INTRODUCTION

1.1 Flow control

Flow control technology has become increasingly important since the late 90's. The potential gains of flow control provide energy efficient and more environmentally friendly vehicles. Flow control usually refers to the use of any passive or active means to manipulate flow in order to achieve a desired objective such as drag reduction or increased heat transfer. Many institutions such as NASA and KTH Mechanics have been conducting many researches on drag reduction and have demonstrated that the concept of using laminar flow control on aircraft has great potential. (NASA report, 1990, Fransson et al., 2006). Laminar flow control is a means of trying to maintain the flow passing over a vehicle in a laminar state, because laminar flow has a considerably lower skin-friction drag compared to a turbulent one. In some applications, the skin-friction drag forms a large portion of the overall drag, and so, using laminar flow control to delay transition can lead to an increase in vehicle speed or the use of less energy for the same speed of travel. Recent developments of laminar flow control include active control methods, wall suction/blow devices, and compliant surfaces. (Gad-el-Hak, 2000)

Considering the development cost and convenience in use, compliant surfaces provide a cheap and easy-applied approach for existing vehicles. They also have

potential for use in noise absorption (Gad-el-Hak, 2000), which is attractive to the transport industry. Another important aspect of compliant surfaces is the analogy with biological systems where it is very common to find a flow past a flexible surface (Djordjevic, 2000). The flow of blood and other biological fluids within the body through the tubes and vessels is a good example. The walls of the vessels are made of tissues and membrane which have viscoelastic properties. In general, understanding the flow past compliant surfaces can have a huge benefit on energy saving in transportation or medical treatment such as cardiovascular reinforced blood vessels.

1.2 Fundamentals

Laminar-turbulent transition for attached boundary layers can be divided into the modes of natural transition or bypass transition, depending on the freestream turbulence intensity level. This project focuses on bypass transition which occurs when the freestream turbulence level is higher than 1%. (Morkovin ,1969) Bypass transition completely bypasses the Tollmien-Schlichting mechanism which is dominant in natural transition as the turbulent free stream disturbances penetrate the boundary layer directly and cause boundary layer fluctuations which grow and lead to the production of turbulence. The response of the boundary layer fluctuations to free stream disturbances is called receptivity which is the initiator of bypass transition. (Reza, 2003)

A boundary layer undergoing bypass transition is characterized by the growth of high and low speed streaks inside the boundary layer generated through the so called Klebanoff mode (Kendall, 1985). Similar streaks are also found near the wall in

turbulent flow (Kim, 2003). Therefore, investigations on bypass transition may also help in the understanding of turbulent boundary layer flow.

A compliant surface is generally known to suppress the generation of turbulence which both delays laminar-turbulent transition and reduces turbulent drag. Researches started with Kramer's experiment in 1957 (Kramer, 1957). His idea of using a compliant coating for drag reduction was motivated by the postulation that dolphins achieved very high speeds through their compliant skins through a natural drag reduction mechanism. Many kinds of compliant surface model have been considered to mimic the dolphin's skin (Carpenter, 1990). These models include rubber-like, plate-spring surface based and volume based compliant surfaces models.

A compliant surface is a wave-bearing medium when a flow passes over it; an interaction takes place between the compliant surface and the surrounding boundary layer. The compliant surface deforms under the pressure fluctuations induced by the free stream. Therefore, if the free stream velocity is too high and the compliant coating is not able to resist the pressure perturbations produced in the free stream, then wall-based instabilities within the coating are triggered (Yeo, 1986).

The use of compliant surfaces has been demonstrated to stabilize and reduce the growth rate of Tollmien-Schlichting instabilities in theory. In principle, natural transition could be delayed indefinitely by use of optimized multiple-panel compliant surfaces (Carpenter, 1998). Also, in turbulent flow, the compliant surface has the ability to reduce the skin-friction drag and wall pressure fluctuations by 7% and 19% respectively (Choi, 1997). This evidence suggests that using compliant surfaces in bypass transition may result in a similar effect with boundary layer velocity fluctuation reduction. In bypass transition, the surface properties allow

disturbances to be absorbed, i.e. damping out the boundary layer fluctuations induced from the free stream flow, and hence the growth rate in receptivity is suppressed. As a result, the laminar region can be extended, thus, less friction drag results in the flow.

1.3 Aim and Objectives

Many compliant surface researches (Benjamine (1963), Carpenter (1985,1998,2000,2002), Choi (1997,2000), Gad-el-Hak (1984,1986,2000,2002), Landahl(1962), and Yeo (1986,1988,1990,1992,1999)) have been done for either natural transition or turbulent flow, but less attention has been paid to boundary layer receptivity in bypass transition prior to the work of Reza (2003). Reza used a numerical method to predict the receptivity behaviour of compliant surfaces, however, the work lacked any experimental evidence to support his predictions. The boundary layer receptivity was also not completely understood. Little is known about boundary layer fluctuations resulting from high free stream turbulence (>1%) over compliant surfaces.

The primary goal of the present investigation is to enhance knowledge of the boundary layer receptivity scenario caused by moderate levels of free stream turbulence (1.0~1.7%) and a compliant surface. Numerical and experimental approaches were used to achieve the key objectives of this research. The main objectives are:

- To study the free stream induced boundary layer receptivity over rigid and compliant surfaces in order to gain further knowledge of the mechanisms.

- To perform experiments on pre-transitional boundary layer receptivity for flow over compliant surfaces, and to investigate compliant surface interactions with boundary layer fluctuations.
- To evaluate the delay in the onset of transition achievable by using compliant surfaces.
- To model the behaviour of a compliant surface and adapt a transition model to predict the changes in boundary layer receptivity which result from damping, compliance and thickness of the compliant coating.
- To explore the possibility of using an optimised compliant surface to achieve turbulent transition delay through the Genetic Evolutionary Algorithm.

The experiments have been designed to validate the numerical results, and provide strong evidence of whether compliant surfaces are effective in transition delay. The numerical predictions help to expand the understanding of the underlying physics which is not possible through experiments alone.

1.4 Thesis content

In Chapter 2, previous work undertaken on the bypass transition and compliant surfaces will be introduced. The experimental set-up, data analysis techniques, measurement procedures and approaches to define the compliant surface properties will be explained in Chapter 3. In Chapter 4, experimental measurements from the rigid surface are shown and validated. These results are used as a benchmark to determine the effect of the compliant surfaces on boundary layer receptivity. The measurements over compliant surfaces, which are compared with

the rigid wall results, are shown in the second part of Chapter 4. The investigations included the streamwise velocity fluctuations, the boundary layer receptivity spectrum and the onset of transition location and are compared with the rigid wall results. In Chapter 5, a visco-elastic compliant surface model is presented and combined with a bypass transition model. The use of a GEA to search for a set of best compliant surface properties to suppress boundary layer receptivity is also presented. The methodology and prediction of the changes in the boundary layer flow characteristics over compliant surfaces are shown and discussed in this chapter. Chapter 6 presents the conclusions of this research.

CHAPTER TWO

LITERATURE REVIEW

2.1 Introduction

Since the first experiments in the 1950's which were conducted by Kramer showed that compliant surfaces have the potential to reduce drag, much attention has been paid to investigating hydrodynamic instabilities within the boundary layer and interactions between the fluid and compliant walls. In engineering applications, if a laminar flow can be maintained indefinitely, huge amounts of energy can be saved due to the fact that the skin-friction drag is as much as an order of magnitude lower in the laminar state than for a turbulent flow.

So far, most researchers such as Benjamin (1963), Carpenter (1985,1998,2000,2002), Choi (1997,2000), Gad-el-Hak (1984,1986,2000,2002), Landahl(1962), and Yeo (1986,1988,1990,1992,1999) have concentrated on natural transition or turbulent flow over a compliant coating, and the hydrodynamic Tollmien-Schlichting(T-S) instabilities over a compliant coating were calculated and proved to be suppressed.(Dixon et al. ,1994 Yeo,1986 and Carpenter, 1998) Bypass transition over a compliant surface is a new field which has not completely been investigated. Reza (2003) used velocity-vorticity (DNS) approaches to examine the receptivity and transition over a rigid and compliant surface. The results are

encouraging and showed that compliant surfaces are remarkably resilient to the growth of boundary layer streaks.

Boiko et al.(1994) detected T-S waves and studied their behaviour with a free stream turbulence level of 1.5%. They found the T-S wave can exist and develop in a similar way as in an undisturbed boundary layer. Therefore, it is important to understand natural transition and bypass transition phenomena. If the receptivity process in bypass transition can be reduced by a certain compliant surface, then the next issue would be to suppress T-S instability.

2.2 Laminar-turbulent transition

The phenomenon of transition is broadly defined as the process through which a flow transforms from laminar to turbulent flow. During the transition, the Reynolds stresses develop within the boundary layer from levels much smaller to levels much greater than the viscous stresses. Transition can be divided into three main modes, natural transition, bypass transition, and separated-flow transition. For attached boundary layers, only natural transition and bypass transition are considered in this project.

2.2.1 Natural transition

Natural transition happens in a low-disturbance environment where the free stream turbulence level Tu <1%. The laminar boundary layer near the leading edge develops and various receptivity processes or initial disturbances set in. Schubauer & Skramstad (1948) found that when the flow is above a certain Reynolds number, a visible increase in wave activity exists within a boundary layer and these waves

which are susceptible to small disturbances are called Tollmien-Schlichting waves (T-S waves). These two-dimensional T-S waves convect downstream with a typical speed of 30%-35% of free stream velocity in zero pressure gradient flow and grow slowly and exponentially in the downstream direction. Once the amplitudes of those instabilities exceed a certain threshold they start to convect and develop unstable three-dimensional waves, which form into hairpin vortices. Vortex breakdown then occurs in regions of highly localised shear resulting in high amplitude fluctuations. Turbulent spots form with locally intense fluctuations. As the turbulence spots propagate, they spread until they coalesce into fully turbulent boundary layer flow. The whole amplification of the T-S waves account for up to 80% of the transition process.

Orr(1907) and Sommerfeld (1908) derived the Orr-Sommerfeld equations from the linearized Navier-Stokes equations. The eigenvalues of the fourth-order linear ordinary Orr-Sommerfeld equation describes the stability characteristic of the boundary layer.

Figure2.1 shows a neutral stability curve. If fluctuations are outside the curve, they will be damped out and inside they will be amplified. The transition prediction is based on these solutions and assumes that transition will occur when T-S waves have been amplified by an semi-empirical determined e^n method.

2.2.2 Bypass transition (Klebanoff mode)

Bypass transition was first proposed by Morkovin (1969) and is caused by a large disturbance in the free-stream turbulence. Klebanoff (1971) was the first

person to identify the occurrence of streamwise elongated structures in the boundary layer subjected to high free-stream turbulence. Arnal and Juillen (1978) measured a boundary layer subjected to freestream turbulence levels higher than 1% , and showed the dominant disturbances inside the boundary layer are low frequency disturbances and not T-S waves. Kendall (1985) denoted these elongated structures (streaks) as Klebanoff mode disturbances. Klebanoff modes are vortical disturbances generated by a periodic, spanwise modulation of the streamwise velocity. They grow and extend downstream.

In boundary layers with free-stream turbulence intensities of 1% or more, large disturbances induced by the free stream penetrate into the boundary layer and it leads to a bypass of the classical scenario which is dominated by slower, exponential amplification of unstable T-S waves and transition occurs rapidly. The main feature of bypass transition is the elongated streaks of high and low streamwise velocity, with a spanwise wavelength of the order of the boundary layer thickness found in the boundary layer.

Jacobs and Durbin (1998, 2001) used direct numerical simulation (DNS) calculation on the bypass transition and provided depictions of the eddies and interactions that occur during the process of bypass transition. At finite Reynolds number, low frequency modes can penetrate the boundary layer but they are generated by viscously decaying freestream motions and cannot lead directly to instability. Once these low frequency perturbations enter into the boundary layer, the low frequency perturbations produce an even lower frequency mode. The very low-frequency perturbations are amplified and elongated in the streamwise direction by the fluid shear stress. They also develop into streaks in the streamwise velocity

contours. Figure 2.2 shows streaks in the boundary layer subjected to high free stream turbulence.

2.2.3 Boundary layer receptivity

Receptivity is the first significant stage of laminar-turbulent transition and it describes the environmental disturbances exciting the boundary layer instabilities which lead to the transition to turbulence. Receptivity is a key issue when bypass transition is mentioned and different from the boundary-layer stability problems which in general are calculated by the Orr-Sommerfield equation to satisfy linear homogeneous equations. The receptivity problem is an initial-value problem, which evaluates the response of the boundary layer to external disturbances. Externally environmental disturbances such as acoustic, freestream turbulence and surface roughness will cause transition by initiating the various instability modes. The initial amplitude of the disturbance is important for the receptivity process, as it will dictate the route of transition. If the initial disturbances are of sufficient large amplitude, non-linear behaviors will be triggered and lead directly into turbulence through bypass transition. For small initial amplitude of disturbance, a more gradual sequence of instantaneous disturbances are initiated which eventually burst into turbulence.

Brandt et al. (2004) simulated the transition induced by free-stream turbulence over than 1% by using a DNS method and concluded the growth of the streak energy inside the boundary layer is proportional to $\mathrm{Re}_x Tu^2$ and is most probably associated with the inlet turbulence. The growth of the perturbations is faster for larger Tu in the nonlinear region and if the nonlinear mechanism is

dominating inside the boundary layer the perturbations behavior can be expressed as $\frac{u_{rms}}{U} \propto \mathrm{Re}_x^{1/2} Tu^2$, the same results showed in Jacobs and Durbin (2001)'s DNS predictions. Fransson et al. (2005) investigated the transition induced by different free-stream turbulence intensities which varied from 1.4% to 6.7%. The results confirmed Brandt's simulation results that the disturbance energy E (u_{rms}^2 / U_∞^2) is proportional to $Tu^2\,\mathrm{Re}_x$. Johnson and Ercan (1999) measured the energy spectrum of the boundary layer fluctuations induced by the free stream disturbances, and a new parameter, the near wall gain, was created to determine the response of the boundary layer to homogeneous isotropic turbulence. The experiments also provided strong evidence to indicate that the fluctuation amplitude (response) in the pre-transitional boundary layer scaled linearly with the level of freestream turbulence.

Using linear scaling of the boundary layer fluctuations from the free stream disturbances, Johnson (2002, 2003) devised a new approach to the prediction of transition using linear theory. The predictions showed a streamwise energy spectrum in good agreement with published empirical correlations and predicted onset of transition Re_{δ^*} for a wide range of pressure gradients with similar trends to the Abu-Ghannam and Shaw (1980) correlations.

The spanwise characteristics of streaks in the bypass transition boundary layer affect turbulent spot generation. The spots form in the minimum spanwise velocity position and so the spanwise fluctuation wavelength limits the spot production rate. Matsubara & Alfredsson (2001) used smoke visualisation and hot-wire anemometry to define the spectrum of the boundary layer streaks subjected to moderate free stream turbulence. The spectrum showed that the low streamwise

frequencies containing the highest energy and the highest spanwise energy were observed at a wavelength of the order of the boundary layer thickness. Lundell &Alfredsson (2004) also determined the physical spanwise scale of the streaks in their experiments. The streaks spanwise scale decrease downstream and in the downstream the scale is about a boundary layer thickness δ.

Yoshioka et al. (2004) used three different grids to determine the spanwise scale of the streaky structures and the results showed that the spanwise spacing of the streaks is constant if the free stream velocity is kept constant. However, if Reynolds number is kept constant, the spanwise separation of the streaks is proportional to the displacement thickness δ^* or $1/U$. Yoshioka's observations therefore lead to the following relation $\frac{\Delta Z_{min} U}{\upsilon} = \text{constant}$, where ΔZ_{min} is the spanwise scale of the streaky structures.

Andersson et al.(1999) and Luchini (2000) used optimal perturbation theory for spatially developing disturbances and showed that the most amplified spanwise wave number (β_w) for streaky structures is $\beta_w = 0.775/\delta^*$, where δ^* is the local boundary layer displacement thickness. In terms of the spanwise scale of the streaky structures, this implies a spanwise streak scale approximately 40% larger than the boundary layer thickness will cause the largest growth at a given streamwise station.

2.3 Prediction of transition

The study of the onset of transition is important for modelling as well as for a basic understanding of the transition process. In the turbomachinery environment, the streamwise pressure gradient and the free stream turbulence strongly influence the

onset of transition; so many previous researches were correlating these two parameters for the start of transition. Free-stream turbulence is perhaps the most important source inducing bypass transition in the boundary layer flow. The two widely-used transition onset correlations are from Abu-Ghannam and Shaw (1980) and Mayle(1991).

Abu-Ghannam and Shaw's experiments provided a correlation for onset of transition in attached boundary layers as a function of turbulence level and pressure gradient. Experimental results noted that the pressure gradient has less effect on the transition onset when the turbulence level is high; also the effect from the turbulence length scale is neglected.

If the turbulence intensity is less than 10% and there is zero pressure gradient, an empirical correlation can be represented as follows

$$\mathrm{Re}_{\theta s} = 163 + \exp(6.91 - 100Tu)$$

Mayle (1991) reviewed the previous experimental literature and fitted all the data into a new empirical formula for the onset of transition Reynolds number, and free stream turbulence intensity in the range from 0.2%~ 9 %.

$$\mathrm{Re}_{\theta s} = 400(100Tu)^{-5/8}$$

Brandt et al. (2004) suggested that transition is triggered when the u_{rms} value reaches a critical threshold. From his simulation results of $u_{rms} \propto \mathrm{Re}_x^{1/2} Tu$, he concluded the transition location Re_s is related to the free stream turbulence intensity by $\mathrm{Re}_{xs}^{1/2} Tu = \text{constant}$. If the nonlinear mechanism is relevant, the relation can change to $\mathrm{Re}_{xs}^{1/2} Tu^2 = \text{constant}$.

Another approach to define onset of transition is that of Johnson (2003) who used a linear perturbation theory to compute the streamlines through a turbulent spot

and suggested the transition could be inferred from laminar fluctuations of the near wall velocity that are induced by free stream turbulence. He argues that if the near wall instantaneous velocity drops below half of the mean flow velocity, local transient separation will occur. The hairpin vorticies co-exist with the separation formation. Another computational result is that when the near wall ($y/\delta \leq 0.3$) local turbulence level reaches 23%, the start of transition occurs.

Fransson et al.(2004) studied the transition zone for FST intensities between 1.4 % and 6.7%. The results showed that the transitional Reynolds number is inversely proportional to Tu^2 .The transition was determined by an intermittency level of $\gamma = 0.5$. The empirical correlation can be represented as $\mathrm{Re}_{x,\gamma=0.5} = 196Tu^{-2}$. The coefficient of 196 can be changed due to the different influences such as the definition of the transitional Reynolds number, the degree of anisotropy, the leading edge suction peaks, the small deviation from a zero pressure gradient throughout the test section, scales and energy spectrum of the free-stream.

In the transition predictions, the coefficients are different for each experimental set-up; therefore, the large degree of empirical contradiction implies that generality of transition correlation is rather limited.

2.4 Studies in boundary-layer flow over a compliant surface

The use of a compliant surface is one of the flow control technologies to manipulate flow and reduce the drag in the shear flow. It provides a rather simple and inexpensive method for application to existing vehicles. Compliant surfaces also provide the potential to inhibit, or to promote the dynamic instabilities that characterize boundary layer flows or pipe flows. Postponement of transition leads to

drag reduction while enhancement leads to turbulence augmentation increasing drag and intensifying heat exchange between the surface and fluid. Other applications include modifying the mass, heat and momentum fluxes and results in change of drag and acoustic properties. Because of these benefits, a compliant surface/ flexible coating has been widely investigated and researched.(Gad-el-Hak, 2002)

2.4.1 Classification of the instabilities over compliant surfaces

Understanding of the hydroelastic stability of a flexible wall is essential to design a drag-reducing compliant coating. When a fluid flows over a flexible coating, a complex interaction between instabilities may appear due to the interaction of two wave-bearing media. Some instabilities are fluid-based and some are wall-based, and the coalescence of both kinds of instabilities can even generate another more powerful instability to hasten the disturbances within the boundary layer to a transitional flow.

There are at least three different classification schemes for instability waves. First of all, according to Landahl (1962) and Benjamin's (1963) classification of instabilities, all the waves can be divided into three classes, which depends on their response to irreversible energy transfer to or from the compliant wall. Class A waves, for example Tollmien-Schlichting waves, can be stabilized if the energy transfer is from the fluid to the coating, but destabilized by dissipation in the wall, as a consequence wall damping can cause the wave excitation and growth. Class B waves, for example traveling-wave flutter instability, have reverse effect of that for Class A. Energy transfer from fluid into the wall causes destabilization , for the reason that amplification of Class B waves happen when the energy flow transfer is more than

the capacity of coating's internal dissipation. Wall damping of compliant surface helps to stabilize Class B waves. Class C waves are similar to Kelvin-Helmholtz instability. They appear when the wall is too soft to resist the pressure distribution of the flow. The energy transfer between solid and fluid in these waves is nearly zero.

The second scheme of classification of instability is from Carpenter and Garrad (1985). They divided waves into fluid-based and wall-based. Tollmien-Schlichting instability is a very typical example of a fluid-based wave. Two types of wall-based or compliance-induced flow instabilities (CIFI) were found in the experiments of Gad-el- Hak (1984) and Gaster (1987) and termed static divergence (SD) and Traveling-wave flutter (TWF).

The divergence instability occurs when the flow pressure exceeds the restorative structural forces of the wall. The divergence instability is a slowly progressive instability, with a low phase speed and zero group velocity. Another feature of the static divergence is an absolute instability developing in both the upstream and downstream directions from the point of initiation. Gad-el-Hak et al. (1984) conducted a flow visualization experiment over a compliant surface of plastisol gel and the results noted SD instability consisting of sharp peaks where the height is the same order as the depth of the gel. The eddy structures above the compliant coating were obviously more intense than those above the rigid wall. (Figure 2.3) The existing peaks of SD instability act as a roughness element on the surface and result in an increase of drag. The onset of SD instability occurs in the turbulent boundary layer when the free stream velocity $U > 3.33C_t$, C_t is the elastic shear-wave speed of the material and is defined as $(G_s/\rho_{cs})^{1/2}$ where G_s is the shear modulus of the compliant surface and ρ_{cs} is the density of the compliant surface.

Hansen et al. (1980) and Duncan et al. (1982) also found the onset of velocity in the turbulent boundary layer appears when $U > 4.5C_t$ and $U > 2.86C_t$ respectively. For static-divergence waves to appear under a laminar flow boundary layer a much higher free stream velocity is needed compared to a turbulent boundary layer. Duncan's results showed this happens when $U > 5.92C_t$ and when $U > 12C_t$ in Gad-el-Hak's prediction.

Wiplier and Ehrensteins (2000) investigated the absolute instability in a boundary layer flow over compliant coatings. The results indicated that the divergence-type instability behaviour is due to the interaction between the stable, upstream propagating evanescent wave mode and a convectively unstable travelling T-S wave.

Lucey and Carpenter(1993) identified Gaster's (1987) finding of a high frequency oscillation measured using a hot-film foil gauge located at the panel's trailing edge. The oscillations are traveling-wave flutter. Carpenter and Garrad (1985) summarized the effect of traveling-wave flutter (TWF) instability. TWF is a wall-based instability and more subtle than the divergence one. TWF instability is characterized by relatively high phase speeds and group velocities and is a convective instability like T-S waves, but travels much faster. It is a very dangerous instability, because under certain circumstances, the TWF instability may interact with T-S waves and produce a sudden onset of transition.

Another wave classification scheme was described by Hansen et al. (1980). They investigated wave structures which are generated in an elastic surface-liquid interface and three distinct types of waves were observed. They used I ,II, III to name these waves. Type I waves occur near the leading edge region and disappear

downstream and this type of wave is associated with a profile irregularity in a compliant surface. Type II waves have been found near the spanwise edge of compliant surfaces and Type III waves were in the interior region of the surface. (Figure 2.5) The onset velocities of these waves are similar for Type II and III. Type I waves have a lower onset velocity.

All the classification schemes help to understand the behavior of instabilities or wave structures over compliant surfaces. The energy classification provides a means to predict how the instabilities respond to changes in the wall properties. The wall-based/fluid-based instability scheme help to identify the major factors which affect the flow over compliant surfaces. Figure 2.5 shows the summary of the classification of the instabilities.

2.4.2 Compliant surface researches

2.4.2.1 Experimental works

Compliant surface research started in the late 1950's; and began with a postulation that dolphins achieved very high speeds through a drag reduction mechanism resulting from their compliant skins. The first experiment done by Kramer used a rubber coating adhesive on a rigid wall towed in Long Beach Harbor, California. His idea was to use an elastic coating to damp out frequencies near the unstable Tollmien-Schlichting wave frequency, to dissipate instability waves, and delay transition. Kramer claimed there was a significant drag reduction by using a compliant surface. Unfortunately, several repeat experiments carried out later on failed to confirm his conclusion.

Gad-el-Hak (1986) used gelatine and plastisol gel to make compliant coatings and detected hydroelastic instabilities in a towing tank. The gelatine and plastisol gel were elastic and viscoelastic coatings, respectively. The results showed that both thick surfaces of elastic and a viscoelastic coating are more susceptible to hydroelastic static-divergence instability. In the experiment, the SD did not yield on an elastic (with low damping) wall due to the fact that the wall damping is essential to cause the divergence instability.

Willis (1986) conducted experiments to study the effect of compliant coating on the evolution of T-S waves on a flat plate boundary layer. The results of the amplification versus speed for various modal frequencies are shown in figure2.6. There is a dramatic reduction in instability growth with a thick soft compliant coating covered with a thin stiff layer.

Choi et al. (1997) conducted drag-reduction experiments in the turbulent boundary layer in a water channel. The compliant surfaces were silicon rubber coatings. The results of the experiments showed there is up to 7% and 19% reduction in the skin-friction and wall-pressure, respectively; and up to 5% reduction in turbulence intensity across the boundary layer was found.

Dinkelacker(1966) conducted a compliant surface test in a water pipe flow and found a modest reduction in drag. However, Krindel and Silberberg(1979) studied the drag force on a Newtonian fluid over a polyacrylamide tube and found the drag force is larger than for a rigid-wall tube even at small Reynolds number where the flow is laminar.

Boundary layer flow is modified by compliant surface motion and the various instabilities created by interactions between the fluid and wall, but basic

characteristics remain unchanged, such as the boundary layer velocity profile. Some changes found in the boundary layer are pressure and velocity perturbations which are required to satisfy the stress and velocity continuity equations as proved by Lee et al. (1995) and Gad-el-Hak et al. (1984).

2.4.2.2 Theoretical works

Early theoretical works done by Benjamin (1963) and Landahl (1962) indicated that increase of the wall compliance would suppress the growth of T-S waves and therefore using compliant surfaces to delay transition was possible and results in drag reduction. Carpenter and Garrad (1985) noted high wall compliance can suppress the T-S waves, but it also develops two wall-based instabilities, traveling-wave flutter (TWF) and static divergence (SD) instability. They investigated Kramer-type isotropic viscoelastic surfaces (a Kramer-type surface is a thin rubber membrane supported by rubber stubs and between the stubs is a viscous fluid) and showed material damping destabilizes the T-S waves and has an opposite effect on the TWF. However, the beneficial effect of damping on the TWF is much more pronounced than the adverse effect on T-S wave. Therefore, the damping in the Kramer coating delayed the onset of the TWF and allowed the use of a more compliant surface.

Yeo(1988) studied the effects of stiffness, thickness of the layer and wall damping on stability, and observed that increase in the stiffness of the layer inhibits compliance-induced flow instabilities(CIFI), but it will cause destabilization in Class A (T-S waves). Increasing wall thickness will expand the unstable frequency band of Class B (CIFI) instabilities and it helps to stabilize both the Class A (T-S waves) and

the local amplification rates at larger Reynolds number Re_{δ^*} . If the damping factor is large enough with a thin wall thickness, the CIFI can be suppressed completely; on the other hand, the critical Reynolds number of T-S waves decreases and hence the T-S waves instability is destabilised. He concluded that there are two crucial factors to delay transition; firstly a sufficiently thick layer to give good Class A (T-S waves) stability performance at higher Reynolds number Re_{δ^*} and secondly sufficient material damping to suppress the Class B (CIFI).

With regard to the boundary layer receptivity research, Reza (2003) used a velocity-vorticity model to investigate the receptivity and transition in the boundary layer over a rigid and compliant surface. The numerical results showed that the compliant surfaces are less susceptible to the growth of Klebanoff-mode waves compared to a rigid wall and the free stream turbulence generates weaker disturbances over a compliant surface. The compliant surface reduces the growth of the streaks. The streaks are weakened by the flexible surface and the spanwise spacing of streaks is increased.

Joslin and Morris(1992) investigated the effect of compliant surface on the secondary instability and found the use of compliant surfaces leads to a significant reduction of growth rate and amplification in the secondary instability. An optimal compliant surface also suppresses the growth and subsequent amplification of primary instability and it delays an explosive secondary instability mechanism.

So far, the use of a compliant surface has been agreed in the majority of literatures to have benefits in reducing skin-friction drag or delay transition.

2.4.3 Optimised properties of the compliant wall

According to the classifications of instability, a compliant wall should have high flexibility and low damping to inhibit the Class A waves. The damping must be large enough to suppress the Class B waves and the compliance must not be so large that the Class C Kelvin-Helmholtz instability can occur. When all these conditions are applied together it makes choosing the compliant surface difficult, as an optimized compliant surface must consider all these factors.

Yeo (1988) studied the influence of wall compliance and damping factor on the Tollmien-Schlichting instability and compliance-induced flow instability (CIFI) and a specific class of four-layer walls was studied to simulate the original Kramer compliant surface. The optimal surface property would be able to suppress the CIFI effectively and keep a low spatial amplification rate for T-S waves. The optimal 4-layer compliant surface has the same order of thickness and Young's modulus as the best of Kramer's original walls obtained from Carpenter & Garrad (1985)'s prediction. The 4-layer wall was composed of one thin, hard layer and three thick, soft layers. The properties of the compliant surfaces used in their study are shown in table 2.1.The wall exhibited potential to extend transition distances to 5.6 times that of a rigid wall.

Dixon et al. (1994) used spectral methods to solve the Orr-Sommerfeld eigenvalue problem for a compliant-wall to investigate the Tollmien-Schlichting Wave instability and Traveling-wave flutter instability. In their research they found that in order to eliminate the Traveling-wave Flutter over a fixed depth of compliant coating, they needed to use a soft substrate (low shear modulus G) accompanied by high wall damping. The growth ratio of Tollmien-Schlichting waves reduced with

decreasing shear modulus until the optimal combination of properties shear modulus G_s=0.55 with damping factor $\xi_s = 0.05$. Further reduction in shear modulus will cause the local amplitude of Traveling-wave Flutter to rise again. They considered the e^7 transition criterion for growth of T-S waves. The onset of transition was delayed from Reynolds number (Re_{δ^*}) 2700 for a rigid wall to 4300 for optimal surface properties, ie, the transition has been delayed 2.5 fold[1]. They also indicated that a two-layer compliant surface provides a more profound effect to suppress the T-S waves, especially at high Reynolds number. The optimized properties of the two-layer wall can delay transition by a factor of 5 times when compared with the rigid wall result.

Davies and Carpenter (1997) concluded that in order to completely suppress the T-S waves in all ranges of Reynolds number, locally tailor made wall properties are needed. The best way to achieve this in practice would be to have a series of relatively short compliant panels (even as short as one T-S wavelength or less) each having properties to match its range of Reynolds numbers. Another advantage of using a series of small panels is that the small panels are less vulnerable to hydroelastic instability than a long one. According to Carpenter's (1993) results even the use of only two panels can lead to a substantial rise in the transition delay compared to a long invariant compliant surface. He used the $e^N (N \approx 7)$ transition model to predict transitional Reynolds number on single- and two-panel compliant walls and compared to rigid wall, transitional Reynolds number is delayed 4.6 and

---

[1] The transition delay factor was defined by Transition delay factor=$\left(\frac{\mathrm{Re}_{\delta^* \, compliant\ surface}}{\mathrm{Re}_{\delta^* \, Rigid\ wall}} \right)^2$

6.05 times respectively.

2.4.4 The junction effect at leading edge

The investigation of the incident wave propagating over the junction between the two wave-bearing medium has been done by Carpenter et al. (2002). If the T-S wave is above the cut-off natural frequency of the compliant surface, three propagating eigenfunctions are found. First of all, in the near leading edge region, a slow-decaying, relative long wave is created by a pseudo-driver at the leading edge. Secondly, the T-S wave will virtually disappear if a sufficient long compliant surface panel is used. The third mode is a vortical wall mode which propagates upstream and can be coupled with a T-S wave and becomes the sole source of the T-S wave downstream of the compliant surface.

Davies and Carpenter (1997) examined the evolution of Tollmien-Schlichting waves over finite compliant panels, and the streamwise development of disturbance kinetic energy propagating on a compliant coating. The results showed that the T-S frequency was either above or below the cut-off natural frequency of the compliant surface coating. The adjustment of the T-S wave with the change from rigid to compliant wall is very rapid. The rapid changes in disturbance kinetic energy at the edge of the compliant panel are mainly due to rapid changes in the streamwise velocity component. In the simulation, no matter whether the T-S wave is above or under the compliant surface cut-off frequency, an abrupt increase of kinetic energy occurs at the edge of the compliant panel which decays in the streamwise direction. The rapid streamwise variations would tend to increase the

receptivity of boundary layers to free stream disturbances, and the sharp changes may result in early turbulent breakdown.

Reza (2003) tested the local behaviour of the panel edges, and tried to identify the local disturbances which occur at the leading edge and trailing edge. He argued that local disturbances generated at leading edge may produce a T-S wave or wall-based instability. The results showed that a T-S wave propagates along the edge of panel; the integral kinetic energy is amplified and reaches a maximum in the vicinity of the leading edge. The amplitude spike of the disturbance at the leading edge may lead to premature transition due to the fact that the amplitude of the incident T-S wave becomes sufficiently large. The increasing wall compliance can not reduce the amplification caused by the junction between the rigid and compliant walls, but it can be controlled by altering the surface geometry.

The junction effect of the compliant surface panel may have great influence on the use of a compliant surface.

CHAPTER THREE

EXPERIMENTAL APPARATUS AND PROCEDURES

3.1 Introduction

The aim of the experiment was to examine whether boundary layer receptivity has an influence on the use of a compliant surface and results in laminar-turbulent transition delay. A hot-wire anemometer was used to measure the change of flow characteristics in the boundary layer such as velocity perturbations, intermittency and energy spectra. Gelatine was chosen for the compliant surface material and was modelled in the ABAQUS finite element software to identify the property parameters. In this chapter, the details of the experimental procedures and apparatus are shown and techniques for the measurements using either in the anemometer or in defining the compliant surface parameters.

3.2 Wind tunnel

The experiments were carried out in an open-circuit, low speed wind tunnel in the Aerodynamics laboratory in the Department of Engineering at the University of Liverpool. This tunnel is equipped with a 5 BHP electric AC motor which drives a fan rotating at a constant angular speed. The range of the wind speed in the current wind tunnel can be varied from 3~20m/s. The test section is the outlet section of the

tunnel and measures 1050mm long×310mm wide×155mm high. The test section had a perspex roof to permit observation of the measurement locations. The test plate was located at the mid height within the test section with the traverse gear clamped at the downstream end of the plate. The details of the wind tunnel with the test section are shown in Figure 3.1(a).

Without placing any grid in the wind tunnel, the mean free stream turbulence level is 0.3% at the leading edge of the test plate. However, for bypass transition, the turbulence level needs to be above 1% (Morkovin 1969) and so in order to increase the free stream turbulence level to meet this criterion a grid is necessary.

The grid used was placed 430mm in front of the leading edge. The mesh size is 12mmx12mm, and the wire is 1.2mm in diameter. The grid porosity is 0.826 (Roach, 1986). The grid increases the turbulence level to 1.8% at the leading edge. Figure 3.1(b) shows the grid. The evolutions of free stream velocity and turbulence level along the plate are shown in the figure 3.2(a) and 3.2(b).

In the current experiments, the wind tunnel speed for the boundary layer receptivity measurements was between 3m/s and 9m/s. The wind tunnel speed was increased for the transition zone measurements such that at the end of transition the velocity was 16m/s.

3.3 Electronic devices

In the current project, a hot-wire anemometer was used to obtain experimental data. A DISA 55P15 boundary layer hot-wire probe was connected to a DISA 55M51 constant Temperature Anemometer (CTA) with a DISA 55D26 signal

conditioner. All of the signals were recorded on a computer via a 16 bit National instrument AT-MIO-16XE-50 Data Acquisition (DAQ) device. The AT-MIO-16XE-50 DAQ is equipped with 8 analogue inputs and 8 digital I/O lines and it was interfaced with Labview software to automate the motion of the traverse stepper-motor and data acquisition. For an analogue input, the maximum sampling frequency is 20,000samples/second if only one channel is used. This frequency limit is sufficient to resolve a turbulent flow. A displacement sensor was also used to measure movement of the compliant surface. A list of the electronic devices for the measurements is:

- DISA 55M51 constant Temperature Anemometer (CTA)
- DISA 55P15 boundary layer hot-wire probe
- DISA 55D26 signal conditioner
- 16 bit National instrument AT-MIO-16XE-50 DAQ card
- Pentium III-500 desktop PC
- Oscilloscope
- Displacement Sensor (Omron Z4W)

Figure 3.3 shows the schematic of the electronic equipment.

3.4 The test plate and compliant surface

The test plate is made of polished aluminium of 15mm thickness. An elliptical leading edge (the axis ratio is 6:1) was used to prevent separation. The full size of the plate is 618mm long ×290mm wide×15mm thick. Figure 3.4 shows the

dimensions of the plate. One side of the plate was designed for compliant surface experiments and one side for rigid wall experiments, therefore, a symmetric leading edge was used to ensure identical influence for each flow at the leading edge.

The plate was located horizontally at the centre height in the wind tunnel section. The plate could be inverted such that the test surface was always the upper one. The rigid surface experiments were performed first, so that they could be validated against previous studies and also used as a benchmark for the compliant surface results. The compliant surface side of the plate has a cavity which was filled with a compliant material. The default depth of the compliant surface was 8mm and the capacity of the cavity in the plate was 1.38 litres.

3.5 Traverse gear design

A traverse gear was used to move a hot-wire across the boundary layer, and so an accurate control system to place the probe in a precise position is essential. The traverse gear was driven by an electromechanical stepper motor to control the vertical movement of the hot-wire probe. The Labview program was used to control the motion of the traverse gear by sending digital pulses to the stepper motor. Two digital pulsed signals were sent from the interface card through the digital I/O lines which are connected to the stepper motor. One of the signals determines the direction of the stepper motor and the other one controls the motor steps.

The traverse gear was designed to access any position in the horizontal direction and is fixed at the end of the plate for two reasons. Firstly, the height of the test section is limited. Secondly, the traverse mechanism can not be supported on a

compliant surface and fixing the traverse gear at the end of plate is an efficient solution. One of the benefits of fixing the traverse gear at the end of the plate is it ensures that the traverse gear moves with the plate if any vibration occurs and hence minimises the effect from vibration. The hot-wire probe support mount slides on the slope of a triangle block which is connected to the lead screw of the stepper motor to convert the horizontal movement into a vertical one as shown in figure 3.4. By controlling the lead screw which moves forwards and backwards, the probe can be moved up and down. The traverse gear design and installation are shown in figure 3.5. The minimum vertical movement of the hot-wire was 0.01mm which corresponds to one step of the motor.

In each set of measurements, the probe was traversed through 40 points across the boundary layer. In the laminar flow, the velocity increases gradually across the boundary layer, so the height increment was set as a constant. However, there is a dramatic velocity increase in the near wall region in a transitional flow or turbulent flow. A logarithm height increment (eq.3.1) was applied so that the measuring points are more concentrated near the surface.

$$H_t = 0.01 \times \left(10^{\frac{n-1}{40} \times 3} \right) \text{ (mm)} \tag{3.1}$$

where n is n^{th} step

3.6 Hot-wire measurement

The hot-wire anemometer has been used extensively for many decades as a research tool in fluid mechanics, therefore the technique is mature and developed. In

the current experiments, a Dantec miniature single-wire boundary layer probe (Probe type 55P15) was used. The wire is made of Tungsten and its effective length is 1.25mm and diameter is 5μm. A hot-wire is able to response to turbulent flow fluctuations to a high frequency. A Dantec Type M55-10series Constant Temperature Anemometer (CTA) was used to maintain the hot-wire at constant temperature and provide the output signal. The overheat ratio was set up at a resistive overheat of 80%.

The main function of the CTA is to maintain the hot-wire temperature by adjusting the supply current and to output the amplified Voltage. The CTA was connected with the NI- DAQ device to transfer all voltage information. In this experiment, a 16-bit, 20k/s, DAQ card (National instrument AT-MIO-16XE-50) was used. The voltage range of the DAQ card was set at 0~5 volts, thus the absolute accuracy of the DAQ device is 1.386 mv. It was calibrated and tested by National Instruments. The sampling rate was set as 10k Hz for a period of time of 50 seconds; and so 500,000 data were stored for each traverse step. 40 traverse steps were taken for each boundary layer profile.

3.6.1 Hot-wire calibration

The hot-wire calibration took place in two wind tunnels. This is because the lowest wind speed of the main wind tunnel test section was in excess of 3m/s. In order to calibrate from 0~3 m/s, a lower speed wind tunnel is needed. The second wind tunnel is also located in the Department of Engineering and provided the lower wind speed and hence increased the accuracy of the calibration. A pressure

transducer, a manometer and electronic devices for hot-wire measurement were used for calibration procedures. The hot-wire probe is placed adjacent to a Pitot static tube which is connected to a manometer and a pressure transducer. The resolution of the pressure transducer is 0.1 Pa. Voltage and static pressure data were recorded. Bernoulli's law was used to convert from pressure to wind speed in the range from 0.5~16.5m/s.

The hot-wire responds according to King's law:

$$E_{voltage}{}^2 = E_{voltage,0}{}^2 + bU^n \tag{3.2}$$

Where $E_{voltage}$ is the voltage across the wire, U is the velocity of the flow normal to the wire. $E_{voltage,0}$, b and n are empirical constants. By applying a least squares fitting technique to the velocity and voltage data, the coefficients $E_{voltage,0}$, b and n in King's law can be obtained. The calibration results are shown in figure 3.6. In the test, the temperature was measured each day to correct the air density and viscosity. In order to compensate for temperature variation during a day, every three hours the anemometer resistance was adjusted for zero flow until the $E_{voltage,0}$ value measured during calibration was obtained. This adjustment ensures that the measurements are all taken with the same overheat ratio no matter what the ambient temperature.

3.7 Materials for the compliant surface

One of the objectives of this experiment is to find the difference in the pre-transitional flow over a rigid surface and a compliant surface. In order to observe the effect of compliant surfaces, a soft, high compliance material was suggested

(Carpenter, 1993). The application and availability of the compliant surface material should also be considered .The material should have the following features:

1. The free surface must be smooth and flush with rigid section at the leading edge.
2. The coating must be homogeneous over the entire layer.
3. Air bubbles must be avoided inside the coating, as it will change the properties.
4. The elastic coefficient of the coating has to be very low and the coating must be able to be deformed by typical forces resulting from the moving air. However, permanent deformation must not occur.
5. The properties of the coating must not change too dramatically during the experiments (24 Hours).
6. The materials have to be easy to obtain and apply to the plate.

To satisfy all the considerations above, gelatine was chosen for this experiment. Gelatine is a substantially pure protein food ingredient, obtained by the thermal denaturation of collagen. Gelatine swells or hydrates when stirred into water. The gelatine process is highly dependent on the solvent temperature, for example, on warming to about 40°C and allowing to hydrate for about 30 minutes, it melts to give a uniform solution. However, if the dry gelatine is dissolved into water at 100°C a dilute solution of the gelatine results. The solvent also affects the hardness of the gelatine. The gelatine in aqueous solution with polyhydric alcohols like glycerol, proplyene glycol, sorbitol etc, results in a firmer gelatine film. In the current experiments, water was used as the solvent for safety and availability reasons.

3.8 Installation of the compliant surface

Different gelatine mixtures can alter the Young's modulus and damping factor of a compliant surface. One of the issues affecting the gelatine properties is solvent temperature. In order to have consistent manufacture procedures, all gelatine powders were dissolved in water at 100°C and the gelatine liquid left to cool down until the temperature of the liquid dropped to 60°C. The gelatine was then poured into the cavity in the aluminium plate. One big problem in the installation of the gelatine coating is to have a flush leading edge. Water gradually evaporates from the gelatine hence the compliant surface thickness decreases along the whole plate. A gap between the leading edge section and the gelatine coating due to shrinkage could also result in flow separation. In order to overcome this problem, cling film (PVC) of thickness 0.1mm ($E = 17kN/m^2$)was placed over the gelatine to prevent the water evaporation and keep the compliant surface the same thickness for the whole experimental time and also to retain a flush leading edge. Another reason to use cling film is that the calculation done by Gaster (1987) indicates a homogenous viscoelastic layer with a thin layer on top has improved stabilizing characteristics compared to a plain homogenous layer. According to this point of view, a cling film layer on top of the gelatine layer can eliminate instability effects within the layer and maximise ability to reduce the boundary layer receptivity.

3.9 Determination of compliant surface properties

Determination of the properties of the compliant surface is an important task but conventional engineering methods are not suitable in the current study. In the following section, an alternative method is presented.

3.9.1 Measuring Young's modulus

Gelatine is a very soft and fragile material; therefore, it is very difficult to use a conventional tension test to measure the Young's modulus. An alternative way to measure the Young's modulus is using Finite Element modelling as suggested by Samani et al.(2003). Samani used an indirect method to obtain the Young's modulus on adipose tissues. The technique worked out the force-displacement indentation response and then determined the tissue's Young's modulus via a theoretical relationship. The theoretical work indicated Young's Modulus (E) is a function of a specimen calibration factor K_1 and force–displacement slope(S_1).

$$E = K_1 S_1 \tag{3.3}$$

K_1 depends on the geometry and boundary conditions but is unrelated to the Young's Modulus. In other words, if a factor K_1 of the specimen can be specified, then Young's Modulus can be obtained by measuring the force-deformation slope. In the current project, Finite Element modelling is using to find the specimen calibration factor K_1.

The ABAQUS Finite Element Software has been widely used for many industrial and academic applications, and it was used in the current project to simulate the deformation of the gelatine coating under certain loads. The boundary

conditions and geometry domain were set up to match the experimental compliant coating (618mm x 290 mm x 8mm), and a load (mass of 50 grams and contact area of 1010 mm^2) was placed at the centre of the surface. The model and meshes are showed in figure 3.7.

The purpose of the simulation was to find out the displacement of the gelatine coating is response to the known force loads. The simulation results are shown in figure 3.8(a) ~(c). Around the edge of the weight, the gelatine is pushed up and the maximum deformation occurs in the centre of the load. This phenomenon was also observed in the experiments.

In the simulation 15 different Young's modulus conditions were tested. The measuring point of displacement is taken at the centre of the load, which is the valley of the deformation. Figure 3.9 shows the Young's modulus against displacement for masses of 10 and 50 grams.

In order to measure the load-displacement slope, a displacement Sensor (Omron LED displacement Sensor model type Z4W-V) was used. The response time of the device is 5ms which corresponds to 200Hz. The resolution of the sensor is 10μm and the tolerance is 0.1mm, the accuracy is 0.1mm. In the experiments, the 10 or 50 grams mass were applied to the centre of the compliant coating which resulted in a displacement of over 0.1mm. The vertical displacement was recorded and then using figure 3.8, the Young's modulus of the material was determined.

3.9.2 Damping factor

Another key property is the damping factor (Γ). In order to define the damping

factor, the compliant surface is regarded as a mass, damper and spring system, as shown in figure 3.10. In a single degree of freedom system, the displacement response x to an initial amplitude x_0 can be written as (Thomson & Dahleh, 1997)

$$x(t) = x_o \cos(\omega_d t - \Phi)\exp(-\varsigma\omega_n t) \tag{3.4}$$

where ω_n is the natural frequency, ω_d is the damped frequency, x_0 is the initial displacement, ς is the damping ratio, $x(t)$ is the displacement, t is the time and Φ is the initial phase angle.

This displacement is shown in figure 3.11

In the experiments, a 50 gram mass was released from a fix height (10 mm) above the compliant surface. The displacements of the mass were recorded. Figure 3.12 shows a typical measured displacement plot for the system. ς can be found from the maximum amplitudes x_i and x_{i+1} of consecutive cycles in the decaying signal.

$$\varsigma = \frac{\ln(\frac{x_i}{x_{i+1}})}{\sqrt{(2\pi)^2 + (\ln(\frac{x_i}{x_{i+1}}))^2}} \tag{3.5}$$

Figure 3.13 shows the energy spectrum for the displacement from which the damped frequency ω_d can be determined. The spring constant $k_{dynamic}$ and system damping factor Γ are then given by

$$k_{dynamic} = m(\frac{\omega_d}{\sqrt{1-\varsigma^2}})^2 \tag{3.6}$$

$$\Gamma = 2m\omega_d \frac{\varsigma}{\sqrt{1-\varsigma^2}} \tag{3.7}$$

where m is the mass in the damper spring system.

3.9.3 Comparison of measurements of the compliant surface properties

If the system concerned can be modelled as a mass spring damper system, the Young's modulus measured statically can be compared with the value measured dynamically by using equation 3.8 and 3.9.

The Young's modulus is defined as :

$$E = \frac{F/A_m}{\Delta\ell/L} = \frac{F}{\Delta\ell}\frac{L}{A_m} \tag{3.8}$$

where

F : *load force*, $\Delta\ell$: *displacement*, L : *thickness of coating*, A_m : *area of loading*

$$\frac{F}{\Delta\ell} = k_{dynamic} \tag{3.9a}$$

$$k_{dynamic} = E\frac{A_m}{L} \tag{3.9b}$$

In the previous section, system damping factor and dynamic spring stiffness were calculated. The two different methods for the same measured area should have the same spring stiffness. The comparison between static spring stiffness and dynamic stiffness is showed in figure3.14 and figure 3.15. There is a very good agreement between the two different methods of calculating spring stiffness and Young's modulus. In general, the dynamic spring stiffness is lower than the static one. This may be due to the energy loss during the impact. Also, a mass spring damper system is not completely accurate model as the mass is distributed, i.e. the spring itself has mass.

The measured system damping factor depends on the parameters of measured area and the coating thickness and this means the system damping factor is not a material property. A damping factor which is independent to these parameters is needed. The damping factor, like the spring constant, is proportional to L and $1/A_m$ and so the material damping factor ξ can be identified as

$$\xi = \Gamma \frac{L}{A_m} \tag{3.9c}$$

The compliant surface properties used in the current study were measured and are shown in table 3.1a .

3.10 Experimental errors estimate

During calibration and experiments using the hot wire, various errors will result. Depending on the environmental circumstances, some of these errors are difficult to reduce, although special procedures were adopted and corrections used to minimise the errors. The current measurements were focused on the boundary layer fluctuations which are provoked by free stream disturbances. The measurement of comparative velocity fluctuations incur less error compared to the mean velocity measurements. The boundary layer receptivity depends on a ratio between fluctuations in the boundary layer and the free stream. Thus, systematic measurement errors associated with both (e.g. errors in calibration) can cancel out. A few important sources of error in the current experiments are

- Drift, noise, repeatability and frequency response of CTA
- Calibration equipment
- Data acquisition related uncertainties
- Vibration of the test system
- Variation in ambient temperature
- Erosion of the hot-wire
- Misalignment angle of hot wire
- Error in determining intermittency
- Manufacture errors at the compliant surface/rigid surface interface
- Manufacture accuracy of the compliant surface

3.10.1 Drift, noise, repeatability and frequency response of CTA

In the current experiments, a Dantec constant temperature anemometer was used. Also, the experiments did not involve any measurements approaching the frequency limit for the anemometer. Therefore, there is no significant uncertainty associated with high frequencies. (Dantec Manual, 1990). The frequency characteristic of the anemometer will not add to the uncertainty, when the frequencies in the flow are below approximately 50% of the cut-off frequency (from the square wave test), which is the case here, as the characteristic is normally flat up to this point. (Dantec Manual, 1990).

3.10.2 Calibration equipment

The calibration procedure constitutes a major source of uncertainty. The current calibration was performed using a pitot tube and inclined manometer. The error in the velocity is related to the error in the manometer reading by

$$\frac{\Delta U}{U} = \frac{\rho_{meths} \times 9.81 \Delta h \sin \alpha}{\rho_{air} U^2}. \tag{3.10}$$

where in this case $\alpha = 15$ degrees. The error Δh in the manometer reading was estimated as 0.1mm and therefore the maximum error in the velocity is 3.4% at the lowest tunnel velocity of 3m/s. As the wind tunnel speed increases, the error decreases rapidly so when the wind speed exceeds 5.5m/s, the error in velocity is below 1%. For the full calibration between 3~15 m/s, the average error in velocity is 0.85%.

3.10.3 Data acquisition related uncertainties

In the current experiments, a 5 volt range and 16 bit resolution A/D card was used, and hence the anemometer voltage is resolved to $\frac{5}{2^{16}} = 8 \times 10^{-5}$ volts. This error has a negligible effect on the velocity measurement.

3.10.4 Vibration of test system

Some vibration of the wind tunnel was unavoidable in the wind tunnel experiments, especially at high velocity. (The vibration increased with wind tunnel speed.) The effect of the vibration at 15 m/s was measured as a maximum wind

tunnel section vertical displacement of 0.2mm~0.5mm. This displacement is small, but any relative motion between the tunnel and hot wire probe can lead to significant measurement error in the thin boundary layer. It can be shown that for a zero pressure gradient boundary layer the change in probe velocity Δu is related to the change in position Δy by $\frac{\Delta u}{u} = \frac{1}{0.332} \mathrm{Re}_x^{0.5} \frac{\Delta y}{x}$ in the boundary layer close to the wall. In this case where at the first measurement station x=112 mm and Re_x=56300, a vibration of amplitude 0.5mm would lead to an error in the rms velocity reading of Δu = 24m/s. The traverse gear was fixed at the end of the plate, so that the motion of the plate and probe were common, and so the relative motion between probe and plate is much smaller. The actual error clearly can not exceed the minimum rms velocity measured in the boundary layer which is typically 0.75 m/s. The actual error can be estimated by extrapolating the rms velocity profile to the wall where the value should be zero. The error estimated by this means is about 0.02 m/s in rms velocity. Vibration has a negligible effect on the mean velocity measurement.

3.10.5 Variation of ambient temperature

The heat transfer from the hot wire is proportional to the difference between the wire and air temperature. If the air temperature changes without a change in wire operating temperature being made an erroneous velocity reading will result. The error in the wire voltage $\Delta E_{voltage}$ is related to the change in air temperature ΔT by

$$\frac{\Delta E_{voltage}}{E_{voltage}} = \left[\left(\frac{(\alpha_{overheatratio} - 1)T_0}{(\alpha_{overheatratio} - 1)T_0 - \Delta T} \right)^{0.5} - 1 \right] \tag{3.11}$$

where T_0 is the initial ambient temperature.(Dantec,2002) From King's law it also follows that

$$\frac{\Delta u}{u} = \frac{2E_{voltage}\Delta E_{voltage}}{n(E_{voltage}^{\ 2} - E_{0,voltage}^{\ 2})} \tag{3.12}$$

and hence

$$\frac{\Delta u}{u} = \frac{2E_{voltage}^{\ 2}\left[\left(\frac{(\alpha_{overheatratio} - 1)T_0}{(\alpha_{overheatratio} - 1)T_0 - \Delta T} \right)^{0.5} - 1 \right]}{n(E_{voltage}^{\ 2} - E_{0,voltage}^{\ 2})} \tag{3.13}$$

where $\alpha_{overheatratio}$ is the which was used 1.8 throughout the current work. To minimise this error the overheat ratio was adjusted to 1.8 (by setting $E_{0,voltage}$, with no flow past the wire, back to the calibration value) every three hours. The maximum change in air temperature was 1°C during this time and hence from the above equation and typical values for $E_{voltage}$, $E_{0,voltage}$,n and T_0, $\frac{\Delta u}{u} = 0.011$. i.e. a maximum error of 1.1% in mean velocity. It should be noted that this source of error has a negligible effect on the local turbulence levels, which are used in the boundary layer receptivity work. Variation in ambient temperature will also lead to an error in determination of air density and viscosity. Air temperature was measured each day and the variation during the day in the lab was never greater than 3°C. This results in a 1% error each in air density and viscosity.

3.10.6 Erosion of hot-wire

Erosion of the hot-wire also affects the flow readings by changing the cold resistance of the wire. To avoid measurement errors caused by erosion of the hot-wire, the wire was replaced every 3 months.

3.10.7 Misalignment angle of hot-wire

When a hot-wire is placed so that its axis is not perpendicular to the flow direction, there will be a component of velocity that is parallel to the axis of the sensor. The effective cooling velocity that the sensor experiences is approximately that which is perpendicular to the sensor; the parallel component has much less effect. Thus, the effective cooling velocity U_{eff} can be obtained from the expression

$$U_{eff} = U\cos\alpha, \tag{3.14}$$

where α is the yaw angle between the flow vector and the normal to the axis of the probe.

According to $U_{eff} = U\cos\alpha$, if the angle is 5 degrees, the error in the reading is 0.4%. In the current experiment, the misalignment angle of the probe is always less than 5 degrees, thus the estimate error is less than 0.4 %.

3.10.8 Error in determining intermittency

The algorithm used in the current work has been developed over a number of years at Liverpool and has been used extensively for determination of intermittency in boundary layers for a wide range of streamwise pressure gradients and freestream turbulence levels. The algorithm is most accurate for low freestream turbulence

levels, as in the present case, where there is a large ratio (usually greater than 10) between the average fluctuation frequency in the laminar and turbulent periods, which means the low pass filtering procedure is effective and not highly sensitive to the filter frequency setting. The ratio of fluctuation amplitudes in the laminar and turbulent periods is also high which means the calculated intermittency is not sensitive to the window size chosen. In these circumstances the error associated with the intermittency has been established in previous work as less than 1%. This error is therefore most significant for intermittencies close to the start and end of transition and it is therefore important to consider the intermittency of the full transition region when estimating the start and end of transition locations.

3.10.9 Manufacturing accuracy of the compliant surfaces

The compliant surface material (gelatine) was placed in the cavity in the plate. During the gelatine setting process, some water evaporates and shrinkage leads to a concave surface forming. This concave surface could result in Taylor Goertler vortices, which promote transition (Dris and Johnson, 2005). In the current experiments, the curvature results from shrinkage of the compliant material and leads to a minimum radius of curvature of 2100 m. This concave effect is too small to cause significant Taylor-Goertler vortex activity.

3.10.10 Manufacturing errors at the compliant surface/rigid surface interface

The main difficulty in the accurate manufacture of the compliant surface is the junction of the rigid wall and compliant surface. If the surface here is not smooth, a

discontinuity will result in a backward- facing step and a separation bubble will form after the junction. The velocity profile will distort after the junction and will lead to a change in Re_θ^2/Re_x. The best fit lines to the rigid and compliant surface results are $Re_\theta^2 = 0.4919 Re_x$ and $Re_\theta^2 = 0.4878 Re_x$ respectively. (Figure 3.16) The gradient difference is 0.83% and this provides a measure of the effect on the boundary layer of manufacturing defects in the geometry of the compliant surface.

3.10.11 Summary of experimental errors

If all these sources of error are taken into account the error in mean velocity measurement is 5.5% at 3m/s (due to the calibration and temperature variations), but drops to less 2.5% for the velocity above 6 m/s. In the case of fluctuating velocity the error is smaller at about 0.02 m/s. The error in Reynolds number due to velocity calibration and ambient temperature variation is up to 4.5% at 6m/s and for intermittency measurement is 1%.

3.11 Data processing

3.11.1 Programming and data acquisition

All the flow measurements were controlled by National instruments Labview 7.0 programs. Post-analysis, such as intermittency calculation, flow quantities and energy spectra were calculated using Matlab. The data logging, traverse gear control system and post-analysis programs were developed by the author. The procedures were validated using a wave generator and vernier caliper. The wave generator created a signal with a certain frequency of either sinusoidal or square wave form

and of known amplitude. The DAQ card receives this signals and determines its frequency (using Fast Fourier Transform) and its magnitude. The maximum difference of measured magnitude and actual one is 3mV. As the hot wire calibration was performed using the card this discrepancy will not affect to the results. The distance moved by the traverse was checked using the vernier caliper and the vertical movement for one step of the motor verified. The acquisition frequency of the DAQ device is up to 20,000 samples/second, and 10,000 samples /second were recorded on the Pentium III-500 computer in the current experiments.

Labview is a dataflow methodology as shown in figure 3.17 and 3.18. The programs control the traverse gear and data logging. The calibrated King's law was a subroutine built-in to the main program to translate raw voltage readings into velocity data. Therefore, the data were stored as velocity rather than voltage. This is convenient for post data analysis.

3.11.2 Frequency spectrum analysis

In the frequency spectrum analysis, the time domain signals are converted into the frequency domain by using a Fast Fourier transform (FFT). The Fast Fourier transform is simply a methodology for performing Fourier transforms faster on a computer. Each signal containing 500,000 data points was analysed using a Fast Fourier transform to determine the amplitudes (power spectrum density) of each frequency.

To get a smooth spectrum curve, the linear vector-average is used. Each signal was divided into 7 segments and a Hanning window is applied to each individual

segment of 2^16(65536) samples to fill in the vector to a length of 2^18(262144). The absolute value of the FFT of each segment vector was calculated individually. Averaging all segments leads to a smoother spectrum.

3.11.3 Gain calculation

The boundary layer receptivity is a key issue in bypass transition, and it describes the response of a boundary layer to disturbances in the freestream. In order to quantify the boundary layer receptivity, the gain has been used to measure the receptivity mechanism and is defined by Johnson and Ercan (1998, 2002, and 2003).

$$Overall\ Gain = \frac{u_{rms}/u}{U_{rms}/U} = \frac{\left(\int_0^\infty e(f)df\right)^{\frac{1}{2}}}{u} \frac{U}{\left(\int_0^\infty E(f)df\right)^{\frac{1}{2}}} \tag{3.15}$$

The gain for a particular frequency is similarly defined as

$$Gain(f) = \left(\frac{e(f)}{E(f)}\right)^{\frac{1}{2}} \frac{U}{u} \tag{3.16}$$

E(f) :energy spectral density in the free stream

e(f): energy spectral density at the near wall ($y/\delta = 0.2$) location in the boundary layer

The time domain signals can be transferred into the frequency domain by using the Fast Fourier Transform. As a consequence, free stream and boundary layer signals can be transferred into their respective energy spectra. In the experiment, the near wall gain is found by measuring the free stream and boundary layer (near wall

$y/\delta = 0.2$) fluctuation energy spectra and using the equation above. Typical spectra (Matsubara & Alfersson, 2001) measured in the boundary layer and free stream are shown in figure 3.19 and the laminar flow near wall gain response to the frequency is presented in figure 3.20.

3.11.4 Intermittency calculation

The intermittency factor, γ, is the fraction of time that the fluid motion is turbulent. Under laminar flow conditions, γ equals zero, and when the transition starts γ is no longer zero due to the present of turbulent signals and γ reaches 1 when the flow becomes fully turbulent.

The intermittency factor (γ) is calculated as

$$Intermittency(\gamma) = \frac{Turbulence\ Time\ Period}{Total\ Time\ Period(Laminar + Turbulence\ Time\ Period)} \quad (3.17)$$

The detection algorithm to select turbulent events was developed by Fasihfar and Johnson (1992). The method defines the minimum free stream turbulence frequency that can be observed in a velocity signal from the boundary layer as $\frac{U}{2\pi\delta}$, where U is the free stream velocity, and δ is the boundary layer thickness. The filter was set up to remove frequencies below $\frac{U}{2\pi\delta}$ which result from the free stream turbulence. The filtered out signals are due to boundary layer receptivity or laminar instability waves. Figure 3.21(a) shows a typical near wall signal (y/δ=0.2) in a transitional flow, the turbulence bursts can be easily identified and the intermittency

in this case is 12.34%. The filtered signal is shown in figure 3.21(b) where the high pass frequency is set at 363.81 Hz. The burst signals remain and the filtered out signals are purely due to the receptivity mechanism.

3.11.4.1 Window size and residence time

The control window size and residence time is a key issue in correctly identifying a turbulent event. The window size is used to detect the turbulent events. If the signal amplitude exceeds the window size threshold, it is counted as a turbulent event. In order to detect the burst or dropout signals, the residence time is used, if the period is shorter than the residence time threshold time, then the signal is considered as part of the turbulent event.

In the current study, the frequency $U/2\pi\delta$ was used as the high pass frequency. The window size was set up as 10% of the local velocity, and $2\pi\delta/U$ as the residence time. The filtered signals were analysed by a detection algorithm, which counts the laminar and turbulent event proportion in the signals.

In figure 3.21(b), the red lines represent a window size equal to 10% of the local velocity, and figure 3.21(c) shows the algorithm decision on turbulence events. The low part of the red line represents the laminar event, and the high part the turbulent event. The algorithm is therefore able to identify any turbulent event within the signals.

3.12 The near wall definition

In the flow region close to the wall some local flow characteristics do not change, such as the local turbulence level, the intermittency and the boundary layer receptivity. The current experimental results and Ercan's (1997) results suggest for $y/\delta \leq 0.3$, the local turbulence level and gain are invariant. (equation 3.15). In this region, $y/\delta \leq 0.3$, the boundary layer receptivity is greatest to the free stream disturbances. In the current study, the near wall measurements were taken at $y/\delta \approx 0.2$. The flow rate in the region between 0 to $y/\delta \approx 0.2$ in the laminar boundary layer equals the flow rate in turbulent boundary layer between $y^+ = 0$ and $7 \sim 13$, which approximately corresponds to the viscous sublayer $y^+ \leq 5$.

CHAPTER FOUR

EXPERIMENTAL RESULTS

4.1 Introduction

The first investigation on a flow over a compliant surface dates back to 1950. Since then most of the works have been done numerically and focused on stability issues of natural transition. The physical phenomenon of bypass transition in a flow over a compliant coating is still not fully understood so the results of the current research can help to perceive the flow character changes over a compliant surface. The experiments were undertaken to see how the compliant surface made changes to the receptivity mechanism for pre-transitional flow in the boundary layer and how the changes are affected by the coating Young's modulus and damping factor. Another aspect of this experimental work is to examine the effect which compliant surfaces have on the transition delay.

The chapter is divided into two parts; the first part describes the measurements on a rigid plate and how empirical correlations of boundary layer receptivity were established. The second part shows results for the flow over compliant surfaces and the results were compared with the benchmark rigid plate results which were established in part one.

4.2 Measurement of boundary layer quantities on a rigid wall

4.2.1 Laminar boundary layer

The Blasius boundary layer profile is the theoretical mean velocity profile when a laminar flow passes over a flat plate under zero pressure gradient and this profile was used to validate the laminar flow experimental measurements. The all measurement were taken under the free stream turbulence level between 1.0% to 1.7%. Figure 4.1 and 4.2 show a number of mean velocity profiles across the boundary layer for different Re_x and free stream turbulence levels. In figure 4.1, the free stream turbulence level is about 1.65%, and the probe location is x=112 mm measured from leading edge and the free stream velocity was varied. In figure 4.2, the free stream velocity was kept the same and the probe was moved to different downstream locations and hence the free stream turbulence level decreases due to the turbulence decay with streamwise distance. The measured points in both figures closely fitted the Blasius profile i.e. for different x locations, tunnel speeds and turbulence levels.

Figure 4.3 and figure 4.4 show that the variations of the non-dimension rms velocities u'/U with the Blasius function $y\sqrt{\frac{U}{\upsilon x}}=(\eta_{Blasius})$ in the laminar boundary layer for the nominal zero pressure gradient. Figure 4.3 shows fluctuation profiles for different Re_x with a free stream turbulence level equal to 1.65%. The peak fluctuation level at Re_x=25700 is 0.037 and occurs where $\eta_{Blasius}$ is around 1.67. The amplitude of the fluctuations increases with Re_x and the peak in the fluctuations is moving slowly towards the wall as Re_x increases. Results in figure 4.4 show the fluctuation profiles at different streamwise locations with a constant wind speed, so

the free stream turbulence level is decreasing with Re_x. Fluctuation profiles in figure 4.4 show similar trends to figure 4.3, the peak is increasing with Re_x but also decreasing with downstream distance due to the decrease in free stream turbulence level. A higher Re_x is therefore accompanied by a lower free stream turbulence. The profiles therefore are very close to each other.

Local turbulence level profiles for a laminar flow are shown in figure 4.5 and figure 4.6. The boundary layer receptivity or overall gain is defined as

$$\frac{u_{rms}/u}{U_{rms}/U} = \frac{local\ turbulence}{F.S.\ turbulence}, \tag{4.1}$$

so if the turbulence level in the free stream is fixed, then the local turbulence level is proportional to overall gain. Ercan (1997) measured local turbulence level profiles of laminar flows and the results showed that the overall gain profile across the boundary layer did not change until the y/δ exceeded 0.3. In the current experiments, for $\eta_{Blasius}$ <1.25 (y/δ <0.3), the local turbulence level is fairly constant and the decrease for y/δ >0.3 corresponding with the same phenomena observed by Ercan. In figure 4.6, the profile at Re_x =208500 is close to the start of transition and the local turbulence level near the wall reaches 21%. Dris (2003) measured the onset transition local turbulence level on a flat plate for different pressure gradient, and found it ranged from 20 to 23%. So, one criterion of start transition is the near wall ($y/\delta = 0.2$) local turbulence level needs to reach 21~23%.

4.2.2 Boundary layer integral quantities

The Boundary layer thickness, δ, is obtained from the mean velocity profile. The boundary layer extends to a distance δ where the velocity reaches 99% of the free stream velocity and this is defined as the edge of boundary layer.

The displacement thickness, δ^*,is determined as $\delta^* = \int_{y=0}^{\delta} (1-\frac{u}{U})dy$ (4.2)

and momentum thickness ,θ ,is $\theta = \int_{y=0}^{\delta} \frac{u}{U}(1-\frac{u}{U})dy$ (4.3)

In order to eliminate the error associated with determining δ , the integration extends into the free stream where both integrands become zero.

Therefore, displacement thickness, δ^* and momentum thickness, θ are calculated as

$$\delta^* = \int_{y=0}^{\infty} (1-\frac{u}{U})dy \tag{4.4}$$

$$\text{and } \theta = \int_{y=0}^{\infty} \frac{u}{U}(1-\frac{u}{U})dy \tag{4.5}$$

The shape factor (H) can be calculated from the displacement and momentum thicknesses as the ratio of δ^* and θ, $H = \frac{\delta^*}{\theta}$. The shape factor varies with Re_θ as shown in figure 4.7. The decrease in the downstream direction is mainly due to a downstream increase in θ in comparison with the Blasius case, whereas the ratio between δ^* and $(vx/U_0)^{1/2}$ in the experiments is close to Blasius value. The reason for an increase in θ is that the unsteady boundary layer perturbations give rise to Reynolds stress which affects the downstream development of the mean flow. Westin et al.(1994) , Roch & Brierley(1992) and Arnal & Juillen (1978) obtained

laminar boundary layer measurements and found the shape factor decreased linearly with the Reynolds number at a rate independent of the free stream velocity.

Blasius(1908) found the exact solution for a zero-pressure laminar boundary layer over a flat plate and the relationship between Re_x and Re_θ is given by

$$\mathrm{Re}_\theta = 0.664\sqrt{\mathrm{Re}_x} \tag{4.6}$$

If the mean velocity profile is represented by the Pohlhausen profile,

$$\frac{u}{U} = 2\left(\frac{y}{\delta}\right) - 2\left(\frac{y}{\delta}\right)^3 + \left(\frac{y}{\delta}\right)^4 + \frac{\lambda}{6}\frac{y}{\delta}\left(1-\frac{y}{\delta}\right)^3 \tag{4.7}$$

the pressure gradient is involved in the correlation between Re_x and Re_θ

$$\frac{\mathrm{Re}_\theta}{\sqrt{\mathrm{Re}_x}} = \sqrt{2\left(\frac{37}{315} - \frac{\lambda}{945} - \frac{\lambda^2}{9072}\right)\left\{\left(2+\frac{\lambda}{6}\right) - \left(\frac{74\lambda}{315} - \frac{2\lambda^2}{945} - \frac{2\lambda^3}{9072}\right) + \left(\frac{3\lambda}{10} - \frac{\lambda^2}{120}\right) - \left(\frac{37\lambda}{315} - \frac{\lambda^2}{945} - \frac{\lambda^3}{9072}\right)\right\}}$$

(4.8) Where $\lambda = \frac{\delta^2}{\nu}\frac{dU}{dx}$

This reduces to $\mathrm{Re}_\theta = 0.685\sqrt{\mathrm{Re}_x}$ for zero pressure gradient $\lambda = 0$.

Reynolds number based on momentum thickness Re_θ against Reynolds number based on x Re_x is exhibited in figure 4.8. If the boundary layer experiences a zero pressure gradient, the relationship between Re_x and Re_θ will follow equation 4.8. The current experimental data fits pressure gradient between $\lambda = 0$ and $\lambda = 2$. (The detail of the pressure gradient calculation is in Appendix A). This therefore indicates that the wind tunnel section is imposing a very slightly favorable pressure gradient.

The skin coefficient C_f is defined as

$$C_f = \frac{\mu(\frac{\partial u}{\partial y})_w}{\frac{1}{2}\rho U^2} \tag{4.9}$$

The Blasius correlation gives,

$$C_f = \frac{0.664}{\sqrt{\mathrm{Re}_x}} \tag{4.10}$$

or

$$C_f = \frac{0.4409}{\mathrm{Re}_\theta} \tag{4.11}$$

Another examination of the results is shown in figure 4.9 and 4.10. These figures present the skin friction coefficient against Re_x and Re_θ, respectively. The skin friction coefficient was calculated by equation 4.9 where the velocity gradient was determined through a straight line fit to the first three data points. The straight line fit typically has a correlation coefficient R^2 >0.90. The data fit the Blasius correlation line, given by equation 4.10 and 4.11. The current measurements agree with the previous studies and showed the reliability of the data acquisition techniques. There is a slightly favorable pressure distribution through the wind tunnel which is due to the blockage associated with the growth of the boundary layer.

4.2.3 Spectrum Analysis

By using the Fast Fourier Transform, the velocity fluctuations signals can be converted into energy spectra. Figure 4.11 show typical energy spectra in the laminar flow. Comparing the magnitude and frequency between the current data and Matsubara &Alderson's experiments (figure 3.17), the tendency is consistent. The

differences appearing in the gain spectrum may result from the differences in Re_θ and wind tunnel speed in the two experiments.

The near wall ($y/\delta = 0.2$) gain spectrum is defined as a power energy level ratio between near wall and free stream (e.q 3.15). The gain spectrum in figure 4.12 shows that the power energy level varies with streamwise frequencies and it can be used to predict the receptivity in the laminar boundary layer. The low frequency has higher gain value compare to the high frequency, so low frequency has most contribution to the receptivity process. Jacobs and Durbin (2001) used DNS calculation to study the bypass transition provoked by free stream turbulence. The simulations showed that the low frequency mode in the free stream enter the boundary layer and produce even lower frequency boundary layer modes. These very low-frequency perturbations are then amplified and elongated in the streamwise direction by the shear. The simulation results agrees with the experimental results in that the low frequency perturbations are dominant the boundary layer receptivity.

4.2.4 Correlation of overall gain

Linear stability theory for laminar boundary layers indicates that transition is predominantly brought about by the amplification of disturbances in the boundary layer. At a critical displacement thickness Reynolds number, the boundary layer becomes susceptible to disturbances that grow and lead to transition. In the experiments, a hot-wire probe was placed at approximately $y/\delta = 0.2$, which is defined as near wall location in the current work, to measure the amplification of

fluctuations originating in the free stream turbulence. 45 different flow conditions have been tested. The laminar Re_θ varied between 59 and 310, and transition started at Re_θ greater than 310. The relationship between overall gain and Re_θ and Re_x are shown in figure 4.13 and figure 4.14 respectively. The results show that there are good correlations between overall gain and Re_θ and Re_x .The empirical correlations in the overall gain $(y/\delta = 0.2)$ are given in the equations 4.12 and 4.13. The boundary layer fluctuation response to the free stream turbulence is linear with Re_θ and it provides strong evidence that the boundary layer receptivity is growing linearly with Re_θ.

The correlation between Re_θ and overall gain is $Gain_{overall}(\mathrm{Re}_\theta) = 0.0423\,\mathrm{Re}_\theta$ (4.12)

The correlation between Re_x and overall gain is $Gain_{overall}(\mathrm{Re}_x) = 0.02954\,\mathrm{Re}_x^{1/2}$ (4.13)

Fransson and Matsubara (2005) studied the bypass transition induced by the free-stream. The free stream turbulence level varied from 1.4% to 6.7%. Experimental results proved that in the initially laminar boundary layer, the disturbed energy $\mathrm{E}(u_{rms}^2/U_\infty^2)$ is proportional to $Tu^2\,\mathrm{Re}_x$. This conclusion is also found in the theoretical results of Andersson et al.(1999) and Luchini(2000) .

The current empirical correlation suggests that

$$\frac{u_{rms}}{u} = 0.02954\,\mathrm{Re}_x^{1/2}\,Tu$$

$$\frac{u_{rms}^2}{U_\infty^2} = 0.0008726\,\mathrm{Re}_x\,Tu^2\,\frac{u^2}{U_\infty^2}$$

and in measurements the $(\frac{u}{U_\infty}) \approx 0.4$ and so

$$\frac{u_{rms}^{\ 2}}{U_\infty^{\ 2}} = 1.39\times10^{-4}\,\mathrm{Re}_x\,Tu^2$$

$$\frac{u_{rms}^{\ 2}}{U_\infty^{\ 2}} \propto \mathrm{Re}_x\,Tu^2 \tag{4.14}$$

The current experimental results therefore lead to the same conclusion. The results showed that the boundary layer receptivity is proportional to $\mathrm{Re}_x^{\ 1/2}$ or Re_θ.

4.2.5 Empirical correlation of gain spectrum

The laminar boundary layer is highly receptive to low frequency velocity perturbations in the free stream turbulence and as demonstrated by Johnson and Ercan's(1997) experiments on a flat plate. They established an empirical correlation where gain is a function of skin-friction coefficient.

$$Gain(\Omega_x) = \frac{1.595E-04}{C_f^{\ -1.827} + (0.015\Omega_x)^2} \tag{4.15}$$

For low frequencies ($\Omega_x = \frac{2\pi f\delta}{U}$, dimensionless frequency less than 0.01) the gain increases with decreasing C_f. The gain starts to decrease when dimensionless frequency is between 0.01 and 0.1.However, Ercan's correlation fits the current results well when Re_θ>200, but underestimates gain when Re_θ is smaller.

Redford (2005) modified Ercan's gain correlations to predict receptivity mechanism in separated boundary layers with a negative skin friction. He used the

Pohlhausen relationship between H and λ, $H = \dfrac{\frac{2}{7} - \frac{\lambda}{120}}{\frac{985}{9009} - \frac{2\lambda}{1485} - \frac{\lambda^2}{9072}}$ and used numerical boundary layer receptivity predictions (Johnson, 2003) to correlate gain as a function of Re_θ and H.

His correlation is

$$Gain(\Omega_x) = \frac{a(H)}{\mathrm{Re}_\theta^{-b} + c(H)\Omega_x^{\,2}} \tag{4.16}$$

where the additional relations are,

$$a(H) = \left(1.17H^2 - 2.9H + 5.81\right)\times 10^{-5}$$
$$b = 2.7$$
$$c(H) = 0.0177H - 0.0229$$

Redford's correlation is suitable for low Re_θ (50~100).

Both Redford and Ercan's prediction of the gain curve is limited to high or low Re_θ, their predictions did not fit well over the whole laminar flow Re_θ range. Therefore, the process of establishing a general gain prediction for all range of Re_θ was investigated here. A typical gain spectrum can be defined by three parameters, the plateau part G_0 which is the low frequency gain, the point, F_c, corresponds to the point where the gain is $1/2\,G_0$, S, decides the slope of the gain decay at high frequency. Therefore, a general form of the gain spectrum can be represented as

$$Gain(\Omega_x) = \frac{G_0}{1 + \left(\frac{\Omega_x}{F_c}\right)^S} \tag{4.17}$$

The three parameters for the gain profile were chosen by nonlinear least-squares data fitting method, which estimates the coefficients of a nonlinear function using least squares.

The correlation of these three parameters for the gain spectra with Re_x and Re_θ are shown in figure 4.15 (a)~(c) and figure 4.16(a)~(c),respectively . There is a very high correlation (R^2 = 0.98 and 0.97) between the low frequency G_0 and Re_x and Re_θ. G_0 increases linearly with Re_θ. G_0 represents the low frequency gain and the low frequency is responsible for the boundary layer receptivity. Blair(1992) and Jacobs & Durbin (2001) also established that laminar boundary layers are most responsive to low frequencies.

The correlation between the slope S and Re_θ is not as strong as for G_0 or F_c, the data are scattering more. However, the general tendency is increasing with Re_θ. The empirical correlation for each coefficient can be represented as a function of Re_θ as follows,

$$G_0 = 2.42\times10^{-4}\,\mathrm{Re}_\theta{}^2 + 7.80\times10^{-2}\,\mathrm{Re}_\theta \tag{4.19}$$

$$\frac{1}{F_c} = 5.53\times10^{-2}\,\mathrm{Re}_\theta + 4.59 \tag{4.20}$$

$$S = 2.10\times10^{-3}\,\mathrm{Re}_\theta + 1.87 \tag{4.21}$$

Therefore, an empirical correlation was established to relate the near wall gain with Re_θ in the boundary layer at $y/\delta = 0.2$

$$Gain(\Omega_x, \mathrm{Re}_\theta) = \frac{2.42\times10^{-4}\,\mathrm{Re}_\theta^{\,2} + 7.80\times10^{-2}\,\mathrm{Re}_\theta}{1+\Omega_x\left(5.53\times10^{-2}\,\mathrm{Re}_\theta + 4.59\right)^{(2.10\times10^{-3}\mathrm{Re}_\theta + 1.87)}} \tag{4.22}$$

Also, all the coefficient can be related to Re_x

$$G_0 = 2.89\times10^{-3}\,\mathrm{Re}_x^{\,0.8} \tag{4.23}$$

$$F_c = 6.96\times10^{-7}\,\mathrm{Re}_x - 5.93\times10^{-4}\,\mathrm{Re}_x^{\,0.5} + 0.18 \tag{4.24}$$

$$S = 3\times10^{-6}\,\mathrm{Re}_x + 2.04 \tag{4.25}$$

$$Gain(\Omega_x, \mathrm{Re}_x) = \frac{2.89\times10^{-3}\,\mathrm{Re}_x^{\,0.8}}{1+\left(\frac{\Omega_x}{6.96\times10^{-7}\,\mathrm{Re}_x - 5.93\times10^{-4}\,\mathrm{Re}_x^{\,0.5} + 0.18}\right)^{(3\times10^{-6}\mathrm{Re}_x + 2.04)}} \tag{4.26}$$

In order to check the empirical gain- Re_θ correlation model, three different Re_θ were chosen to validate the model prediction as shown in figure 4.17. The empirical model provides an excellent fit to near wall signal gain data and hence proves the model is able to give a good near wall boundary layer receptivity correlation through the whole Re_θ range in a laminar flow. The empirical correlation between gain and streamwise frequencies (Ω_X) for various Re_θ is shown in figure 4.18. Johnson and Ercan (1997) measured the near wall gain over a flat plate and obtained similar results. The low frequency plateaus extend to a dimensionless frequency of 0.04 and drop to a gain of 1 at a frequency equal to 0.2. However, the amplitudes of the magnitude of gain spectrum for the current data are a bit higher than in Ercan's experiments. A reasonable explanation of this contradiction is that boundary layer receptivity is influenced not only by free stream

turbulence intensity, which plays the most important role, but also its spatial scale, energy spectrum and degree of isotropy and homogeneity.

In figure 4.19 (b), the contour graph shows that when the dimensionless low frequency is less than 0.02, there is a plateau for each Re_θ.Hence, the region of dimensionless frequency less than 0.02 can be referred to the Gain as a low frequency region. In figure 4.19 (a), it is very obvious that the whole low frequency region gain is increased with Re_θ . The gain starts to decrease when the dimensionless frequency reaches 0.02. The gain has decreased to 1 when the dimensionless frequency equals 0.2.

4.2.6 Start of Transition

The transition detection experiments were performed using hot-wire signals. Intermittency measurements across boundary layer in laminar and turbulent flow were conducted by Ercan (1997) and Klebanoff (1955). Their results demonstrated that the intermittency remains invariant between the wall and $y/\delta \approx 0.2$ in both laminar flow and turbulent flow. In a laminar flow with zero pressure gradient, $y/\delta \approx 0.2$ corresponds to u/U =0.4. In the measurements, the hot-wire probe was placed at a fixed streamwise distance and a point where u/U=0.4 approximately in order to determine the onset of transition.

Once the wire positioned at position the wind tunnel speed was increased gradually until the first turbulence bursts appeared on the oscilloscope when the turbulent event occurrence level (intermittency) was calculated to be between 0.5%~1%, which transition is considered to have started. The hot-wire position then adjusted so that u/U =0.4 again and the intermittency measurement was repeated..

The free stream turbulence level has been identified as one of most important parameters to determine the onset of transition. The author has also examined some previous experimental correlations due to Abu-Ghannam and Shaw(1980) , Mayle(1991), and Ercan(1997) . All the correlations were established on a flat plate with zero pressure gradient and simply defined the start of transition Re_θ to the free stream turbulence level Tu relationship. The correlations are listed as following:
Abu-Ghannam and Shaw(1980) showed the correlation between Re_θ and turbulence level for the start of transition, and in their correlation took account of the minimum stability value of 163 which corresponds to the low part of Tollmien-Schlichting stability loop.

$$\mathrm{Re}_{\theta s} = 163 + \exp(6.91 - 100Tu) \tag{4.27}$$

The skin friction coefficient provides a good indication of the transition location and in the Abu-Ghannam and Shaw's experiment the minimum skin coefficient was regarded as the onset of transition. In the current experiment the location for onset of transition was taken directly from the intermittency 0.5% point.

Mayle(1991) examined several experimental data in the literature and used them to determine a new correlation. The equation was

$$\mathrm{Re}_{\theta s} = \frac{400}{(100Tu)^{5/8}} \tag{4.28}$$

Ercan and Johnson (1997) measured start of transition at various freestream turbulence levels. The results correlated the Re_θ and turbulence level. The equation is

$$\mathrm{Re}_{\theta s} = 370(100Tu)^{-0.625} \tag{4.29}$$

In the current experiment, the hot-wire probe was placed at 9 different streamwise locations and the onset of transition determined for different free stream turbulence levels. The criterion to decide the onset of transition was an intermittency value of 0.5%~1%. The results of onset of transition in the current experiment together with Abu-Ghannam and Shaw and Mayle and Ercan's correlations are illustrated in figure 4.20. Comparing the current data with the Abu-Ghannam and Shaw, and Mayle and Ercan's correlations it can be concluded that the tendencies are similar, but the difference between those curves could be due to different leading edge conditions or turbulence length scale. The results showed that the current data is scattered between Mayle and Ercan's experimental correlation when the free stream turbulence level is less than 1.5%. The transition happened earlier when the free stream turbulence level is higher than 1.5%. Brandt et al. (2004) used DNS to predict the transition for different length scales in the free-stream and the results shown that the transition location moves to lower Reynolds numbers by increasing the integral length scale in the free-stream. A reasonable explanation for differences in the onset of transition can be different integral length scale in the free-stream, and the method to determine the onset of transition.

The onset of transition varies in different experiments because of the definition of the transitional Reynolds number; therefore, if the influence of the compliant surface is to be compared with a rigid surface, a correlation for a rigid surface must be established. Hence, if the free stream turbulence intensity between 1.1% and

1.7%, the empirical correlations between the turbulence level and the $Re_{\theta s}$ (Start of transition) and Re_{xs} are shown as follows:

$$Re_{xs} = -2.66\times10^{11}Tu^3 + 1.17\times10^{10}Tu^2 - 1.88\times10^{08}Tu + 1.24\times10^{06} \quad (4.30)$$

$$Re_{\theta s} = -3.86\times10^{08}Tu^3 + 1.53\times10^{07}Tu^2 - 2.19\times10^{05}Tu + 1416.4 \quad (4.31)$$

4.2.7 Intermittency distribution

The Intermittency distribution provides an insight into the flow phenomena of boundary layer flow transition. Also, the intermittency distribution gives a method to judge transition delay or promotion on a compliant surface. In order to compare with the compliant surface data, results on a rigid surface were measured and validated with experiments from the literature.

Dhawan and Narasimha (1957) considered a breakdown model that assumed all turbulence spots originate at the start of transition location. They examined many experimental data sets and found they all correlated with.

$$Intermittency(\gamma) = 1 - e^{-A\xi^2} \quad (4.32)$$

where $\xi = \dfrac{x - \{x\}_{ts}}{\{x\}_{\gamma=0.75} - \{x\}_{\gamma=0.25}}$, A=0.412

They concluded that whatever the cause of transition, all transition regions have a similar intermittency distribution.

Abu-Ghannam and Shaw(1980) used a similar approach to obtain the intermittency distribution.

$$Intermittency(\gamma) = 1 - e^{-5\eta^3} \quad (4.33)$$

Here $\eta = \frac{\mathrm{Re}_x - \mathrm{Re}_{xs}}{\mathrm{Re}_{xe} - \mathrm{Re}_{xs}}$, Re_{xs} is Reynolds number at start of transition and Re_{xe} is Reynolds number at end of transition.

The results of current experiments are shown in figure 4.22. Two sets of data are shown, and the two intermittency curves are close to each other. When the measured data is compared with Narasimha's correlation, it suggests that the transition region happens in the similar way independent of different environments. The measured data have a better fit with Abu-Ghannam and Shaw's correlation as was also suggested in the Ercan(1997)'s experiments.

4.3 Measurement of boundary layer quantities on compliant surfaces

The compliant surfaces were made of gelatine and the geometry of the test plate is identical with that for a rigid surface (details are in Chapter 3). The only factors changing during the experiments are atmosphere pressure and humidity which vary from day to day. The temperature and pressure were measured for each experiment and allowed for in the data calculation. The uncertainty in the ambient conditions is less than 2% change. (A 3 K change in temperature and 1 kN/m^2 change in pressure) All measurements from the compliant surface were compared with the rigid wall results which were discussed in the previous section. The free stream turbulence level in the test cases ranged from 1.0% to 1.7%.

4.3.1 Laminar boundary layer

The mean velocity across the boundary layer over a compliant surface of 4mm coating thickness is shown in figure 4.23.The current data is fitted very well by the laminar zero pressure gradient Blasius profile. Lee & Fisher (1995) and Gad-el-Hak & Blackwelder (1984), used hot-film and hot-wire anemometry to investigate the interaction and stability issues over a compliant surface respectively. In their measurements, there were no changes in the mean velocity profiles over a compliant surface and the velocity profiles matched the Blasius profile. The current results agree with these measurements and show that the compliant surface does not have a significant effect on the mean velocity.

The measurements showed a compliant surface does not alter the mean flow velocity profile. Therefore, the relationship between Re_x and Re_θ would be similar to the rigid wall results which follows a Pohlhausen Re_x - Re_θ relationship (equation 4.8). The relationship between Re_x and Re_θ over compliant surfaces is shown in figure 4.24. All the data are scatter between the curves for Pohlhausen $\lambda = 0$ and $\lambda = 2$. According to the mean velocity profile and Re_x - Re_θ graph, there is strong evidence that the test environments for the compliant and rigid surface were very similar and hence any changes are due to the compliant surface interaction with the fluid.

4.3.2 The correlation of compliant surface properties and near wall gain

The first series of compliant surface experiments was set up with a coating depth of 8mm (Table 3.1 b) . The free stream velocities were measured as either 4.5 m/s or 6.5 m/s. The gain improvement (ratio of the gain to the rigid wall gain) as a

function of dimensionless Young's modulus and Re_x is shown in figure 4.25 and 4.26. Figure 4.25 and 4.26 have similar trends in gain improvement, but the $U \approx 6.5m/s$ results have a smaller reduction gain area than for $U \approx 4.5m/s$. The region near the leading edge has significant gain amplification with a maximum amplification of 32~34% when $E/\rho U^2$ is around 195 for $U \approx 6.5m/s$, and 26%~28% when $E/\rho U^2$ is around 150 for $U \approx 4.5m/s$. As a result, the magnitude of amplification increases with *U*. The large amplification region grew and the reduction region diminished for higher *U*, and so this results in an earlier onset of transition.

The evidence showed the compliant surface triggered the boundary layer fluctuations at the upstream locations (small Re_x) with a reduction in the receptivity in the streamwise direction.

The gain reduction can be seen for $U \approx 4.5m/s$, when $Re_x \geq 10000$ and for $U \approx 6.5m/s$ when $Re_x \geq 115000$. Unfortunately, the reduction of gain at the downstream locations cannot compensate for the large gain increase upstream, therefore, there was no transition delay found for the 8mm compliant surface coating.

According to the dimensional analysis (Appendix B), the dimensionless coating thickness could affect the boundary layer receptivity. Therefore, an improvement in the transition delay was sought by reducing the depth of coating to 4mm. By reducing coating thickness, the system damping factor was increased with a similar Young's modulus value, which could result in changes of gain amplification. It has previously been realised that the near wall receptivity is not only affected by Young's modulus but also by the damping factor. The theoretical work of Landahl (1962), Benjamin (1963) and Duncan et al. (1982) has suggested that the damping

factor causes a phase difference between coating and fluid motion and therefore the damping factor affects the existence of the hydroelastic instability waves. Also, the uneven surface plots in figure 4.25 and 4.26 may be due to the differing damping factors. As a consequence, material damping is an essential parameter for a compliant surface to inhibit development of the boundary layer receptivity in practice.

From the dimensional analysis (Appendix B), the dimensionless group concerned only with the compliant surface properties is $\frac{\xi^2}{E\rho_{cs}L^2}$.(Hereafter referred to as α_c) . The measured gain improvement corrects well ($R^2 \geq 0.6$) against α_c at the different streamwise stations as shown in figure 4.27.

Figure 4.28 depicts a smoother surface when the damping term is included when compared to figure 4.26. The gain amplification increases with a growth in α_c in the upstream region (x<195mm). In the downstream region (when Re_x is above 120000), the greatest reduction in receptivity occurs when α_c is between 2.25 and 3.75. The results show that α_c has a different effect on fluctuation generation at different measurement locations and suppresses fluctuation development most effectively at the most downstream position.. This parameter α_c is therefore useful in characterising boundary layer receptivity over compliant surfaces.

4.3.3 Near wall gain under the influence of compliant surfaces

Nine different compliant surfaces of 4mm coating thickness have been tested and the results are shown in table 4.1 but here only 4 cases are discussed. These four cases were chosen because of their distinguishing features. Near wall gain in these

four cases are shown in figure 4.29. In each test, the tunnel was kept at a constant wind speed ($U \approx 6.5m/s$), and the hot-wire probe was traversed at various streamwise stations. Thus, the increase of Re_x or Re_θ resulted from the increase in streamwise distance. Owing to the fact that Re_θ is integrated from the velocity profile and is affected by the near wall measurements, the uncertainty is in the range of 2%~5%. On the other hand, Re_x was calculated directly from the velocity and distance from the leading edge and the error reading in the distance was less than 1% and therefore the value is more reliable than that for Re_θ. Figures 4.29(a), (b) have very similar trends, thus, in the following discussion results will be presented using Re_x instead of Re_θ.

The near wall overall gain against Re_x on the rigid surface was established in the previous section. Comparing compliant surface boundary layer receptivity with the rigid wall value, all the compliant surfaces had increased near wall receptivity near the leading edge (figure 4.30a and table 4.1). A comparison of receptivity on a compliant surface with that on a rigid wall is illustrated in figure 4.29(a) (b). The compliant surface with has a maximum 22.2% increase in near wall boundary layer receptivity compared to the rigid wall in the leading edge region. The gain near the start of the compliant surfaces increases with the surface property α_c.

Once the boundary layer is flowing over the compliant surface, the boundary layer fluctuations start to be suppressed. The higher values of property α_c lead to larger suppression of boundary layer receptivity in the streamwise direction and vice versa.(Figure 4.30b) This results in the lowest boundary layer receptivity in the middle range of α_c. The maximum reduction can be seen when a compliant surface

with $\alpha_c = 3.49$ was used, where there was 11.3% and 10.0% reduction at Re_x equals 124400 and 151300 respectively.

The reason for the large amplification of gain in the leading edge region may be due to the fact that the flow over the compliant surface and the motion of the compliant surfaces generate local disturbances and the energy was transferred from the surface into the fluid. Hansen et al. (1980) observed the wave structure generated by compliant surfaces and he found some waves (which he defined as Type I wave) occur near the leading edge region and disappear downstream; those waves may be responsible for the increase of the gain. Davies & Carpenter (1997) have investigated the T-S wave propagation from rigid to compliant wall. The results showed the rapid changes in disturbance kinetic energy at the start of the compliant surface panel are found and is mainly due to the rapid changes in the streamwise velocity fluctuations. The streamwise fluctuations increased near the leading edge but were attenuated downstream. Their results agree with the experimental observation that rapid streamwise variations tend to increase the receptivity of a boundary layer to free-stream disturbances.

4.3.4 The influence of the compliant surface properties on the receptivity mechanism across the boundary layer

The near wall boundary layer receptivity is high near the leading edge and then decreases gradually in the downstream direction, as found in the previous section. In order to have a more precise view of the receptivity mechanism now consider the whole boundary layer. Attention is put on the u-velocity fluctuations across the boundary layer. Three cases were chosen to investigate u-velocity fluctuations

across the boundary layer compared to the rigid wall. Maximum decrease and increase in receptivity cases are chosen and the third case is a receptivity reduction case. The compliant surface with $\alpha_c = 6.13$ triggered the largest increase of 22.2% in the boundary layer receptivity at x=112 mm (near the leading edge region). Fluctuations across the boundary layer are shown in figure4.31 (a)~(d). The peak in the fluctuations across the boundary layer in both compliant surface and rigid surface cases appears around $y\sqrt{\frac{U}{\upsilon x}}$=1.75. In order to make an accurate comparison, two rigid cases were chosen, one case with a slightly higher Re_x than the compliant surface case and the other with a lower Re_x. The interpolated profile was calculated to match the compliant surface measurement Re_x. Data show that the upstream has a profound increase in the fluctuations compared to a rigid wall case, with a 14.1% increase in the peak for the compliant surface. Further downstream, the increase of fluctuation peaks diminishes. The increases at 195mm, 277mm and 340mm are 2.1%, 0.07% and -2.4% respectively.

The trend for the gain profiles across the boundary layer can be observed from the local turbulence level profiles. Figure 4.32(a)~(d) illustrate the receptivity mechanism across the boundary layer for a compliant surface with $\alpha_c = 6.13$. The most influenced boundary layer region by this type of compliant surface is near the surface where $0< y\sqrt{\frac{U}{\upsilon x}} <1$. The changes in the local turbulence level are caused by the compliant surface and smaller changes are observed close to the free stream. The free stream turbulence level remains the same compared to the rigid surface results. The local turbulence profiles over the compliant surface of $\alpha_c = 6.13$ also show that

the influence from this type of compliant surface can enhance the receptivity mechanism in the entire boundary layer near the leading edge.

Another case to discuss here is the compliant surface with $\alpha_c = 3.49$ which was responsible for the greatest reduction in the downstream near wall boundary layer receptivity. The results are taken from four streamwise positions at x=112mm, 195mm, 277mm and 340mm,and when compared with the rigid wall results showed that the peaks of fluctuations were reduced by 2.1%, 4.9%, 9.6% and 10.2% respectively (figure 4.33) . The effects of the compliant surface reduce the amplitude of the fluctuations across the boundary layer but do not alter the shape of the fluctuation profile across the boundary layer.

The local turbulence profiles for flow over the compliant surface with $\alpha_c = 3.49$ are shown in figures 4.34(a)~(d). The effect on the compliant surface in the upstream region(x<195mm) showed that the receptivity increases in the very near wall region but this increase in receptivity did not continue for long in the downstream direction. At the location x=195mm the extra receptivity has decayed away. In the downstream region where x>277mm, the receptivity mechanism is weakened by the compliant surface when the boundary layer $y\sqrt{\frac{U}{\upsilon x}}$ is less than 2.

The third case to address here is another near wall receptivity reduction case where the compliant surface properties result in $\alpha_c = 2.65$ .The fluctuations across the boundary layer are shown in figure4.35(a)~(d). The peaks of the fluctuation were reduced by 5.5%, 7.5%, 10.1% and 8.9% from upstream to downstream respectively compare to the rigid plate results. The fluctuation was suppressed most in the downstream region where x is greater than 277mm.

The local turbulence levels for the compliant surface with $\alpha_c = 2.65$ (Figure 4.36) shows similar trend. The local turbulence level in the boundary layer was reduced at all measurement locations. The compliant surface damped out most boundary layer fluctuations when the x location was greater than 277 mm and $\eta_{Blasius} \leq 2$ and the reduction occurred through the entire boundary layer but remained the same in the freestream.

The aforementioned discussion provides strong evidence that compliant surfaces are capable of suppressing suppressed the receptivity not only in the near wall region but also across the whole boundary layer. The fluctuations can be increased or decreased by different compliant surfaces. In general, the compliant surface reduces the level of fluctuations much more at the downstream stations and a reasonable explanation could be the energy absorbed because of the damping factor becomes more effective with distance downstream.

4.3.5 The influence of the compliant surface properties on the onset of transition

For the rigid surface, the onset of transition is shown in figure 4.21 and has been discussed in the previous sections. A relationship between onset transition Re_x and turbulence level has been established. The onset of transition was measured at the different streamwise locations (figure 4.37). The compliant surface with $\alpha_c = 4.94$ caused premature transition (around 25% in terms of Reynolds number Re_x earlier compared to the rigid surface) when the free stream turbulence level is 1.66% and x is 112mm. However, when the measurement location moves downstream, the transition promotion percentage is reduced, and when the probe is

moved to x >277mm, the onset of transition is close to the rigid wall case and the transition promotion reduces to 2~3%. Two more cases are shown in figure 4.37, and shown that the promotion of transition decreases with Re_x and increases with α_c (when $\alpha_c > 3.49$). This evidence shows that the disadvantage of the compliant surface is the extra fluctuations generated at the start of the compliant surface, which results in premature transition at the higher tunnel velocities. The advantage of a compliant surface is when the flow has passed some distance over the compliant surface, when a certain amount of the boundary layer fluctuations are absorbed by the compliant surface and therefore the onset of transition is delayed compared with the rigid surface.

4.3.6 The influence of the compliant surface properties on transition delay

The previous discussion was concerned with the boundary layer receptivity in the laminar flow, and it showed that all the compliant surfaces were able to slow the development of boundary layer receptivity in the downstream direction.(Figure 4.30a). In principle, if the boundary layer receptivity is suppressed, consequently the transition will be delayed.

In order to prove this point, transitional flow measurements were taken. The probe was fixed at the location 340mm from the leading edge where the laminar boundary layer receptivity was suppressed (from the aforementioned discussion) and the wind tunnel speed was increased from 9m/s to 15 m/s to move the transition zone past the probe. Even though the previous results showed the compliant surfaces were able to suppress the boundary layer receptivity, this may not be the case for higher-speed flows as the streaks will become unsteady at higher speed. Any

measured transition delay would be valuable because it proves the use of a compliant surface can delay transition.

The boundary layer intermittency was calculated for a probe position where $u/U = 0.4$ for different free stream velocity conditions. Figure 4.38 shows the intermittency against Re_x which represents the route of transition. The results showed the best transition delay was up to 3% compare to the rigid wall when the property of the compliant surface gave $\alpha_c = 3.49$. 1.5% transition delay was also found when the compliant surface with $\alpha_c = 2.65$ was used. Those two compliant surfaces have suppressed the boundary layer receptivity by 10% at the downstream measurement location, which were the two highest reductions for the nine compliant surfaces tested.

In the experiment, three surface with $\alpha_c = 2.65, \alpha_c = 1.61, \alpha_c = 0.45$ have also been tested. For these three compliant surfaces, Young's modulus was fixed at around 4000 $\mathrm{N/m^2}$, and therefore the variations in α_c are due to the changes in damping factor. It can been seen in the figure (the cross, square and circle symbols) that the percentage of transition delay goes up with increase in α_c. (The maximum transition delay occurs at $\alpha_c = 2.65$).

Two transition promotion cases with high properties value of $\alpha_c = 4.89$ and $\alpha_c = 6.37$ were also discussed here. The percentage of transition delay decreases with descending α_c after the maximum transition delay surface when $\alpha_c = 3.49$. The promotion of the transition is due to the increase boundary layer receptivity at the start of the compliant surface in the pre-transitional region. According to the results shown in figure 4.27 and 4.28, the higher α_c created more boundary layer fluctuations at the start of the compliant surface. If the fluctuations generated at the

start of the compliant coating exceed the amount the compliant surface can absorb then these fluctuations can develop into turbulent spots and lead to premature transition.

To summarize the evidence from the preceding discussions, compliant surfaces are able to delay transition by damping out the fluctuations in the boundary layer, and the behaviour of transition delay concurs with the boundary layer receptivity improvement found at the downstream measurement locations.

4.3.7 The investigation on gain spectrum over compliant surfaces

The laminar boundary layers are most responsive to low frequency disturbances; however, when the frequency of the disturbance is low less spots are generated when the critical amplitude is reached. The highest frequencies decay too rapidly to have much effect on the receptivity. Mayle et al. (1997, 1998) determined that streamwise wavelengths of 17-20δ were the most significant in the transition process. Therefore, these disturbances in the middle- frequency range play the most important role for boundary layer transition.

Gain*frequency(Gain multiplied by frequency) values provide a clear indication of spot generation ability. The frequency band is split into 3 regions. The lowest range of frequency is defined as frequencies below that where the amplitude is 1/3 of the highest amplitude obtained for all frequencies i.e. -5db point. The middle range of frequency is defined as the range where the amplitude is above 1/3 of amplitude ie. between the -5db points and the top range is frequencies above the upper -5db point. Figure 4.39 illustrates the definition of these low, middle and high ranges of frequencies. The frequencies corresponding to the peak are for wavelengths

between 15-20 δ which demonstrates that the gain*frequency curve agrees with Mayles's finding for the significant wavelength in the transition process.

The gain*frequency spectrum analysis at four streamwise stations are shown in figure 4.40 (a) ~ (d) respectively. The shaded area depicts the middle-frequency band for the rigid wall results using the gain- Re_x corrections from equation 4.26.

The compliant surfaces have most influence on the high and middle-frequency band at the upstream stations where the start of the compliant surface panel, in particular when α_c is greater than 4. This increase in boundary layer receptivity results in earlier spot generation in the flow and hence earlier transition.

Once the flow has moved downstream over the compliant surface, the high and middle band frequencies begin to dissipate. Figure 4.40 (b)~(d) show that the evolution of this energy dissipation in the spectrum due to the compliant surface. The peak in the gain*frequency curve is reduced for all the compliant surfaces with the α =2.65 and 3.49 surfaces having the maximum reduction by the final station. When $\alpha_c < 2$, the gain*frequency spectrum only dissipates slowly over the compliant surface, whereas, the high α_c results show rapid energy dissipation in the middle-frequency range in the streamwise direction. According to the results, the optimal α_c value for a compliant surface for the pre-transitional region is in the range between 2.65 and 3.49. This result concurs with the findings for boundary layer receptivity and transition delay.

To sum up the evidence from the spectra; the compliant surface absorb the energy from the high to middle range of frequency and makes the receptivity weaker than for the rigid wall.

CHAPTER FIVE

TRANSITION MODEL OVER A COMPLIANT SURFACE

5.1 Introduction

A model for pre-transitional boundary layer fluctuation response to free stream disturbances was developed by Johnson (2002, 2003). The model is based on the fact that the velocity and pressure fluctuations measured in the pre-transitional boundary layer scale linearly with the free stream turbulence level, and hence linear theory can be applied to evaluate the boundary layer receptivity.

Yeo (1986, 1988) used a visco-elastic layer compliant surface model to predict compliant surface induced flow instabilities and Tollmien-Schlichting instability. By using the concept of wave propagation in the compliant surface, the coating stress-strain relationship can be obtained and so the stress-strain relationship at the interface between fluid and compliant surface provides a bridge to link the receptivity model and compliant surface model. By bringing together the compliant surface model (Yeo, 1986) with the Johnson transition model the prediction of boundary layer receptivity over a compliant surface is possible.

The Genetic Evolutionary algorithm (GEA) provides an efficient search method to find optimised properties for the compliant surface. Here details of how the GEA has been adapted for use with the compliant surface boundary layer receptivity model and predictions for optimised surfaces.

5.2 Methodology of prediction of boundary layer receptivity

A receptivity prediction model was devised by Johnson (2002, 2003). The model calculated the response of the boundary layer to free stream turbulence which is represented by superposition of vortex arrays. The current work has improved the receptivity prediction procedure and predictions of streamwise gain spectrum and onset of transition. The spanwise gain spectrum has also been studied for the first time.

The numerical experiments are used to investigate the boundary layer receptivity to free-stream disturbances which are considered as arrays of free stream vortices with various frequencies and orientations (Figure 5.1).

In the model, the laminar fluctuations can be approximated as linear perturbations to a non-developing (inviscid) boundary layer whose profile is given by the 6^{th} order polynomial profile.

$$\frac{u}{U} = 2(\frac{y}{\delta}) - 5(\frac{y}{\delta})^4 + 6(\frac{y}{\delta})^5 - 2(\frac{y}{\delta})^6 \tag{5.1}$$

The momentum equations governing the linear perturbation are as follows

$$\frac{\partial u'}{\partial t} + \frac{1}{\rho}\frac{\partial p'}{\partial x} + U\frac{\partial u'}{\partial x} + v'\frac{\partial U}{\partial y} - \upsilon\nabla^2 u' = 0 \tag{5.2}$$

$$\frac{\partial v'}{\partial t} + \frac{1}{\rho}\frac{\partial p'}{\partial y} + U\frac{\partial v'}{\partial x} - \upsilon\nabla^2 v' = 0 \tag{5.3}$$

$$\frac{\partial w'}{\partial t} + \frac{1}{\rho}\frac{\partial p'}{\partial z} + U\frac{\partial w'}{\partial x} - \upsilon\nabla^2 w' = 0 \tag{5.4}$$

and the continuity equation;

$$\frac{\partial u'}{\partial x}+\frac{\partial v'}{\partial y}+\frac{\partial w'}{\partial z}=0 \tag{5.5}$$

The fluctuations are fully three-dimensional and viscid, and the perturbation to the steady flow is assumed to be periodic in the x and z-directions and in time t, and to decay exponentially in the streamwise direction through viscous dissipation. Therefore, if spanwise symmetry about z= 0 is assumed, the fluctuations in u,v, w and p can therefore be represented as follows:

$$\frac{u'}{U}=u_p e^{i\Omega_X(X-cT)}\cos(\Omega_Z Z)e^{-\beta X} \tag{5.6}$$

$$\frac{v'}{U}=v_p e^{i\Omega_X(X-cT)}\cos(\Omega_Z Z)e^{-\beta X} \tag{5.7}$$

$$\frac{w'}{U}=w_p e^{i\Omega_X(X-cT)}\sin(\Omega_Z Z)e^{-\beta X} \tag{5.8}$$

$$\frac{p'}{\rho U^2}=p_p e^{i\Omega_X(X-cT)}\cos(\Omega_Z Z)e^{-\beta X} \tag{5.9}$$

where X, Y, Z and T are dimensionless coordinates and time (as defined in the nomenclature). Ω_X and Ω_Z are the dimensionless angular frequencies in the streamwise and spanwise directions respectively, c is the dimensionless perturbation convection velocity and β is the dimensionless streamwise decay coefficient.

Substituting the equations 5.6~5.9 into 5.2~5.5 and after the equations are rearranged

$$\left[\frac{1}{\mathrm{Re}_\delta}\left(\Omega_Z{}^2-D^2-(i\Omega_X-\beta)^2\right)+(i\Omega_X-\beta)\left(\frac{u}{U}\right)-i\Omega_X c\right]u_p+\frac{Du}{U}v_p+(i\Omega_X-\beta)p_p=0 \tag{5.10}$$

$$\left[\frac{1}{\mathrm{Re}_\delta}\left(\Omega_Z{}^2 - D^2 - (i\Omega_X - \beta)^2\right) + (i\Omega_X - \beta)\left(\frac{u}{U}\right) - i\Omega_X c\right]v_p + Dp_p = 0 \quad (5.11)$$

$$\left[\frac{1}{\mathrm{Re}_\delta}\left(\Omega_Z{}^2 - D^2 - (i\Omega_X - \beta)^2\right) + (i\Omega_X - \beta)\left(\frac{u}{U}\right) - i\Omega_X c\right]w_p - \Omega_Z p_p = 0 \quad (5.12)$$

The continuity equation is $(i\Omega_X - \beta)u_p + Dv_p + \Omega_Z w_p = 0$ (5.13)

where $D = \frac{d}{dy}$

5.2.1 The free stream perturbations

The pressure fluctuation in the free stream can be obtained by combining equations 5.10 to 5.13

$$\left(\Omega_X{}^2 + \Omega_Y{}^2 + \Omega_Z{}^2 - \beta^2 + i2\beta\Omega_X\right)p_p = 0 \quad (5.14)$$

Because $\Omega_X, \Omega_Y, \Omega_Z \neq 0$, the only solution is $p_p = 0$

The equation 5.10 in the free stream can be rewritten as

$$\left[-\beta + i(1-c)\Omega_X + \frac{1}{\mathrm{Re}_\delta}\left(\Omega_X{}^2 + \Omega_Y{}^2 + \Omega_Z{}^2 - \beta^2 + i2\beta\Omega_X\right)\right]u_p = 0 \quad (5.15)$$

The real and imaginary part should equal zero respectively.

$$c = 1 + \frac{2\beta}{\mathrm{Re}_\delta} \quad (5.16)$$

$$\beta^2 + \mathrm{Re}_\delta \beta - \left(\Omega_X{}^2 + \Omega_Y{}^2 + \Omega_Z{}^2\right) = 0 \tag{5.17a}$$

for positive $$\beta = \frac{-\mathrm{Re}_\delta + (\mathrm{Re}_\delta{}^2 + 4(\Omega_X{}^2 + \Omega_Y{}^2 + \Omega_Z{}^2))^{0.5}}{2} \tag{5.17b}$$

for typical boundary layers with any combinations of frequencies,

$$\mathrm{Re}_\delta >> (\Omega_X{}^2 + \Omega_Y{}^2 + \Omega_Z{}^2)$$

$$\beta \cong \frac{(\Omega_X{}^2 + \Omega_Y{}^2 + \Omega_Z{}^2)}{\mathrm{Re}_\delta} \tag{5.18}$$

The convective velocity can be written as

$$c \cong \left(1 + 4\left(\left(\frac{\Omega_X}{\mathrm{Re}_\delta}\right)^2 + \left(\frac{\Omega_Y}{\mathrm{Re}_\delta}\right)^2 + \left(\frac{\Omega_Z}{\mathrm{Re}_\delta}\right)^2\right)\right)^{0.5} \tag{5.19}$$

The amplitude of free stream perturbations can be written as

$$A \cong A_0 e^{\frac{-\mathrm{Re}_{x_0}}{\mathrm{Re}_\delta(\Omega_X{}^2+\Omega_Y{}^2+\Omega_Z{}^2)}} \tag{5.20}$$

Where A_0 is its amplitude at some arbitrary x=0 datum (Re_x =0, the inlet condition). The Re_{x0} alters the integral length of turbulence, so if Re_{x0} is high, the shorter turbulence length scales will have decayed more quickly than the larger turbulence scales.

Substituting the equations 5.18 and 5.19 into equations 5.10 to 5.12, and given the free stream condition that Du =0 and $\frac{u}{U}=1$, a 4th order v equation can be obtained for the free stream.

$$\left[-D^4+\left(\Omega_X{}^2-\Omega_Y{}^2+\Omega_Z{}^2-\beta^2+2i\beta\Omega_x\right)D^2+\left(\Omega_X{}^2+\Omega_Z{}^2-\beta^2+2i\beta\Omega_X\right)\left(\Omega_Y{}^2\right)\right]v_p=0 \tag{5.21}$$

The four solutions for the v velocity are $\sin(\Omega_Y Y)$, $\cos(\Omega_Y Y)$, $e^{-\sqrt{\Omega_z{}^2-(i\Omega_x-\beta)^2}Y}$ (decay term) ,and $e^{\sqrt{\Omega_z{}^2-(i\Omega_x-\beta)^2}Y}$ (growth term).

$$v_p=a_1\sin(\Omega_Y Y)+a_2\cos(\Omega_Y Y)+a_3e^{-\sqrt{\Omega_z{}^2-(i\Omega_x-\beta)^2}Y}+a_4e^{\sqrt{\Omega_z{}^2-(i\Omega_x-\beta)^2}Y} \tag{5.22}$$

a_1, a_2, a_3, a_4 are arbitrary coefficients .

Similar equations for u and w perturbations can also be presented as combinations of these four solutions. One boundary condition should be provided that the perturbations in the far field free stream are considered as a series of vortices, so the exponential growth term should vanish leaving the sine, cosine and decay terms.

5.2.2 Boundary layer fluctuations

By replacing the convective velocity c and streamwise decay coefficient β, in the equations 5.10~5.13, the boundary layer fluctuation response to the free stream turbulence can be found by solving the ordinary differential equations.

$$\left[-\frac{1}{\mathrm{Re}_\delta}\left(D^2+\Omega_Y{}^2\right)+\left(i\Omega_X-\beta\right)\left(\frac{u}{U}-1\right)\right]u_p+\frac{Du}{U}v_p+\left(i\Omega_X-\beta\right)p_p=0 \tag{5.23}$$

$$\left[-\frac{1}{\mathrm{Re}_\delta}\left(D^2+\Omega_Y{}^2\right)+\left(i\Omega_X-\beta\right)\left(\frac{u}{U}-1\right)\right]v_p+Dp_p=0 \tag{5.24}$$

$$\left[-\frac{1}{\mathrm{Re}_\delta}\left(D^2+\Omega_Y{}^2\right)+\left(i\Omega_X-\beta\right)\left(\frac{u}{U}-1\right)\right]u_p+\frac{Du}{U}v_p+\left(i\Omega_X-\beta\right)p_p=0 \tag{5.25}$$

The continuity equation is $\left(i\Omega_X-\beta\right)u_p+Dv_p+\Omega_Z w_p=0,\ D\equiv\frac{d}{dy}$ (5.26)

By combining 5.23~5.26, a fourth order differential equation in v_p can be obtained.

$$\left[-D^4+\left[\mathrm{Re}_\delta\left(i\Omega_X-\beta\right)\left(\frac{u}{U}-1\right)+\Omega_X^2-\Omega_Y^2+\Omega_Z^2-\beta^2+2i\beta\Omega_X\right]D^2-\mathrm{Re}_\delta\left(i\Omega_X-\beta\right)\frac{\left(D^2u\right)}{U}\right.$$

$$\left.+\left(\Omega_X^2+\Omega_Z^2-\beta^2+2i\beta\Omega_X\right)\left(\Omega_Y^2+\mathrm{Re}_\delta\left(i\Omega_X-\beta\right)\left(1-\frac{u}{U}\right)\right)\right]v_p=0 \tag{5.27}$$

Pressure fluctuations can be obtained by combining the X and Z momentum equations and continuity equation

$$p_p=\left(\frac{1}{\Omega_Z{}^2-\left(i\Omega_X-\beta\right)^2}\right)\left[-\frac{1}{\mathrm{Re}_\delta}\left(D^2+\Omega_Y{}^2\right)+\left(i\Omega_X-\beta\right)\left(\frac{u}{U}-1\right)\right]Dv_p+\left(i\Omega_X-\beta\right)\left(\frac{Du}{U}\right)v_p$$

(5.28)

Then the u fluctuation solution can be found from the X-momentum equation and the w fluctuation can be solved from the continuity equation and the final u,v,w have to satisfy the continuity equation.

For a rigid wall three boundary conditions are provided at the wall, $u'=v'=w'=0$, the remaining boundary conditions obtained by matching the free stream vortex array with the velocity components.

5.2.3 Near wall overall gain

The current research, and Johnson and Ercan (1999) experimental results both suggest that for the boundary layer where $y/\delta \leq 0.2$ for a zero pressure gradient, the local turbulence level remains constant and results in an invariant energy spectra. Therefore, the region of $y/\delta \leq 0.2$ is regarded as the near wall region and this is where the measurement of the boundary layer receptivity is taken. The near wall gain in the numerical calculation is defined as $Gain = \frac{u'U}{(U'^2 + V'^2)^{0.5} u}$ and this is evaluated at y=0.2δ. The overall gain is the mean gain for all orientations and directions of the perturbation vortices.

The boundary layer receptivity was calculated for free stream vortices (Figure 5.1) with 360 vortex axis orientations and 100,000 different vortex wavelengths from 10δ~1000δ.. The pre-transitional flow was calculated for the range of Re_θ= 100~300, and Re_{x0} is 2,000,000.

An unstructured adaptive grid in the Ω_Y, Ω_Z plane was used in the calculation. The advantage of this kind of grid is higher resolution to define the high gain frequency bands which indicate strong response of the boundary layer fluctuations for a particular frequency of the free stream disturbance.

5.3 The code validation (Zero pressure gradient boundary layer)

5.3.1 Streamwise frequencies

The numerical results were validated with the experimental measurements to examine the integrity of the numerical methods. Figure 5.2 shows the near wall gain variation with the streamwise frequency Ω_x for Re_{x0} =2,000,000. The results show

that for streamwise spatial frequencies the boundary layer is most receptive to lower frequency ,therefore identifying the freestream near streamwise vortices as being the source of these low frequencies. The predicted gains in figure 5.2 are close to the measured values obtained by the current experiments shown in figure 4.18.

5.3.2 Onset of transition

Experimental results in the current study suggest that transition commences when local turbulence level reaches 21%~23%. This finding has also been demonstrated by Johnson and Fasihfar (1992). The criterion where transition starts at a local turbulence level of 21% provides a simple theory to determine the start of transition Re_{θ_t} for different free stream turbulence intensities. The results are shown in Figure 5.3. The empirical correlations due to Ercan and Mayle and the current experimental results are also shown on the same graph. The current prediction of the onset of transition is consistent with the empirical correlations.

5.3.3 Spanwise frequencies

To understand the streaks in the bypass transition boundary layer, it is important to discuss the spanwise wavelength spectrum which affects the turbulence spot generation. Yoshioka et al.(2004)'s experimental results noted that the higher free stream turbulence level causes a smaller spanwise scale of streaks in the boundary layer, also the spanwise scales decrease with an increase in free stream velocity. This evidence proves the small spanwise scale of streak results in early transition. He also established the relationship $\frac{\Delta Z_{\min} U}{\upsilon} = \text{constant}$, which can be

rewritten $\frac{\Delta Z_{min}}{\delta^*}\mathrm{Re}_{\delta^*} = \text{constant}$, where ΔZ_{min} is the physical spanwise spacing of the streaks.

Matsubara & Alfredsson (2001) used smoke visualisation and hot-wire anemometry to determine the streak spanwise size and showed the spanwise size approaches 3δ ($9\delta^*$) in the upstream region but the physical spanwise scale decreases in the streamwise direction to δ ($3\delta^*$) at the downstream position. The results are shown in figure 5.4.

These studies have proved that the boundary layer is most receptive to a narrow range of spanwise wavelengths which are the order of the boundary layer thickness. According to the visualisation and two-wire correlation measurements, the streak was identified to have more or less the same physical spanwise scale during the boundary layer development. Thus, the dimensionless size of the wavelength ($\Delta Z_{min}/\delta$) should decrease in the streamwise direction due to the growth of the boundary layer thickness. The Matsubara and Alfredsson's experimental results (figure 5.4) suggests that the Andersson (1999) and Luchini (2000) simulation solution for optimal transient spanwise length of 1.4δ should not be constant.

In figure 5.5(g) and 5.6(g), the averaged spanwise scale is calculated from integration of the x and y frequency by using e.q. 5.29. $\mathrm{Re}_\theta = 100$, the peak of $Gain_Z$ appears around a Ω_Z frequency of 0.4, which corresponds to a wavelength of 2.5δ, according to equation 5.30. At $\mathrm{Re}_\theta = 300$, the dominant wavelength for boundary layer receptivity is around 0.8δ. The numerical predictions of dominant wavelength for boundary layer streaks agree with Matsubara and Alfredsson's

experimental results shown in figure 5.4 and the relationship between Re_{δ^*} and dimensionless spanwise scale of streak follows the Yoshioka & Fransson correlation where $\frac{\Delta Z_{\min}}{\delta^*}\mathrm{Re}_{\delta^*}$ is a constant.

$$Gain_Z{}^2 = \int_0^\infty \int_0^\infty Gain(\Omega_X, \Omega_Y, \Omega_Z)^2 d\Omega_X d\Omega_Y \tag{5.29}$$

$$\lambda_w = \frac{U}{2\pi f} = \frac{\delta}{\Omega_Z} \tag{5.30}$$

Figure 5.5 and 5.6 show the gain values plotted against the spanwise and normalwise frequency Ω_Y and Ω_Z for different Ω_X. At the lowest Reynolds number station (Re_θ=100), the most receptive frequencies are found in the Ω_Z frequency band between 0.2~0.6. The receptive region does not change with streamwise frequency, and the peak in the spanwise near wall gain remains at 0.4 for all streamwise frequencies. Figure5.6 shows a higher Reynolds number (Re_θ=300) case. The most receptive spanwise frequency is in the range from 0.75 to 1.75, with the peak of averaged near wall spanwise gain appearing at a frequency of Ω_Z=1.2. The peak of spanwise gain moves towards high frequency when streamwise frequency is increasing, but the amplitude of gain diminishes at high streamwise frequency. The receptive frequency shift may result in the non-linear mechanism which is observed as unsteadiness or wiggles in the smoke visualisation.

The validations showed that the current model can predict the receptivity mechanism, streak structures and the onset of transition; therefore, the compliant

surface model can be added to the receptivity model to examine the effect of the compliant surface on the streaks in the bypass transition boundary layer.

5.4 The compliant surface model

Initially a simple spring-damper system beneath a membrane model was combined with the receptivity model, where the shear stress was ignored in the calculation. However, the results for spectrum and gain improvement contradicted the experimental results. A two-dimensional spring-damper system under a membrane also was tested. The predictions for the spectrum were still very poor. Therefore, the wave motion in the visco-elastic coating was included using the model presented by Yeo(1986, 1988).

A wave-sustained, homogenous and isotropic compliant coating can be modelled as a linear combination of waves which propagate in the perpendicular (Y) and parallel (X) directions.

The equations of the surface waves in a homogenous and isotropic Voigt (a purely viscous damper and purely elastic spring connected in parallel) material were derived for a single-layer viscoelastic compliant surface coating. The thicknesses of the viscoelastic layers is L_s and the position of the interface between layer are Y_0, Y_1. On its lowest boundary, the compliant material is attached to a rigid wall, and the fluid passing over the top layer imposes the flow pressure.

5.4.1 The wave motion in visco-elastic coating

Some understanding of how a compliant surface responds to flow can be gained through studying the free-surface waves of the coating. It was pointed out by

Rayleigh (1887), that the surface waves can be modelled as a linear combination of parallel and perpendicular wave propagation displacement. The waves in the parallel propagation direction are called transverse displacement waves, and in the perpendicular direction, they are called longitudinal displacement waves.

The governing equations of motion of an isotropic linear elastic material can be expressed in terms of the displacements by using Navier's equations which were also used by Yeo(1986) and Dixon et al.(1994)

$$\rho_{cs}\frac{\partial^2\eta}{\partial t^2} = (K_s + \frac{1}{3}G_s)\nabla(\nabla\cdot\eta) + G_s\nabla^2\eta - \rho_{cs}g\hat{y} \tag{5.31}$$

$$\rho_{cs}\frac{\partial^2\eta}{\partial t^2} = (K_s + \frac{4}{3}G_s)\nabla(\nabla\cdot\eta) - G_s\nabla\times(\nabla\times\eta) - \rho_{cs}g\hat{y} \tag{5.32}$$

The body force is not taken into account in the calculation.

The vector η corresponds to the displacements of the material and η can also be represent as $\eta = \eta_x\vec{i} + \eta_y\vec{j}$ where η_x and η_y are the horizontal and vertical components, ρ_{cs} is the mass density of the compliant coating. G_s and K_s are the shear and bulk modulus respectively. From G_s and K_s , the compliant surface properties can be determined as:

$$E = \frac{9K_sG_s}{3K_s + G_s}\quad \lambda = \frac{1}{3}(3K_s - 2G_s), \nu = \frac{3K_s - 2G_s}{6K_s + 2G_s},$$

where λ , is Lame's constant which is related to Young's modulus E and ν is Poisson's ratio of the material.

The non-dimensional parameters can be expressed as:

$$G_s^* = \frac{G_s}{\rho U^2},\ K_s^* = \frac{K_s}{\rho U^2},\ E_s = \frac{E}{\rho U^2}$$

$$\eta^* = \frac{\eta}{\delta},\ \eta_x^* = \frac{\eta_x}{\delta},\ \eta_y^* = \frac{\eta_y}{\delta} \tag{5.33}$$

$$\xi_s = \frac{\xi}{\rho UL},\ L_s = \frac{L}{\delta},\ \rho_r = \frac{\rho_{cs}}{\rho},$$

$$\sigma^* = \frac{\sigma}{\rho U^2}, \tau^* = \frac{\tau}{\rho U^2}$$

where L : thickness of compliant coating, σ :normal stress and τ :shear stress, ξ :damping factor. So, the non-dimensional form of equation 5.32 is

$$\rho_r \frac{\partial^2 \eta^*}{\partial t^2} = (K_s^* + \frac{4}{3} G_s^*) \nabla(\nabla \cdot \eta^*) - G_s^* \nabla \times (\nabla \times \eta^*) \tag{5.34}$$

Figure 5.8 shows two basic types of wave motion for mechanical waves in compliant surfaces. In the studies, for the first type, the material is assumed to be elastic-dilatational (K_s is real) and the particle displacement is parallel to the direction of wave propagation. For the second type, the material is Voigt-deviatoric and the particle displacement is perpendicular to the direction of wave propagation and with damping, which means a complex form of G_s,

$$G_s^* = 2(\rho_r C_t^{*2} - i\Omega_X c\xi_1) \tag{5.35}$$

Where ξ_1 is a semi-empirical parameter for damping factor, $\xi_1 = \mathrm{Re}_x \xi_s$

Experimental results demonstrated that the distance the flow passes over the compliant surface will affect the interaction between flow and compliant surface. Therefore, the damping factor involves Re_x which reflects the distance of flow over

the compliant surface.

The displacement can be decomposed into a vector field using two vector functions, one of which is irrotational ($\nabla\times(\nabla\varphi)=0$) and the other which is solenoidial ($\nabla\cdot(\nabla\times\vec{\psi})=0$) therefore, $\eta^{*}=\nabla\varphi+\nabla\times\vec{\psi}$

Where ψ is referred to as a vector potential and φ is referred to as scalar potential . The advantage of doing this is to separate the displacement field into compression waves and shear waves and will allow each to be dealt with separately.

$$(K_s^{*}+\frac{4}{3}G_s^{*})\nabla\nabla\cdot\{\nabla\varphi+\nabla\times\vec{\psi}\}-G_s^{*}\nabla\times\nabla\times\{\nabla\varphi+\nabla\times\vec{\psi}\}-\rho_r\frac{\partial^2}{\partial t^2}\{\nabla\varphi+\nabla\times\vec{\psi}\}=0 \quad (5.36)$$

$$\nabla\cdot(\nabla\times\vec{\psi})=0,\ \nabla\times(\nabla\phi)=0,\ \nabla\cdot(\nabla\varphi)=\nabla^2\varphi$$

$$(K_s^{*}+\frac{4}{3}G_s^{*})\nabla(\nabla^2\varphi)-G_s^{*}\nabla\times\nabla\times\nabla\times(\vec{\psi})-\rho_r\frac{\partial^2}{\partial t^2}\{\nabla\varphi+\nabla\times\vec{\psi}\}=0 \quad (5.37)$$

$$\nabla\times\nabla\times(\nabla\times\vec{\psi})=\nabla(\nabla\cdot(\nabla\times\vec{\psi}))-\nabla\cdot\nabla(\nabla\times\vec{\psi})=-\nabla^2(\nabla\times\vec{\psi})$$

$$(K_s^{*}+\frac{4}{3}G_s^{*})\nabla(\nabla^2\varphi)-G_s^{*}\nabla\times(\nabla^2\vec{\psi})-\rho_r\frac{\partial^2}{\partial t^2}\{\nabla\varphi+\nabla\times\vec{\psi}\}=0 \quad (5.38)$$

$$\nabla\left[(K_s^{*}+\frac{4}{3}G_s^{*})\nabla^2\varphi-\rho_r\frac{\partial^2\varphi}{\partial t^2}\right]+\nabla\times\left[G_s^{*}\nabla^2\vec{\psi}-\rho_r\frac{\partial^2\vec{\psi}}{\partial t^2}\right]=0 \quad (5.39)$$

Each term in the brackets must be independently zero, so the scalar wave equation and vector wave equation can be expressed in equation 5.40.

$$\begin{aligned}\nabla^2\varphi-\frac{1}{C_l^{*2}}\frac{\partial^2\varphi}{\partial t^2}&=0\\ \nabla^2\vec{\psi}-\frac{1}{C_t^{*2}}\frac{\partial^2\vec{\psi}}{\partial t^2}&=0\end{aligned} \quad (5.40)$$

in which C_l * and C_t * are the complex bulk and shear wave velocities respectively,

where $$C_l^* = \left(\frac{3K_s^* + 4G_s^*}{3\rho_r}\right)^{1/2} \quad C_t^* = \left(\frac{G_s^*}{\rho_r}\right)^{1/2} \tag{5.41}$$

These equations show that the total motion is composed of a curl-free wave travelling with a speed C_l, and a divergence-free wave travelling with a speed C_t.

The displacement field is:

$$\begin{aligned} \eta_x^* &= \eta_{x,\ell}^* + \eta_{x,t}^* = \frac{\partial \varphi}{\partial x} - \frac{\partial \bar{\psi}}{\partial y} \\ \eta_y^* &= \eta_{y,\ell}^* + \eta_{y,t}^* = \frac{\partial \varphi}{\partial y} + \frac{\partial \bar{\psi}}{\partial x} \end{aligned} \tag{5.42}$$

Consider the wave solution for the compression and shear waves

$$\begin{aligned} \varphi &= \varphi(y) e^{i\Omega_X (X - cT)} \\ \bar{\psi} &= \bar{\psi}(y) e^{i\Omega_X (X - cT)} \end{aligned} \tag{5.43}$$

After substituting these into (5.36)

$$\frac{d^2\varphi}{dy^2} - B_L^2 \varphi = 0, \frac{d^2\bar{\psi}}{dy^2} - B_T^2 \bar{\psi} = 0 \tag{5.44}$$

$$B_L = \Omega_x \left(1 - \frac{c^2}{C_l^{*2}}\right)^{\frac{1}{2}}, B_T = \Omega_x \left(1 - \frac{c^2}{C_t^{*2}}\right)^{\frac{1}{2}}$$

These in turn have general solutions of the form

$$\begin{aligned} \varphi &= B_1 e^{B_L y} + B_2 e^{-B_L y} \\ \bar{\psi} &= B_3 e^{B_T y} + B_4 e^{-B_T y} \end{aligned} \tag{5.45}$$

The B_1, B_2, B_3, B_4 are complex constants for the homogenous layers.

So the displacement can be expressed as

$$\begin{aligned} \eta_x^* &= B_1 \left(i\Omega_x e^{B_L Y}\right) + B_2 \left(i\Omega_x e^{-B_L Y}\right) + B_3 \left(-B_T e^{B_T Y}\right) + B_4 \left(B_T e^{-B_T Y}\right) \\ \eta_y^* &= B_1 \left(B_L e^{B_L Y}\right) + B_2 \left(-B_L e^{-B_L Y}\right) + B_3 \left(i\Omega_x e^{B_T Y}\right) + B_4 \left(i\Omega_x e^{-B_T Y}\right) \end{aligned} \tag{5.46}$$

The normal force and shear force exerted on the compliant coating can be represented by the following equations.

$$\left(K_s^* + \frac{1}{3}G_s^*\right)\left(\frac{\partial \eta_x^*}{\partial x} + \frac{\partial \eta_y^*}{\partial y}\right) + 2G_s^*\left(\frac{\partial \eta_y^*}{\partial y}\right) = \sigma^* \quad \text{(Normal Force)} \quad (5.47)$$

$$G_s^*\left(\frac{\partial \eta_x^*}{\partial y} + \frac{\partial \eta_y^*}{\partial x}\right) = \tau^* \quad \text{(Shear Force)} \quad (5.48)$$

And the displacements can be obtained from equation 5.46

Therefore, the displacement and the force loads on the compliant coating can be expressed in the form of $S(y) = Q(y)B$ where $S(y) = \left[\eta_x^* \quad \eta_y^* \quad \sigma^* \quad \tau^*\right]^T$

$$\begin{bmatrix} \eta_x^* \\ \eta_y^* \\ \sigma^* \\ \tau^* \end{bmatrix} = \begin{bmatrix} i\Omega_X e^{B_L Y} & i\Omega_X e^{-B_L Y} & B_T e^{B_T Y} & -B_T e^{-B_T Y} \\ B_L e^{B_L Y} & -B_L e^{-B_L Y} & -i\Omega_X e^{B_T Y} & -i\Omega_X e^{-B_T Y} \\ H_3 e^{B_L Y} & -H_3 e^{-B_L Y} & H_1 e^{B_T Y} & H_1 e^{-B_T Y} \\ H_0 e^{B_L Y} & H_0 e^{-B_L Y} & -H_2 e^{B_T Y} & H_2 e^{-B_T Y} \end{bmatrix} \begin{bmatrix} B_1 \\ B_2 \\ B_3 \\ B_4 \end{bmatrix} \quad (5.49)$$

where

$$H_0 = 2G_s^* B_T^2 + \left(K_s^* + \frac{1}{3}G_s^*\right)\left(B_L^2 - \Omega_X^2\right)$$
$$H_1 = G_s^*\left(B_T^2 + \Omega_X^2\right)$$
$$H_2 = i2\Omega_X B_T G_s^*$$
$$H_3 = i2\Omega_X B_L G_s^*$$

5.4.2 The Coupling of fluid and wall motions

Yeo (1986) dealt with the stability problem which involves eigen-solutions to the Orr-Sommerfeld equation. The boundary layer receptivity is an initial problem and different to the stability calculation. Therefore, the adaptation of the compliant surface model and boundary layer receptivity model was the contribution for the current work. The main difficulty encountered in the present project is associated

with the coupling between the fluid flow and the compliant surface wall.The fluid flow generates forces which drive the wall while the resulting wall motion strongly influences the flow field and it is difficult to achieve a stable iterative scheme. Luo & Pedley (1996) and Davies(1995) assumed the displacement solutions are fully periodic in time which allows all time derivative quantities to replace Q by $i\Omega Q$ where Ω is the disturbance frequency and the stable scheme produced satisfactory results. The receptivity model is based on the same assumption with full periodicity in time and so similar techniques were used.

The boundary conditions between the fluid and solid are important aspects to deal with the interaction between fluid and compliant surface. For a linear problem, the boundary conditions have to satisfy velocity and stress continuity at the wall/fluid interface. The linearized conditions on the velocity and stress are given by

$$u_p + DU_W \eta_y{}^* = \frac{\partial \eta_x{}^*}{\partial t} \quad \text{and} \quad v_p = \frac{\partial \eta_y{}^*}{\partial t} \tag{5.50}$$

The presence of the term involving DU_W, the non-dimensional undisturbed velocity gradient at the wall, is the contribution representing the displacement of the mean flow.

There are 4 boundary conditions on the interface fluid and compliant surface

$$\begin{aligned} -i\Omega_X c\eta_x{}^* &= u_p + DU_W \eta_y{}^* \\ -i\Omega_X c\eta_y{}^* &= v_p \\ \sigma_W{}^* &= \left(\frac{2}{\mathrm{Re}_\delta} Dv_p - p_p \right) \\ \tau_W{}^* &= \left(\frac{1}{\mathrm{Re}_\delta} (Du_p + ((i\Omega_X - \beta) + \frac{D^2 U_W}{i\Omega_X c}) v_p) \right) \end{aligned} \tag{5.51)~(5.54}$$

These equations show the forces and displacements from the fluid side, and $D \equiv \frac{d}{dY}$

In the Rigid wall case

$$\eta_x{}^* = 0, \eta_y{}^* = 0, \sigma_W{}^* = -p_p, \tau_W{}^* = \frac{1}{\mathrm{Re}_\delta} Du_p$$

Rearranging equations 5.51~5.54

$$\eta_x{}^* = \frac{1}{-i\Omega_X c} u_p + \left(\frac{1}{(i\Omega_X c)^2} DU_W \right) v_p \tag{5.55}$$

So the matrix of the interface between fluid/wall becomes

$$\begin{bmatrix} \eta_x{}^* \\ \eta_y{}^* \\ \sigma_w{}^* \\ \tau_w{}^* \end{bmatrix} + \begin{bmatrix} 0 \\ 0 \\ p_p \\ 0 \end{bmatrix} = \begin{bmatrix} \frac{1}{-i\Omega_X c} & 0 & \frac{DU_W}{(i\Omega_X c)^2} & 0 \\ 0 & 0 & \frac{1}{-i\Omega_X c} & 0 \\ 0 & 0 & 0 & \frac{2}{\mathrm{Re}_\delta} \\ 0 & \frac{1}{\mathrm{Re}_\delta} & \frac{1}{\mathrm{Re}_\delta}((i\Omega_X - \beta) + \frac{D^2 U_W}{i\Omega_X c}) & 0 \end{bmatrix} \begin{bmatrix} u_p \\ Du_p \\ v_p \\ Dv_p \end{bmatrix} \tag{5.56}$$

The coupling of the shear stress perturbation was omitted in many previous studies, e.q. Fraser (1984) and Fraser & Carpenter (1985), where it was assumed the fluid shear stress τ is much smaller than the fluid normal stress σ. Craik(1966) discovered that a long wavelength low Reynolds number instability exists when the air flows over a liquid layer, and Yeo(1987) suggested the omission of shear stress is justifiable at moderate to large Reynolds number. For a low frequency and low Reynolds numbers, the shear stress τ has a similar order to the normal stress σ. Therefore, the shear stress should be taken into account in the current model.

5.4.3 A single layer model of compliant surface

The depiction of the compliant surface is shown in figure 5.9 and according to equation 5.49; the compliant surface model can be presented as

$$\begin{bmatrix} \eta_x^* \\ \eta_y^* \\ \sigma^* \\ \tau^* \end{bmatrix}_{Y_0} = \begin{bmatrix} i\Omega_X e^{B_L Y} & i\Omega_X e^{-B_L Y} & B_T e^{B_T Y} & -B_T e^{-B_T Y} \\ B_L e^{B_L Y} & -B_L e^{-B_L Y} & -i\Omega_X e^{B_T Y} & -i\Omega_X e^{-B_T Y} \\ H_3 e^{B_L Y} & -H_3 e^{-B_L Y} & H_1 e^{B_T Y} & H_1 e^{-B_T Y} \\ H_0 e^{B_L Y} & H_0 e^{-B_L Y} & -H_2 e^{B_T Y} & H_2 e^{-B_T Y} \end{bmatrix}_{Y_0} \begin{bmatrix} B_1 \\ B_2 \\ B_3 \\ B_4 \end{bmatrix} \quad (5.57)$$

$$\begin{bmatrix} \eta_x^* \\ \eta_y^* \\ \sigma^* \\ \tau^* \end{bmatrix}_{Y_1} = \begin{bmatrix} i\Omega_X e^{B_L Y} & i\Omega_X e^{-B_L Y} & B_T e^{B_T Y} & -B_T e^{-B_T Y} \\ B_L e^{B_L Y} & -B_L e^{-B_L Y} & -i\Omega_X e^{B_T Y} & -i\Omega_X e^{-B_T Y} \\ H_3 e^{B_L Y} & -H_3 e^{-B_L Y} & H_1 e^{B_T Y} & H_1 e^{-B_T Y} \\ H_0 e^{B_L Y} & H_0 e^{-B_L Y} & -H_2 e^{B_T Y} & H_2 e^{-B_T Y} \end{bmatrix}_{Y_1} \begin{bmatrix} B_1 \\ B_2 \\ B_3 \\ B_4 \end{bmatrix} \quad (5.58)$$

$$H_0 = 2G_s^* B_T^2 + \left(K_s^* + \frac{1}{3}G_s^*\right)\left(B_L^2 - \Omega_X^2\right)$$
$$H_1 = G_s^*\left(B_T^2 + \Omega_X^2\right)$$
$$H_2 = i2\Omega_X B_T G_s^*$$
$$H_3 = i2\Omega_X B_L G_s^*$$

Because Y_1 and Y_0 refer to the same layer, the coefficient B will be the same, combining equation 5.57 and 5.58 to eliminate the unknown matrix B a new equation can be obtained as 5.59 to show how the displacement and stresses change in a compliant coating.

$$\begin{bmatrix} \eta_x^* \\ \eta_y^* \\ \sigma^* \\ \tau^* \end{bmatrix}_{Y_0} = \begin{bmatrix} i\Omega_X e^{B_L Y_0} & i\Omega_X e^{-B_L Y_0} & B_T e^{B_T Y_0} & -B_T e^{-B_T Y_0} \\ B_L e^{B_L Y_0} & -B_L e^{-B_L Y_0} & -i\Omega_X e^{B_T Y_0} & -i\Omega_X e^{-B_T Y_0} \\ H_3 e^{B_L Y_0} & -H_3 e^{-B_L Y_0} & H_1 e^{B_T Y_0} & H_1 e^{-B_T Y_0} \\ H_0 e^{B_L Y_0} & H_0 e^{-B_L Y_0} & -H_2 e^{B_T Y_0} & H_2 e^{-B_T Y_0} \end{bmatrix} \begin{bmatrix} i\Omega_X e^{B_L Y_1} & i\Omega_X e^{-B_L Y_1} & B_T e^{B_T Y_1} & -B_T e^{-B_T Y_1} \\ B_L e^{B_L Y_1} & -B_L e^{-B_L Y_1} & -i\Omega_X e^{B_T Y_1} & -i\Omega_X e^{-B_T Y_1} \\ H_3 e^{B_L Y_1} & -H_3 e^{-B_L Y_1} & H_1 e^{B_T Y_1} & H_1 e^{-B_T Y_1} \\ H_0 e^{B_L Y_1} & H_0 e^{-B_L Y_1} & -H_2 e^{B_T Y_1} & H_2 e^{-B_T Y_1} \end{bmatrix}^{-1} \begin{bmatrix} \eta_x^* \\ \eta_y^* \\ \sigma^* \\ \tau^* \end{bmatrix}_{Y_1}$$

(5.59 a)

$$\begin{bmatrix} \eta_x^* \\ \eta_y^* \\ \sigma^* \\ \tau^* \end{bmatrix}_{Y_0} = \begin{bmatrix} & CS(i,j) & \end{bmatrix} \begin{bmatrix} \eta_x^* \\ \eta_y^* \\ \sigma^* \\ \tau^* \end{bmatrix}_{Y_1}$$

where $CS(i,j) =$

$$\begin{bmatrix} i\Omega_X e^{B_L Y_0} & i\Omega_X e^{-B_L Y_0} & B_T e^{B_T Y_0} & -B_T e^{-B_T Y_0} \\ B_L e^{B_L Y_0} & -B_L e^{-B_L Y_0} & -i\Omega_X e^{B_T Y_0} & -i\Omega_X e^{-B_T Y_0} \\ H_3 e^{B_L Y_0} & -H_3 e^{-B_L Y_0} & H_1 e^{B_T Y_0} & H_1 e^{-B_T Y_0} \\ H_0 e^{B_L Y_0} & H_0 e^{-B_L Y_0} & -H_2 e^{B_T Y_0} & H_2 e^{-B_T Y_0} \end{bmatrix} \begin{bmatrix} i\Omega_X e^{B_L Y_1} & i\Omega_X e^{-B_L Y_1} & B_T e^{B_T Y_1} & -B_T e^{-B_T Y_1} \\ B_L e^{B_L Y_1} & -B_L e^{-B_L Y_1} & -i\Omega_X e^{B_T Y_1} & -i\Omega_X e^{-B_T Y_1} \\ H_3 e^{B_L Y_1} & -H_3 e^{-B_L Y_1} & H_1 e^{B_T Y_1} & H_1 e^{-B_T Y_1} \\ H_0 e^{B_L Y_1} & H_0 e^{-B_L Y_1} & -H_2 e^{B_T Y_1} & H_2 e^{-B_T Y_1} \end{bmatrix}^{-1}$$

(5.59 b)

Two boundary conditions are the x and y displacement at the foundation which are zero, $\eta_x^*\big|_{Y_1} = 0$ and $\eta_y^*\big|_{Y_1} = 0$

$$\begin{bmatrix} \eta_x^* \\ \eta_y^* \\ \sigma^* \\ \tau^* \end{bmatrix}_{Y_0} = \begin{bmatrix} CS(1,1) & CS(1,2) & CS(1,3) & CS(1,4) \\ CS(2,1) & CS(2,2) & CS(2,3) & CS(2,4) \\ CS(3,1) & CS(3,2) & CS(3,3) & CS(3,4) \\ CS(4,1) & CS(4,2) & CS(4,3) & CS(4,4) \end{bmatrix} \begin{bmatrix} 0 \\ 0 \\ \sigma^* \\ \tau^* \end{bmatrix}_{Y_1} \tag{5.60}$$

From 5.60, the one new boundary condition (5.61) at the interface between fluid and compliant coating can be established.

$$\begin{bmatrix} \eta_x^* \\ \eta_y^* \end{bmatrix}_{Y_0} = \begin{bmatrix} CS(1,3) & CS(1,4) \\ CS(2,3) & CS(2,4) \end{bmatrix} \begin{bmatrix} CS(3,3) & CS(3,4) \\ CS(4,3) & CS(4,4) \end{bmatrix}^{-1} \begin{bmatrix} \sigma^* \\ \tau^* \end{bmatrix}_{Y_0} \tag{5.61}$$

In the dimensionless procedures, the densities used in the dimensionless terms are different in fluid and compliant surface and therefore, the fluid dimensionless term are scaled in order to have consistent forces between fluid and compliant wall. The fluid-wall boundary condition is shown in equation 5.62. The LHS presents the forces and displacement of the compliant surface and the RHS is the fluid pressure and shear caused by the velocity fluctuations.

$$\begin{bmatrix} \eta_x^* \\ \eta_y^* \\ \sigma^* \\ \tau^* \end{bmatrix}_{Y_0} = \begin{bmatrix} \frac{1}{-i\Omega_X c} & 0 & \frac{DU_W}{(i\Omega_X c)^2} & 0 \\ 0 & 0 & \frac{1}{-i\Omega_X c} & 0 \\ 0 & 0 & 0 & \frac{2}{\mathrm{Re}_\delta} \\ 0 & \frac{1}{\mathrm{Re}_\delta} & \frac{1}{\mathrm{Re}_\delta}((i\Omega_X - \beta) + \frac{D^2 U_W}{i\Omega_X c}) & 0 \end{bmatrix} \begin{bmatrix} u_p \\ Du_p \\ v_p \\ Dv_p \end{bmatrix} - \begin{bmatrix} 0 \\ 0 \\ p_p \\ 0 \end{bmatrix} \quad (5.62)$$

5.4.4 The adaptation of the receptivity programme and the compliant surface model

In order to solve the 4th order v_p equation for the boundary layer fluctuations (equation 5.27) for the compliant surface, two extra conditions are considered. They are the velocity and gradient of velocity at the boundary wall. The rigid wall solutions are still solutions of the differential equations for the current problem.

In order to satisfy the compliant surface boundary conditions, two extra solutions are gained. The solution procedure is as follows. First of all, the v perturbation velocities are calculated through the 4th order v_p differential equation 5.27 and the pressure solutions calculated from equation 5.28, but in this case two extra solutions are included, when $v \neq 0$ and $dv/dy \neq 0$ at the wall. The u_p perturbation velocities which correspond to these three solutions are then obtained from the X-momentum equation.

In equation 5.62, the RHS strain and stress from the fluid can be calculated for an individual v_p, u_p, p_p solution.

The linear combination between the rigid wall solution, velocity at the wall solution and the velocity gradient at the wall solution is shown in equation 5.63 .

$$v_p = v_{p,rigid} + a_1 v_{p,compliant,1} + a_2 v_{p,compliant,2}$$

$$u_p = u_{p,rigid} + a_1 u_{p,compliant,1} + a_2 u_{p,compliant,2} \tag{5.63}$$

$$p_p = p_{p,rigid} + a_1 p_{p,compliant,1} + a_2 p_{p,compliant,2}$$

where $v_{p,rigid}, u_{p,rigid}, p_{p,rigid}$ is the solution calculated from rigid surface ($v_p = 0, \partial v_p / \partial y = 0$), $v_{p,compliant,1}, u_{p,compliant,1}, p_{p,compliant,1}$ is the solution calculated from boundary condition ($v_p = 1, \partial v_p / \partial y = 0$),and $v_{p,ompliant,2}, u_{p,compliant,2}, p_{p,compliant,2}$ is the solution calculated from boundary condition ($v_p = 0, \partial v_p / \partial y = 1$).

As the motion of the compliant surface is considered as two-dimensional, the w_p perturbation velocity at the wall remains zero.

In order to find the coefficient a_1 and a_2 in equation 5.63, another boundary condition equation 5.61 is applied. The final v_p, u_p, p_p solution satisfies the X, Y, Z momentum equations and also satisfies the strain-stress equation for the compliant surfaces.

5.5 The validation between numerical predictions and experimental measurements

5.5.1 General tendency of gain improvement

Owing to the fact that no relevant experiments have been found in the literature, the validation of the numerical model has to rely on the experimental works discussed in the previous chapter. The numerical predictions and the experimental work (figure 5.10) show similar trends. Figure 5.11 and 5.12 indicate the predictions of gain improvement (ratio of boundary layer receptivity of compliant surface and rigid wall) versus compliant surface properties at the most upstream and most downstream location for the pre-transitional boundary layer respectively. The prediction in the upstream region, which is shown in figure 5.11,

presents an excellent match between experimental and numerical work. Downstream (figure 5.12), there is a similarity between the predictions and experimental measurements; however, the magnitude of gain reduction does not match well. A reasonable explanation of this contradiction may be due to the exclusion of the junction between the compliant surface and flat plate in the calculation which is responsible for the extra disturbances and energy generation at the edge of the panel. (Discussions have been made in chapter 4.5). The current model treats the surface as an infinite panel covering the entire rigid base and does not take into account any junction with the compliant surface panel. The numerical assumption which differs from the experimental reality may result in underestimating the effect caused by the leading edge and the influence on downstream flow.

Another possible reason would be the decay term β with x distance. In the current model only the positive value is considered for the forced vibration associated with bypass transition. The negative value which is associated with the convective waves was ignored. In the experimental environment, convective instabilities such as T-S wave and Traveling-wave flutter instabilities may exist when flow passes over a compliant surface and this affects the receptivity mechanism. The interactions of these convective instabilities were not considered in the current model and it may lead to the difference between the predictions and measurements.

In general, the numerical predictions demonstrate the features of boundary layer receptivity over compliant surfaces. Figure 5.13 showed the overall gain reduction/promotion tendency in the numerical results, and these results are showing a similar contour plot compared with the experimental measurements, figure 4.35.

Both of the results show that the highest reduction region appears between $\alpha_c = \frac{\xi^2}{E\rho_{cs}L^2}$ of 2.5and 4 when Re_x is greater than 100,000. Promotion of gain happens when Re_x is small and with high α_c.

5.5.2 Validation of streamwise spectra

The streamwise spectra provide information to aid understanding of the influence of compliant surfaces on the boundary layer receptivity, and also to validate the integrity of the compliant surface model. The compliant surfaces with $\alpha_c = 6.13$ and $\alpha_c = 3.49$ are discussed here, which were also used in the previous chapter (chapter 4.3.7, figure 4.40). Figure 5.14~5.17 demonstrate the changes in streamwise gain spectra when flow passes over the compliant surfaces. The effect for the compliant surface with $\alpha_c = 6.13$ was illustrated in figure 5.16 and 5.17. An increase in the gain spectra appears in the middle range of frequency where the peak of gain*f is and the spectrum are skewed towards the high frequency region compared with the rigid surface case, the same phenomena has also been observed in the experiments (figure 4.40). When the Re_θ increases to 200 and above, the peak in gain*f is less skewed and attenuated, moreover the intensity of the gain is reduced for high frequency. The tendency again agrees with the experimental measurements but the amount of gain reduction is not as much as in the experimental results. The spectra for the flow over the compliant surface with properties of $\alpha_c = 3.49$ are shown in figure 5.15 and 5.16. The gain reduction for high frequency begins upstream, and when Re_θ is greater than 200, the peak in gain*f in the high

frequency region of gain*f are all reduced in comparison with the rigid surface. All these features are also found in figure 4.42.

For the boundary layer spectrum, the tendency of the gain improvements is similar in the numerical and experimental results. The capacity of numerical model has therefore been demonstrated to predict the gain promotion/reduction tendency and gain spectra of streamwise frequency. Therefore, based on the model results, a compliant surface can be used to suppress boundary layer receptivity and an optimised compliant surface with the minimum receptivity can lead to transition delay.

5.5.3 Effect of material damping and wall compliance on boundary layer receptivity

According to the current experiments and the literature review, material damping, wall compliance which is associated with Young's modulus and coating thickness are the three main controllable factors to affect the boundary layer receptivity. The use of damping and wall compliance to control instabilities in natural transition were discussed in the Carpenter, Yeo and Gad-el-Hak studies. In this section the influence of material damping, wall compliance and coating thickness on bypass transition flow will be discussed. Figure 5.18 and 5.19 shows that the influence of material damping on different wall compliance and coating thickness at Re_θ=100 and 300 respectively. The reason for choosing Re_θ=100 and 300 is because the influences of a compliant surface on the flow are markedly different between these two Reynolds number.

When the Reynolds number Re_θ =100, a profound increase of gain was found for a thick coating and high wall compliance (low G_s * and therefore low C_t *)

for any kind of damping levels. In the current investigation, a maximum gain improvement (ratio of boundary layer receptivity of compliant surface and rigid wall) reached 8 times for C_t * =0.2, ξ_s=200, L_s =10 when compared to the rigid wall. For high Reynolds number (Re_θ =300, downstream station), the tendency of the gain improvement has changed compared with the upstream region (Re_θ =100). In figure 5.19(a), for a low damping level of ξ_s=50, the receptivity were suppressed totally for any wall compliance and coating thickness condition. When the damping factor was over 100, the gain was promoted by 20%~60% compared to the rigid wall, which is much less than for the upstream region, where the improvement of gain increased dramatically. The higher damping factor shows its ability to reduce the boundary layer receptivity by a higher percentage when flow passes from upstream to downstream.

Figure 5.20 and 5.21 show another influence aspect of the compliant surface, the coating thickness, for boundary layers with $\mathrm{Re}_\theta = 100$ and $\mathrm{Re}_\theta = 300$ receptivity. The downstream station again has a greater gain reduction or smaller gain promotion compared to the upstream stations. There are 4 different coating thicknesses presented and gain reduction can be achieved by using a thin coating with high wall compliance for all kinds of damping level. The coating thickness has a significant effect on reduction/promotion of gain, and a thin coating showed a greater potential to reduce boundary layer receptivity. (5.20(a) and 5.21(a))

The predicted behaviour of receptivity response to compliant surfaces at the upstream station has lots of similarities to the generation of static-divergence instability which is caused by the surface motion and the predictions reflect the assumptions made in the numerical model. The numerical model only considers the

positive decay term β in x, and the model is capable of predicting absolute waves, such as static-divergence instability, but convection waves, such as T-S wave are ignored as they result from the negative decay term β.

In Gad-el-Hak's (1984) paper, he referenced a private communication with Ash and Ash who used a thin and tightly stretched layer of Mylar to suppress the static-divergence waves and which also resulted in reducing the dynamic response of the surface. Yeo (1990) examined the static divergence instabilities by using numerical approaches , and he concluded that the static-divergence instability could be brought about by increasing damping when a wall is sufficiently soft, which suggests that high material damping may be a necessary criterion for the existence of static-divergence instability.

The simulation results correspond with the experimental findings that thicker compliant surfaces lead to gain increase. Another agreement with the Gad-el-Hak (1984) experiments is that he indicated that the thick surface is more susceptible to static divergence hydroelastic instability than a thin one. His experiments were conducted in a water channel and no static divergence instabilities were found in the laminar boundary layer. However, in the Hansen and Hunston (1976)and Duncan et al.(1982) studies, the static-divergence waves can be detected in the laminar boundary layer but they require a higher free stream velocity for the onset of static-divergence instability. In the turbulent boundary layer, the onset of static-divergence instability occurs for a free stream velocity around $U > 2.86C_t$, compared to $U > 5.92C_t$ in the laminar boundary layer. The evidence proved SD instabilities can exist in the laminar boundary layer. Therefore, when flow passes over a compliant surface in a high turbulence environment, the high boundary layer receptivity can be

an initiator of the static-divergence waves and this would lead to premature transition. The static-divergence instability could be very susceptible to and a distinguishing feature in bypass transition over the compliant surface. The current study and the literature suggest use of a high compliance, thin coating and high damping can suppress growth of boundary layer receptivity and with low damping static-divergence waves appearance at upstream station can be prevented, and hence can benefit transition delay.

5.5.4 Analysis of streamwise gain spectra over the compliant surfaces

The effect of material damping, wall compliance and coating thickness were considered in the previous section and the investigation now considers the streamwise spectrum over compliant surfaces. The coating thickness is kept constant at 5δ, and the selection of non-dimensional parameters, material damping ξ_s and wall compliance C_t*, were used to understand the promotion of energy level caused by the compliant surfaces. The individual effect on gain spectra at Re_θ=100 are shown in figure 5.22 and 5.23.

Figure 5.22 illustrates the effect of progressively increasing the wall compliance, which decreases C_t*. When $C_t^* \to \infty$, the wall becomes rigid and $C_t^* \to 0$ means a soft, higher compliance coating is being used. For a level of damping of 50 (figure 5.22(a)), the variations of the gain improvement are not very obvious, but a higher compliance coating leads to larger gain reduction. When the level of damping is over 100(figure 5.22(b) and (c)), the influence from the wall compliance is perceivable. A higher compliance coating will lead to more energy in the receptivity mechanism. The low streamwise frequencies are less effected by the

wall compliance, but the wall compliance has more influence on boundary layer fluctuations with high and middle ranges (0.01~0.05) of frequency.

The effect of material damping is shown in figure 5.23. The curves in the figure demonstrate that the higher damping level promotes the energy in the boundary layer fluctuations at Re_θ=100. An increasing damping factor leads to an increase in the peaks and they move towards high frequency. As a result, the high damping level promotes the energy at high frequency.

When the Reynolds number reaches 300, the previous results suggest the most receptivity mechanisms are suppressed when compared to a rigid wall. Analysis shows that the results for wall compliance between C_t*=0.1~0.3 and the rigid surface are very close. It is difficult to determine the difference in the figures. Therefore, softer coating, higher compliance wall parameter will be discussed here for C_t* ranges from 0.01 to 0.1.

Compared to the rigid wall case, gain*f is suppressed in all the presented cases. Figure 5.25 shows the effect of damping on gain*f with a constant C_t*. The damping plays a role on the gain reduction. A higher damping level causes more reduction in the energy of boundary layer fluctuations. The effect of wall compliance is demonstrated in figure 5.24. It shows a more compliant wall leads to more reduction in the boundary layer receptivity and the most of gain*f reduction was found at high frequency. When the damping factor reaches to 150 and low C_t*, the low frequency energy is reduced by the compliant surface (figure 5.24 (c)).

Overall, comparison between numerical and experimental results illustrates some common features and the coating with high damping factor (ξ_s) promotes greater receptivity at the upstream station and reduces receptivity more downstream.

The role of the wall compliance does not have a very clear and conclusive trend because different damping factors result in different tendencies of gain. In order to achieve suppression of the receptivity mechanism, a compliant wall with high damping factor and more wall compliance is required.

5.5.5 Analysis of spanwise spectra over the compliant surfaces

The spanwise spectrum for various levels of wall compliance (C_l *)and damping factor(ξ_s)are shown in figure 5.26 and 5.27. Figure 5.26 shows spanwise frequency gain spectra at $\mathrm{Re}_\theta = 100$, and a most receptive frequency can be found at the peak positions. The most receptive frequency changes when the overall receptivity is suppressed, but not in the gain promotion cases. In the gain promotion cases, the changes in receptive frequency is not obvious no matter what variations of damping factor or wall compliance are made in almost an identical manner to the rigid wall. The increase/decrease in the amplitudes of spanwise gain corresponds to the changes in the streamwise gain. Higher wall compliance promotes receptivity when ξ_s is over 100. In the downstream region (Re_θ =300), the gain is most likely to be suppressed. Figure 5.27 shows clearly the changes of spanwise spectra which result from wall compliance when receptivity is reduced. The most receptive spanwise frequency increases with the wall compliance which results in a higher suppression of the gain. Comparisons between figures 5.27 (a)~(c) show that the higher damping level also causes a higher spanwise gain reduction.

The predictions show that the Klebanoff mode, which is seen as the streaks, shrinks either in the spanwise size or in the strength when receptivity is suppressed.

On the other hand, when the receptivity is promoted, this results in the amplitude of the streaks being enhanced but not in their spanwise size.

5.6 Optimisation Work

Optimisation of the surface properties is another important contribution of this work in identifying compliant surface properties which will suppress boundary layer receptivity. Owing to the fact that searching for the best properties of a compliant surface by experimental testing is time consuming, an efficient search method through all possible materials to achieve a minimum boundary layer receptivity becomes attractive. The ability of the compliant surface model to predict gain increase/decrease trends was validated with experimental results as shown in the previous sections. In this section, the compliant surface receptivity model is integrated with a searching method. The predictions from this integrated model will lead to results for the optimised properties for minimum receptivity.

In order to pinpoint optimised properties to minimise the receptivity, an efficient searching method should be applied to look at all possible compliant surface properties. Many searching methods have been used, such as least square method, genetic evolutionary algorithm and the Goal attainment method. Genetic evolutionary algorithms are regarded as one of the most efficient methods, and are widely used in engineering applications. Therefore, this approach was adopted here. This section will explain how the optimisation algorithm works with the compliant wall receptivity model to find the best performing combination of compliant surface properties, which suppress boundary layer receptivity the most.

5.6.1 Basic principle of the Genetic Evolutionary algorithm

Genetic Evolutionary algorithms (GEA) are inspired from natural selection and survival of the fittest in the biological world. GEA differ from more traditional optimization techniques in that they involve a search from a "population" of solutions, not from a single point. Each iteration of a GEA involves competitive selection that eliminates poor solutions. The solutions with high fitness are recombined with other solutions by swapping parts of the solution with one another. Another feature of the GEA is mutation where a small change to a single element of the solution is made, and hence results in a search across all possible answers. Recombination and mutation are used to generate new solutions that are biased towards regions of good solution. The process of the genetic evolutionary algorithm is as follows:

1. Coding
2. Choose initial population
3. Evaluate the individual fitnesses of a certain proportion of the population
4. Select pairs of best-ranking individuals to reproduce
    a. Apply crossover operator
    b. Apply mutation operator
5. Repeat steps 3 and 4
6. Until terminating condition

5.6.1.1 Coding

The first stage of the GEA is coding, solutions are represented in binary as strings of 0s and 1s. Each binary substring representing each parameter with the desired precision are concatenated to form a string or chromosome. The process is analogous to the biological genes which form the chromosome.

5.6.1.2 Population

The evolution starts from a population of completely random individuals and happens in generations. A set of 1 or 0 strings form the population and the number of the strings is the size of the population. The population defines the number of solutions the GEA explores in the solution space. If a large population is chosen, only a few generations will be possible before reaching the maximum number of evaluations, and if a small population is chosen, more generations have opportunity to evolve and it may therefore lead to premature convergence. Therefore, a proper size for the population is an important decision.

5.6.1.3 Selection

Offspring for the next generation of the population of organisms are generated, based on the processes of selection and reproduction of selected individuals through genetic operators; crossover and mutation.

There are two ways to select the offspring-tournament selection and roulette wheel selection. Owing to the fact that the roulette wheel selection has premature convergence and weak promotion of better strings (Goldberg, 1989), tournament selection was used. Deterministic tournament selection selects the best individual in

any tournament for crossover. Selection pressure can be easily adjusted by changing the tournament size. If the tournament size is larger, weak individuals have a smaller chance of selection.

Crossover is a mating operator that provides random chromosome exchange. Conventional crossover can be performed with one-point, two-point and multi-point crossover positions. One-point and two-point crossover are often used owing to the fact that the multi-point crossover tends to liken random shuffle operators and loses the true meaning of the crossover. The crossover point is chosen randomly and the vector components of both strings are exchanged, either side of the points. A simple example is shown in figure 5.28.

The mutation operator attempts to mimic the general diversity in nature's populations of genetic material. In the algorithm, the mutation operator leads to searching in a new field to look for any better or more successful solutions. Typical genetic algorithms have a fixed, very small probability of mutation of the order of 0.01 or less. Based on this probability, the new child organism's chromosome is randomly mutated, typically by flipping bits in the chromosome data structure.

5.6.1.4 Terminating condition

The termination condition is set up when a fixed number of generations is reached and the highest ranking individual's fitness is reaching or has reached a plateau such that successive iterations no longer produce better results.

5.6.2 Settings in the current study

The current work initializes 50 random samples of material properties as a population. Each set of compliant surface material properties were binary coded as three chromosomes. The individual fitness was evaluated by the boundary layer receptivity programme and the smaller values of receptivity were given a stronger position to be selected for the next generation. Tournament selection with a shuffling technique for choosing the highest 20 ranking pairs for mating is used in the selection scheme. The routine continues with jump mutation, creep mutation, and single-point crossover. Niching is a non-compulsory feature used in a GEA, but was used here. The process of Niching allows the overall population to simultaneously focus in more than one region of search space. The routine repeats until the termination criterion is satisfied, when 50 generations is reached and the highest ranking individual's fitness has reached a plateau such that 10 successive iterations no longer produce better results.

The code is presently set for a maximum population size of 50, 30 chromosomes (binary bits) and 3 parameters. The total generation is 50, the probability of crossover is set at 0.5, and the probability of mutation at 0.02. The reason for this choice was because it has the best performance (Carroll, 2006). The whole process of cooperation between GEA and compliant surface receptivity model is shown in figure 5.29. The limit for wall compliance (C_l^*), damping factor(ξ_s) and coating thickness (L_s) for the calculation set-up are 0.05~1, 0.3~300 and 0.1~10 respectively.

5.7 Optimal compliant surface properties for receptivity suppression

The optimal compliant surfaces are calculated by a GEA and three parameters, coating thickness, wall compliance and damping factor were optimised to obtain a minimum receptivity. The optimal compliant surface properties for receptivity suppression are shown in table 5.2. Figure 5.30 shows the gain results of the optimal surface and the rigid wall. The optimal surface results suggest that in order to have maximum receptivity suppression, a high wall compliance is needed to respond to the fluid pressure fluctuations. Therefore, a low constant C_t* (C_t*=0.05 which is bottom limit for the calculation set-up) is obtained for optimal wall compliance and it allows a large displacement of the coating to interact with the flow perturbations.

With regards to the wall thickness, the optimal thickness is shown in figure 5.31(a). The optimal wall thickness increases with Re_θ and it ranges from 2.30δ to 4.47δ. The best fit for optimal coating thickness and Re_θ follows the equation $\mathrm{L}_{\text{optimal thickness}} = \left(-5.02\times10^{-5}\mathrm{Re}_\theta^{\,2} + 2.88\times10^{-2}\mathrm{Re}_\theta\right)\delta$, a gradual coating thickness increase is required for receptivity suppression. Due to the fact that the boundary layer grows with the Reynolds number, in the reality of manufacture, an optimal coating thickness will increase much more with Re_θ (distance downstream).

The optimal results in figure 5.31 (b) show that variable material damping is needed to minimise the receptivity over the compliant surfaces. The optimal material damping changed dramatically when the Reynolds number is less than 200 and the lowest damping factor is $\xi_s = 140$ when Re_θ 150~175. When Reynolds number is over 175, the optimal damping factor increases significantly and reaches $\xi_s = 300$ (the upper limit of the calculation set-up) for Re_θ over 200.

Figure5.32 shows the reduction amount and percentage reduction variation with the Re_θ. The reduction amount increases with the Re_θ but it can not catch up the receptivity growth rate in the boundary layer, and therefore the percentage reduction is decreasing with Re_θ. The results explain that the single layer compliant surface can suppress the boundary layer receptivity but it can not reduce it sufficiently to prevent transition. In the spectrum analysis (figure 5.33), the optimal compliant surface does reduce all frequencies in the spectrum in any Re_θ case.

To sum up, high wall compliance and a gradually growing coating thickness is needed for an optimal compliant surface and the optimal material damping depends on Re_θ. By using a series of optimised properties for suppressing boundary layer receptivity, a reduction of receptivity of 9.6% can be achieved.

CHAPTER SIX

CONCLUSIONS

6.1 Introduction

The objective of the current study was to enhance knowledge of boundary layer receptivity resulting from moderate levels of free stream turbulence (1.0~1.7%) for flows over compliant surfaces. The investigations were through experimental and numerical methods.

6.2 Conclusions for experimental work

Experiments have been developed to examine the differences of boundary layer receptivity between rigid wall and compliant surfaces. All the tests were done with zero streamwise pressure gradient and free stream turbulence levels in the range from 1.0% to 1.7%. The main findings of the experimental work are:

6.2.1 Rigid surface

- The overall gain is a measure of boundary layer receptivity and is defined as $Gain_{overall} = \frac{u_{rms}/u}{U_{rms}/U} = \frac{local\_turbulence}{F.S.\_turbulence}$, and therefore represents the response of the boundary layer to the free stream disturbances. All measurements were taken for a boundary layer position of y/δ=0.2 but the

gain is more or less invariant close to this position. The correlation between Re_θ and gain was found to be

$Gain_{overall} = 0.0423\mathrm{Re}_\theta$.

- A typical gain spectrum can be presented in the form $Gain(\Omega_x) = \frac{G_0}{1+(\frac{\Omega_x}{Fc})^S}$, where G_0 is the gain on the plateau part of the spectrum curve and is therefore the low frequency gain. F_c, is the frequency where the $G_0/2$. S is the gradient of the attenuation slope and defines the gain decay at high frequency. The correlation for the gain with streamwise frequency Ω_x and Reynolds number is

$$Gain(\Omega_x, \mathrm{Re}_\theta) = \frac{2.42\times10^{-4}\,\mathrm{Re}_\theta^{\,2} + 7.80\times10^{-2}\,\mathrm{Re}_\theta}{1+\left(\Omega_x\left(5.53\times10^{-2}\,\mathrm{Re}_\theta + 4.59\right)\right)^{(2.10\times10^{-3}\mathrm{Re}_\theta + 1.87)}}$$

- The experimental results obey the criterion for start of transition that the near wall local turbulence level reaches 21%~23%. This agrees with Ercan (1997)'s results.
- The free stream turbulence intensity ranged from 1.0% to 1.7%. The correlation for the free-stream turbulence and onset of transitional Reynolds number is:

$\mathrm{Re}_{\theta s} = -3.86\times10^{08}\mathrm{Tu}^3 + 1.53\times10^{07}\mathrm{Tu}^2 - 2.19\times10^{05}\mathrm{Tu} + 1416.4$

and this result is consistent with Mayle(1991)'s experimental results.

6.2.2 Compliant surface

- The measurements showed that the compliant surfaces do not affect the laminar mean flow velocity profile. Therefore, the correlation between Re_x and Re_θ follows the Blasius Re_x - Re_θ relationship.
- The best transition delay was found using a compliant surface with $\frac{\xi^2}{E\rho_{cs}L^2}$=3.49 ,where the transitional Reynolds number was delayed by 3%.

  In the pre-transitional boundary layer the maximum fluctuation levels were reduced by 2.1%, 4.9%, 9.6% and 10.2% at the four streamwise stations where x=112mm, 195mm, 277mm and 340mm respectively. This evidence demonstrated that the use of compliant surfaces can reduce the boundary layer fluctuations and result in transition delay.
- The receptivity of the flow over the compliant surface has a sudden increase at the leading edge but then decreases gradually in the streamwise direction. The effects on receptivity suppression of the compliant surface improve in the downstream direction. The longer the flow is passing over the compliant surface the more the boundary layer fluctuations and energy are absorbed by the compliant surface. The reason for the profound receptivity increase at the leading edge may result from disturbance kinetic energy generated at the junction between the rigid panel and compliant coating or new waves which are created on the compliant surfaces near the leading edge.
- At a fixed coating thickness, the correlations between gain improvement (ratio of gain overall of compliant surface and rigid wall) and surface properties (E, ξ and L) are well presented as $Gain_{overall}$ *improvement*

$= f\left(\frac{\xi^2}{E\rho_{cs}L^2}, \mathrm{Re}_x\right)$. The tendencies in the gain improvement versus $\frac{\xi^2}{E\rho_{cs}L^2}$ change with Reynolds number. The gain amplification increases with a growth in $\frac{\xi^2}{E\rho_{cs}L^2}$ in the upstream region (x<195mm), but in the downstream region (when Re_x is over 100000), the greatest gain reduction occurs when $\frac{\xi^2}{E\rho_{cs}L^2}$ is between 2.25 and 3.75.

- In the gain spectrum analysis, the middle range of streamwise frequencies is most affected by the compliant surfaces. Compared to the rigid wall spectrum, distinct peaks are found in the middle range of frequencies in the leading edge region, which therefore contribute to the overall gain increase. Once the flow moves downstream from this region, the energy dissipation takes effect starting with higher streamwise frequencies but later with the middle range of frequencies. At the downstream stations, the energy of the high and middle range of frequencies is dissipated by the compliant surfaces and it weakens the receptivity mechanism.

6.3 Conclusion for numerical work

A method of deriving a theoretical model to predict the boundary layer receptivity for flow over compliant surfaces has been developed. The model combined the receptivity model which was devised by Johnson (2003) and a volume-based compliant surface model. Many modifications have been made to

improve the predictions, such as the streamwise gain spectra on either a rigid or compliant surface wall. The conclusions from the numerical work are:

6.3.1 Rigid surface

- The modified model has improved the predictions in the streamwise receptivity spectra on the rigid surface and the onset of transition is close to the experimental measurements.
- The predictions for the most receptive spanwise wavelength are in good agreement with Matsubara and Alfredsson's (2001) experimental results. When $\mathrm{Re}_\theta = 100$, the dominant spanwise wavelength is 2.5δ. At $\mathrm{Re}_\theta = 300$, the dominant wavelength in the boundary layer is around 0.8δ. The investigation also found that at low Reynolds number, the most receptive spanwise frequencies do not change for different streamwise frequencies, so the structure of the streaks is stable. When the Reynolds number is high ($\mathrm{Re}_\theta = 300$), the dominant spanwise frequency does vary with higher streamwise frequency resulting in higher spanwise frequency, and this may explain the unsteadiness observed in smoke visualisations.

6.3.2 Compliant surface

- A compliant surface boundary layer receptivity model has been developed. The results for gain improvement and streamwise gain spectrum were validated through the experimental work and the validations demonstrated the integrity of the model and that the predictions are able to capture the features which were observed in the experiments.

- The investigations into the boundary layer receptivity of the flow over compliant surfaces with different wall properties (material damping, coating thickness, wall compliance) indicate that thickness has a significant effect on the reduction/promotion of gain, and a thin coating has more potential to reduce boundary layer receptivity. A high damping factor results in receptivity promotion at low Reynolds number, but the reverse is true at high Reynolds number, i.e. higher damping level causes reduction. For the wall compliance, a more compliant wall has greater interaction between the fluid and the compliant coatings. Therefore, the receptivity mechanism is more susceptible to high compliance walls which lead to higher promotion or reduction in gain.
- The predictions showed that the influence of the compliant surface on leading edge receptivity growth is similar to the influence on static divergence instability. Therefore, static-divergence instability could be very susceptible to compliant surfaces and result from leading edge receptivity growth in bypass transition. The current study suggests the use of high compliance, low damping thin coatings can prevent leading edge receptivity growth.
- The researches on the spanwise scale of the streaks show that boundary layer receptivity suppression leads to the streaks shrinking in both spanwise wavelength and strength. On the other hand, if the receptivity is promoted, the spanwise size of the streaks does not grow and only the amplitude of the streaks is enhanced.

- The optimized properties suggest that in order to suppress the boundary layer receptivity, a high compliance wall (low C_t^*) is needed for any Reynolds number. The optimized coating thickness increases with Reynolds number. The damping factor plays very contradictive roles in the boundary layer receptivity suppression. At low Reynolds number, the damping factor is required to be as low as possible to prevent leading edge receptivity growth which is caused by the compliant coating. The optimised damping level is (260~140) .At high Reynolds number, the damping factor needs to be large enough to damp out the fluctuations and therefore, when the Reynolds number is over 200, the optimised damping factor increase until it reaches the upper limit, $\xi_s = 300$, which was set up for the calculations.
- The optimised compliant surface properties for suppressing boundary layer receptivity achieved a reduction in receptivity of 10%.

6.4 Future work

The current studies have demonstrated the use of compliant surfaces can achieve bypass transition delay; however, the following future work can help to improve understanding of boundary layer receptivity for flow over compliant surfaces.

- Multiple hot-wires can be used in the measurements to determine the spanwise scale. This can help to identify the streak structure when subjected to high free stream turbulence intensity and provide evidence to validate the numerical model predictions.

- In order to understand the capacity of compliant surfaces for transition delay, higher free stream turbulence levels should be tested.
- There are many different types of the compliant surface model. Others kinds of visco-elastic model should be adopted which may improve the predictions.

REFERENCES

Abu-Ghannam, B. J., and Shaw, R. (1980). "Natural transition of boundary layers - the effects of turbulence, pressure gradient, and flow history." J. Mech. Eng. Sci., 22(5), 213-228.

Andersson, P., Berggren M., and Henningson D. S. (1999). "Optimal disturbances and bypass transition in boundary layers." Physics of Fluids, 11, 134-150.

Arnal, D., and Juillen, J. (1978). "Contribution experimentale a l'etude receptivitc d'une couche limite laminaire, a la turbulence de l'ecoulement general." ONERARapport Technique, No 1/5018 AYD.

Asai, M., Minagawa, M., and Nishioka, M. (2002). "The instability and breakdown of a near-wall low-speed streak." J. Fluid Mech., 455, 289-314.

Benjamine, T. B. (1963). "The threefold Classification of Unstable Disturbances in the Flexible Surface Bounding Inviscid Flows." J. Fluid Mech., 16, 436-450.

Bertolotti, F. P. (1997). "Response of the Blasius boundary layer to free-stream vorticity", Phys. Fluids ,9, 2286-2299.

Blair, M. F. (1992). "Boundary layer Transition in Accelerating Flows With intense Freestream Turbulence: Part-1 Disturbance Upstream of Transition Onset." J. Fluid Engineering, 114,312-321.

Blair, M. F. (1992). "Boundary layer Transition in Accelerating Flows With intense Freestream Turbulence: Part-2 The Zone of Intermittent Turbulence." J. Fluid Engineering, 114,322-332.

Boiko, A. V., Westin, K. J. A., Klingmann, G. B., Kozlov, V. V. and Alferdsson, P.H. (1994). "Experiments in a boundary layer subjected to free stream turbulence. Part2. The role of TS-waves in the transition process." J. Fluid Mech., 281,219-245.

Brandt, L., Schlatter, P., and Henningson, D. S. (2004). "Transition in boundary layers subject to free-stream turbulence." J. Fluid Mech., 517,167-198.

Brandt, L., and Henningson, D. S. (2002). "Transition of streamwise streaks in zero-pressure-gradient boundary layers." J. Fluid Mech., 472,229-261.

Canepa, E., Ubaldi, M., and Zunino, P. (2002). "Experiences in the application of intermittency detection techniques to hot-film signals in transitional boundary layers." The 16th symposium on measuring techniques in Transonic and Supersonic Flow in Cascades and Turbomachines, Cambridge UK.

Carpenter, P.W. (1990). "Status of transition delay using compliant walls." In Bushnell DM, Hefner JN, editors. Viscous drag reduction in boundary layers. Washington, DC: AIAA, 1990. p. 79–113.

Carpenter, P.W. (1993). "The optimization of multiple-panel compliant walls for delay of laminar-turbulence transition." AIAA J., 31,1187-1188.

Carpenter, P.W. (1998). "Current status of the use of wall compliance for laminar-flow control." Experimental Thermal and Fluid Science, 16, 133-140.

Carpenter, P. W., Davies, C. and Lucey, A. D. (2000). "Hydrodynamics and compliant walls: Does the dolphin have a secret?" Current Science, 79,758-764.

Carpenter, P. W. and Garrd, A. D. (1985). "The Hydrodynamic Stability of Flows over Kramer-Type Compliant Surface. Pt.1. Tollmien-Schlichting Instabilities." J. Fluid Mech.,155, 465-510.

Carpenter, P.W., Sen, P.K., Hegde, H. and Davies, C. (2002). "Wave propagation in flow across junction between rigid and flexible wall." IMECE paper no.2002-32202.

Carroll, D. L. (2006). Genetic Evolutionary Algorithm programme, private communication.

Choi, K. S. (2000). "European drag-reduction research- recent developments and current status." Fluid Dynamics Research, 26, 325-335.

Choi, K.S., Yang, X., Clayton, B.R., Glover, E.J., Atlar, M., Semenov, B.N., and Kulik, V.M. (1997) "Turbulent drag reduction using compliant surfaces." Proc. R. Soc. London. , 453, 2229-2240.

Craik, A.D. D. (1966). "Wind-generated waves in thin liquid films" J. Fluid Mech., 26,369.

Daniel, A. P., Gaster, M., and Willis, G. J. K. (1987). "Boundary layer Stability on compliant surfaces." British Maritime Technology Ltd., UK., Report, April.

Dantec 55M01 CTA Bridge Manual (1990)

Dantec Dynamics,(2002). "How to measure turbulence with hot-wire anemometers".

Davies, C. (1995). "Evolution of Tollmien-Schlichting waves over a compliant panel." PhD thesis, University of Warwick, UK.

Davies, C., and Carpenter, P. W. (1997). "Numerical simulation of the evolution of Tollmien-Schlichting waves over finite compliant panels." J. Fluid Mech., 335,361-392.

Davies, C., and Carpenter, P. W. (1997). "Instability in a plane channel flow between compliant walls." J. Fluid Mech., 352, 205-243.

Dhawan, S., and Narasimha, R. (1957). "Some properties of boundary layer flow during the transition from laminar to turbulent motion." J. Fluid Mech., 3, 418-436.

Dietz, A. J. (1999). "Local boundary-layer receptivity to a convected free-stream disturbance." J. Fluid Mechanics, 378, 291-317.

Dinkelacker, A. (1966). "Preliminary experiments on the influence of flexible walls on boundary layer turbulence." J. Sound &Vibration, 4(2), 187-214.

Dixon, E. A., Lucey, A. D., and Carpenter, P.W. (1994). "Optimization of Viscoelastic Compliant Walls for Transition Delay." AIAA , vol.32, No.2, 256-267.

Djordjevic, D. V. (2000). "On the Fluid over a Compliant wall." The scientific journal Facta Universitatis, series Mechanics, Automatic control and Robotics, 2(10), 1219-1232.

Dris, A. (2003). "Boundary layer transition on a flat plate and concave surfaces." PhD thesis, University of Liverpool.

Dris, A. and Johnson, M.W. (2005). "Transition on concave surfaces", ASME Jnl. of Turbomachinery, 127, 507-511.

Duncan, J. H., Waxman, A. M. and Tulin, M. P. (1982). "Dispersion relationships for waves at the interface between a single layer visco-elastic compliant coating and a turbulent flow." Hydronautics Tech. Rep., 8111-1.

Ercan A. H. (1997). "Experimental analysis and modelling of boundary layer transition." PhD thesis, University of Liverpool.

Fasihfar, A., and Johnson M. W. (1992). "An improved boundary layer transition correlation." ASME paper No. 92-GT-245.

Fransson, J. H. M., Talamelli, A., Brandt, L. and Cossu, C. (2006), Phys. Rev. Lett. 96, 064501.

Fransson, J. H. M, Matsubara, M., and Alfredsson P. H. (2005). "Transition induced by free-stream turbulence." J. Fluid Mech., 527, 1-25.

Fraser, L. A. (1984). "The hydrodynamic stability of flows over homogeneous elastic layers." Euromech Colloquium 188 , 23-26 Sept. 84, University of Leeds, UK.

Fraser, L. A., and Carpenter, P. W. (1985). "A numerical investigation of hydroelastic and hydrodynamic instabilities in laminar flows over compliant surfaces comparing of one or two layers of viscoelastic materials." In Numerical Methods in Laminar and Turbulent Flows, 1171, Pineridge.

Fung, Y.C. (1965). Foundations of solid mechanics. Prentice Hall.

Gad-el-Hak, M. (1986). "The response of elastic and viscoelastic surfaces to a turbulent boundary layer." J. of Applied Mechanics, 53, 206-212.

Gad-el-Hak, M.(2000). Flow control: Passive, Active and Reactive Flow Management. Cambridge University Press.

Gad-el-Hak, M. (2002). "Compliant coatings for drag reduction.", Progress in Aerospace Science, 38, 77-99.

Gad-el-Hak, M., Blackwelder R. F., and Riley J. J. (1984). "On the interaction of compliant coatings with boundary-layer flows." J. Fluid Mech., 140, 257-280.

Gaster, M. (1965). "On the Generation of Spatially Growing Waves in a Boundary layer." Journal of Fluid Mechanics, 22,433-441.

Gaster M. (1987). "Is the dolphin a red herring?" In: Liepmann , H.W., Narasimha, R, editors. Turbulence management and relaminarisation. Berlin: Springer, 285–304.

Goldberg, D. E. (1989). Genetic Algorithm in search optimisation and machine learning. Addison-Wesley publishing Ltd.

Hansen, R. J. and Hunston, D. L., (1974). "An experimental Study of Turbulent Flows over Compliant Surfaces," J. Sound & Vibration, 34, 297-308.

Hansen, R. J. and Hunston, D. L., (1976). "Further Observations on Flow-Generated Surface Waves in Compliant Surface." J. Sound & Vibration, 46, 593-596.

Hansen, R. J. and Hunston, D. L. (1983). "Fluid Property Effects on Flow-Generated Waves on a Compliant Surface." J. Fluid Mech., 133,161-177.

Hansen, R. J., Hunston, D. L., Ni, C. C., Reischman, M. M. and Hoyt, J. W. (1980). "An Experimental Study of Flow-Generated Waves on a Flexible Surface." J. Sound & Vibration, 68,317-334.

Henningson, D. S., Lundbladh, A., and Johansson, A. V. (1993). "A mechanism for bypass transition from localized disturbances in wall-bounded shear flows." J. Fluid Mech., 250, 169-207.

Hussaini, M. Y., and Voigt, R.G., (1990). Instability and Transition-Volume I, Springer-Verlag.

Inasawa, A., Lundell, F., Matsubara, M., Kohama, Y., and Alfredsson, P. H. (2003). "Velocity statistics and flow structures observed in bypass transition using stereo PTV." Exp. Fluids, 34(2), 242-252.

Jacobs, R. G. and Durbin, P. A. (1998). "Shear sheltering and the continuous spectrum of the Orr-Sommerfeld equation." Phys. Fluids, 10, 2006-2011.

Jacobs, R. G., Durbin P. A.(2001) "Simulations of bypass transition," Journal of Fluid Mechanics, 428, 185-212.

Johnson, M. W. (1994). "Bypass transition model for boundary layers." J. Turbomach., 116(4), 759-764.

Johnson, M. W. (2001). "On the flow structure within a turbulent spot." Int. J. Heat Fluid Fl., 22(4), 409-416.

Johnson, M. W. (2002). "Predicting transition without empiricism or DNS." J. Turbomach., 124(4), 665-669.

Johnson, M. W. (2003). "A receptivity based transition model." 2003 ASME Turbo Expo, Jun 16-19, Atlanta, GA, United States, 723-728.

Johnson, M. W., and Ercan, A. H. (1996). "A Boundary layer transition model." Proceedings of the 1996 International Gas Turbine and Aeroengine Congress & Exhibition, Jun 10-13 1996.

Johnson, M. W., and Ercan, A. H. (1997). "Predicting bypass transition: A physical model versus empirical correlations." Proceedings of the 1997 International Gas Turbine & Aeroengine Congress & Exposition.

Johnson, M. W., and Ercan, A. H. (1999). "A physical model for bypass transition." Int. J. Heat Fluid Fl., 20(2), 95-104.

Johnson, M. W., and Fashifar, A. (1994). "Statistical properties of turbulent bursts in transitional boundary layers." Int. J. Heat Fluid Fl., 15(4), 283-290.

Joslin and Morris, (1992). "Compliant surface, Effect of compliant walls on secondary instabilities in boundary layer transition." J. AIAA-92-30-2.

Kendall, J. M. (1985). "Experimental study of disturbances produced in a pre-transitional laminar boundary layer by weak free-stream turbulence." AIAA paper, 85, 1695.

Kim, J. (2003). "Control of turbulent boundary layers." Phys. Fluids, 15(5),1093-1105.

Klebanoff, P. S. (1971). "Effect of free-stream turbulence on a laminar boundary layer." Bull. Am. Phys. Soc., 16, 1323.

Kramer, M. O. (1957). "Boundary layer stabilization by distributed damping." J. Aeronaut Sci., 24,459-460.

Krindel, P., and Silberberg, A. (1979). "Flow through gel-walled tubes." Journal of Colloid and Interface Science, 71(1), 39-50.

Landahl, M. T. (1962). "On the stability of a laminar incompressible boundary layer over a flexible surface." J. Fluid Mech., 13, 609-632.

Lee, T., Fisher, M., and Schwarz, W. H. (1995). "Investigation of the effects of a compliant surface on boundary-layer stability." J. Fluid Mech., 288,37-58.

Lucey, A. D., and Carpenter, P. W., (1993). "The hydroelastic stability of three-dimensional disturbances of a finite compliant wall." J. Sound & Vibration, 165, 527-552.

Luchini, P. (1996). "Reynolds number independent instability of the boundary-layer over a flat surface." J. Fluid Mech., 327,101-115.

Luchini, P. (2000). "Reynolds number independent instability of the boundary-layer over a flat surface: optimal perturbations." J. Fluid Mech., 404,289-309.

Lundell, F., and Alfredsson, H. P., (2004). "Streamwise scaling of streaks in laminar boundary layers subjected to free-stream turbulence." Phys. Fluid ,16,1814-1817.

Luo, X. Y. and Pedley, T. J. (1996). "A numerical simulation of unsteady flow in a 2-D collapsible channel." J. Fluid Mech.,314,191-225.

Luo, H. and Bewle, T. (2003). "Design, modeling, and optimization of compliant tensegrity fabrics for the reduction of turbulent skin friction." SPIE Paper ,5049-5057.

Matsubara, M., and Alfredsson, P. H., (2001). "Disturbance growth in boundary layers subjected to free-stream turbulence." J. Fluid Mech., 430, 149-168.

Mayle, R. E. (1991). "The role of laminar-turbulent transition in gas turbine engines." J. Turbomach., 113, 509-537.

Mayle, R. E., and Schultz, A. (1997). "The path to predicting bypass transition." J. Turbomach., 119(3), 405-411.

Mayle, R.E., Dullenkopf, K. and Schultz, A. (1998). "The turbulence that matters." J. Turbomach., 120, 402-409.

Morkovin, M. V. (1969). On the many faces of transition. Viscous Drag Reduction, C. S. Wells, ed., Plenum, New York.

Mosta, S. S. and Sibanda, P. (2003). "On the stability analysis of thermally stratified channel flow with a compliant boundary." Int. J. of Heat and Mass transfer, 46, 939-948.

Nishiokam, M., and Morkovin, M.V. (1986). "Boundary-layer receptivity to unsteady pressure gradients: experiments and overview." J. Fluid Mech.,171, 219-261.

Orr, W. M. (1907). "The stability or instability of the steady motions of a perfect liquid and of a viscous liquid." Proc. Roy. Irish Acad. Sect. A, 27, 9-68, 69-138.

Redford, J.A. and Johnson, M.W. (2005). "Predicting transitional separation bubbles," J. Turbomach., 127, 2005, 497-501.

Reshotko E., (1976). "Boundary-Layer Stability and Transition." Annu. Rev. Fluid Mech., 8, 331-349.

Reza, A. (2003). "Receptivity and transition in boundary layer over a rigid and compliant surfaces." PhD thesis, University of Warick.

Riley, J. J., Gad-el-Hak, M., and Metcalfe, R. W. (1988). "Compliant Coatings." Annu. Rev. Fluid. Mech., 20, 393-420.

Roach, P. E. (1986). "Generation of nearly isotropic turbulence downstream of streamwise tube bundles." Int. J. Heat Fluid Fl., 7(2), 117-125.

Roach, P. E., and Brierley, D. H. (1992). "The influence of a turbulent free-stream on zero pressure gradient transitional boundary layer development." In Numerical Simulations of Unsteady Flows and Transition to Turbulence, Cambridge University Press, 319-347.

Samani, A., Bishop, J., Luginbuhl, C., and Plewes, D. B. (2003) "Measuring the elastic modulus of ex vivo small tissue samples." Physics in Medicine and Biology, 2183-2198.

Saric, W. S., Reed H. L., and Kerschen E. J. (2002). "Boudnary-layer receptivity to freestream disturbances." Annu. Rev. Fluid Mech., 34, 291-319.

Schlichting, H., and Gersten, K. (2000). Boundary layer theory, Springer-Verlag.

Schubauer, G. B., and Skramstad, H. K. (1948). "Laminar-boundary-layer oscillations and transition on a flat plate." NACA Rept. 909.

Silberberg, A. (1987). "Physico-chemical hydrodynamics in turbulent flows close to an interface." Physico Chemical Hydrodynamics 9 , 419.

Srivatsan, L., and Kumaran, V. (1997). "Flow Induced instability of the Interface between a Fluid and a Gel." Journal de Physique II France, 6, 947-963.

Sommerfeld, A. (1908). "Ein Beitrag zur hydrodynamischen Erklaerung der turbulenten Fluessigkeitsbewegungen." Proc. Fourth Internat. Cong. Math., Rome, 116-124.

Stieger, R. (2002). "The effects of wakes on separating boundary layers in low pressure turbines." Ph.D. Thesis, Cambridge University, Cambridge.

Thomson W.T., and Dahleh, M. D. (1997) Theory of Vibrations with Applications (5th Edition), Prentice Hall (New Jersey).

Wang, T. , Keller F. J., and Zhou D. (1996). "Flow and Thermal Structures in a Transitional Boundary Layer." Experimental Thermal and Fluid Science, 12,352-363.

Westin, K. J. A., Bakchinov, A. A., Kozlov, V. V. and Alferdsson, P. H.(1998). "Experiments on localized disturbances in a flat plate boundary layer. Part 1. The receptivity and evolution of a localized free stream disturbance." Eur. J. Mech. B./Fluids, 17(6), 823-846.

Westin, K. J. A., Boiko, A. V., Klingmann, G. B., Kozlov, V. V. and Alferdsson, P.H. (1994). "Experiments in a boundary layer subjected to free stream turbulence. Part1. Boundary layer structure and receptivity." J. Fluid Mech., 281,193-218.

White, F. M. (1991). Viscous fluid flow, McGraw-Hill.

Willis, G. J. K. (1986). "Hydrodynamic stability of boundary layer over Kramer type compliant surfaces." PhD thesis, University of Exeter.

Wiplier, O., and Ehrensteins, U. (2000). "Numerical Simulation of linear and nonlinear disturbance evolution in a boundary layer with compliant walls." Journal of Fluids and Structures,14, 157-182.

Wiplier, O., and Ehrensteins, U. (2001). "On the absolute instability in a boundary-layer flow with compliant coatings." Eur. J. Mechs. B./Fluid , 20, 127-144.

Wundrow, W. D., and Goldstein M. E. (2001). "Effect on a laminar boundary layer of small-amplitude streamwise vorticity in the upstream flow." J. Fluid Mech., 426, 229-262.

Yeo, K S. (1986). "The stability of flow over flexible surfaces." PhD thesis ,University of Cambridge.

Yeo, K S. (1988). "The stability of boundary-layer flow over single-and multi-layer viscoelastic wall." J. Fluid Mech., 196, 359-408.

Yeo, K S. (1990). "The hydrodynamic stability of boundary-layer flow over a class of anisotropic compliant walls." J. Fluid Mech., 220,125-160.

Yeo, K S. (1992). "The three-dimensional stability of boundary-layer flow over compliant walls." J. Fluid Mech., 238, 537-577.

Yeo, K S., Khoo, B. C., and Zhao H. Z.(1999). "The convective and absolute instability of fluid flow over viscoelastic compliant layers." J. Sound & Vibration, 223, 379-398.

Yoshioka, S., Fransson, J. H. M., and Alfredsson, P. H. (2004). "Free stream turbulence induced disturbances in boundary layers with wall suction." Physics of Fluids, 16, 3530-3539.

Tables

Layer no.	L_s (thickness)	C_t * (Shear speed)	ξ_s (material damping)	K_s * (Bulk modulus)
1	0.5	2.0	0.0049	500
2	1.5	0.8	0.0049	500
3	1.0	0.4	0.0294	0.267
4	0.5	0.8	0.0049	500

Table 2.1 Data for compliant wall experiments (Yeo, 1988)

E_{static} N/m2	$E_{dynamic}$ N/m2	(coating L thickness) mm	$k_{stastic}$ N/m	$k_{dynamic}$ N/m	(Damping Γ factor) N·s/m	$\left(\Gamma L/A\right)_{=\xi}$ N·s/m2
700	900	4	168	215	1.65	7.17
1500	2000	4	229	353	2.48	14.18
3800	3600	4	669	627	1.90	10.87
3900	3800	4	687	658	2.25	12.83
4000	4000	4	704	709	0.95	5.44
4200	4000	4	739	695	1.80	10.26
5000	5300	4	867	912	4.12	23.52
9000	8100	4	2288	2050	5.89	25.61
9900	8700	4	2516	2189	6.07	26.39
600	--	8	--	--	--	--
2200	--	8	--	--	--	--
3200	--	8	--	--	--	--
8300	--	8	--	--	--	--
7000	--	8	--	--	--	--
8900	--	8	--	--	--	--
11300	--	8	--	--	--	--

Table 3.1 The compliant surface material properties in the experiment
(-- represents no measurement data available)

	$E_{dynamic}$	ξ (Damping factor)	$\frac{\xi^2}{E\rho_{cs}L^2}$	Coating thickness	x			
					112	195	277	340
Gain improvements-100%	N/m2	N·s/m^2		mm	mm	mm	mm	mm
	900	7.33	3.49	4	12.25%	0.44%	-11.34%	-9.99%
	2000	11.03	6.13		22.26%	7.52%	-4.49%	-4.59%
	3600	10.87	2.00		0.86%	-0.77%	-8.83%	-7.47%
	3800	12.83	2.65		2.59%	1.83%	-10.60%	-9.82%
	4000	5.44	0.45		1.02%	1.12%	-7.87%	-4.51%
	4000	10.26	1.61		5.00%	0.00%	-7.89%	-6.08%
	5300	18.29	6.37		24.29%	12.74%	-2.67%	-5.12%
	8100	26.18	4.94		18.62%	10.01%	-3.98%	-3.22%
	8700	26.98	4.89		11.19%	5.80%	-5.62%	-5.42%

Table 4.1 Gain improvements along the streamwise direction

E(Young's Modulus)	Damping factor	Re_θ=100	Re_θ=150	Re_θ=200	Re_θ=250	Re_θ=300
N/m^2	N·s/m^2					
900	7.33	1.11	0.98	0.94	0.96	0.98
2000	11.03	1.37	1.11	0.97	0.98	0.98
3600	10.87	1.16	1.04	0.98	0.99	0.99
3800	12.83	1.22	1.06	0.99	0.99	0.99
4000	5.44	0.99	0.98	0.98	0.99	0.99
4000	10.26	1.14	1.03	0.98	0.99	0.99
5300	18.29	1.50	1.18	1.02	1.00	1.00
8100	26.18	1.29	1.10	1.03	1.01	1.00
8700	26.98	1.24	1.08	1.02	1.01	1.01

Table 5.1 Predictions of gain improvement for compliant surfaces

Re_θ	C_f *	ξ_s damping factor	L_s Coating thickness	η * displacement	gain for compliant surface	gain for Rigid wall	Percentage reduction
100	0.0051	259.52	2.30	0.10	1.12	1.39	19.80%
125	0.0052	224.03	2.62	0.13	1.95	2.38	18.41%
150	0.0050	139.55	3.34	0.13	3.09	3.67	15.76%
175	0.0051	147.50	4.38	0.15	4.55	5.28	13.95%
190	0.0051	230.00	3.80	0.16	5.58	6.40	12.76%
200	0.0050	295.71	3.53	0.18	6.32	7.21	12.42%
225	0.0050	297.55	3.81	0.20	8.45	9.52	11.23%
250	0.0050	294.13	4.14	0.22	10.92	12.12	9.94%
300	0.0051	297.63	4.47	0.25	17.01	18.43	7.69%

Table 5.2 Optimal compliant surface results

Figures

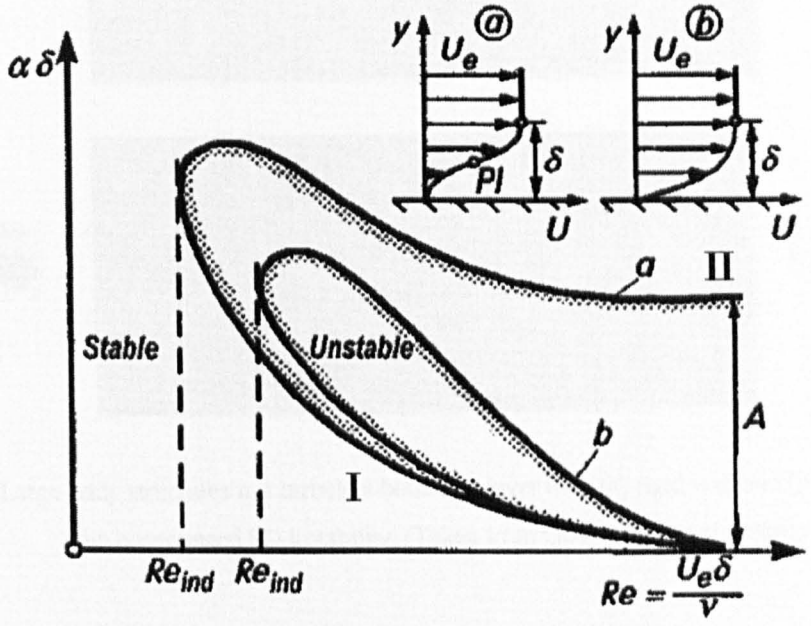

Figure 2.1. Stability curves for a, separating flow and b attached.

(Taken from Schlichting&Gersten,2000)

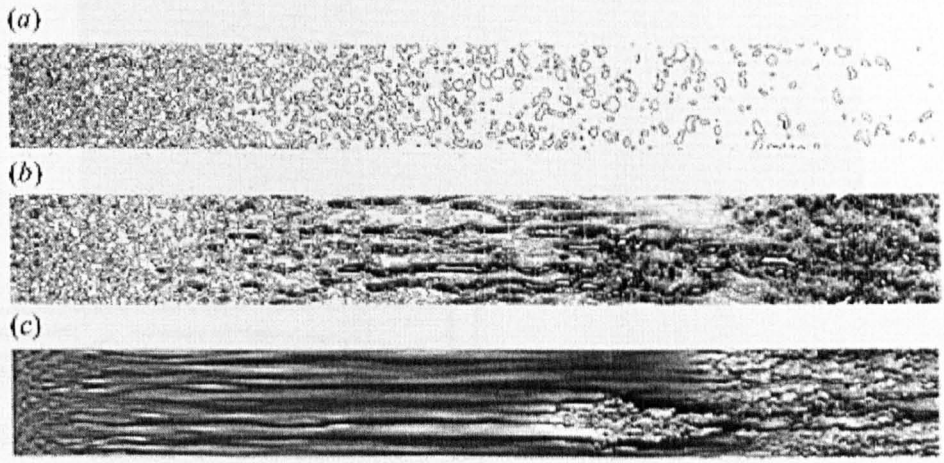

Figure2.2 Boundary layer subjected to high free stream turbulence level (a) in the free-stream (b)at y~δ (c) at y~$1/3\,\delta$ where $\mathrm{Re}_\theta = 250$ (Taken from Jacobs and Durbin (2001))

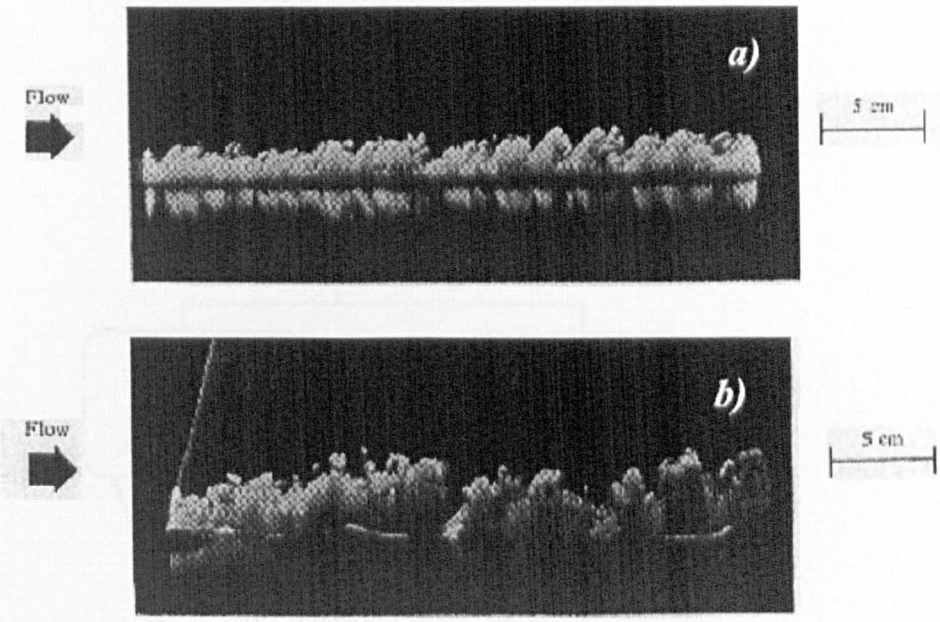

Figure 2.3 Large-eddy structures in a turbulent boundary layer over (a) rigid wall and (b) compliant wall with pronounced SD instability. (Taken from Gad-el-Hak et al (1984))

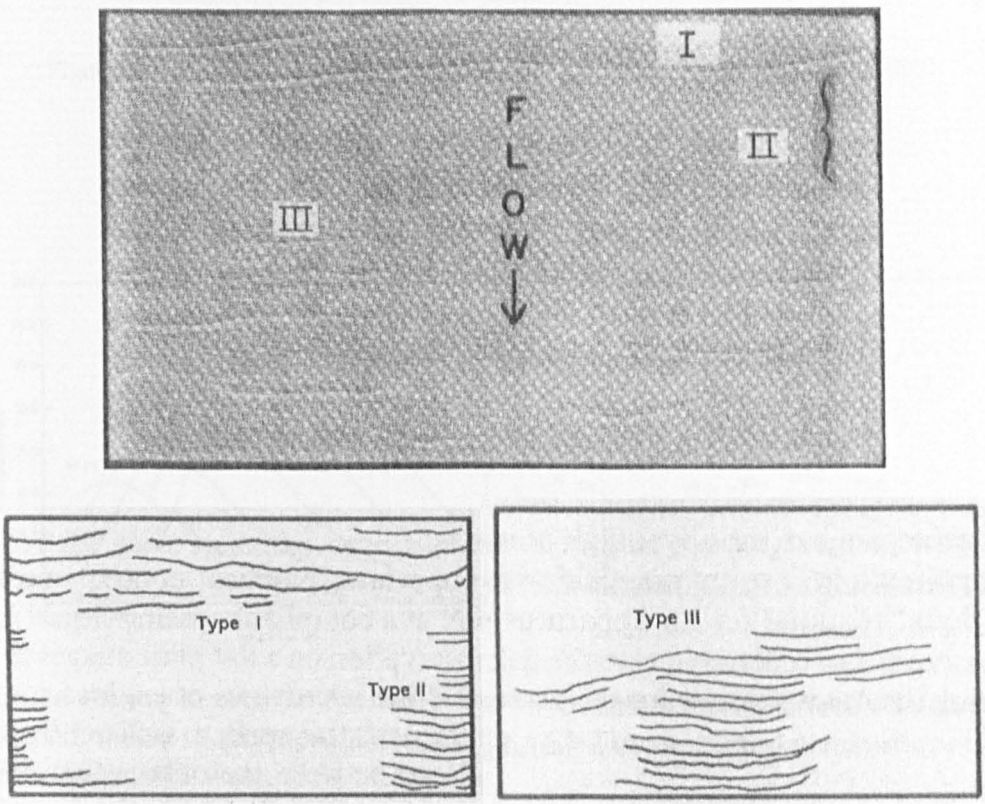

Figure 2.4 Identification of the types of waves , fluid velocity of 1.8m/s

(Taken from Hansen et al.1980)

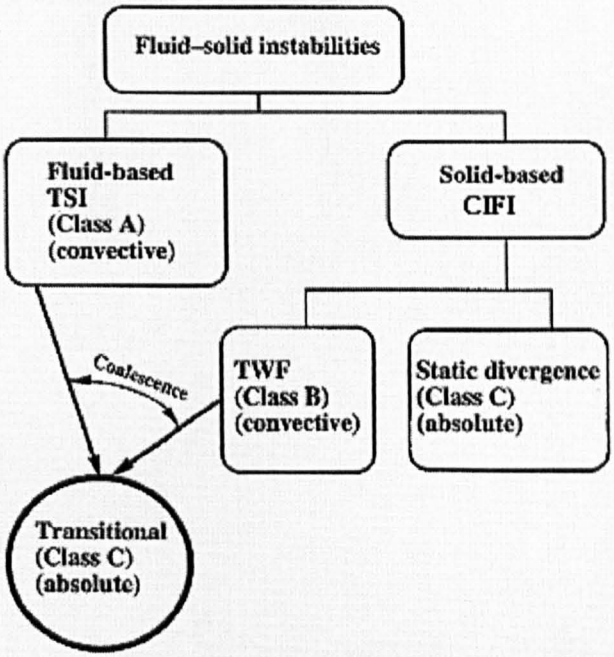

Figure2.5 Classifications of Fluid-solid instability (Taken from Gad-el-Hak ,2002)

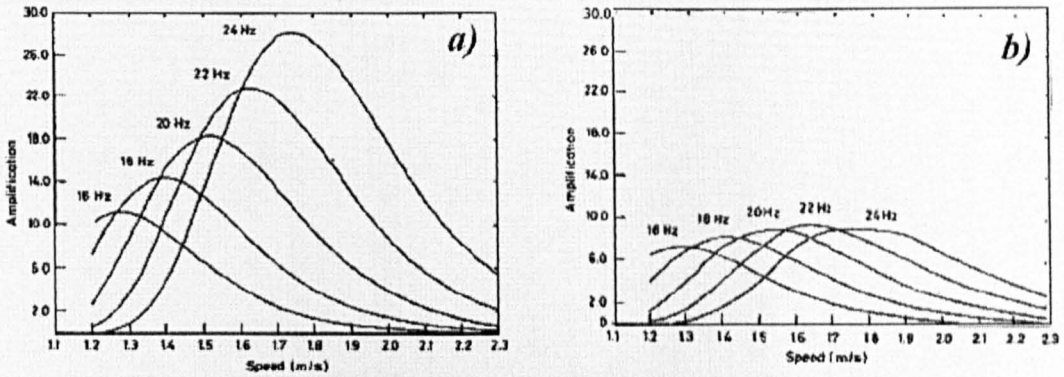

Figure 2.6 The amplification factor versus the speed for various modal frequencies for (a) rigid wall and (b) flexible coating. (Taken from Willis, 1986)

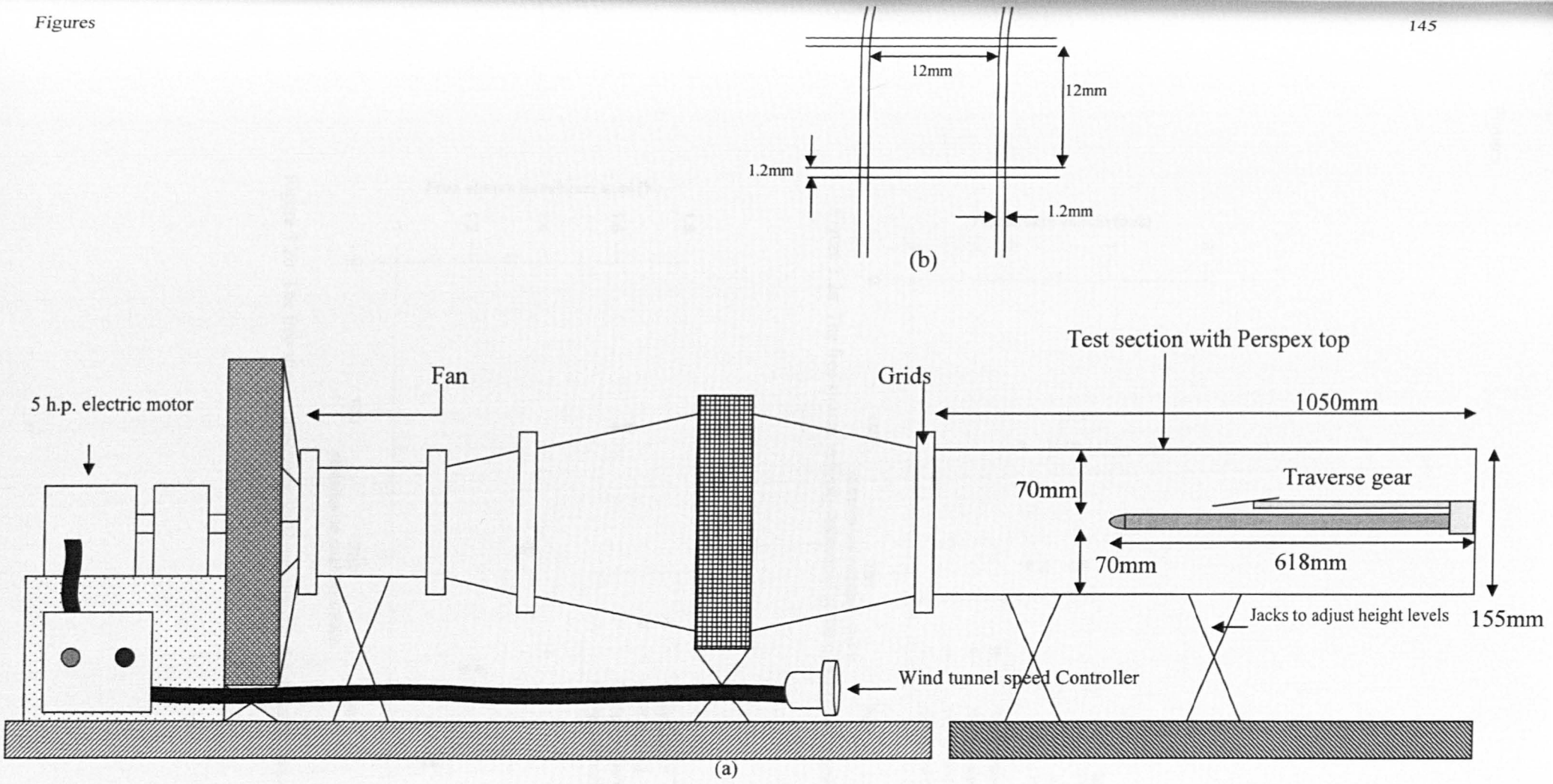

Figure 3.1 (a) Arrangements of wind tunnel and work section (b) Grid information

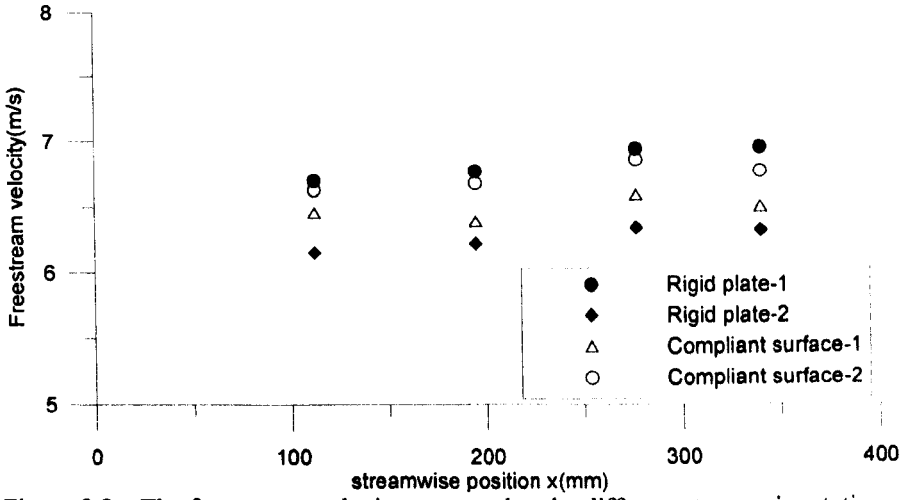

Figure 3.2a The free stream velocity measured at the different streamwise stations

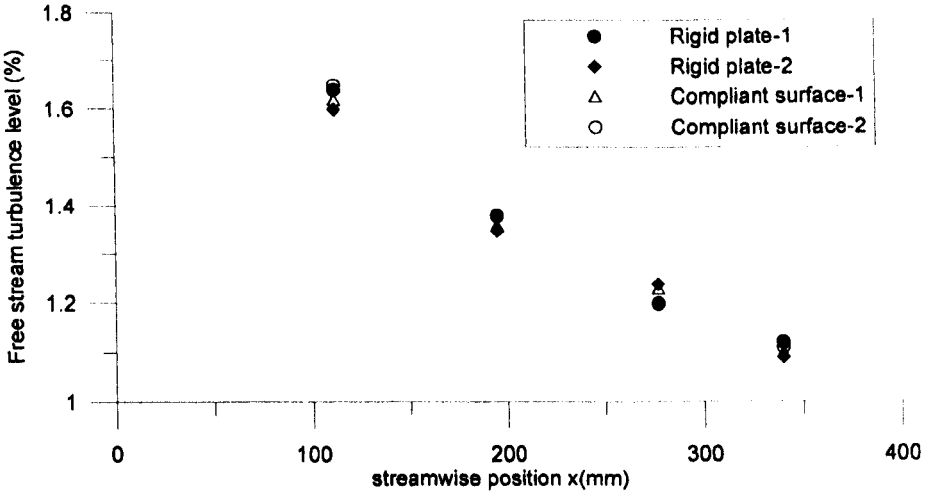

Figure 3.2b The free stream turbulence level measured at the different streamwise stations

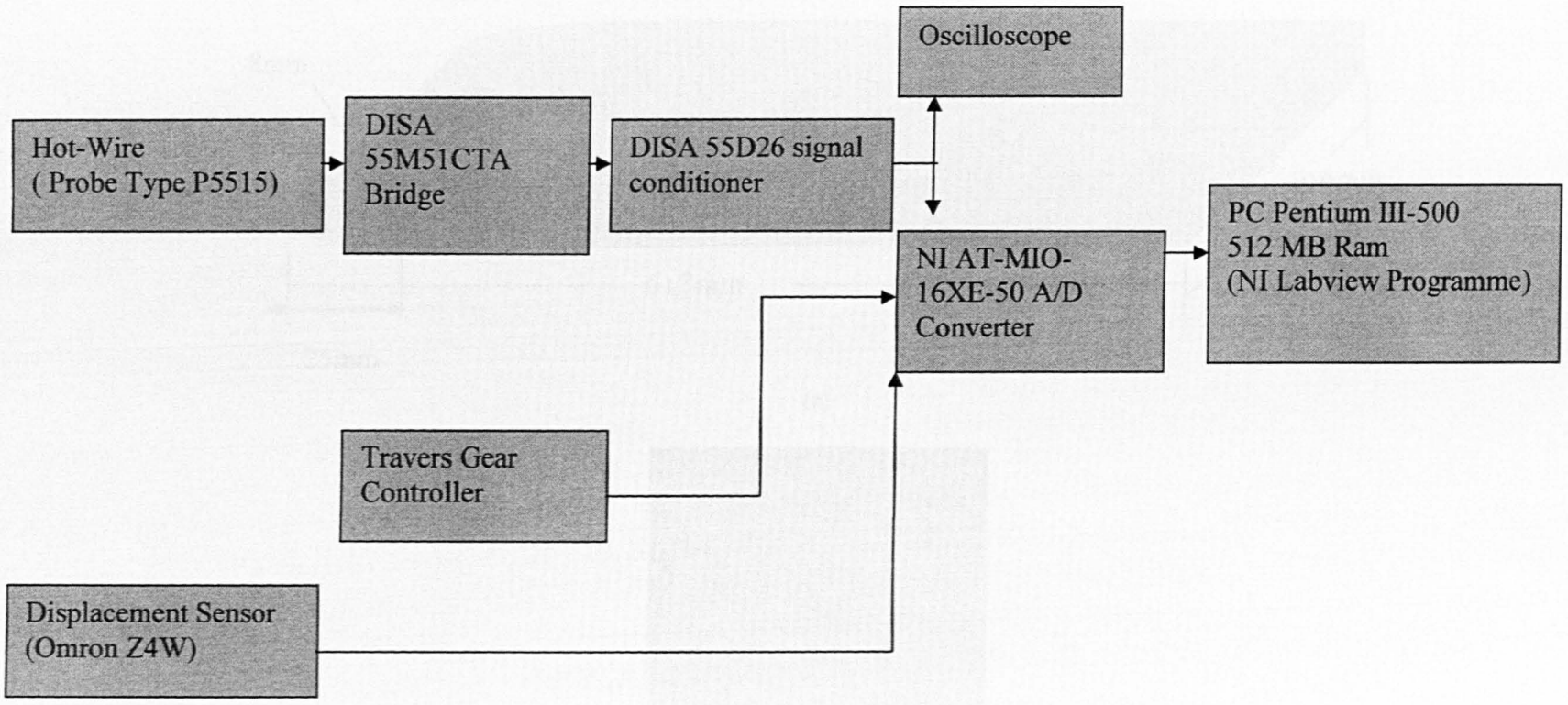

Figure 3.3 Arrangement of electronic devices

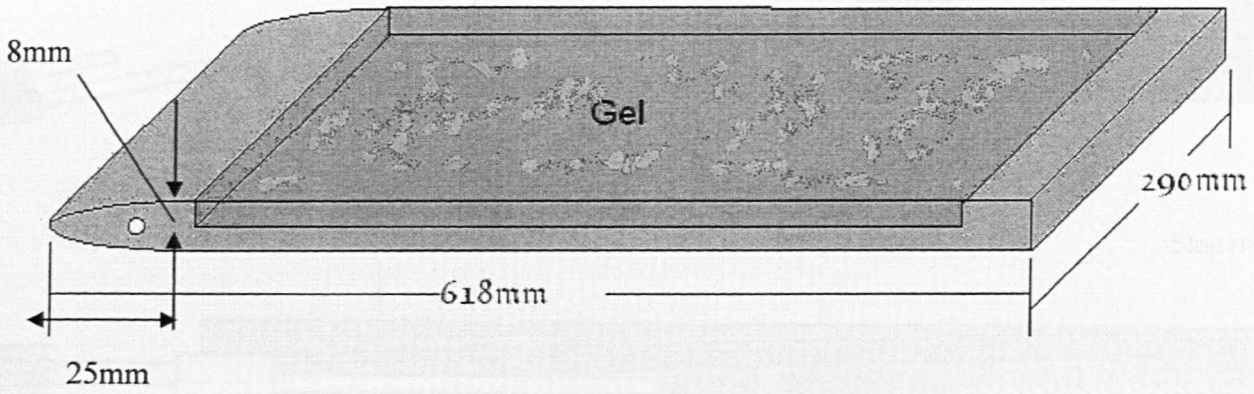

(a)

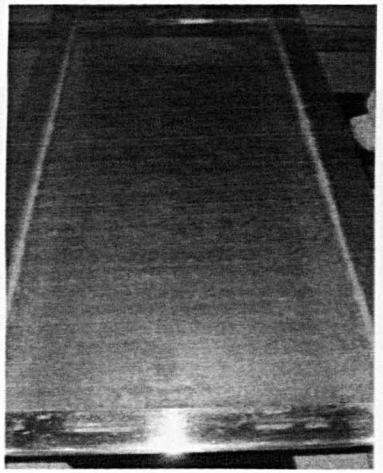

(b)

Figure 3.4 (a) The dimensions of the compliant surface plate (b) photograph of the plate used in the experiments

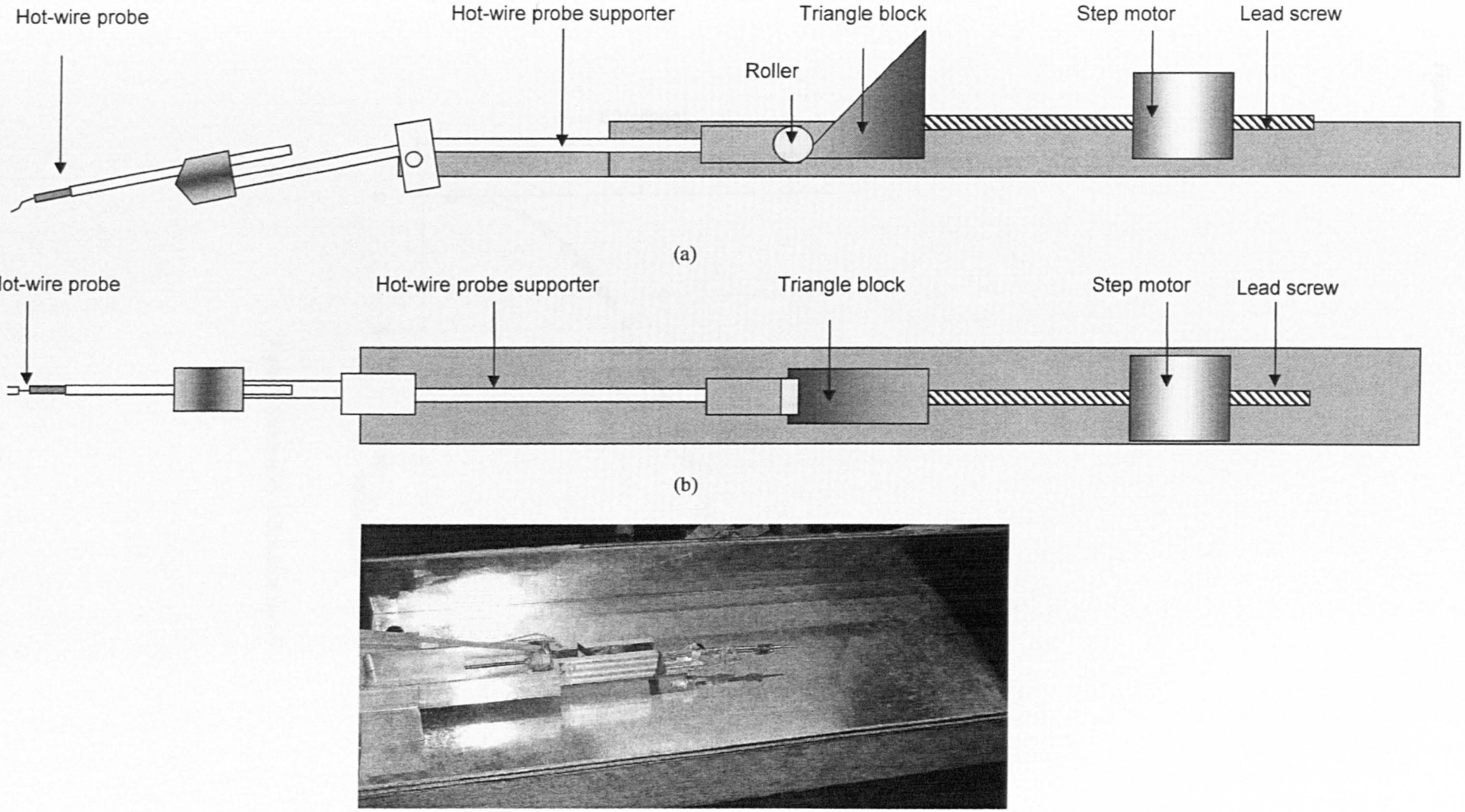

Figure 3.5 Automated traverse gear (a) side view (b) top view (c) the traverse gear on the plate

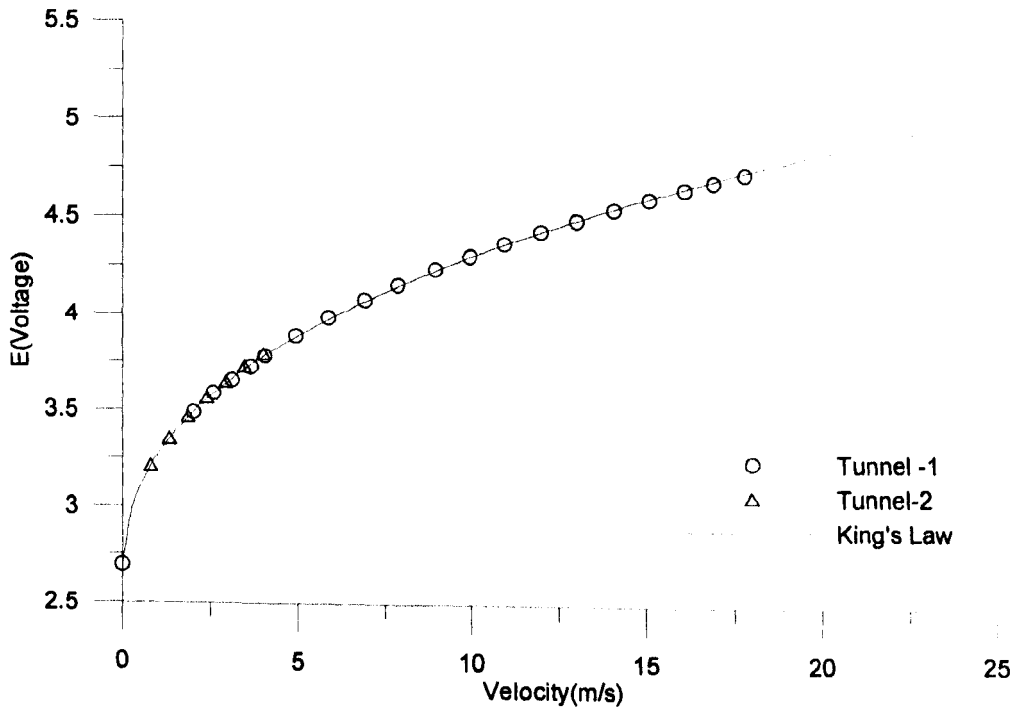

Figure3.6 Hot-wire Calibration curve

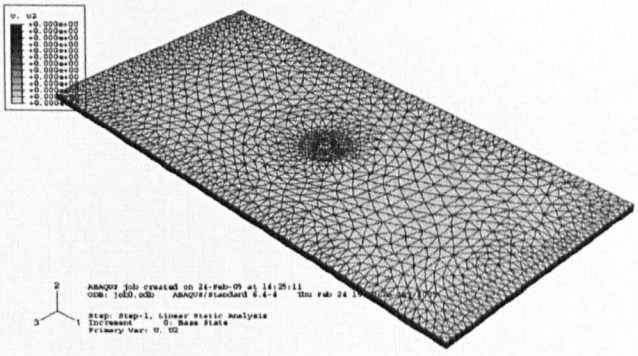

Figure 3.7 The compliant surface model in ABAQUS (zero loaded)

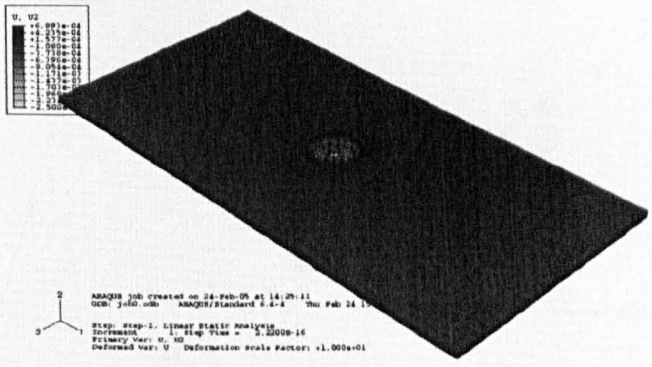

(a)

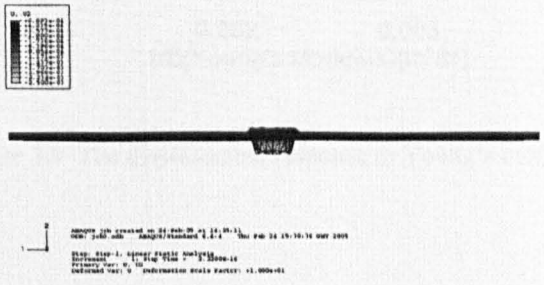

(b)

Figure 3.8 The compliant surface deformation due to the weight of 50 grams mass computed in ABAQUS (Deformation scaled by 10 in vertical direction)
(a) Iso-view (b) side view

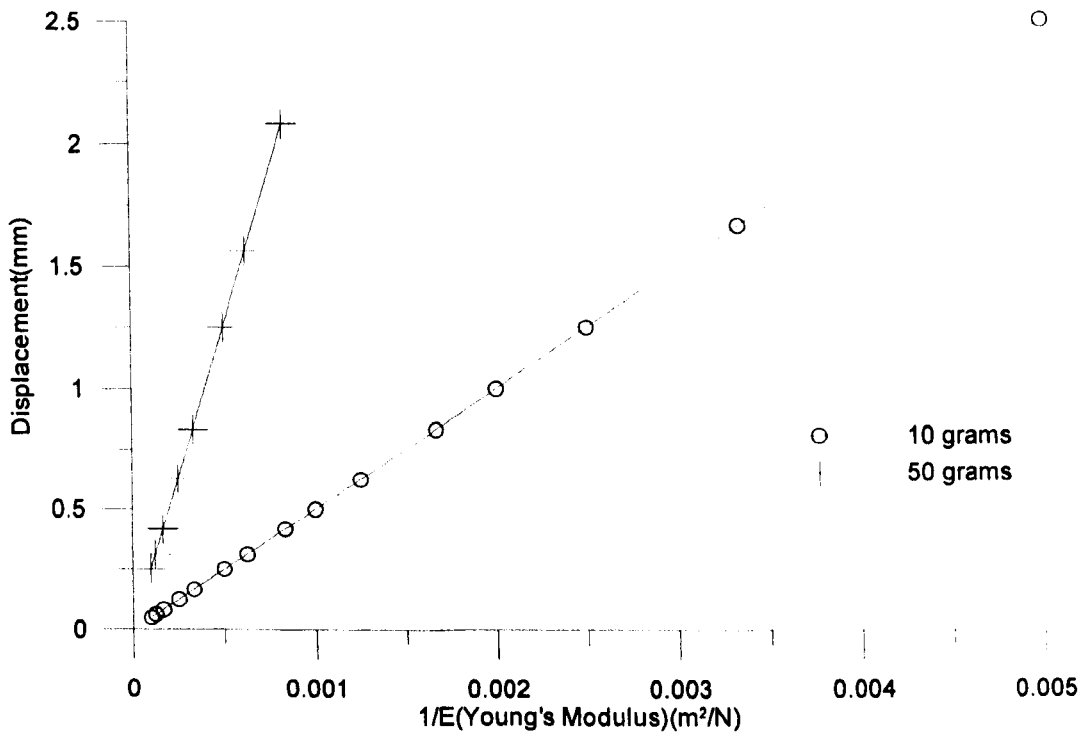

Figure 3.9 The displacement response to Young's modulus

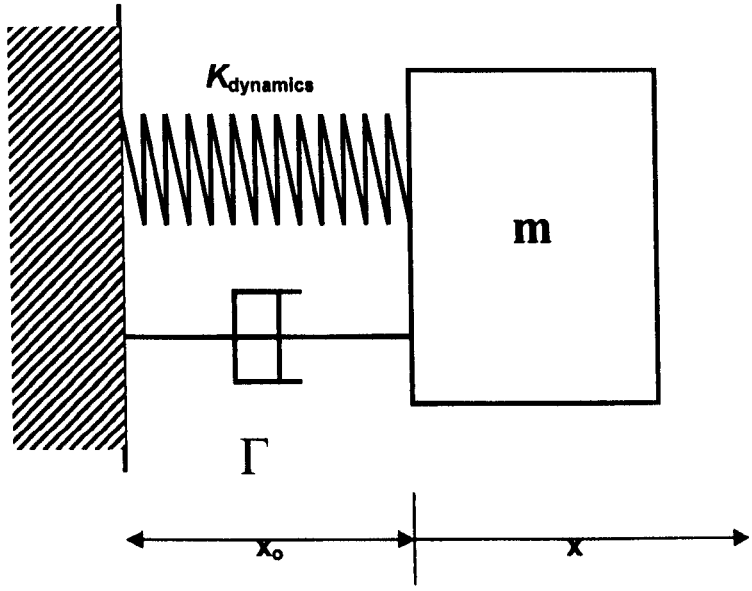

Figure 3.10 Mass spring-damper system

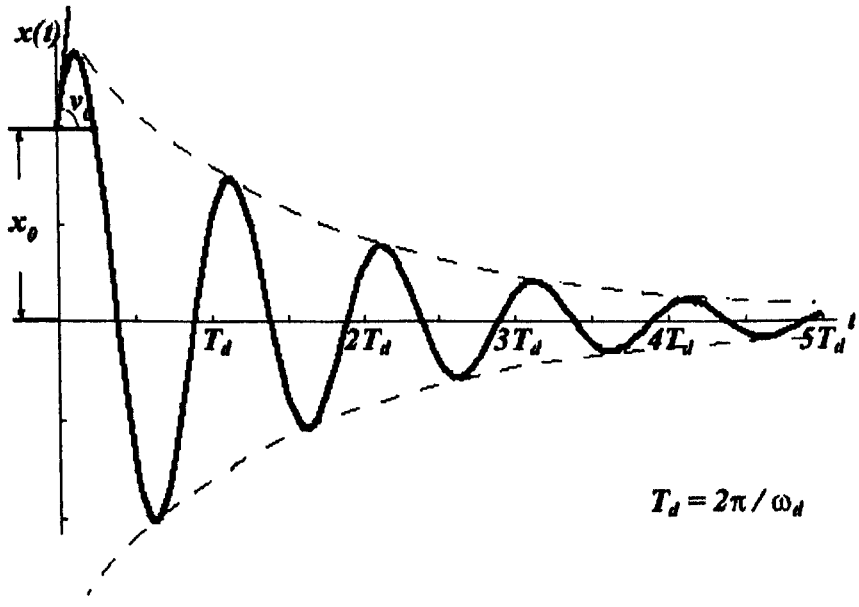

Figure 3.11 Damped displacements with time

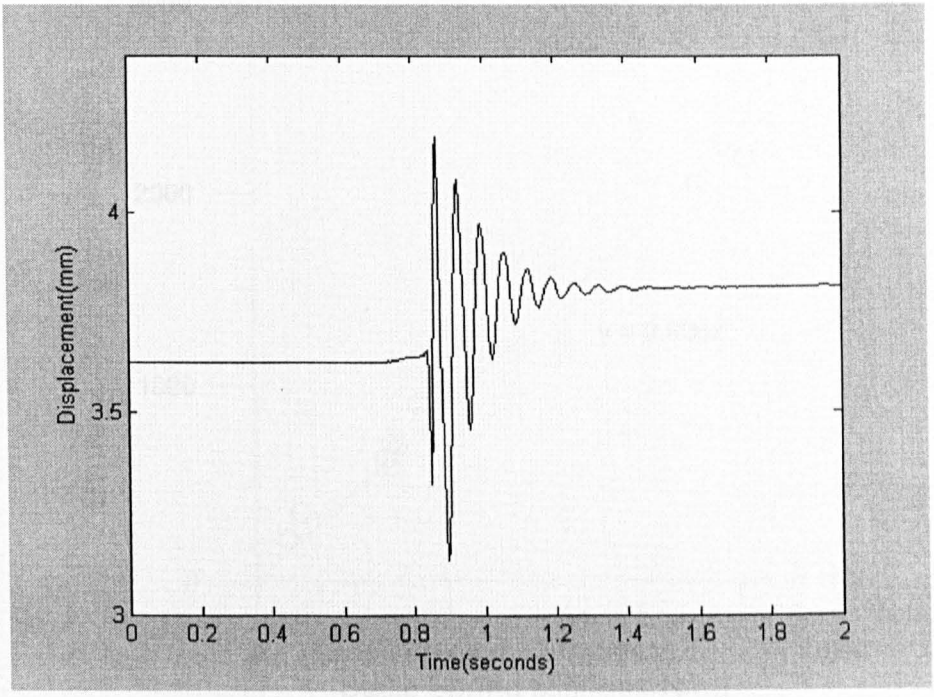

Figure3.12 The displacement of compliant surface

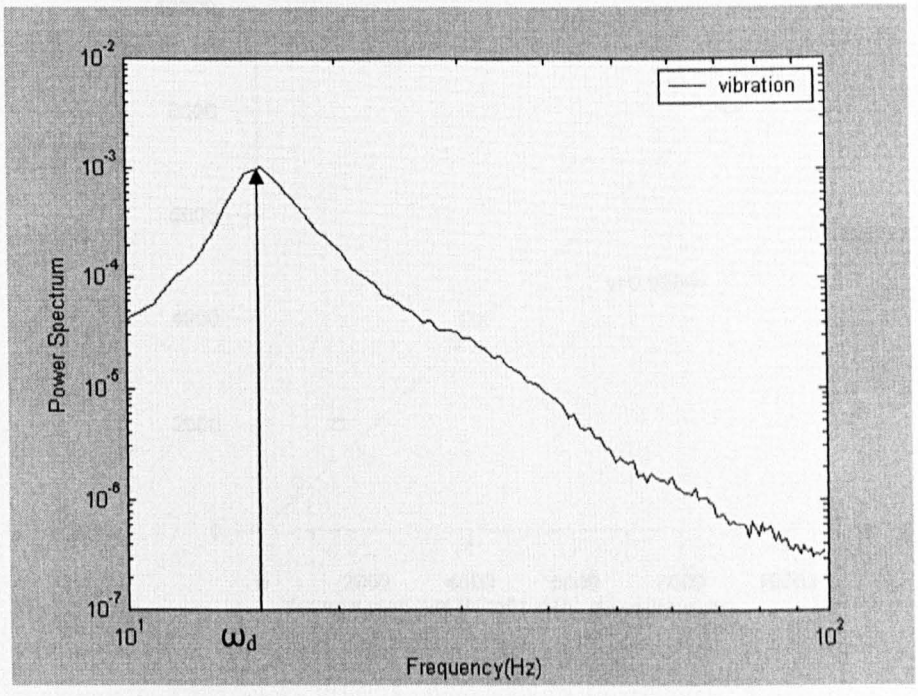

Figur3.13 The spectrum of displacement of compliant surface

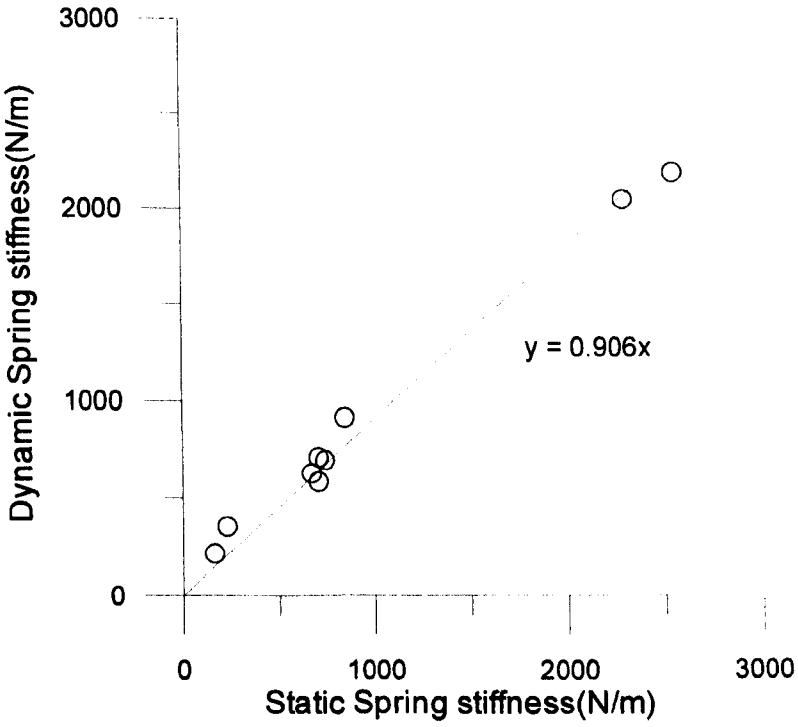

Figure3.14 Comparison between dynamic and static spring stiffness

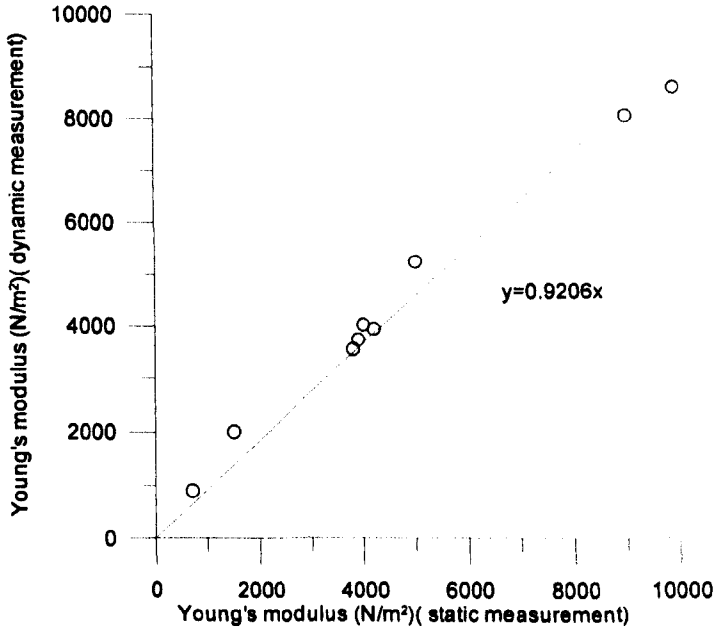

Figure3.15 Comparison between dynamic and static Young's modulus

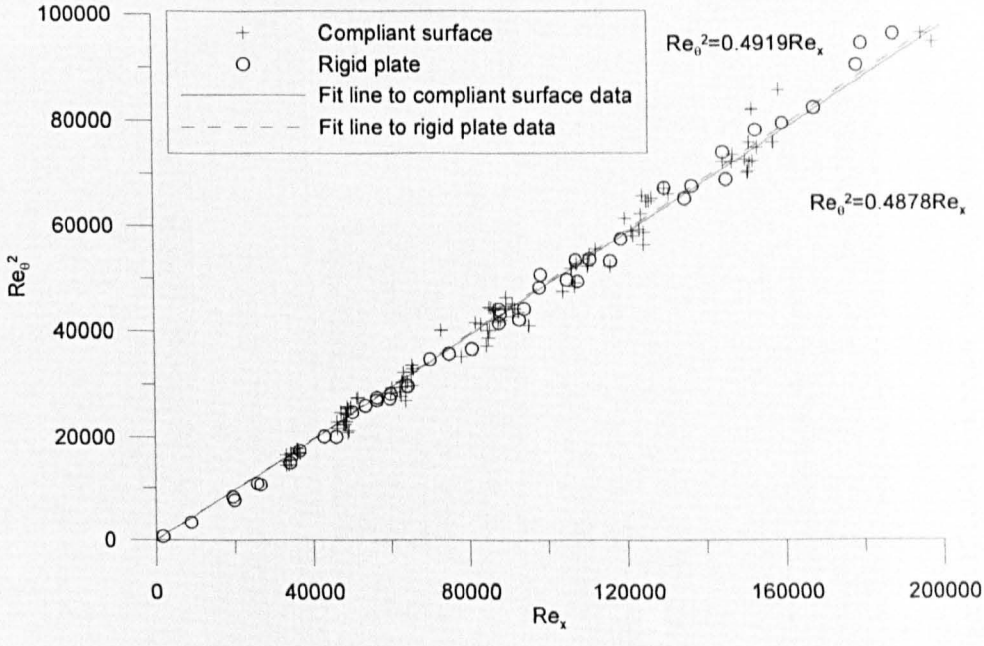

Figure 3.16 The boundary layer development over the rigid and compliant surfaces

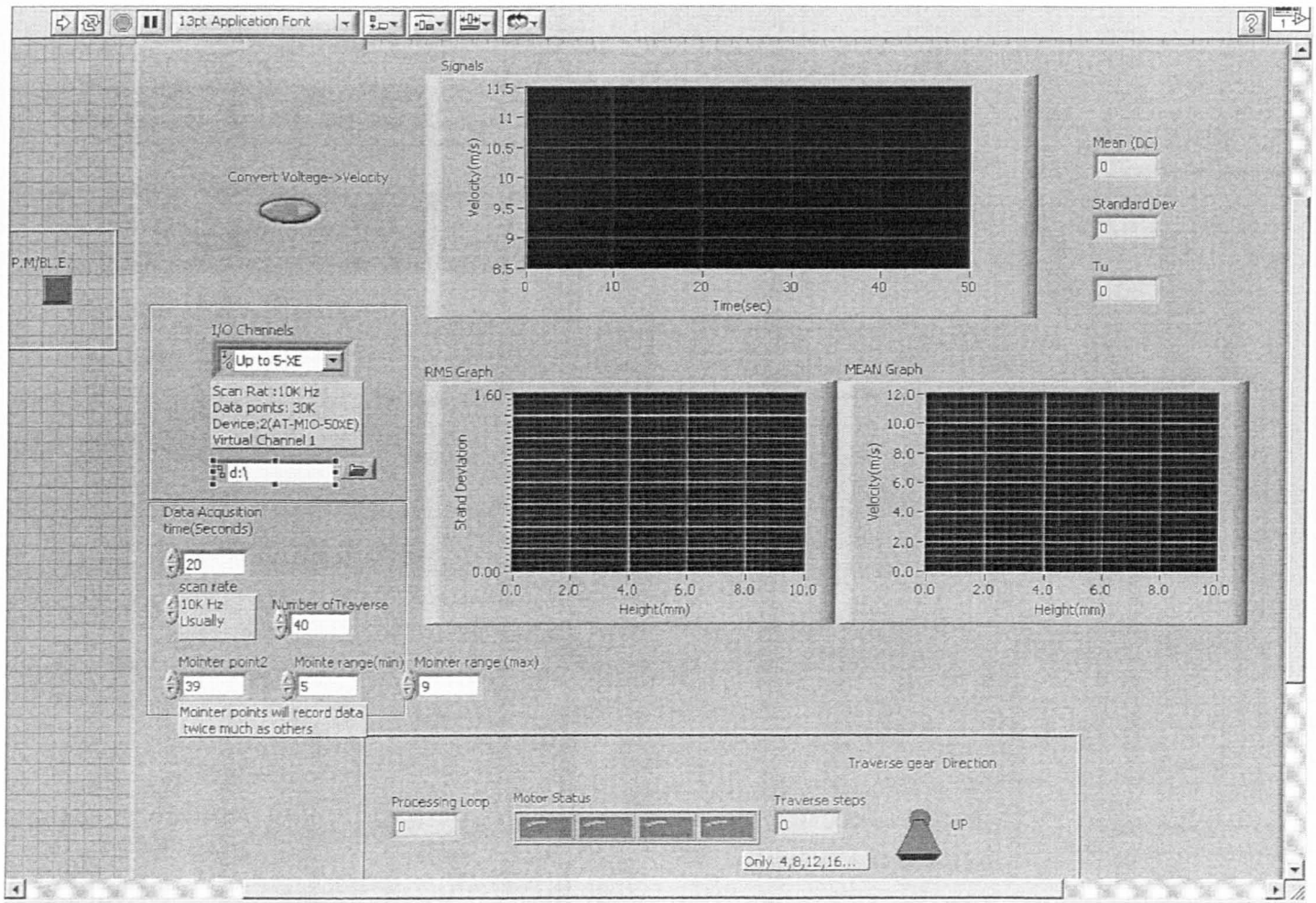

Figure 3.17 Labview program data acquisition panel

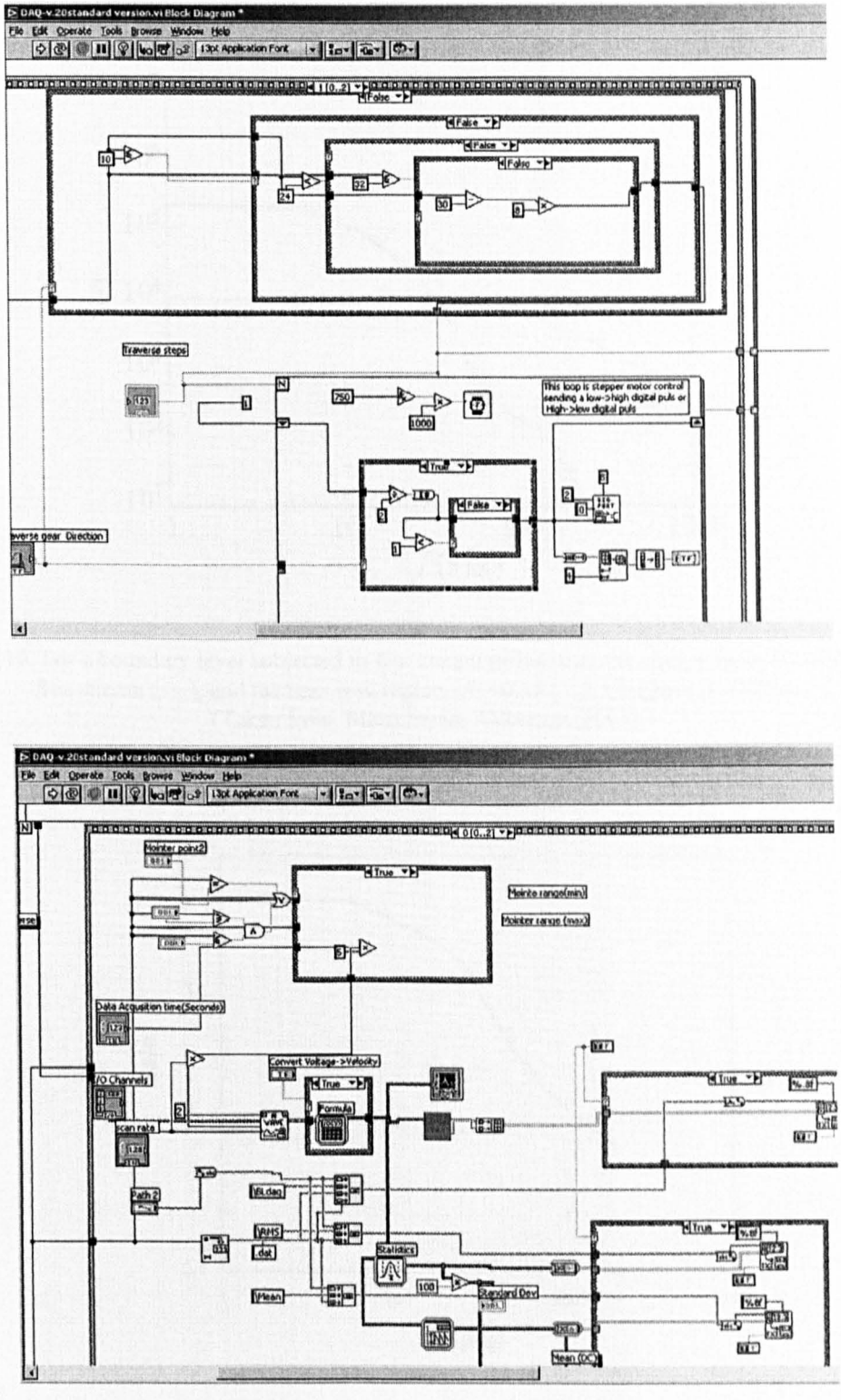

Figure 3.18 Labview program data acquisition programme (top: traverse gear control subroutine, bottom: data acquisition subroutine)

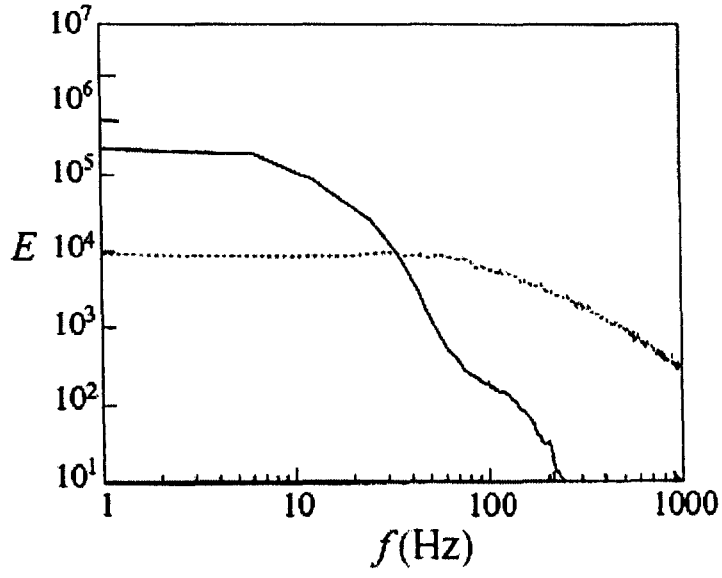

Figure 3.19. For a boundary layer subjected to free stream turbulence, the energy spectral density in the free stream (·····), and the near wall region y/δ =0.25 (—). U=12m/s, x=500mm
(Taken from Matsubara& Alfersson ,2001)

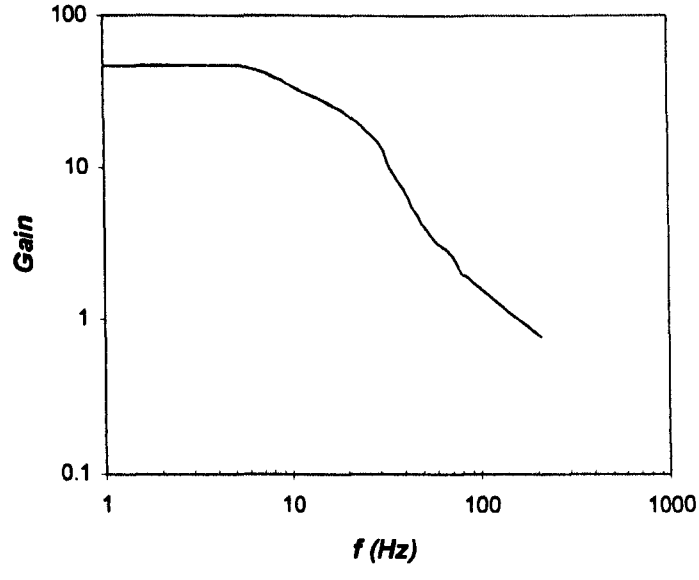

Figure3.20 Near wall gain spectra in laminar flow from data in figure 3.19

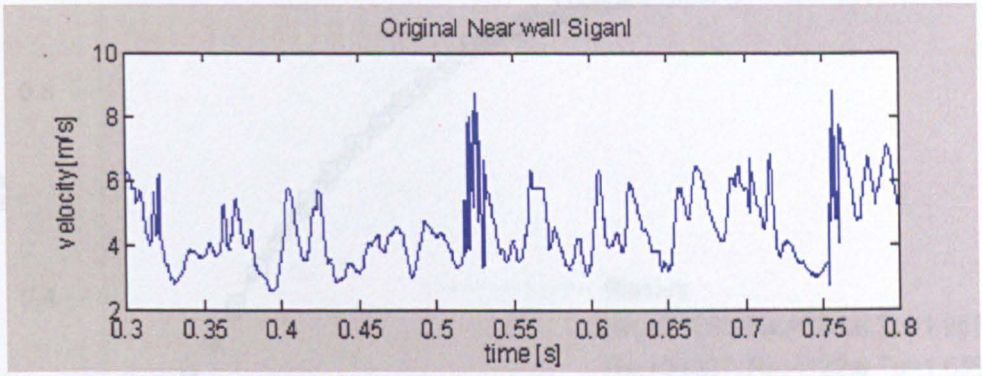

(a)

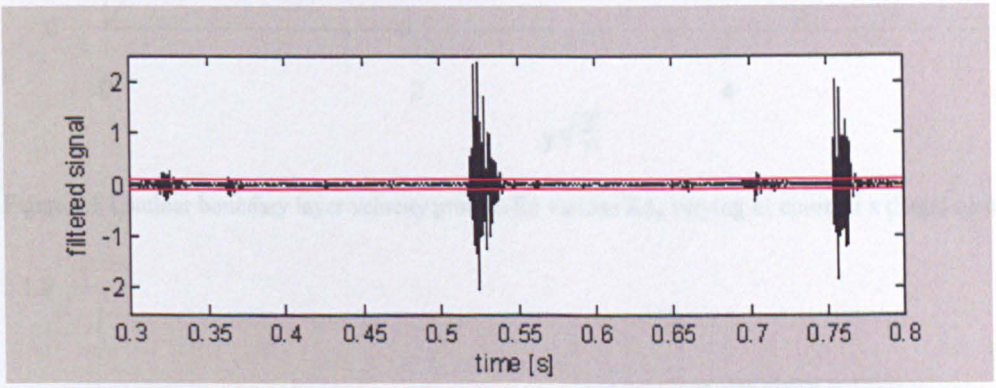

(b)

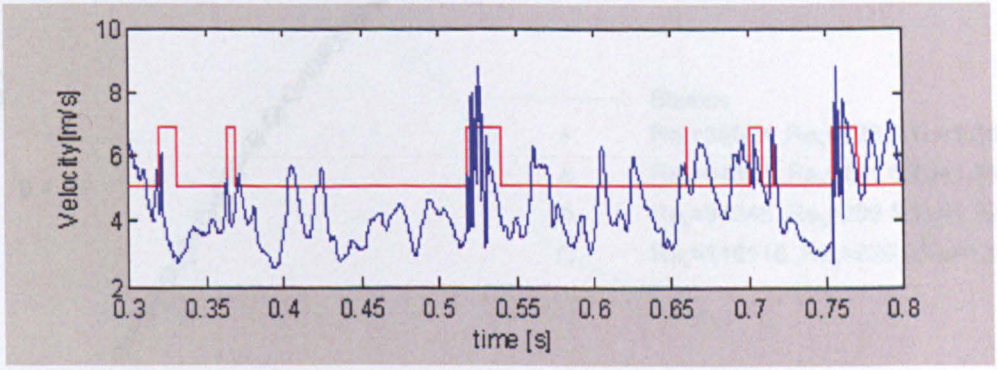

(c)

Figure 3.21 Near wall signal in transitional flow (a) original signal (y/δ=0.2) (b) Filtered signal with 363.8Hz high-pass filter (c) The signals with turbulent event selection ($\gamma = 12.34\%$)

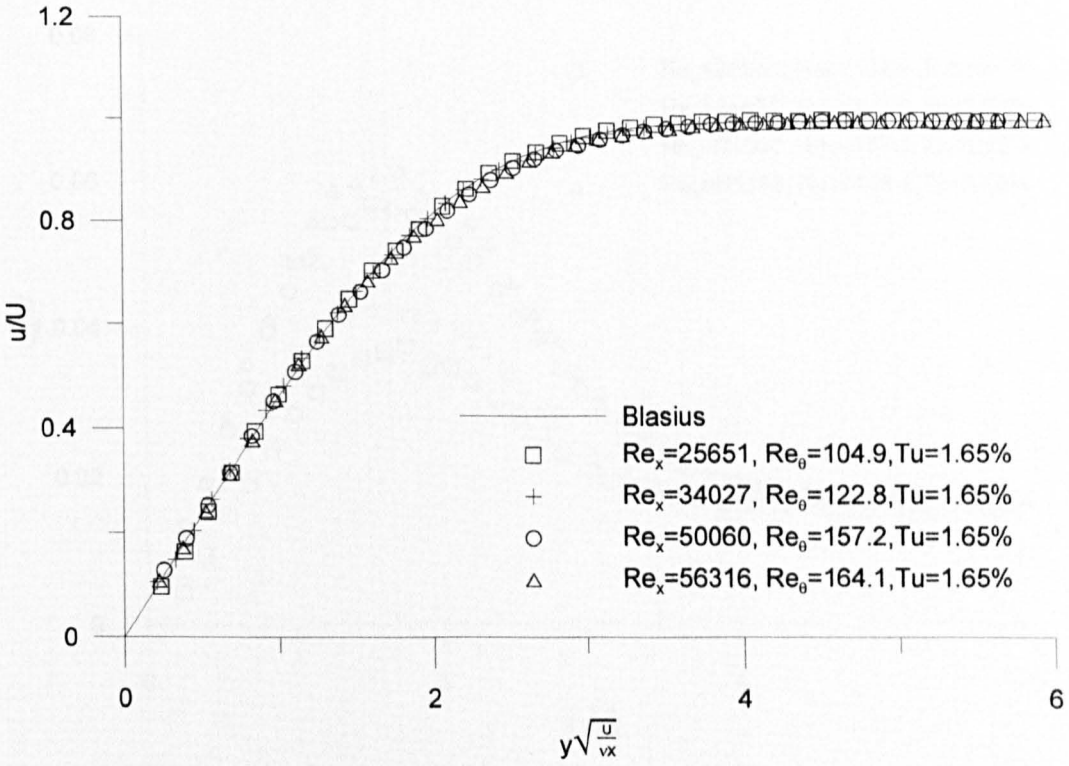

Figure 4.1 Laminar boundary layer velocity profiles for various Re_x varying U, constant x (Rigid surface)

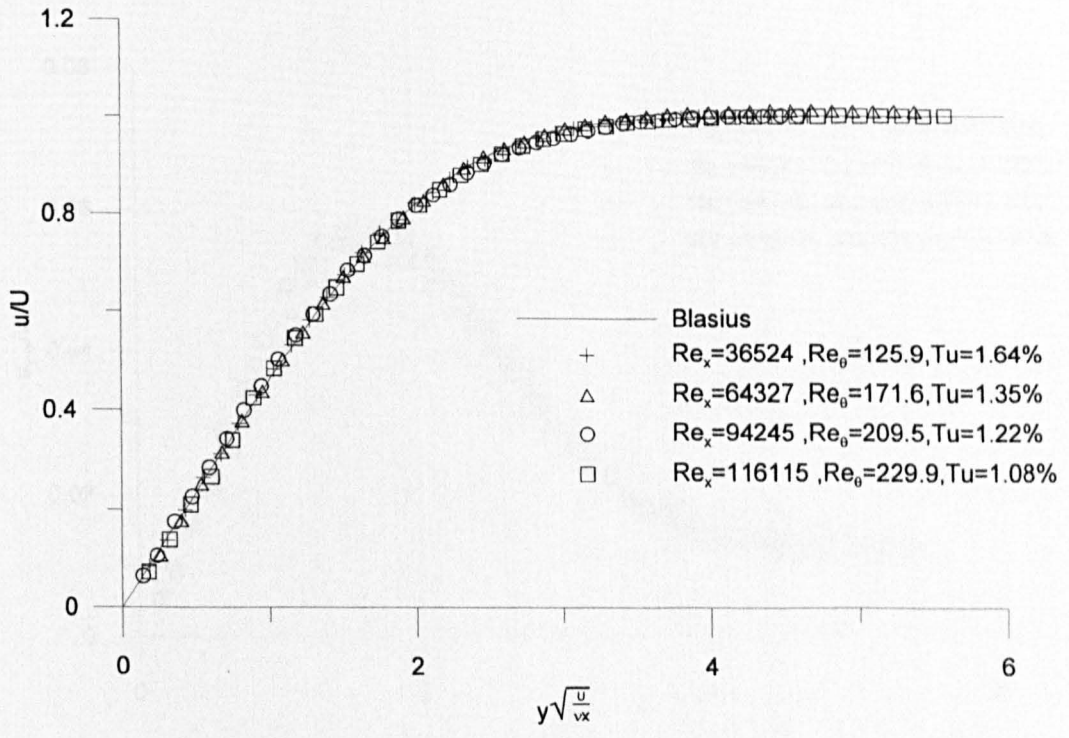

Figure 4.2 Laminar boundary layer velocity profiles for various Re_x varying x , constant U (Rigid surface)

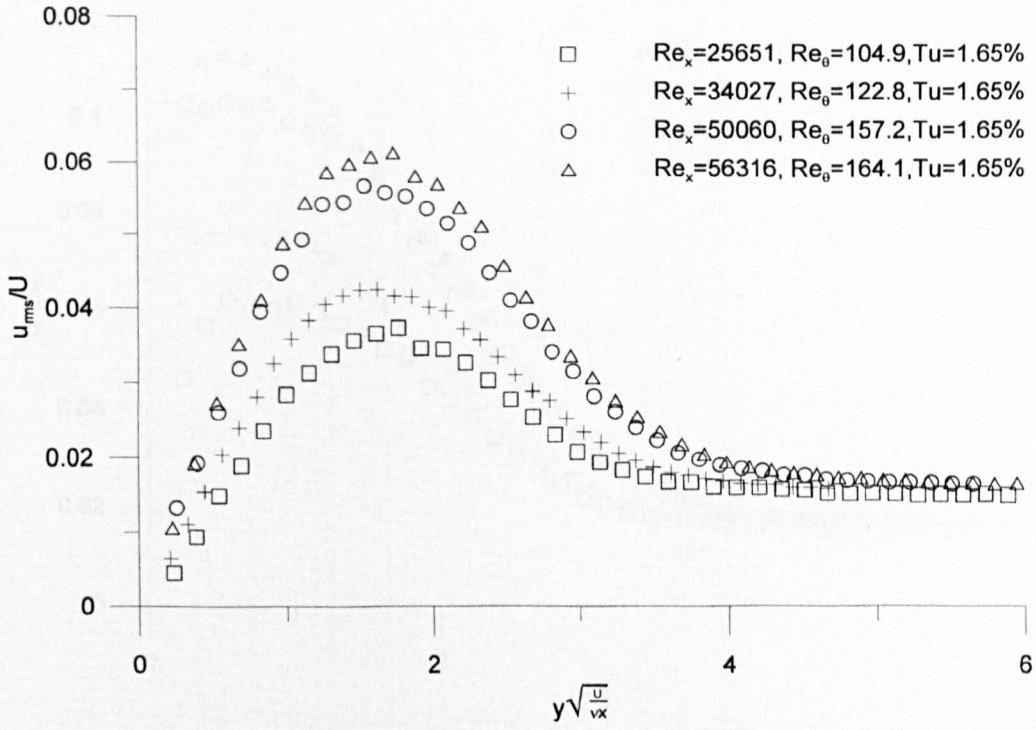

Figure 4.3 Laminar boundary layer velocity fluctuation profiles for various Re_x varying U, constant x (Rigid surface)

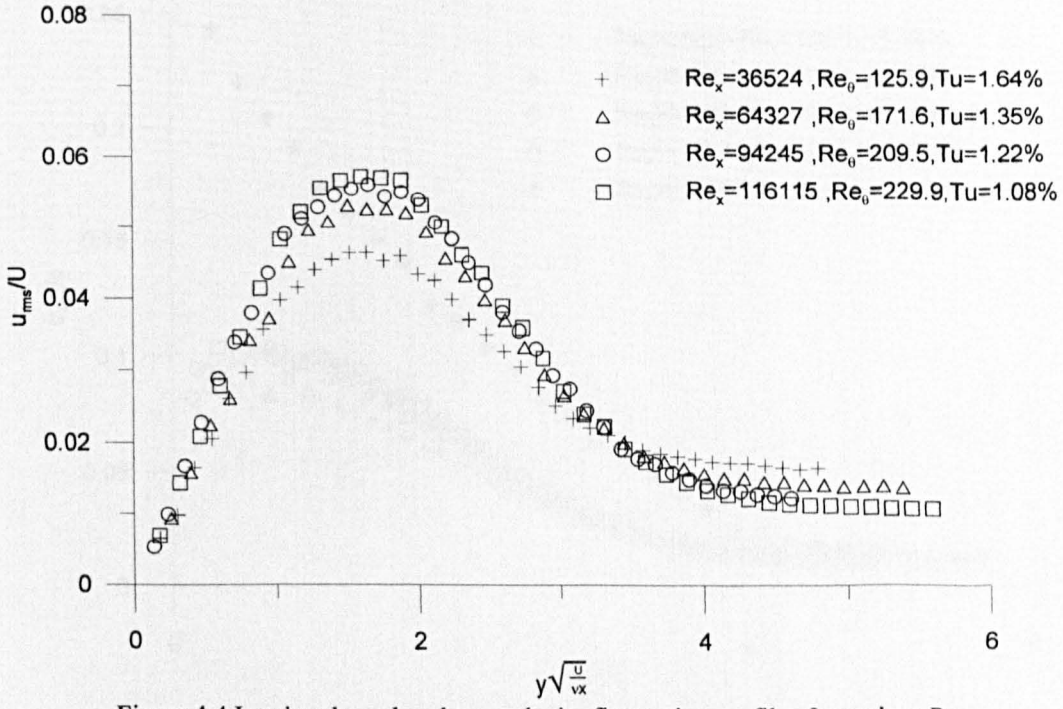

Figure 4.4 Laminar boundary layer velocity fluctuation profiles for various Re_x varying x, constant U (Rigid surface)

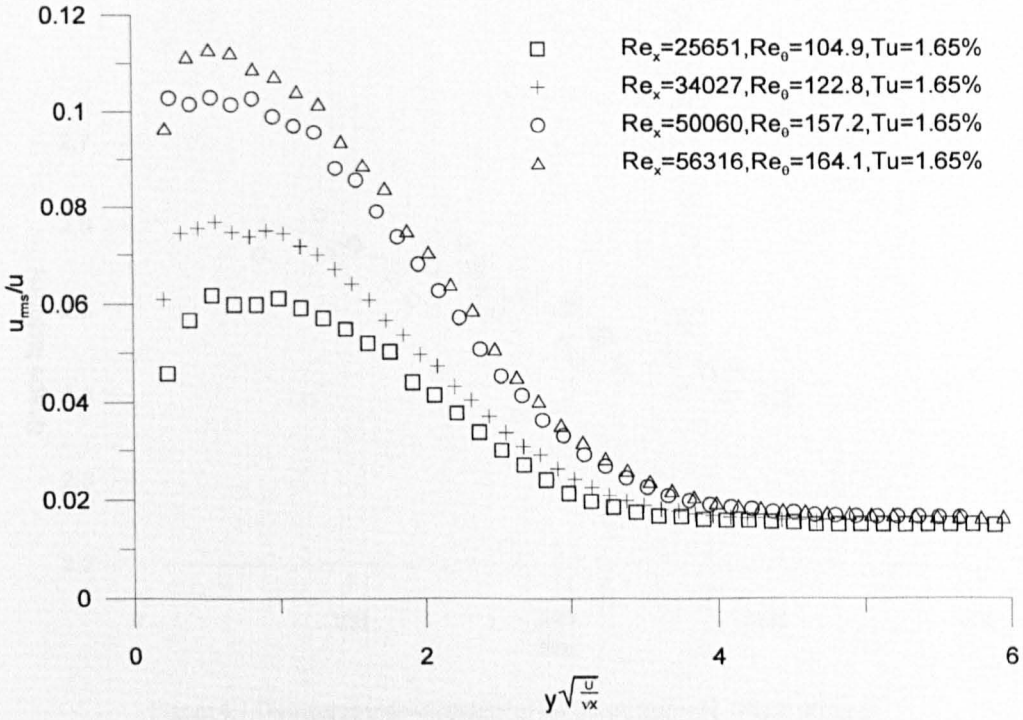

Figure 4.5 Laminar boundary layer local turbulence profiles for various Re_x varying U, constant x (Rigid surface)

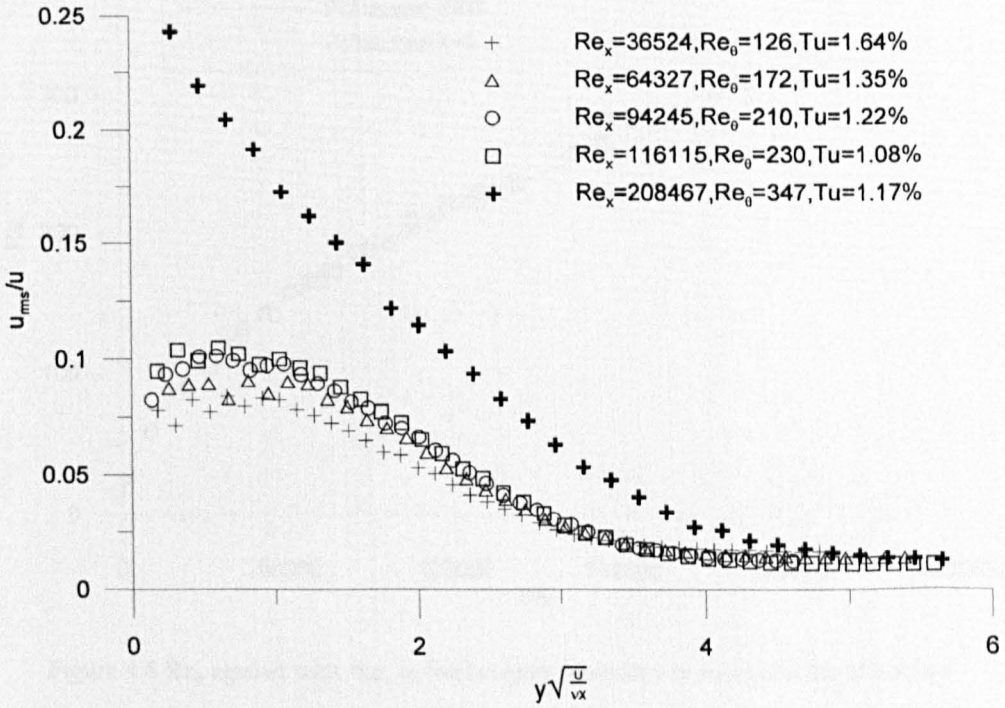

Figure 4.6 Laminar boundary layer local turbulence profiles for various Re_x varying x, constant U (Rigid surface)

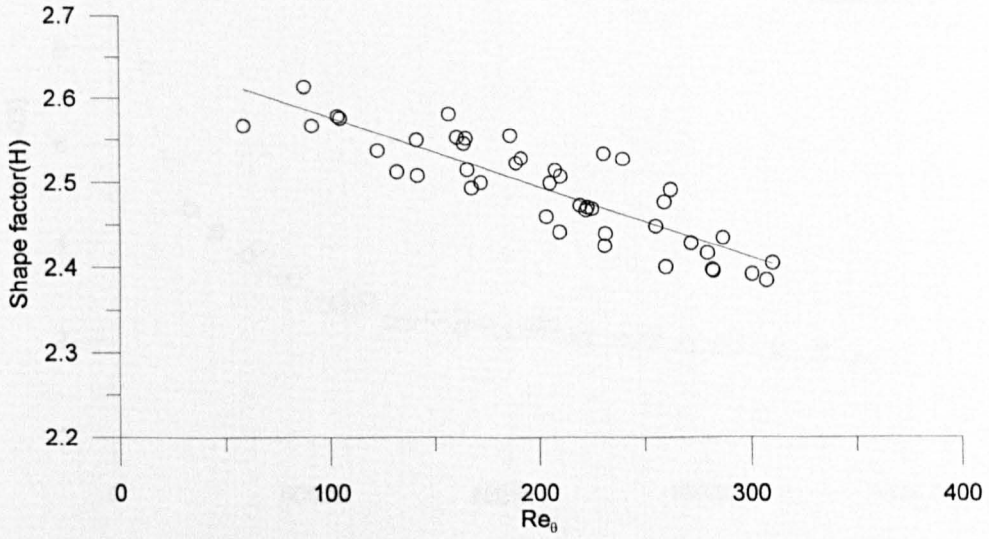

Figure 4.7 Downstream development of the shape factor H. (Rigid surface)

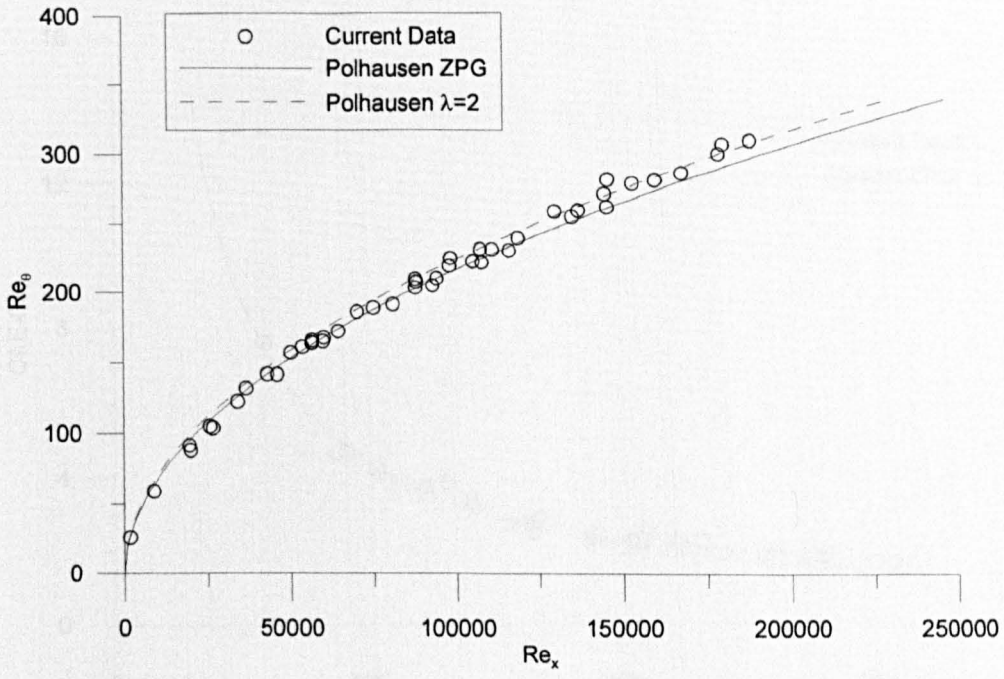

Figure 4.8 Re_θ against with Re_x in the Laminar boundary layer over a Rigid Surface

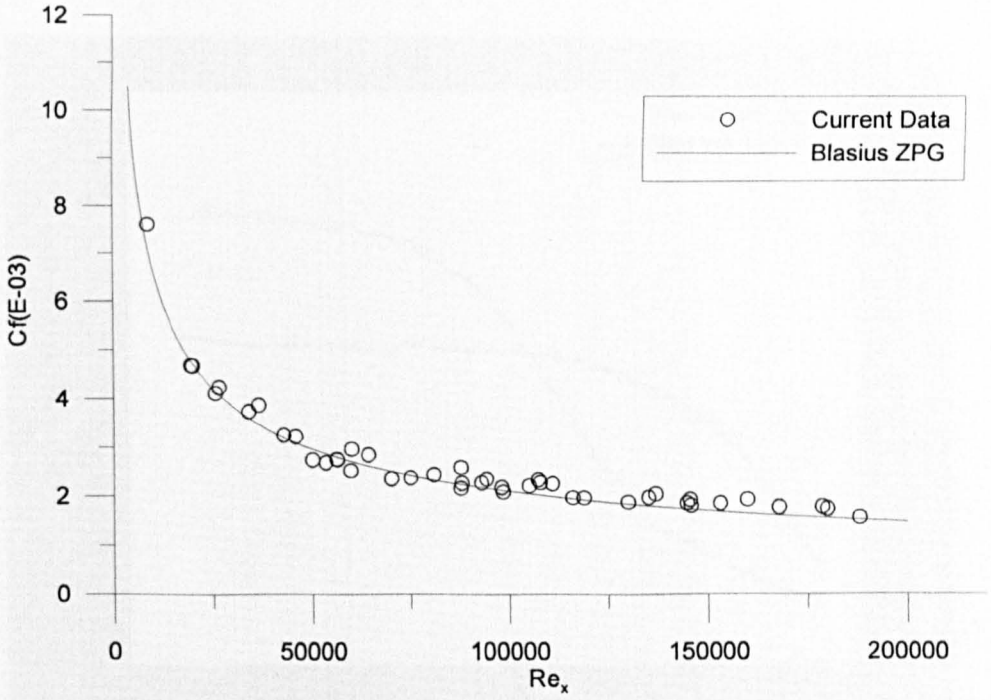

Figure4.9 Variation of local skin friction with length Reynolds number (Rigid surface)

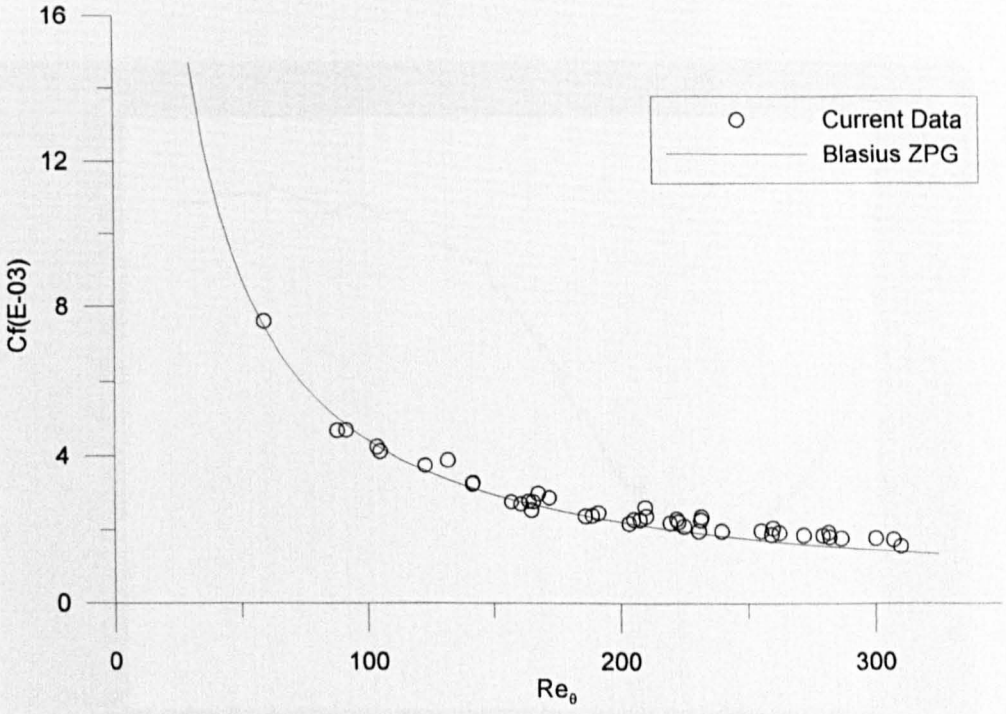

Figure4.10 Variation of local skin friction with momentum thickness Reynolds number (Rigid surface)

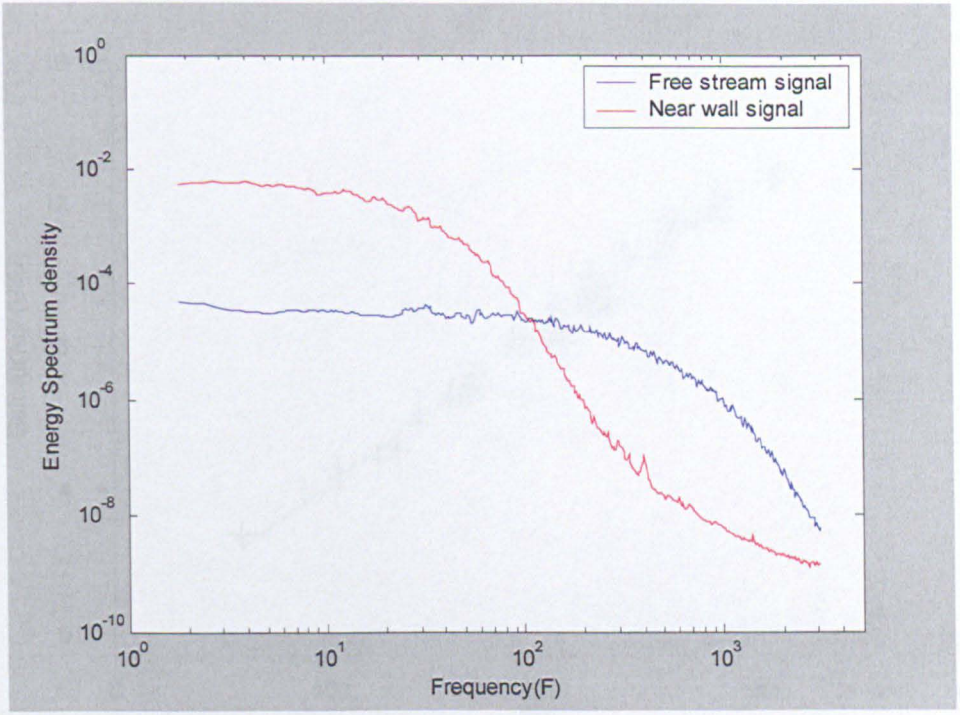

Figure4.11 Laminar flow energy spectral density in free stream and near wall region

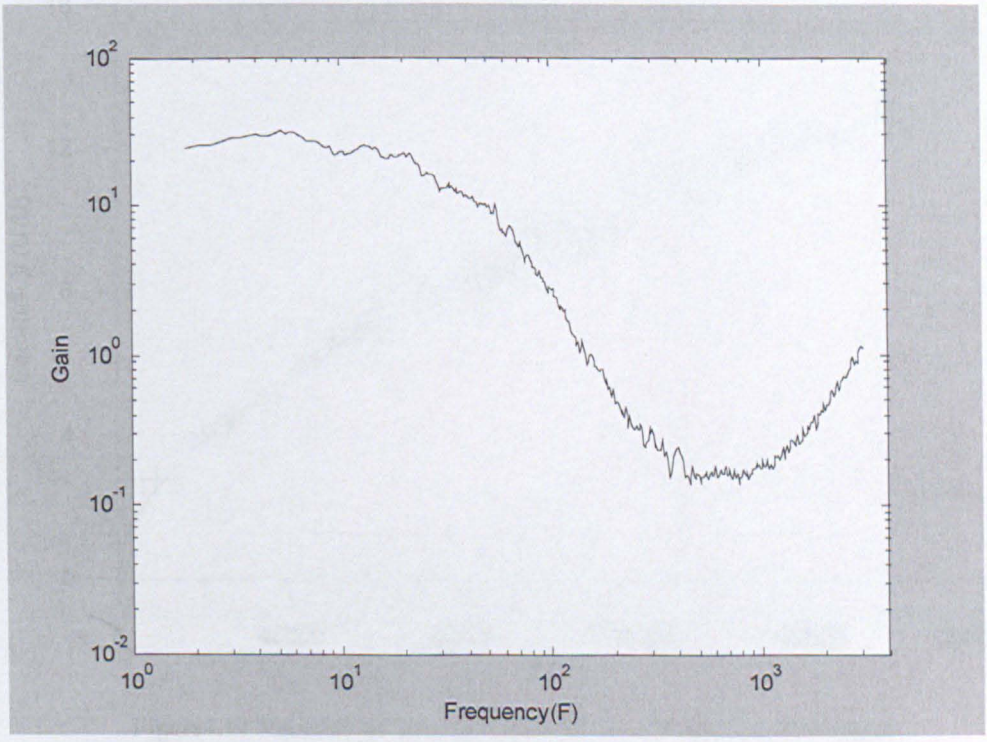

Figure4.12 Gain spectra in laminar flow (U=7.15m/s Tu=1.34 %,Re_{θ}=208)

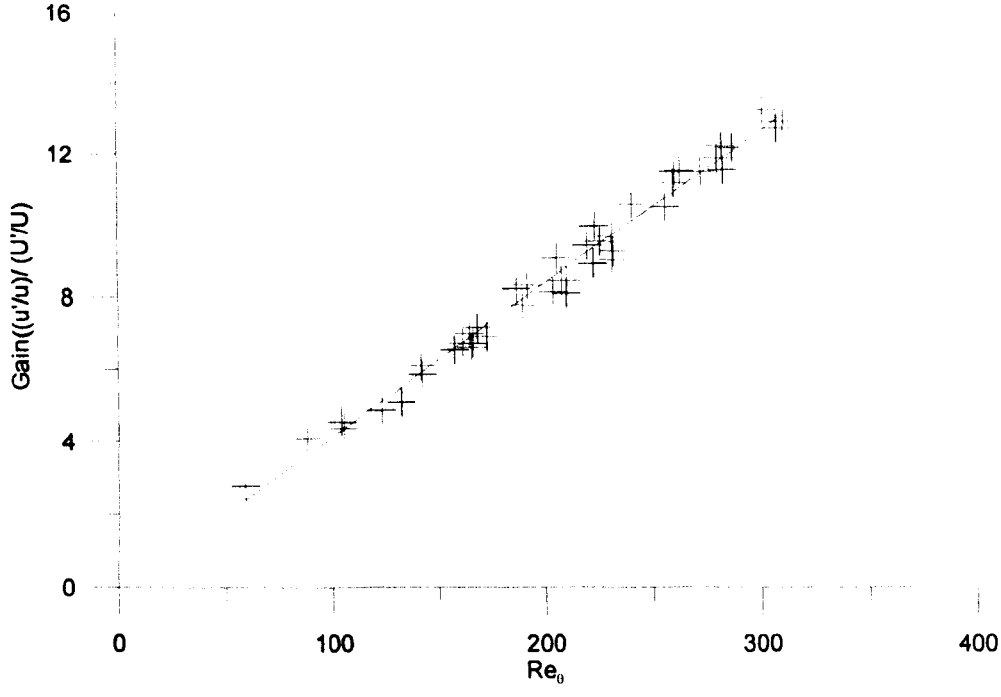

Figure4.13 Variation of near wall gain factor with Re_θ (Rigid Surface)

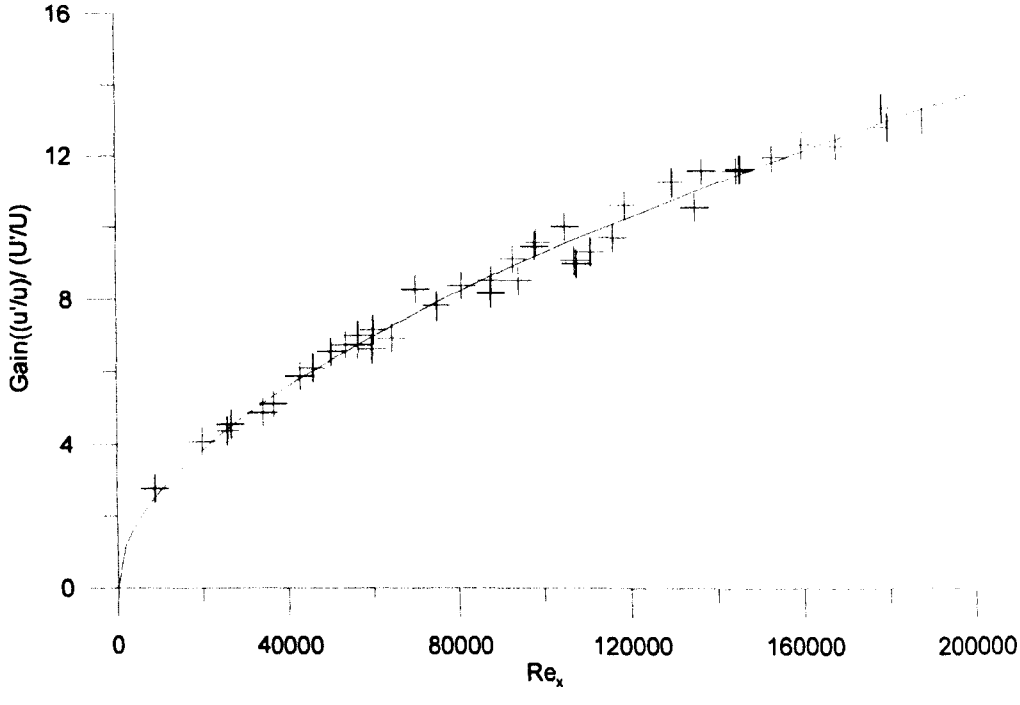

Figure4.14 Variation of near wall gain factor with Re_x (Rigid Surface)

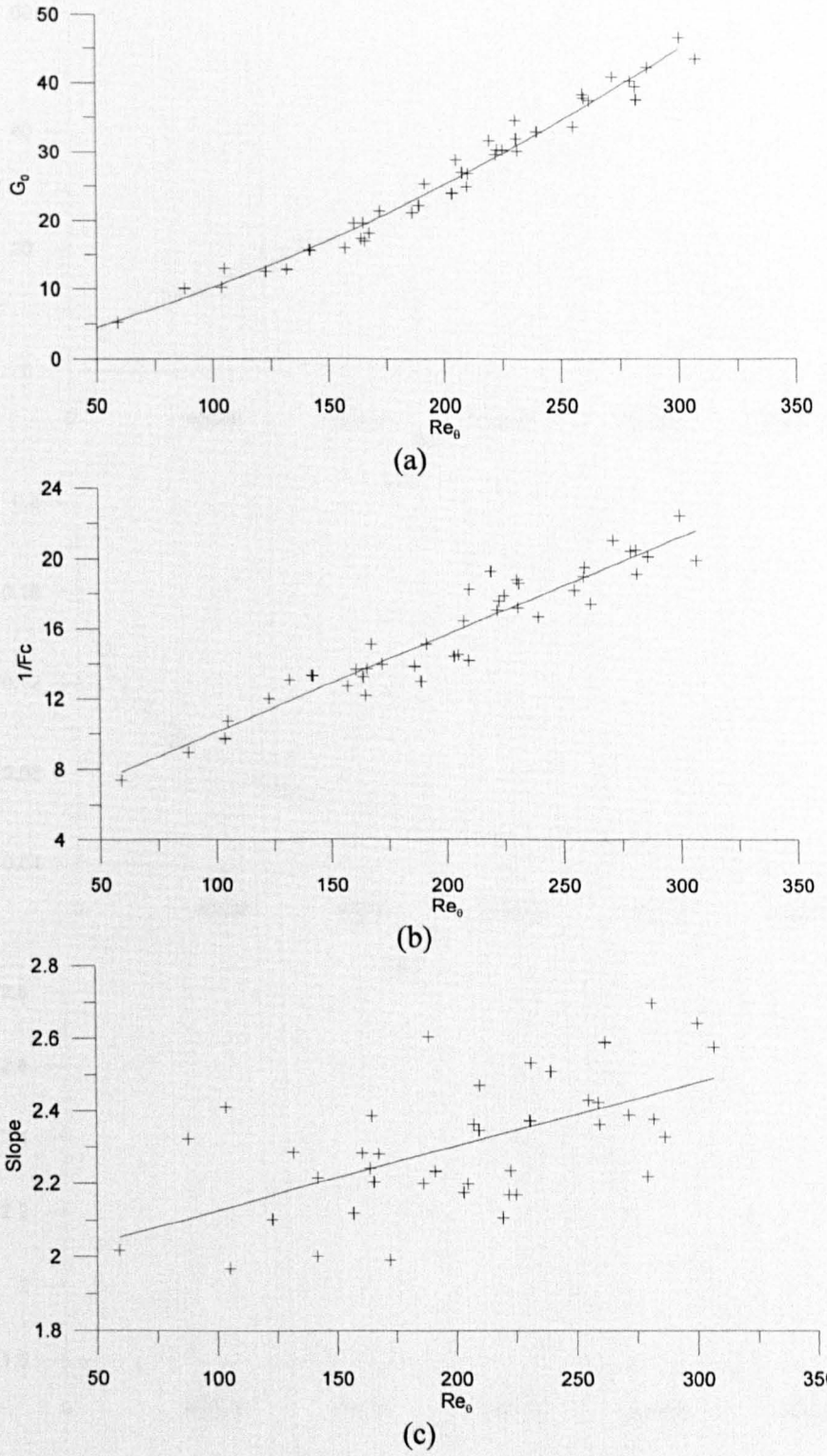

Figure 4.15 The empirical correlation in Re_θ with gain spectrum parameters (a) low frequency: G_0 (b) frequency at 1/2 G_0: F_c (c) gradient of slope: S

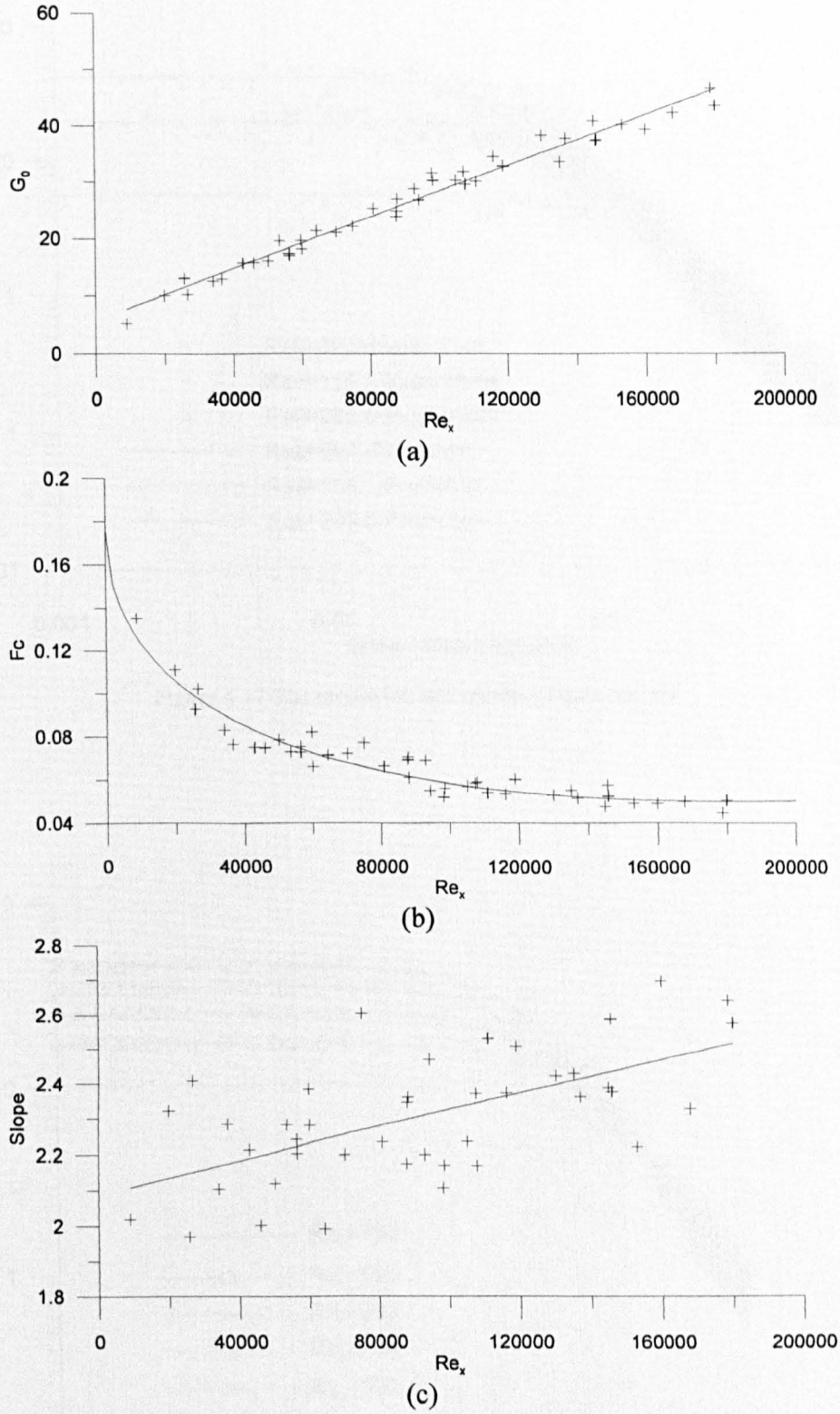

Figure 4.16 The empirical correlation in Re_x with gain spectrum (a) low frequency: G_0 (b) frequency at $1/2\,G_0$: F_c (c) gradient of slope: S

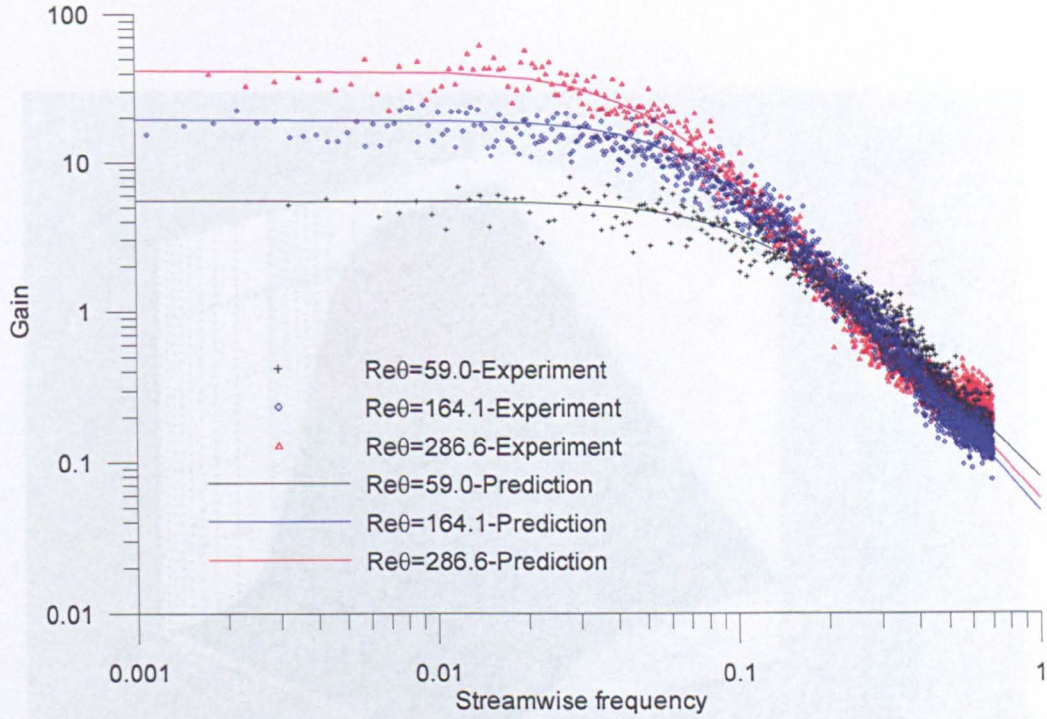

Figure 4.17 The prediction and measured gain spectra

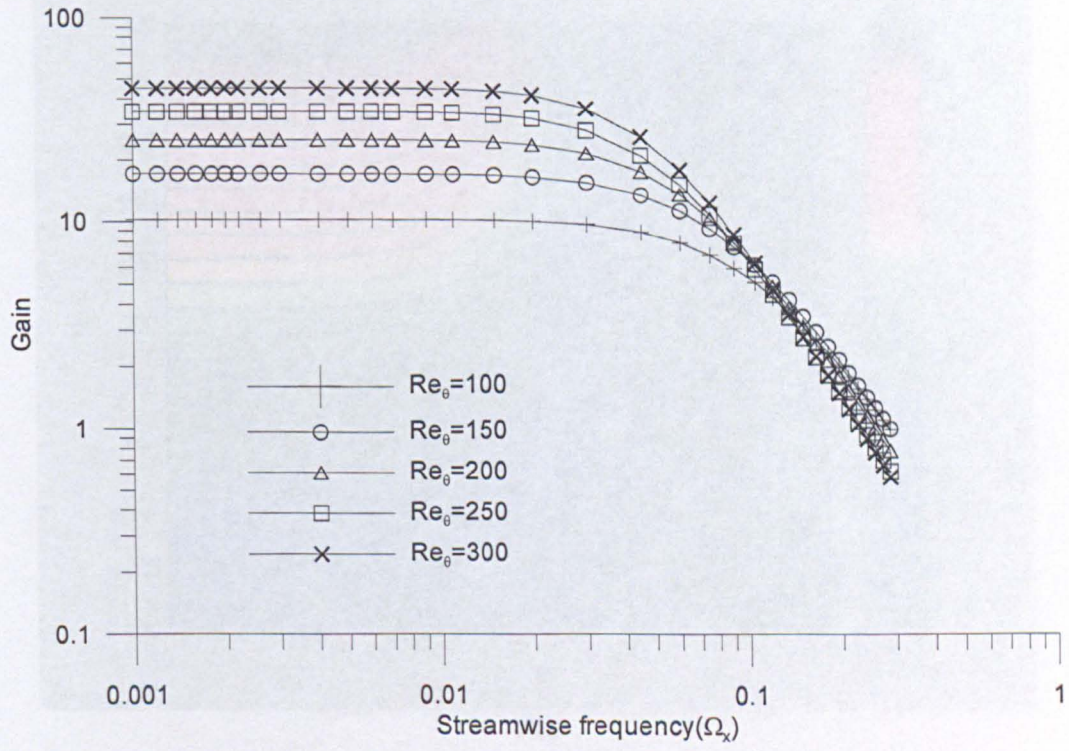

Figure 4.18 The empirical gain correlation with streamwise frequency

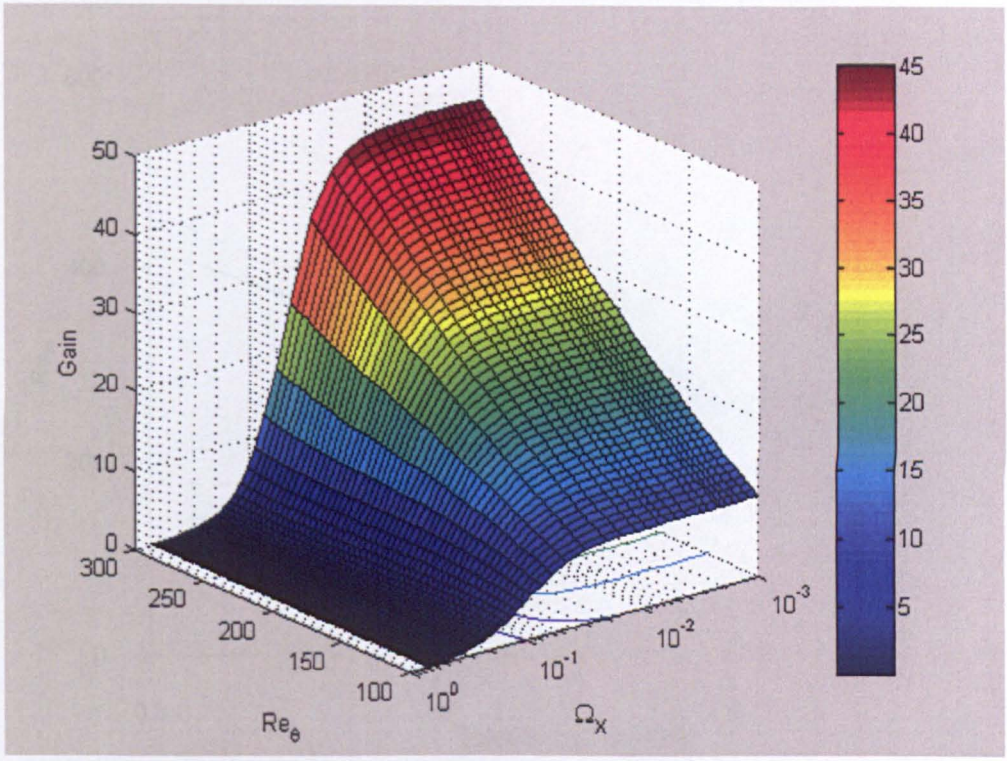

(a)

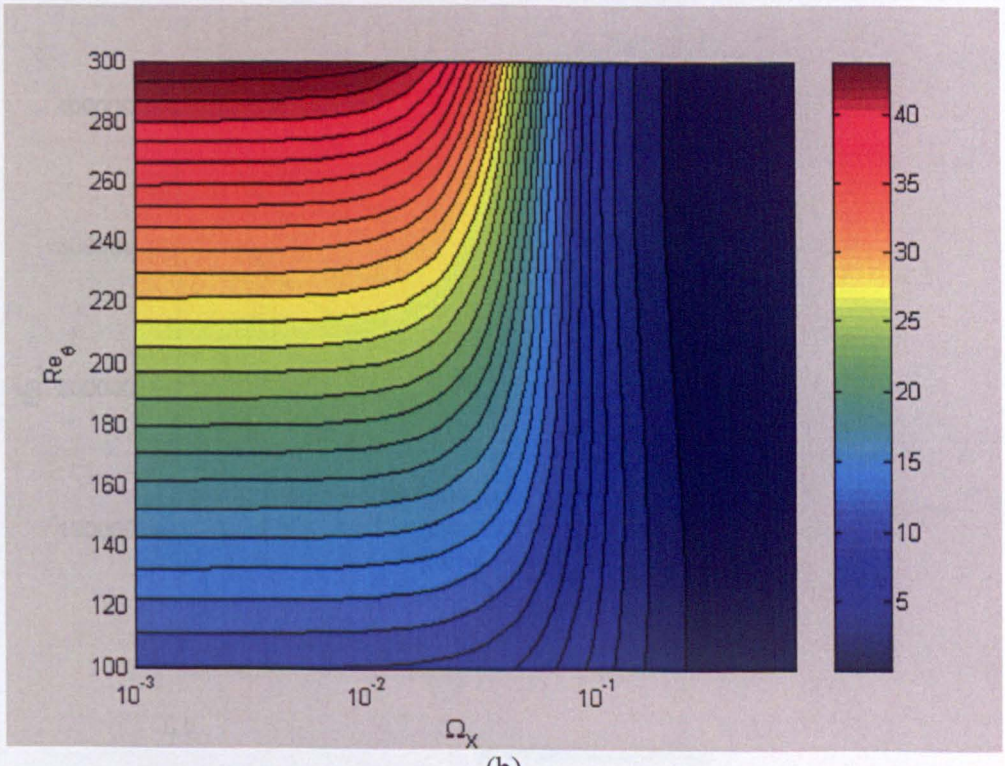

(b)

Figure 4.19 The empirical gain correlation with streamwise frequency and Re_θ
(a) surface plot (b) contour plot

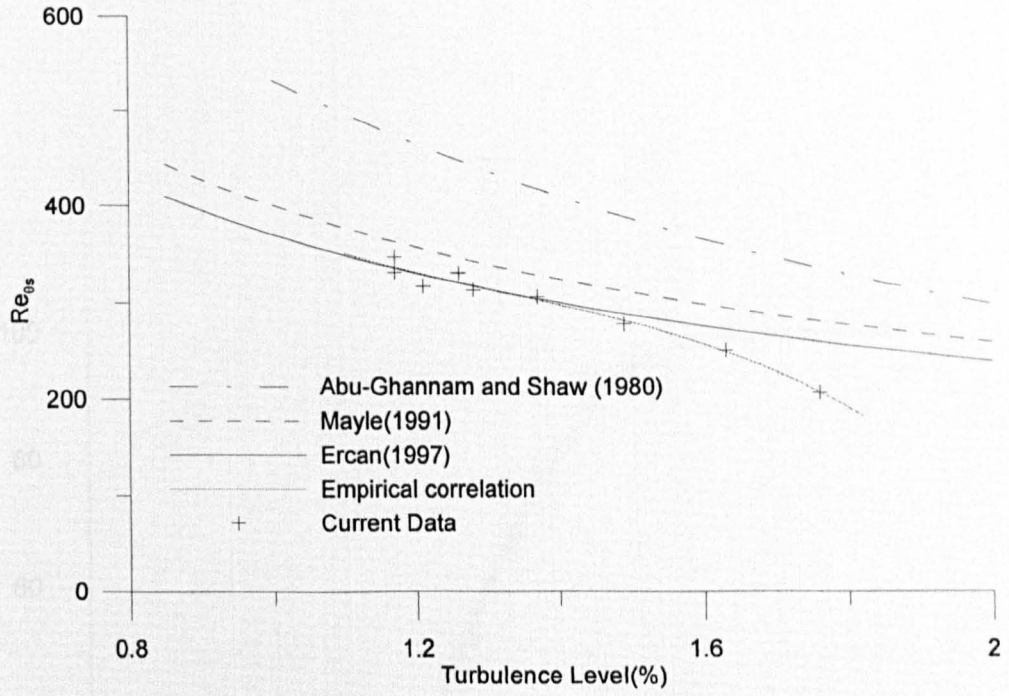

Figure 4.20 Effect of turbulence levels on Re_θ at start of transition (Rigid Surface)

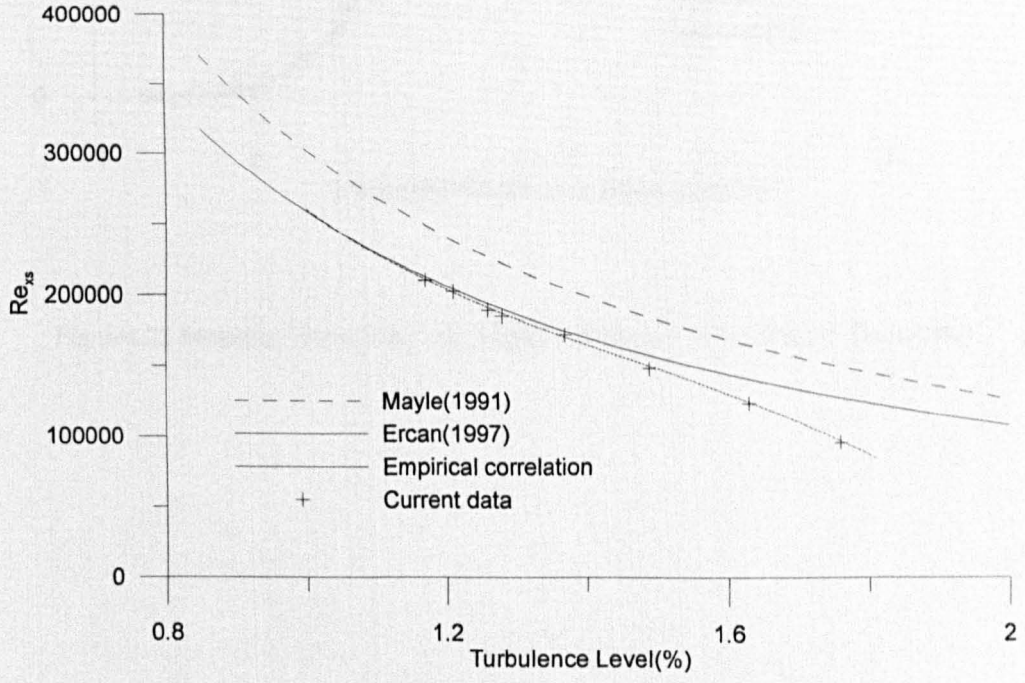

Figure 4.21 Effect of turbulence levels on Re_x at start of transition (Rigid Surface)

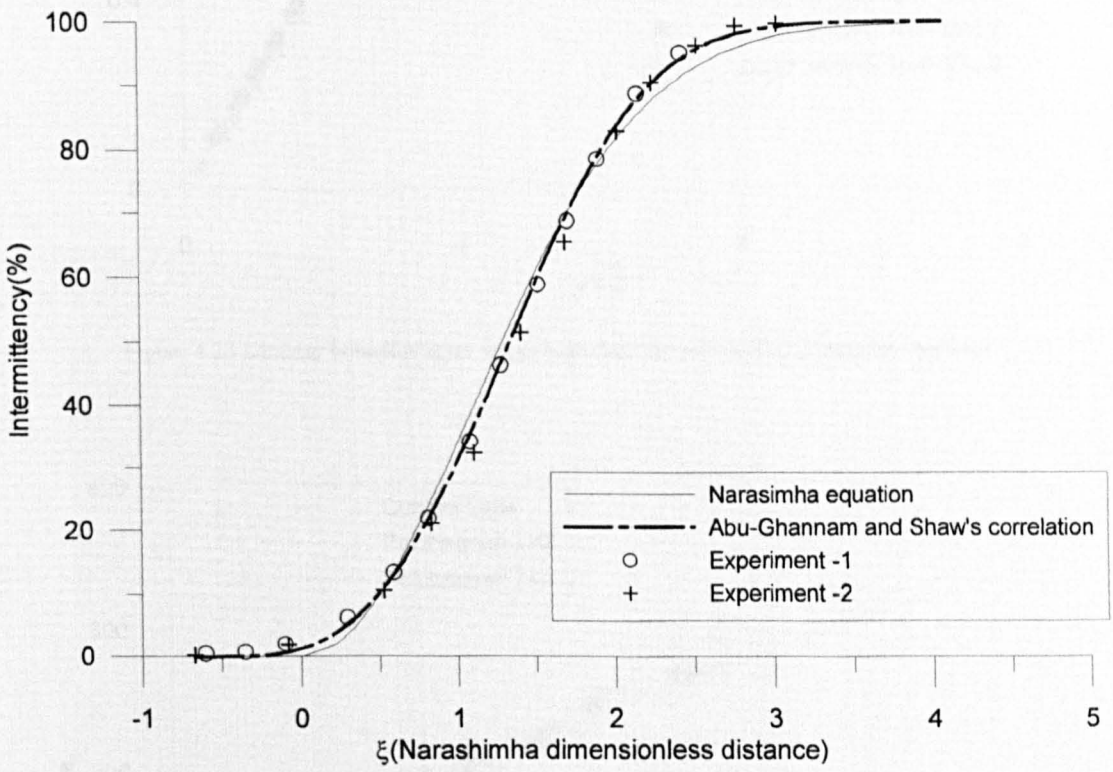

Figure4.22 Measured intermittency for Rigid Surface (o , Tu=1.22% , +, Tu=1.17%)

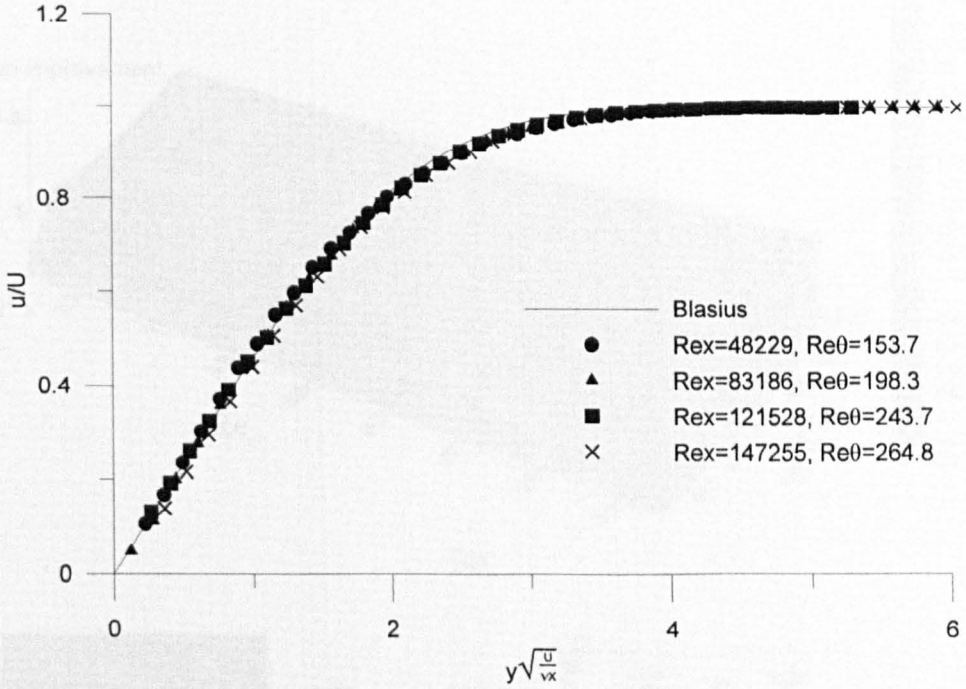

Figure 4.23 Laminar boundary layer velocity profiles for various Rex (compliant surface)

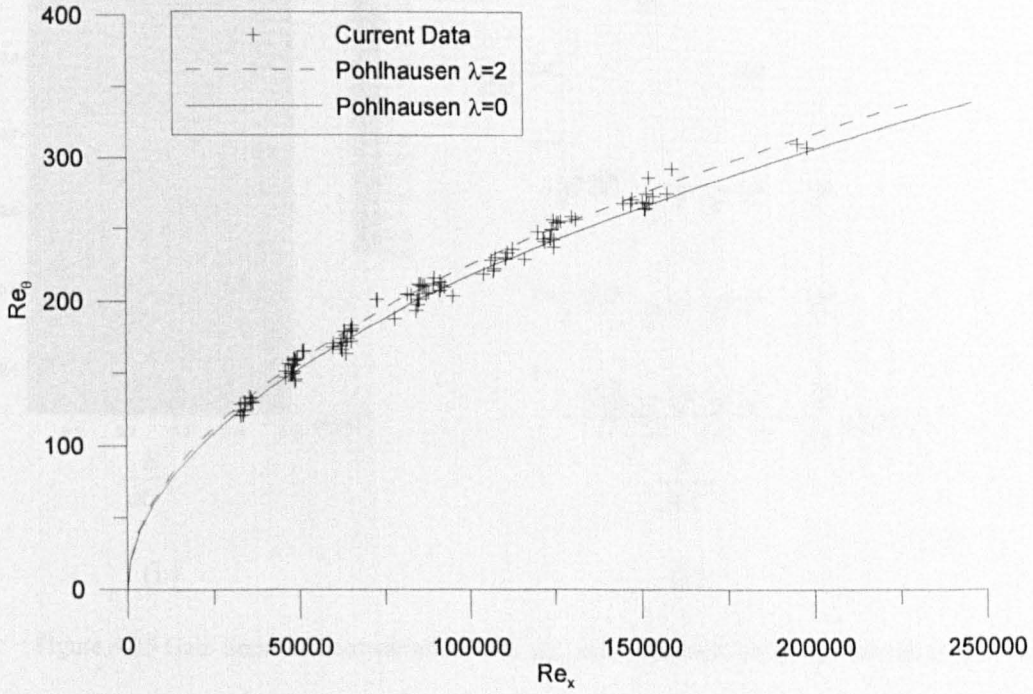

Figure 4.24 Re_θ versus Re_x in the laminar boundary layer over compliant surfaces

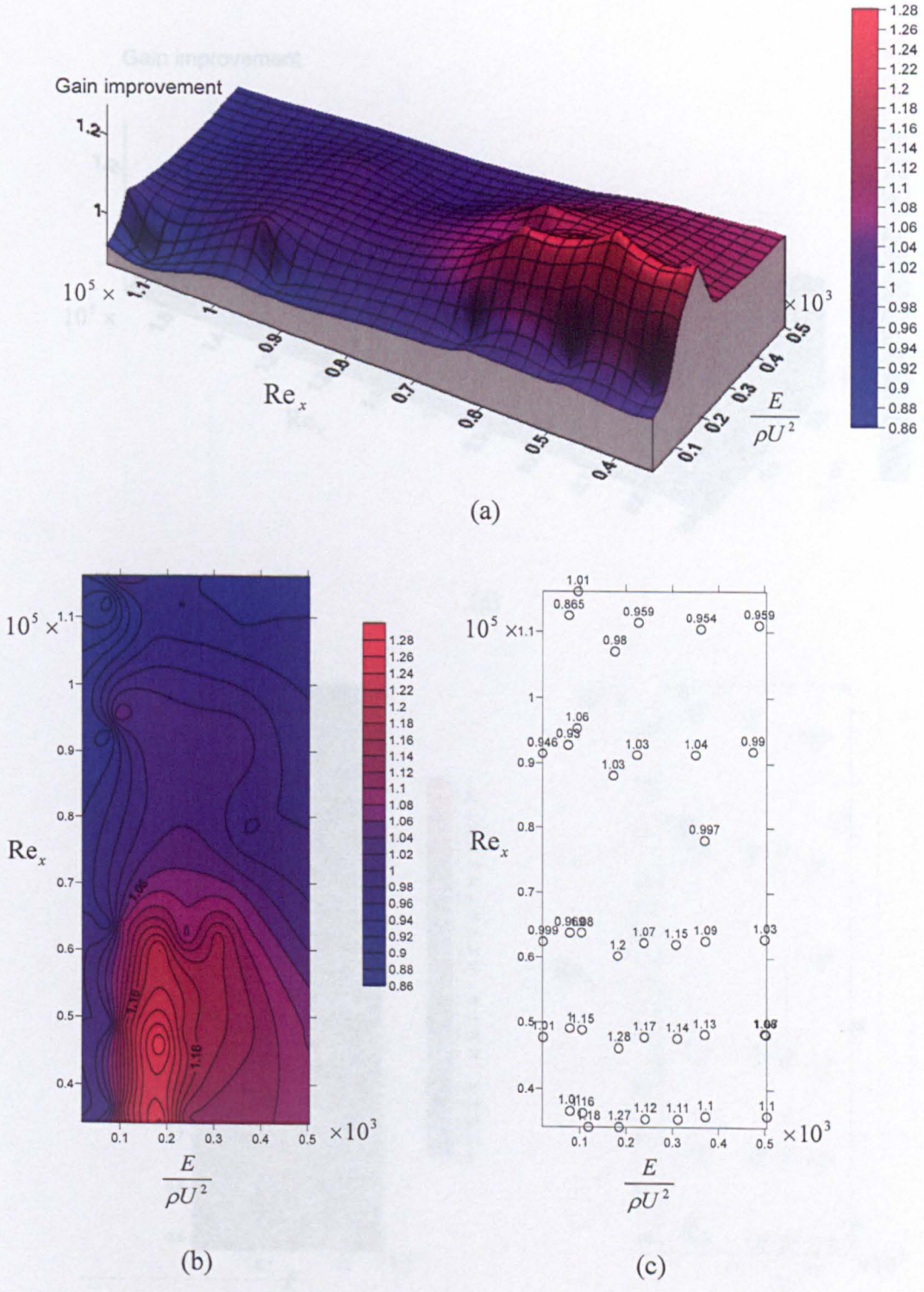

Figure 4.25 Gain improvement variation with Re_x and compliant surface properties $E/\rho U^2$ at $U \approx 4.5 m/s$ (a) mesh plot (b) contour plot (c) raw data

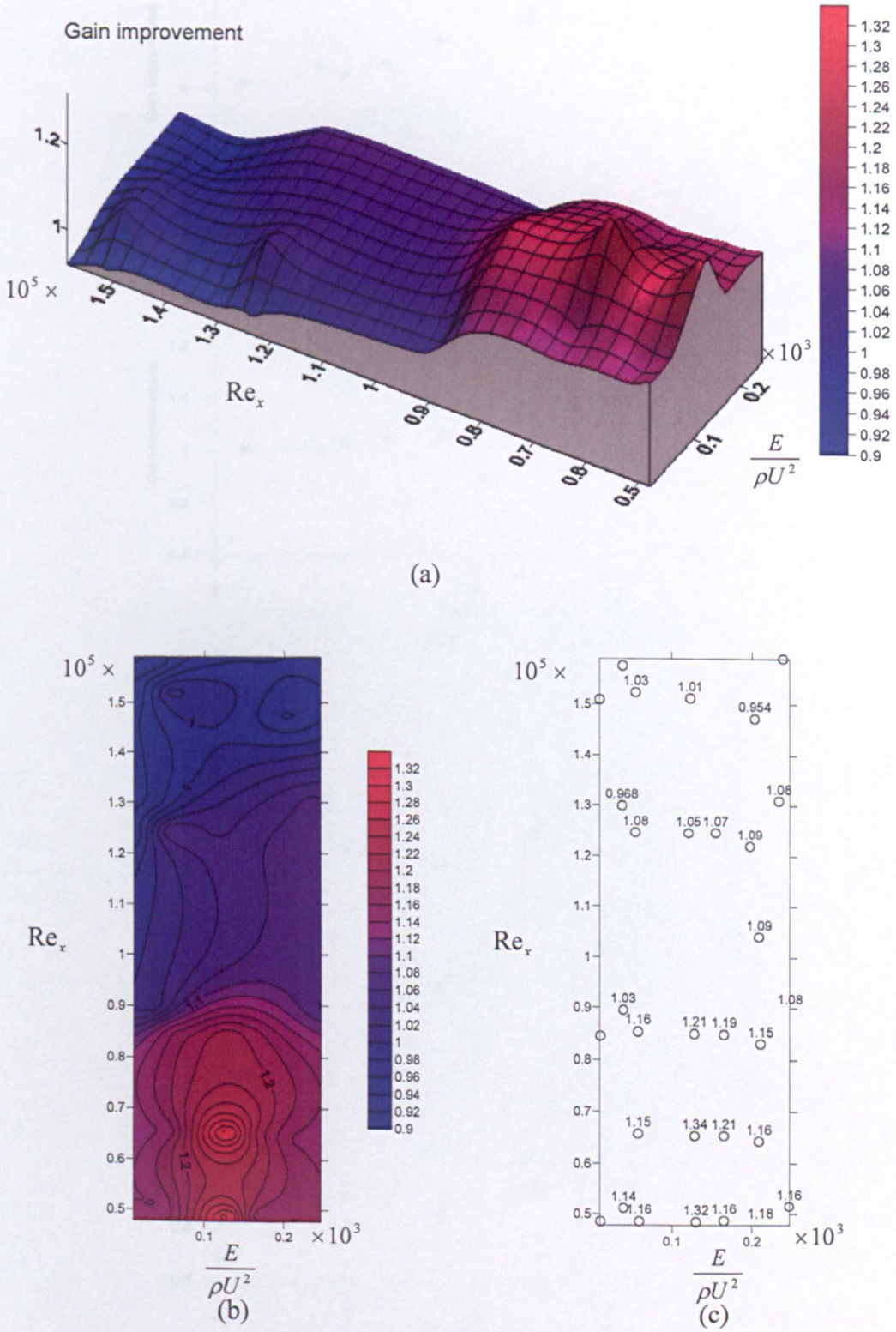

Figure 4.26 Gain improvement variation with Re_x and compliant surface properties $E/\rho U^2$ at $U \approx 6.5 m/s$ (a) Mesh plot (b) Contour plot (c) Raw data distribution

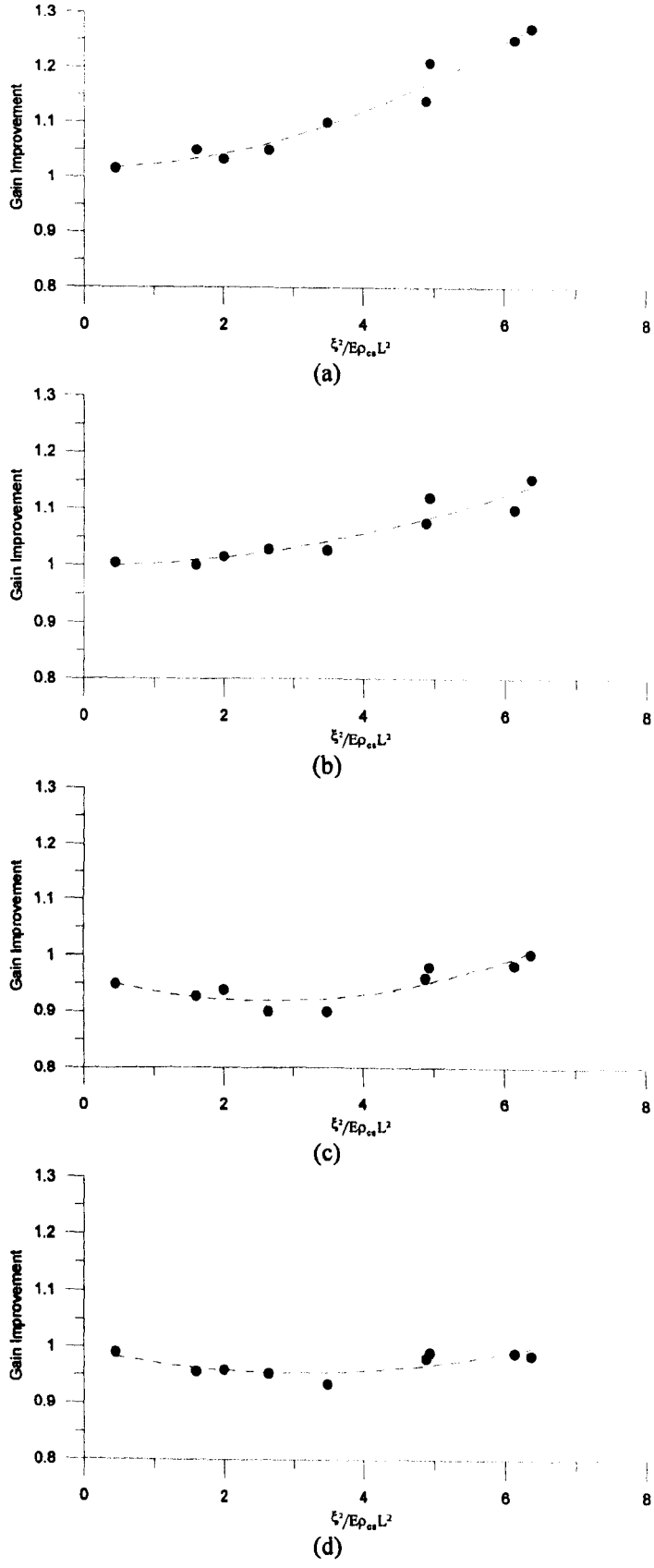

Figure 4.27 Correlations of $\frac{\xi^2}{E\rho_{cs}L^2}$ and gain improvement
(a)x=112mm (b)x=195mm (c)x=277mm(d)x=340mm

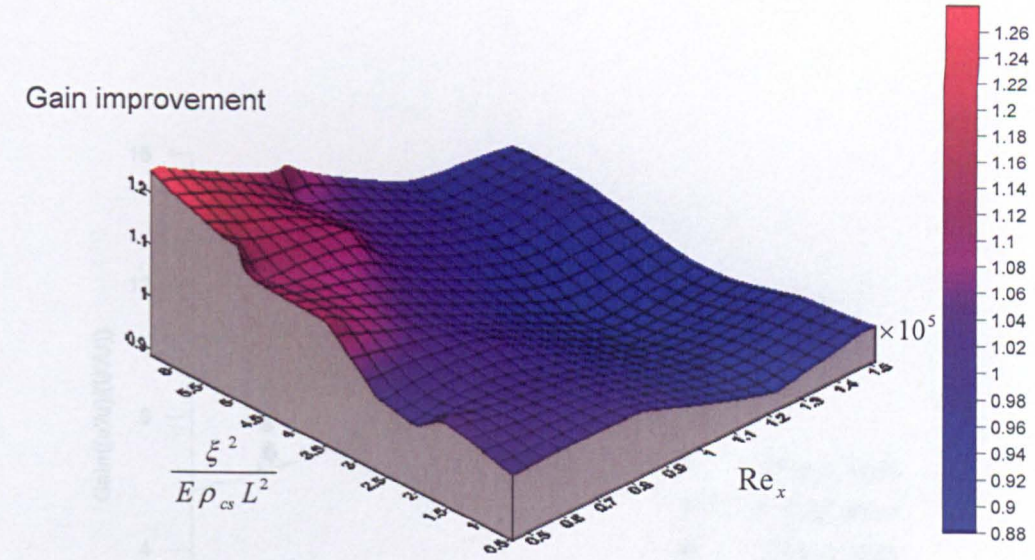

(a)

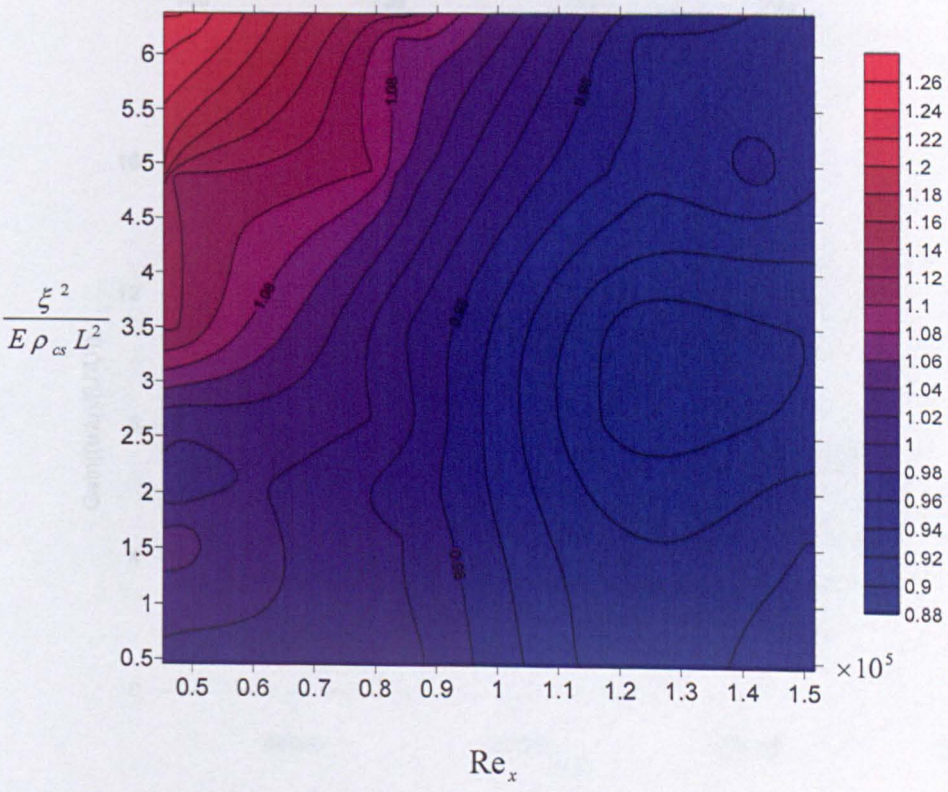

(b)

Figure 4.28 Correlation of gain amplification and compliant surface properties $\frac{\xi^2}{E\rho_{cs}L^2}$ at $U \approx 6.5m/s$ (a) Mesh plot (b) Contour plot

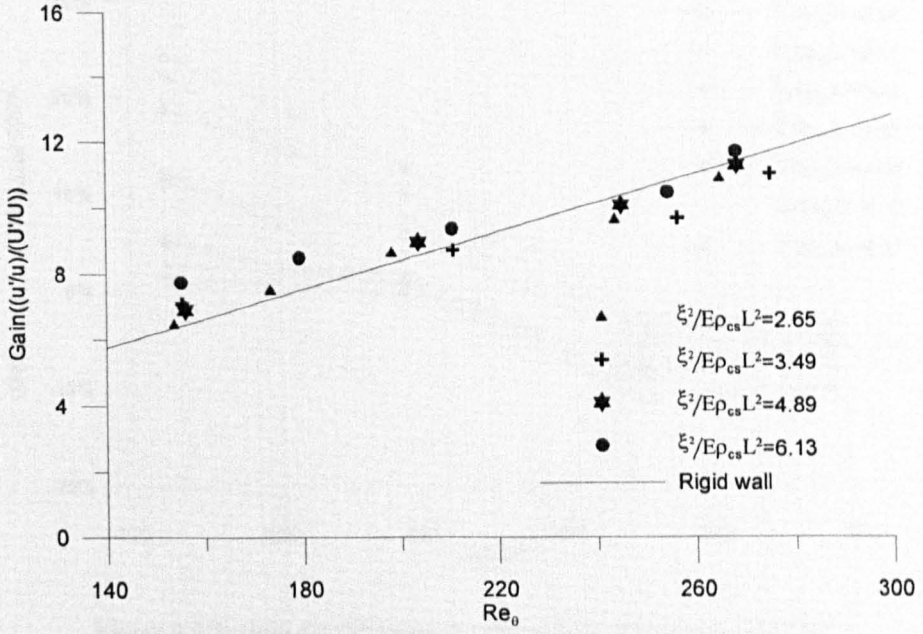

(a)

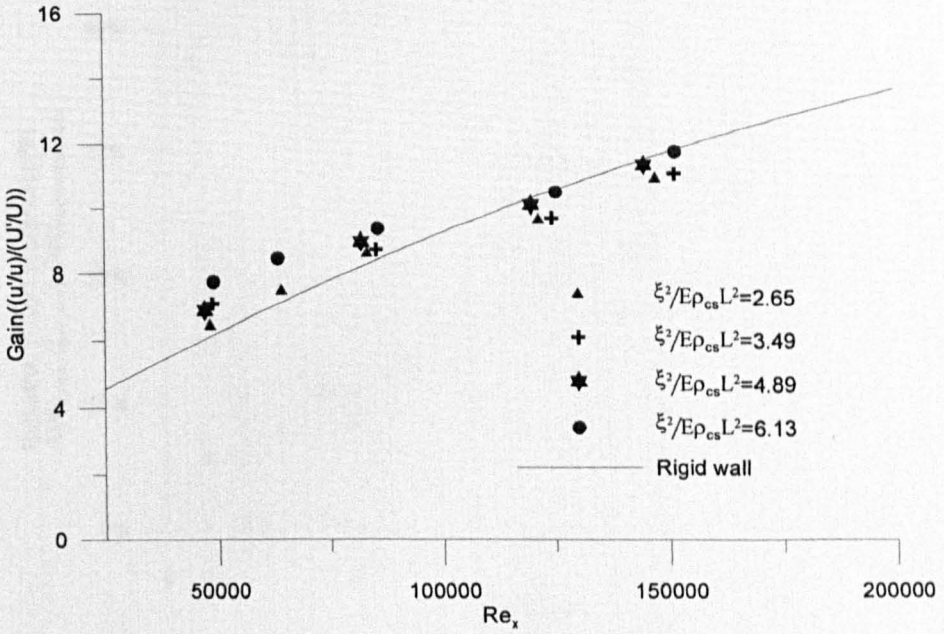

(b)

Figure 4.29 Near wall boundary layer receptivity over compliant surfaces
(a) overall gain vs Re_θ (b) overall gain vs Re_x

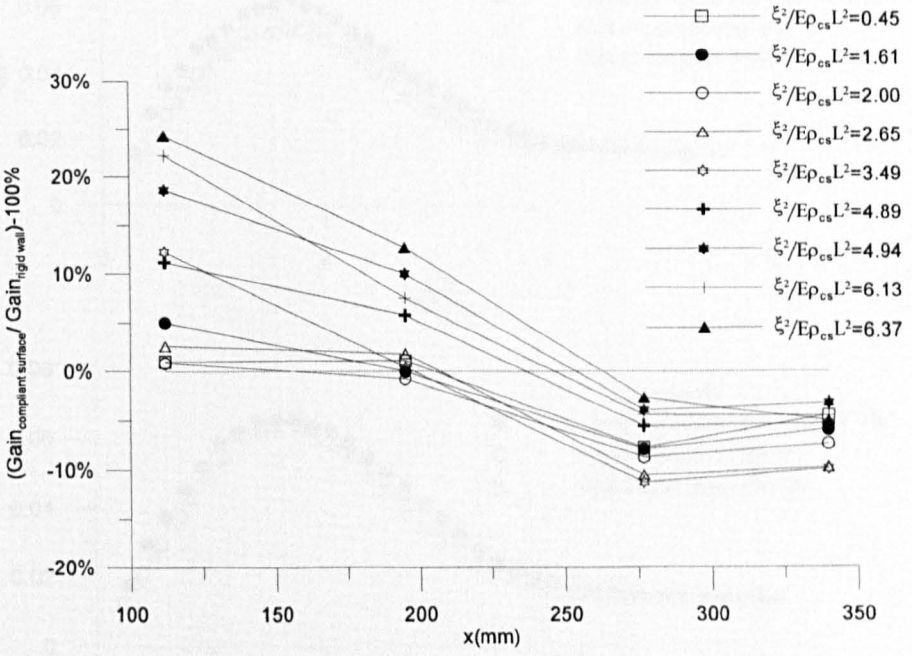

Figure 4.30a Gain amplification evolution with streamwise direction

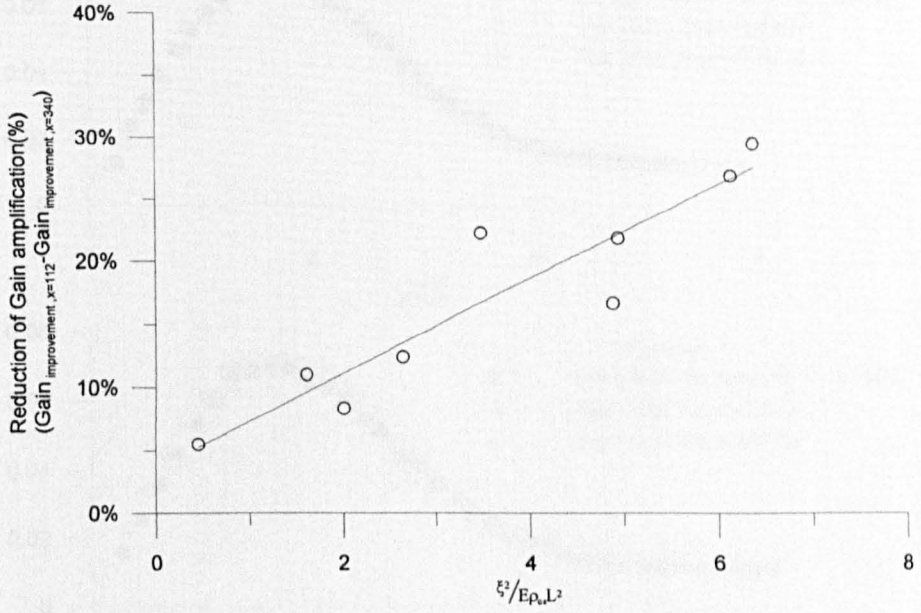

Figure 4.30b Reduction of gain amplification due to different material properties

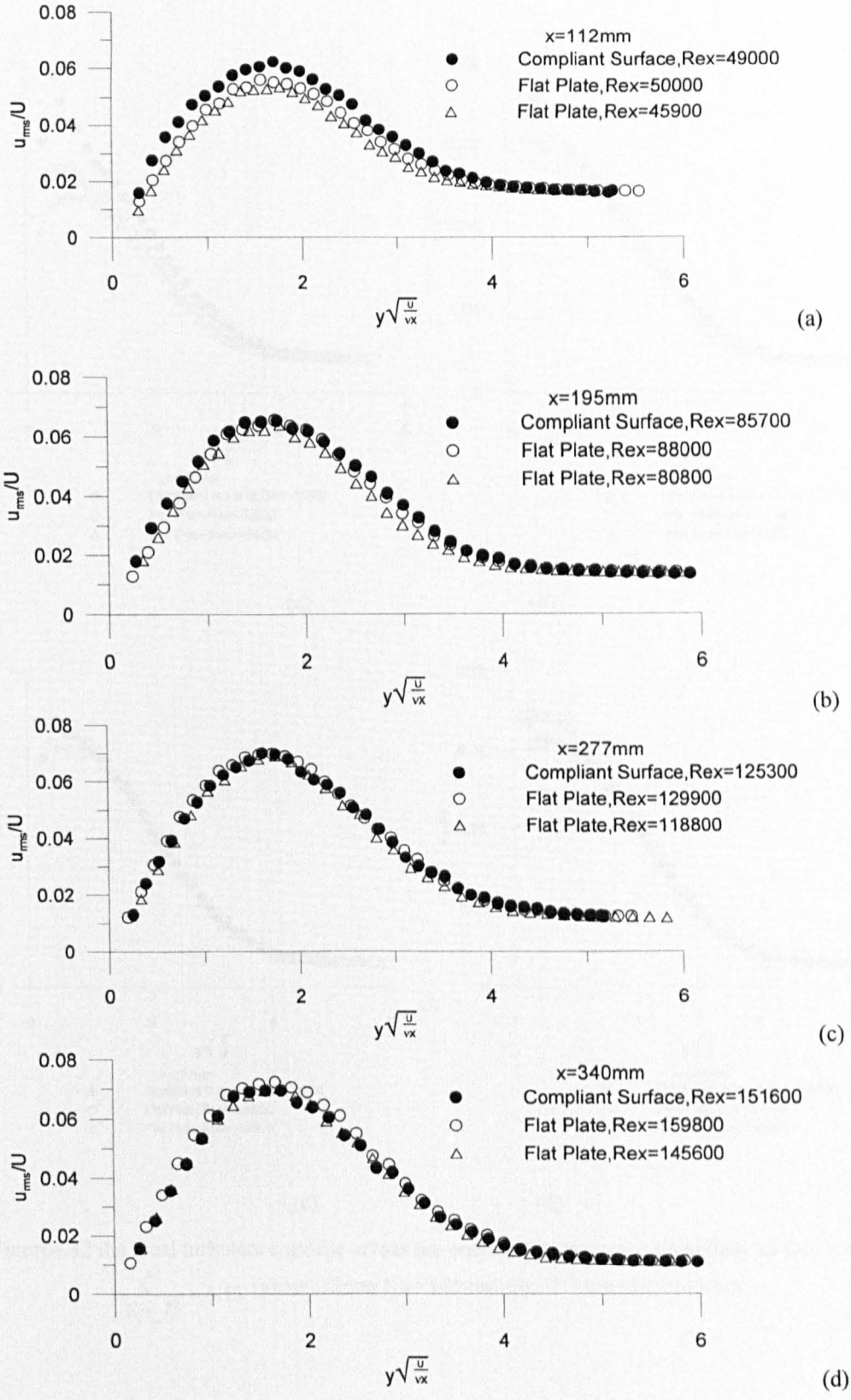

Figure4.31 The boundary layer fluctuations over a compliant surface with $\frac{\xi^2}{E\rho_{cs}L^2} = 6.13$

(a) x=112mm (b)x=195mm(c)x=277mm(d)x=340mm

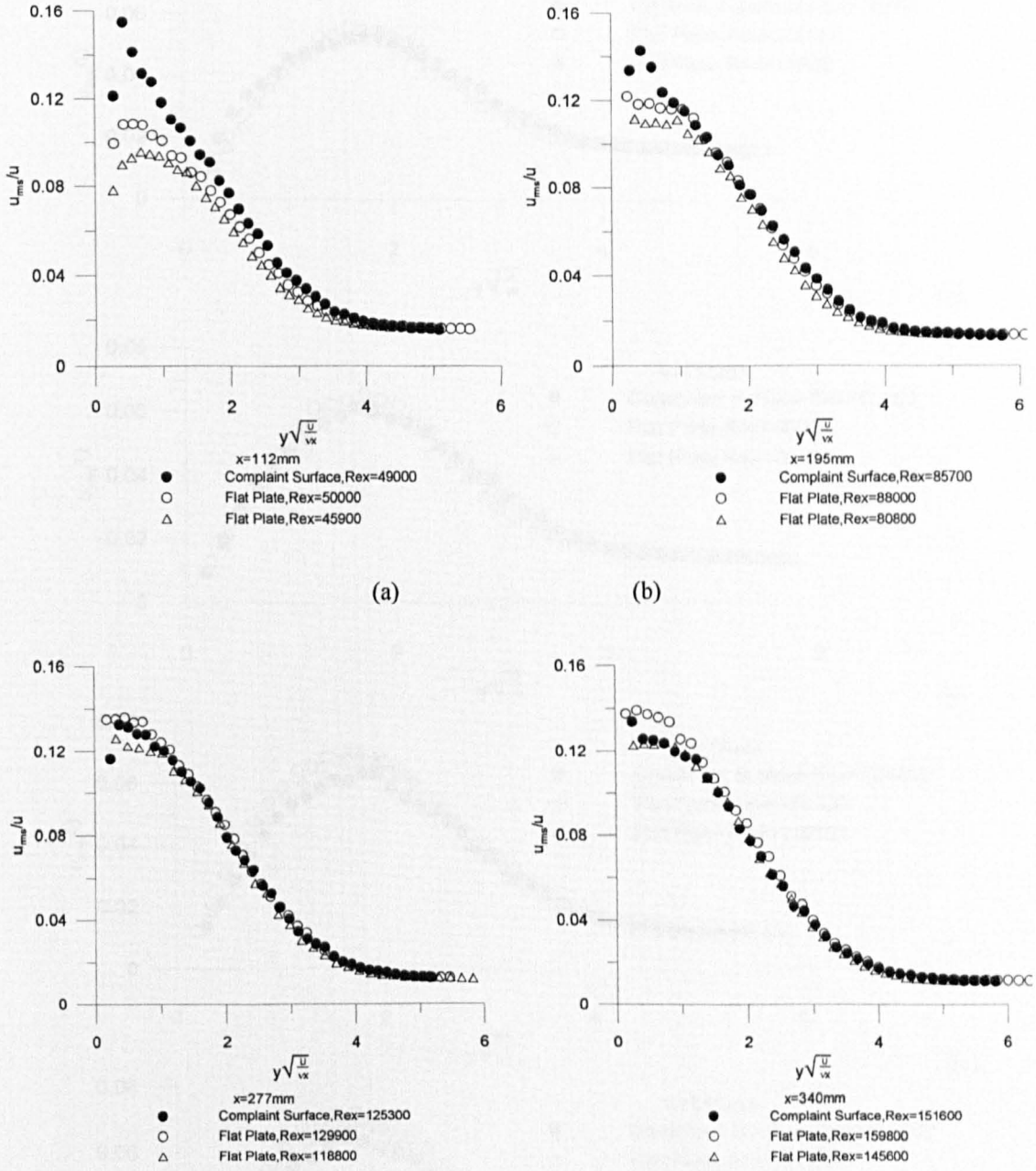

Figure4.32 the local turbulence profile across the boundary layer over a compliant surface with $\frac{\xi^2}{E\rho_{cs}L^2} = 6.13$ (a) x=112mm(b)x=195mm(c)x=277mm(d)x=340mm

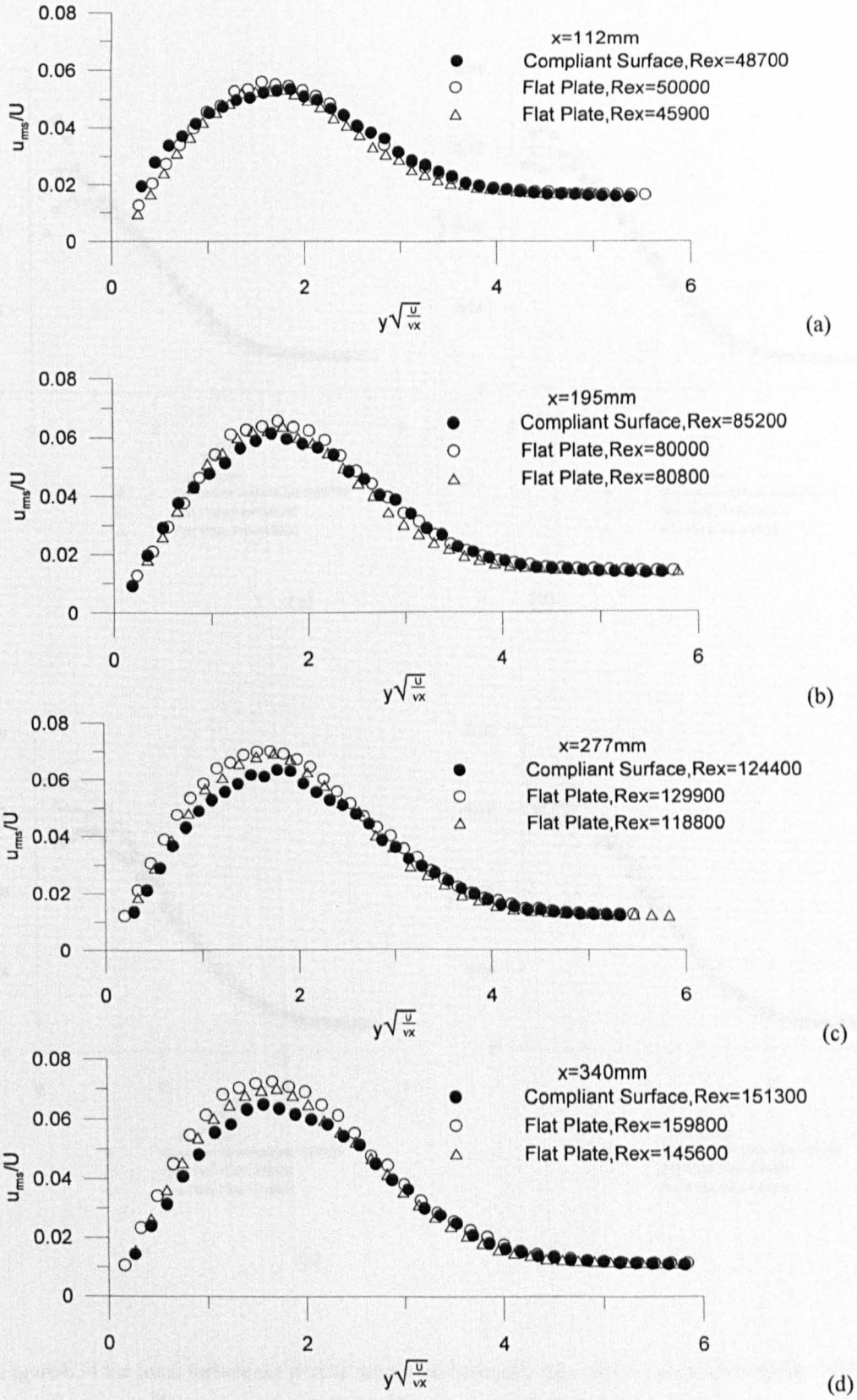

Figure4.33 The boundary layer fluctuations over a compliant surface $\frac{\xi^2}{E\rho_{cs}L^2} = 3.49$

(a) x=112mm (b)x=195mm(c)x=277mm(d)x=340mm

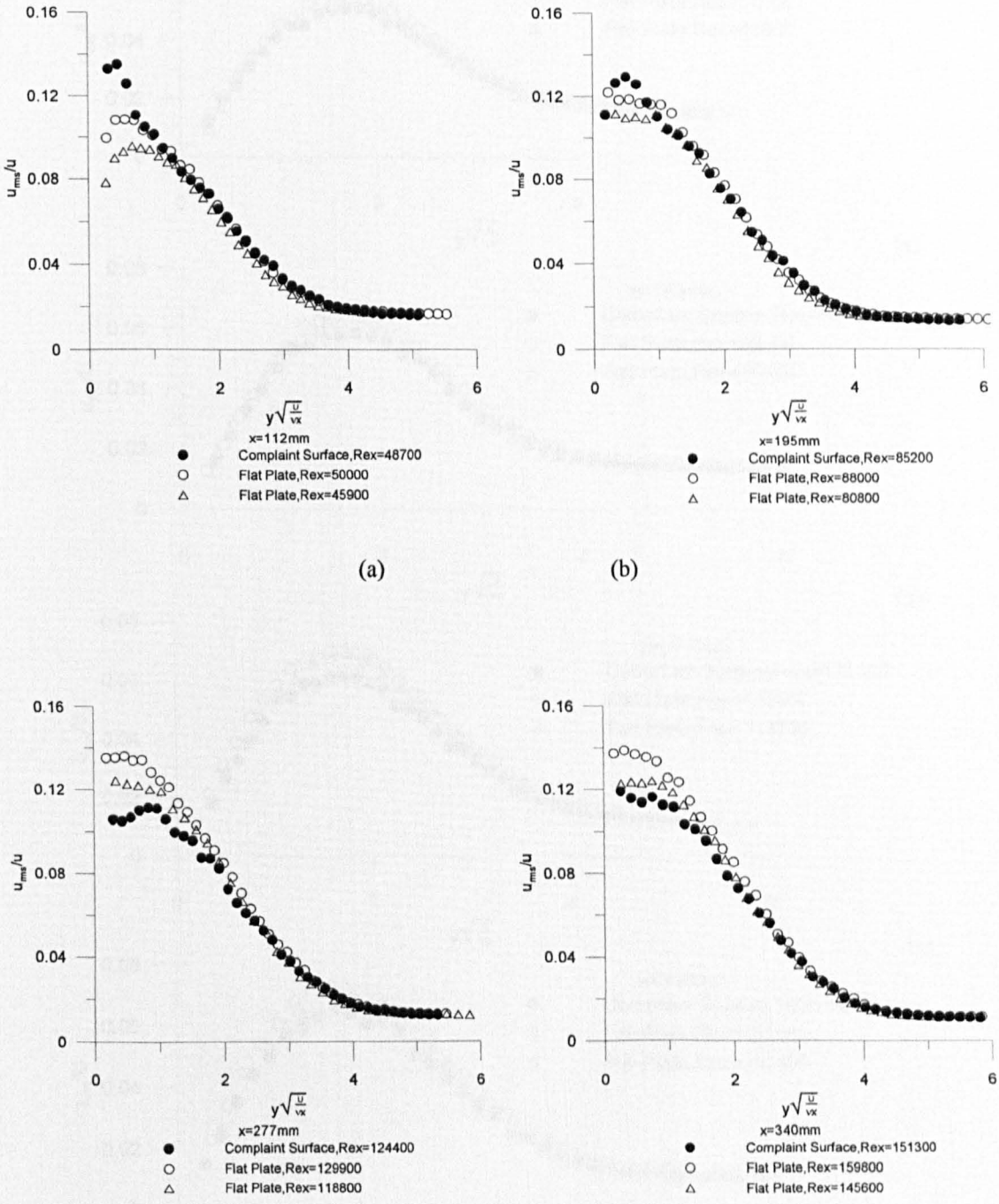

Figure4.34 the local turbulence profile across the boundary layer over a compliant surface with $\frac{\xi^2}{E\rho_{cs}L^2} = 3.49$ (a) x=112mm(b)x=195mm(c)x=277mm(d)x=340mm

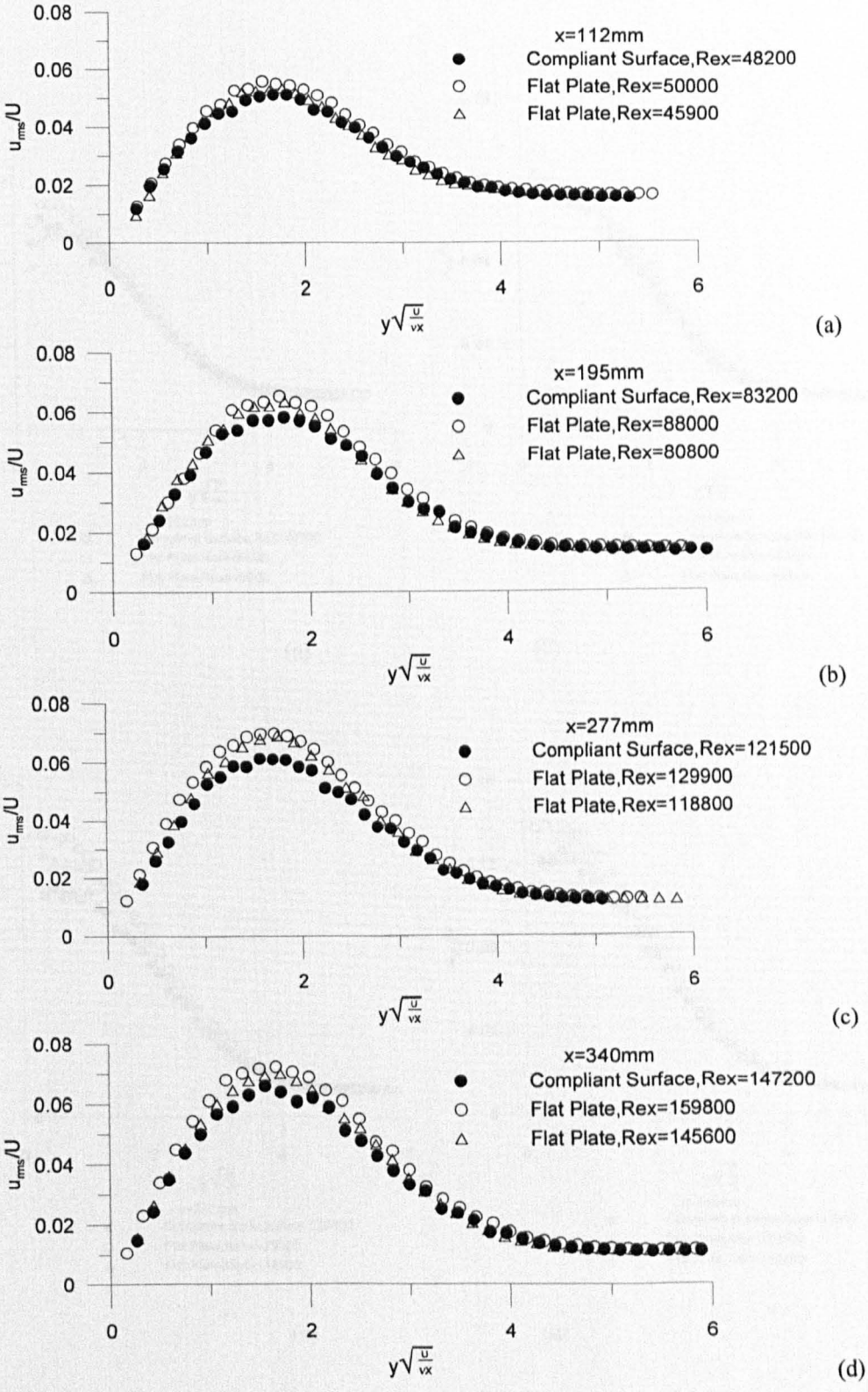

Figure4.35 The boundary layer fluctuations over a compliant surface with $\frac{\xi^2}{E\rho_{cs}L^2} = 2.65$

(a) x=112mm (b)x=195mm(c)x=277mm(d)x=340mm

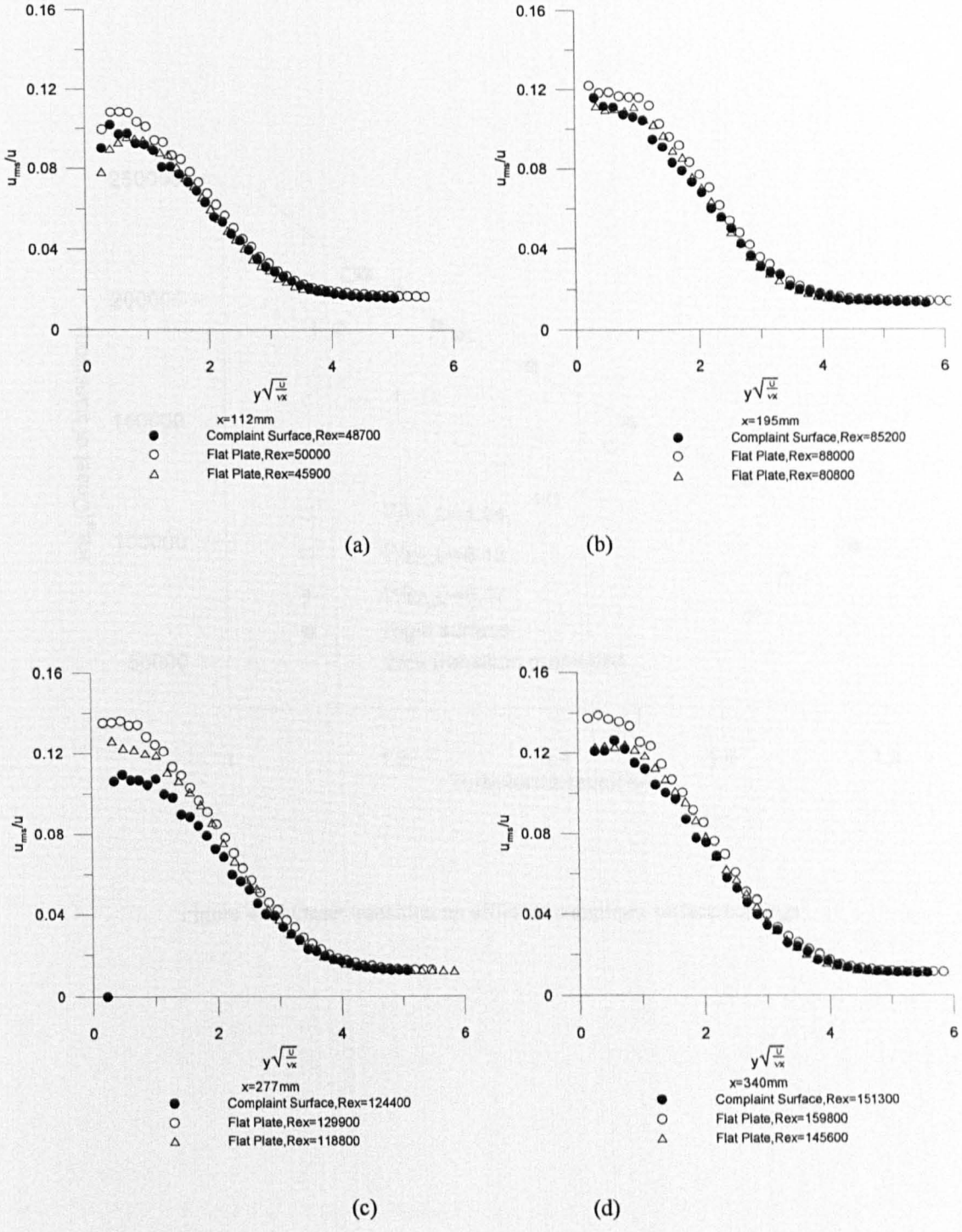

Figure4.36 the local turbulence profile across the boundary layer over a compliant surface with $\frac{\xi^2}{E\rho_{cs}L^2} = 2.65$ (a) x=112mm (b) x=195mm(c) x=277mm(d) x=340mm

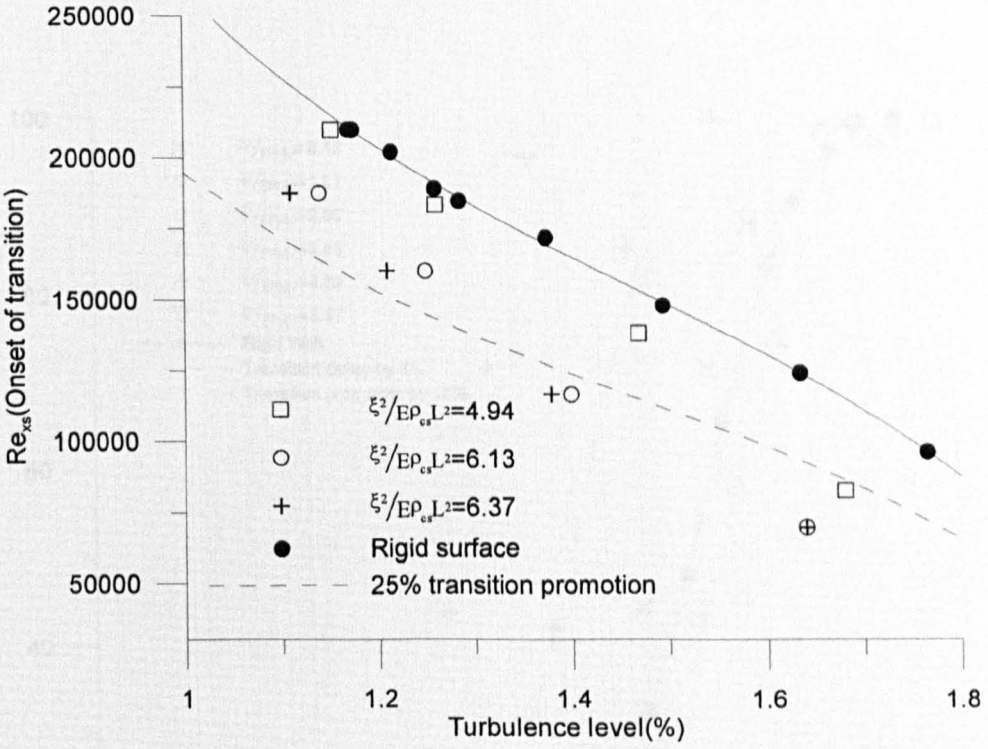

Figure 4.37 Onset transition on different compliant surface coatings

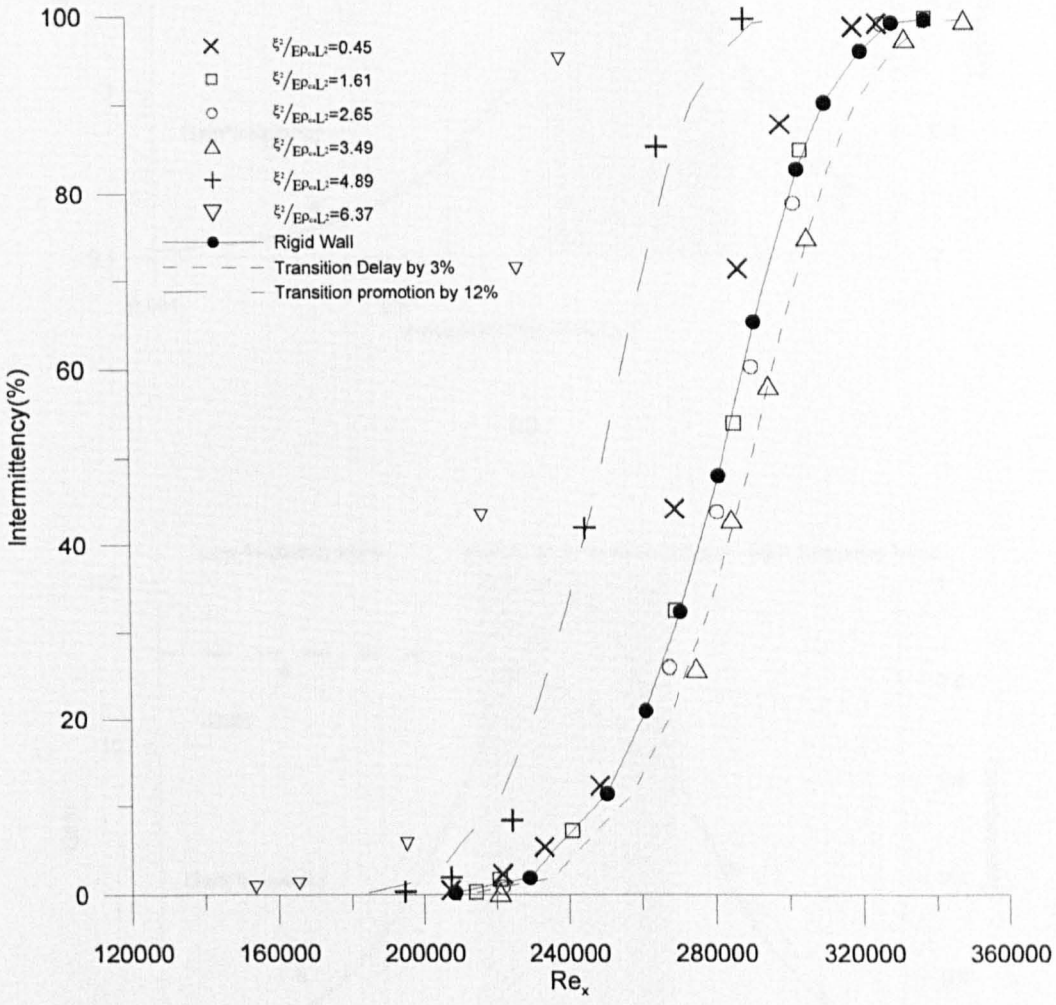

Figure 4.38 Intermittency against Re_x on different compliant surfaces

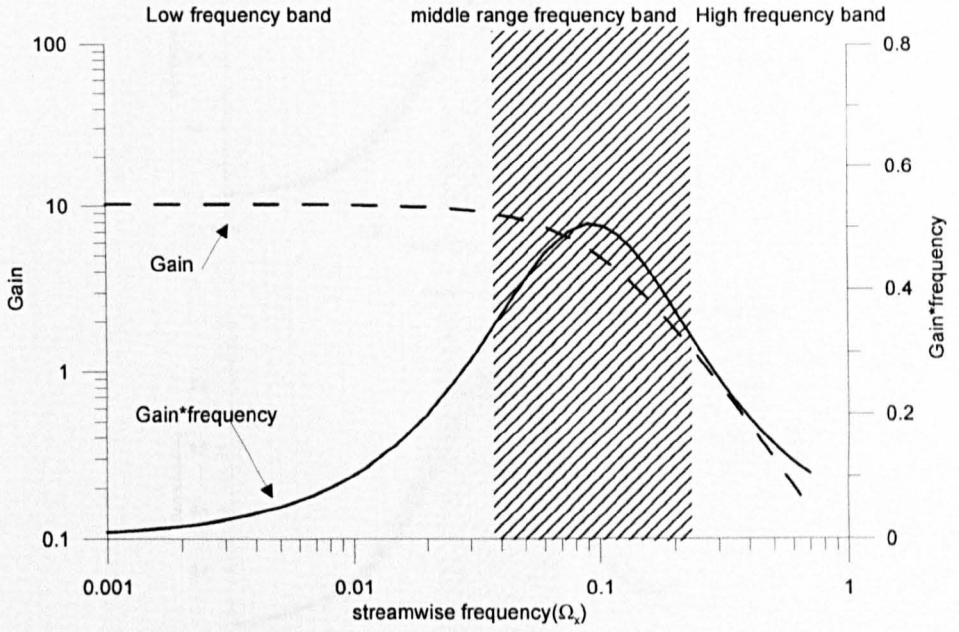

(a)

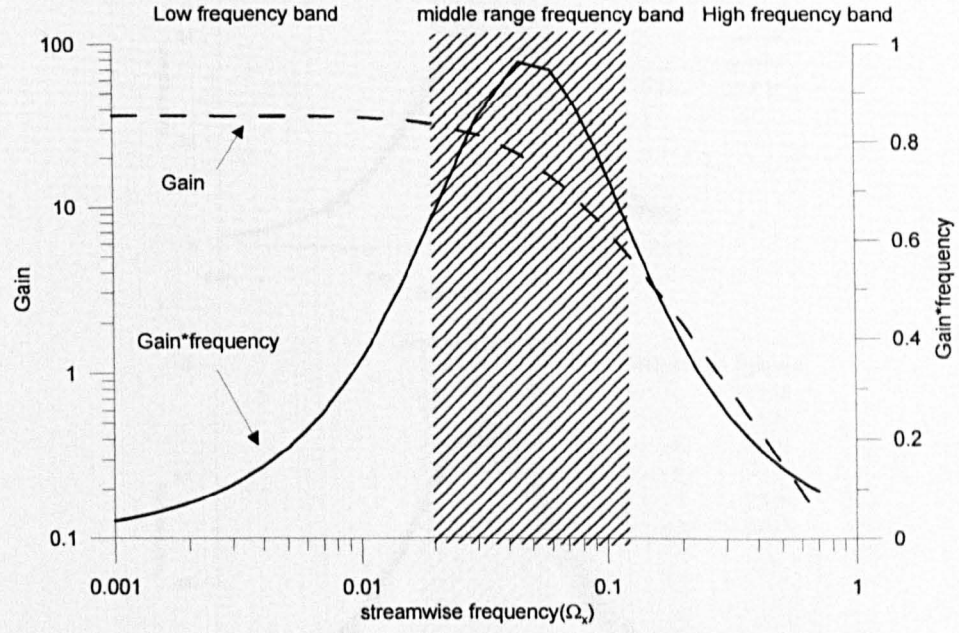

(b)

Figure4.39 The determination of frequency bands (a) $\mathrm{Re}_\theta = 100$ (b) $\mathrm{Re}_\theta = 300$

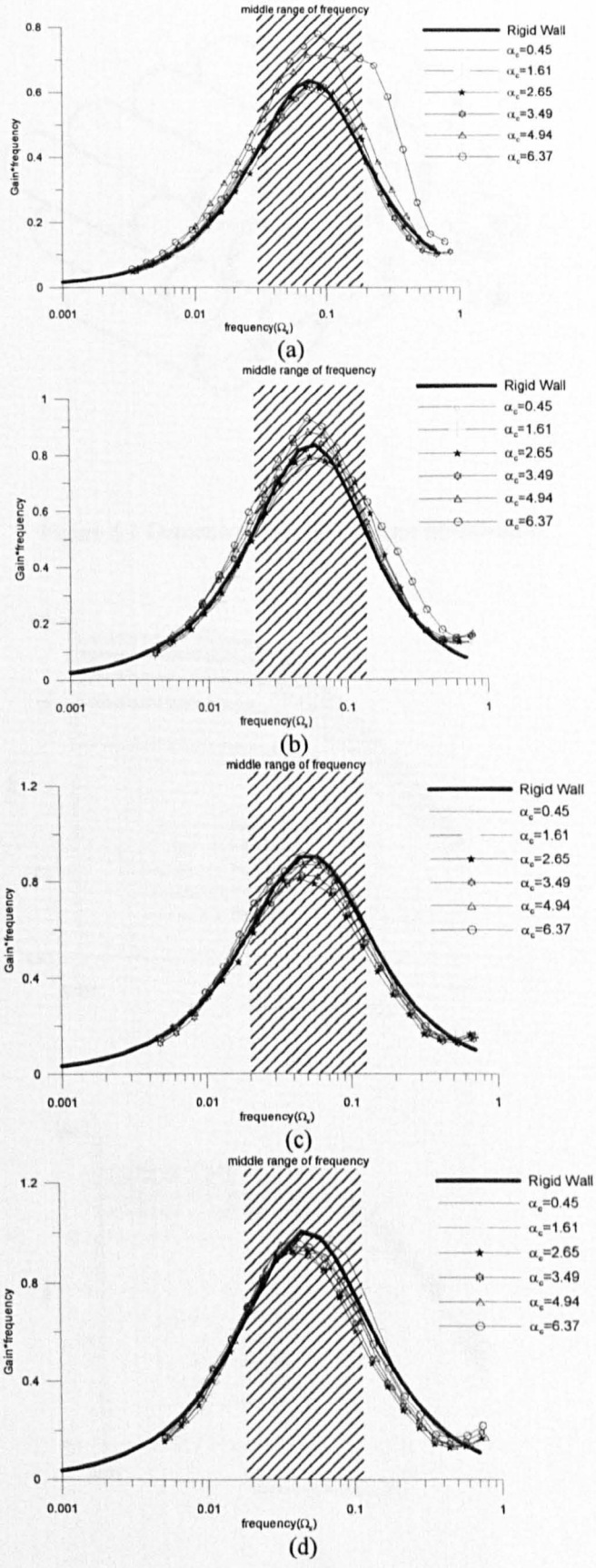

Figure 4.40 Spectra of gain*f over compliant surfaces
(a) x=112mm (b) x=195mm (c) x=277mm (d) x=340mm

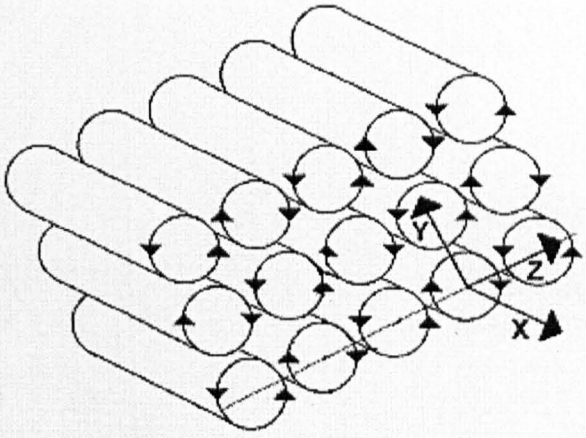

Figure 5.1 Depiction of the free stream disturbances

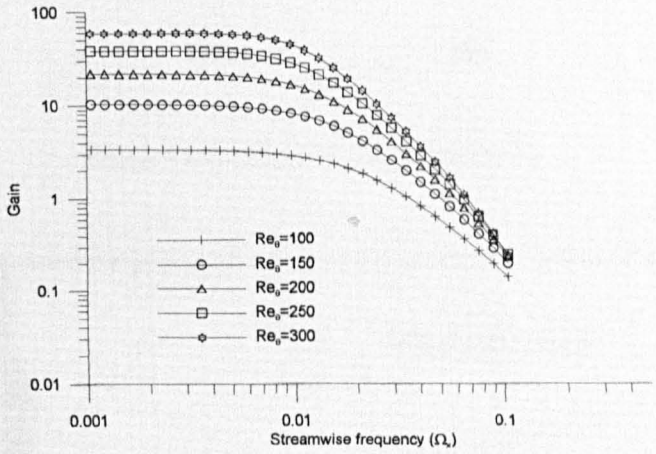

(a)

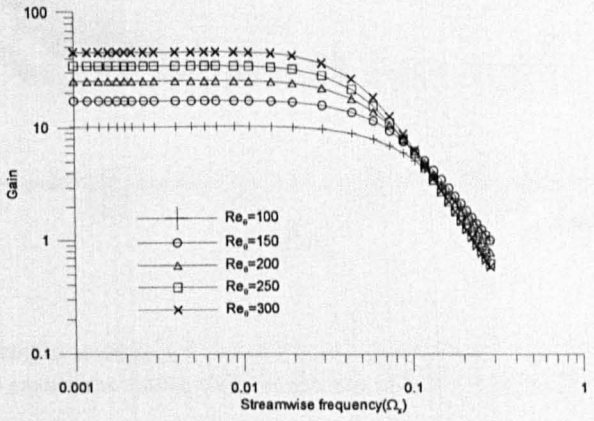

(b)

Figure 5.2 Streamwise gain spectrum (a) numerical predictions (b) experimental measurements

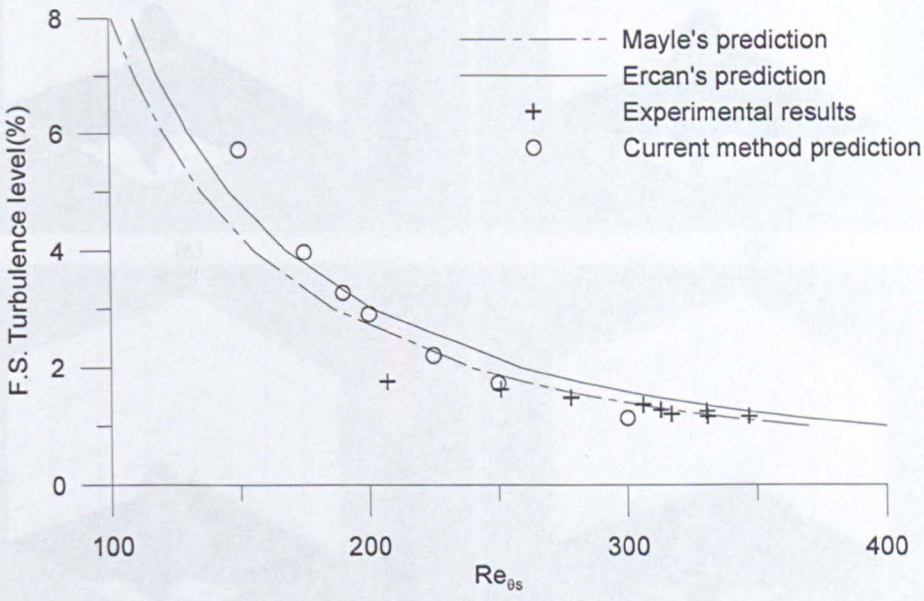

Figure 5.3 Prediction of the transition start

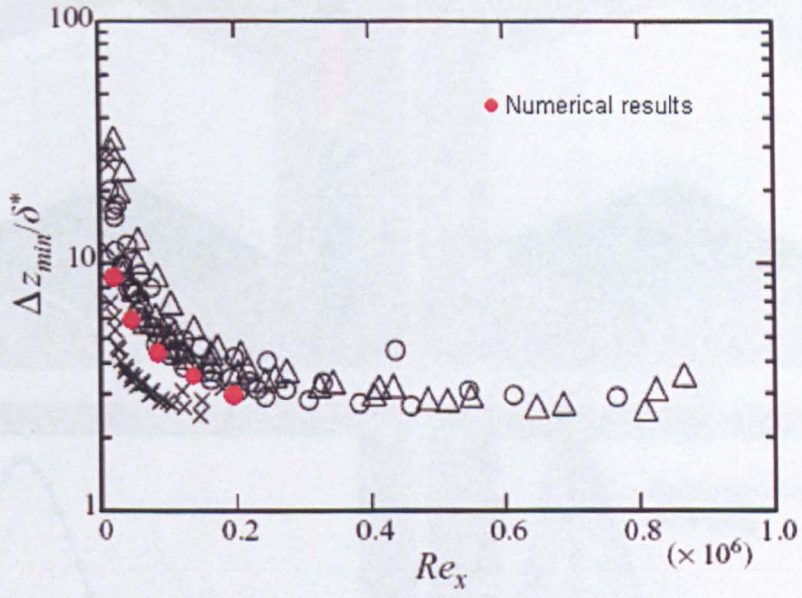

Figure 5.4 Spanwise wavelengths at different free stream turbulence levels Δ , Tu=1.5%, O ,Tu=2.2%, ×,Tu=6.6% , • ,current model predictions (taken from Matsubara & Alferdsson, 2001)

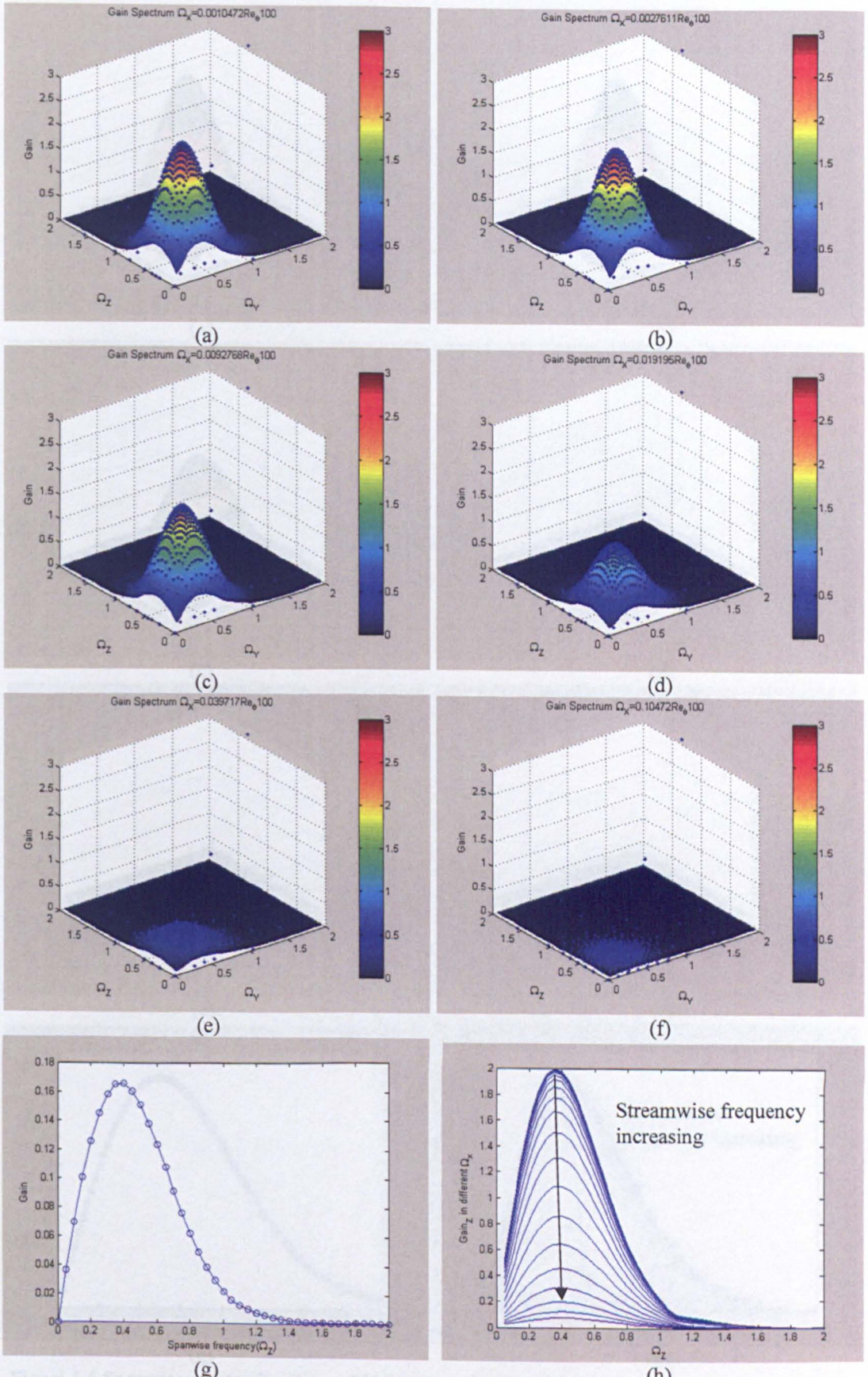

Figure 5.5 Spanwise spectra for $\mathrm{Re}_\theta = 100$ (a) $\Omega_x = 0.00104$ (b) $\Omega_x = 0.00276$ (c) $\Omega_x = 0.00927$ (d) $\Omega_x = 0.0191$ (e) $\Omega_x = 0.0397$ (f) $\Omega_x = 0.104$ (g) Averaged spanwise near wall gain (h) peak in spanwise near wall gain at different streamwise frequencies

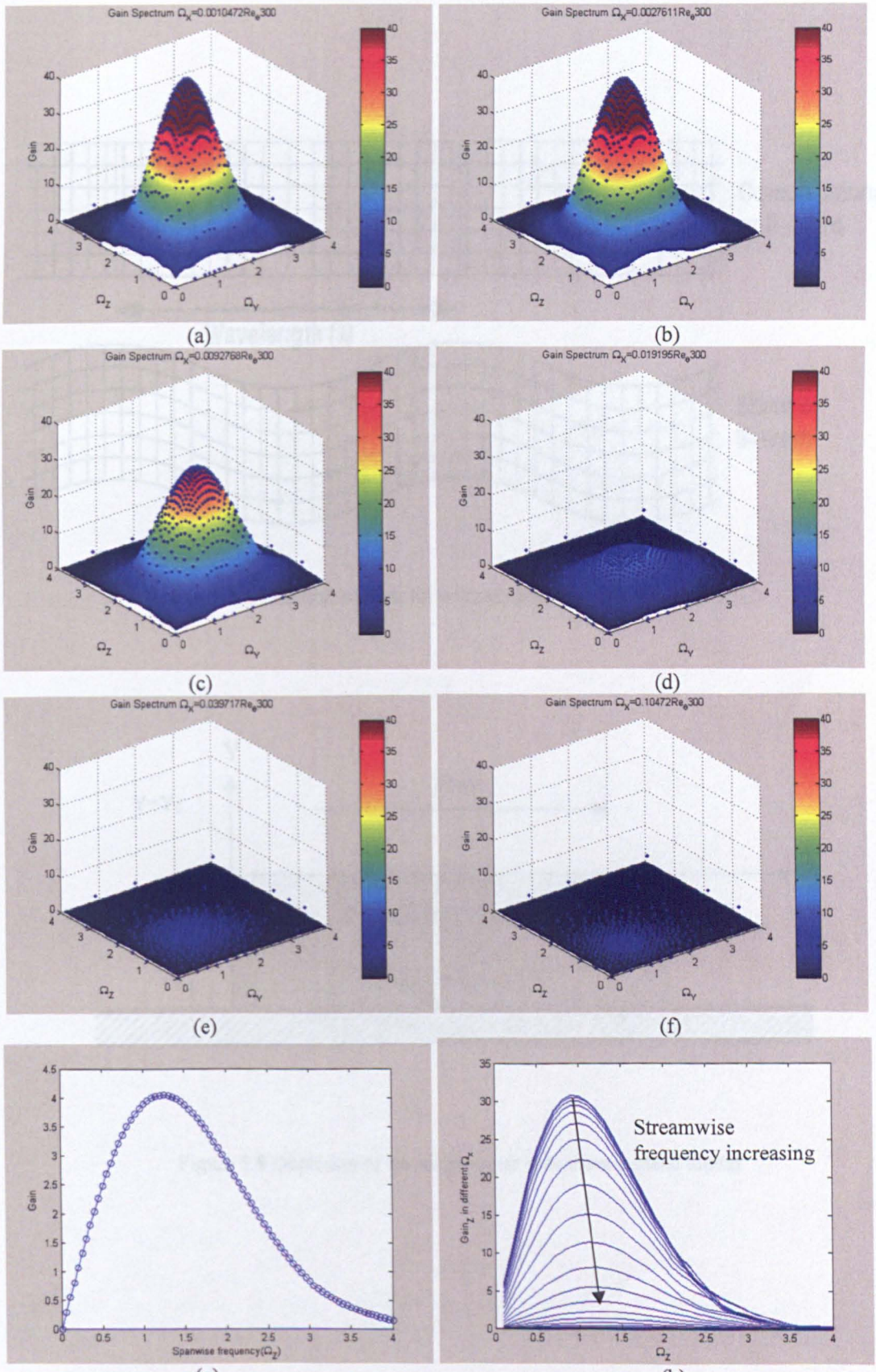

Figure 5.6 Spanwise spectra for $Re_\theta = 300$ (a) $\Omega_x = 0.00104$ (b) $\Omega_x = 0.00276$ (c) $\Omega_x = 0.00927$ (d) $\Omega_x = 0.0191$ (e) $\Omega_x = 0.0397$ (f) $\Omega_x = 0.104$ (g) Averaged spanwise near wall gain (h) peak in spanwise near wall gain at different streamwise frequencies

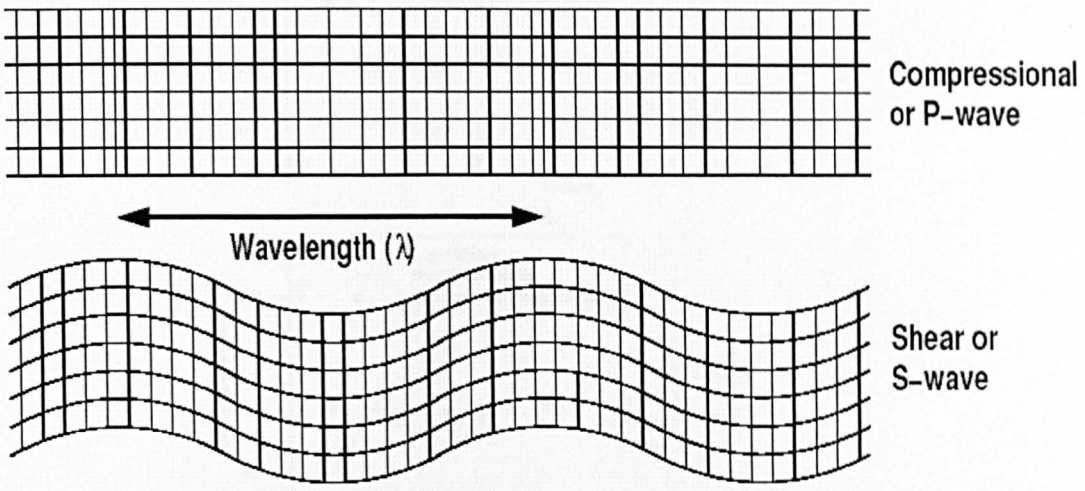

Figure5.8 Particle motion for compression and shear waves

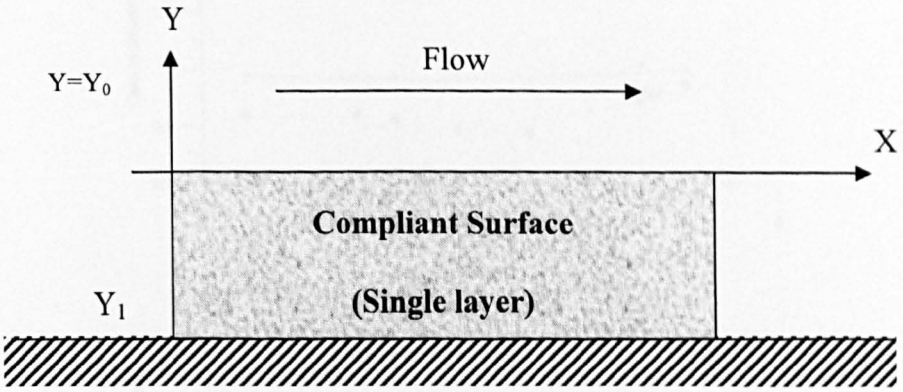

Figure 5.9 Depiction of the single-layer compliant surface model

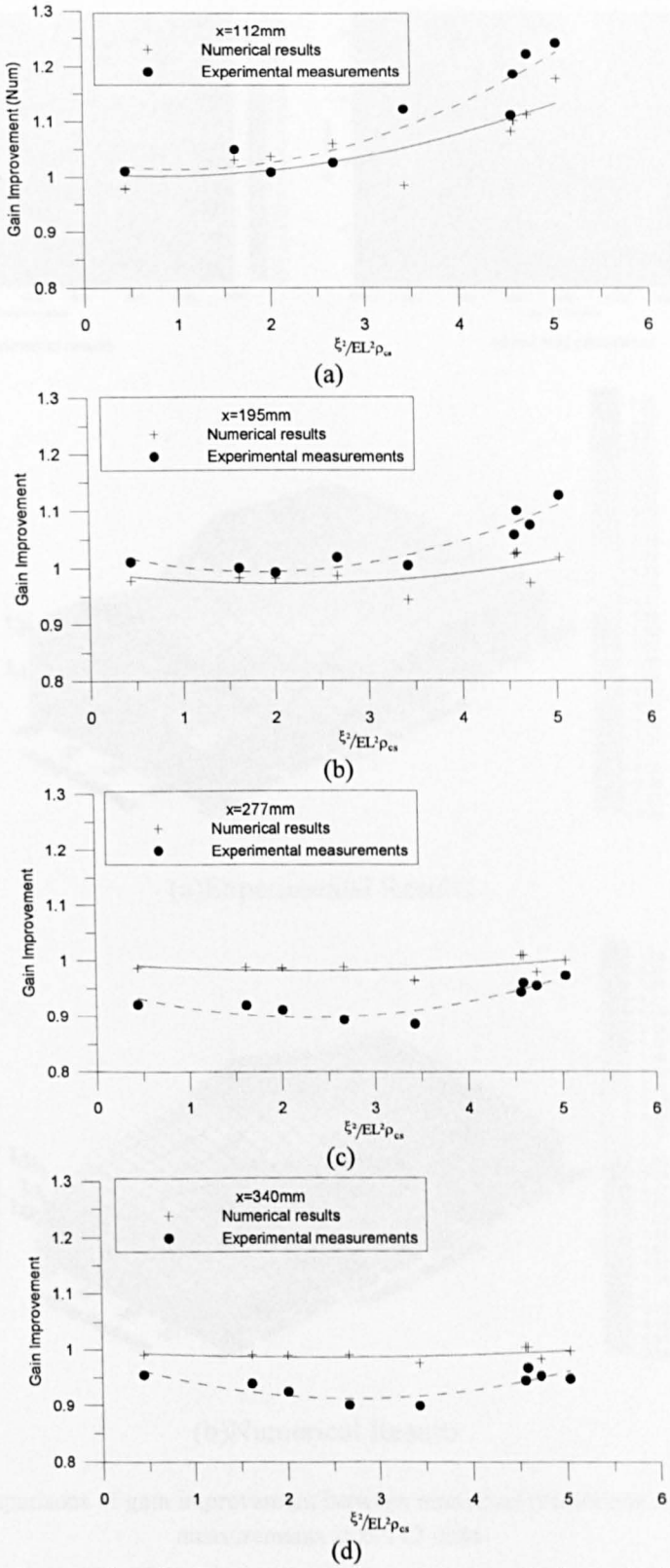

Figure 5.10 Comparisons of gain improvement between numerical predictions and experimental measurements at different streamwise stations (a) x=112mm (b) x=195mm (c) x=277mm (d) x=340mm

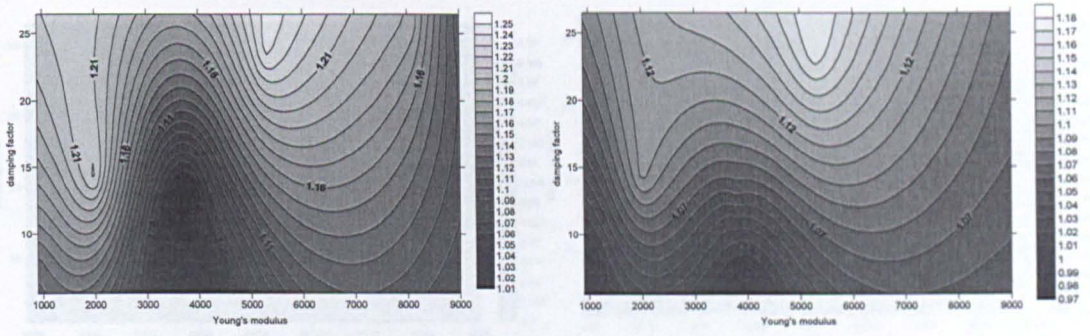

Experimental results Numerical predictions

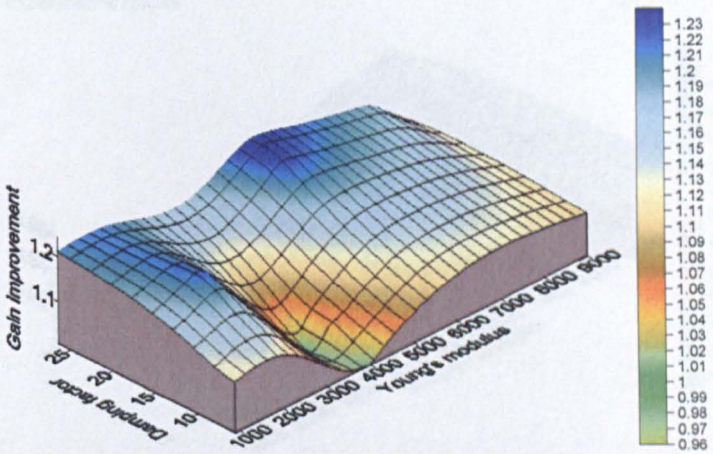

(a)Experimental Results

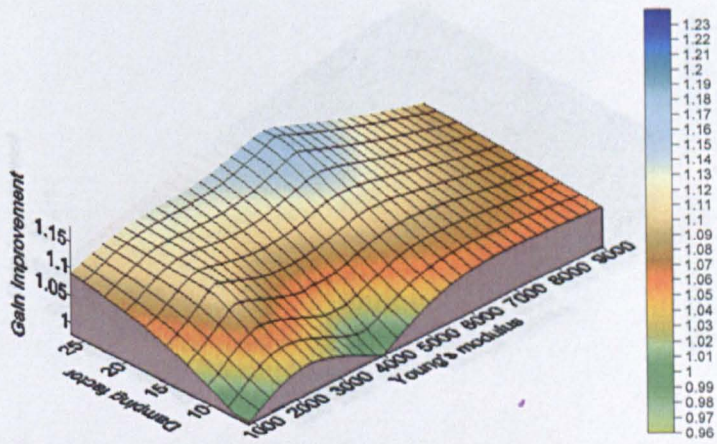

(b)Numerical Results

Figure 5.11 Comparisons of gain improvement between numerical predictions and experimental measurements at x=112 mm

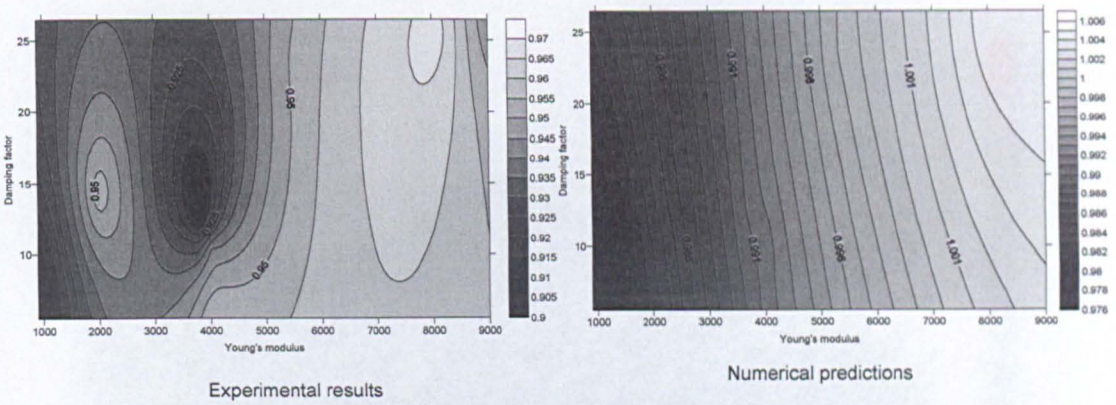

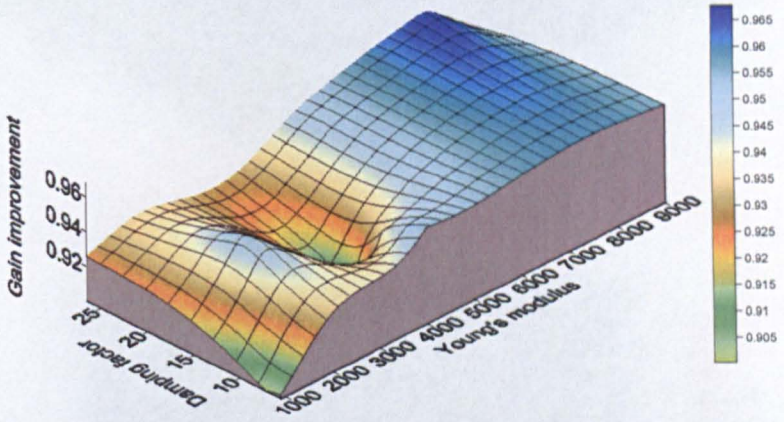

(a)Experimental Results

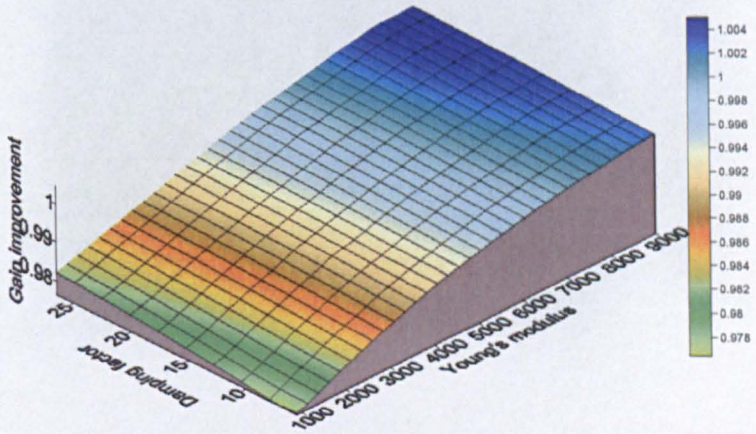

(b)Numerical Results

Figure 5.12 Comparisons of gain improvement between numerical predictions and experimental measurements at x=340mm

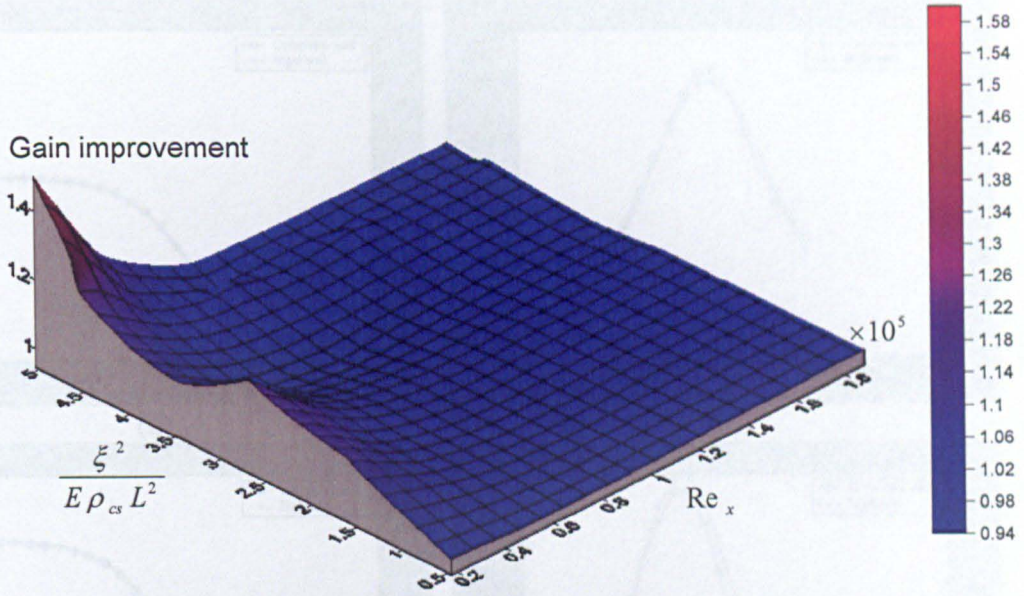

(a)

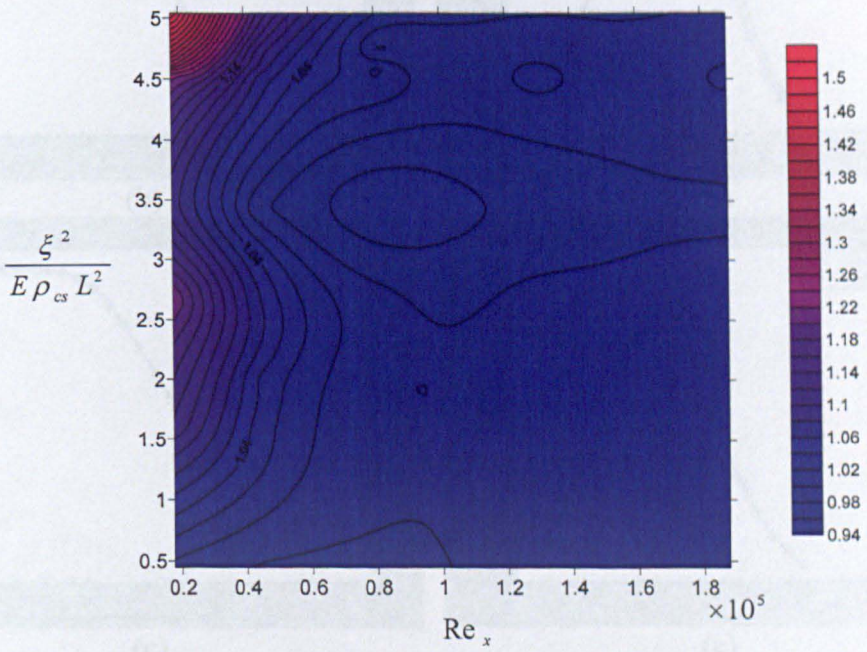

(b)

Figure 5.13 Numerical results of correlation of gain amplification and compliant surface properties $\frac{\xi^2}{E\rho_{cs}L^2}$ at $U \approx 6.5m/s$ (a) Mesh plot (b) Contour plot

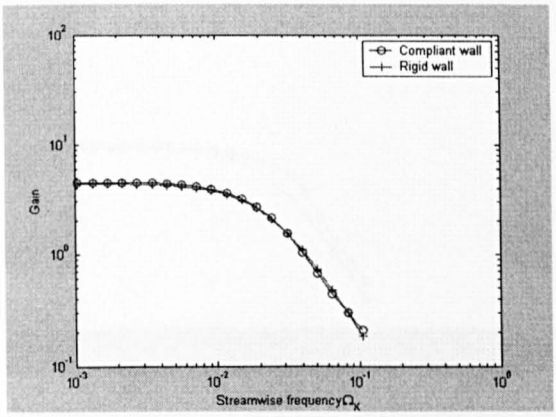

(a)

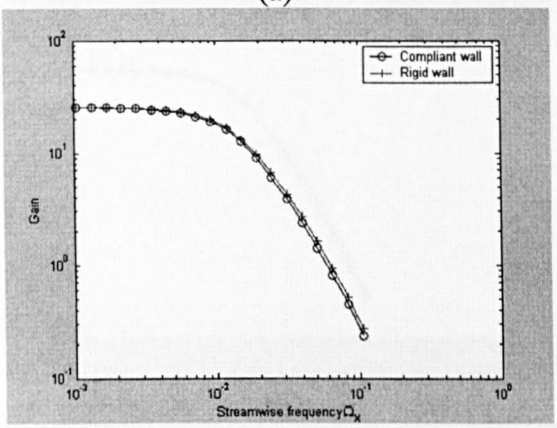

(b)

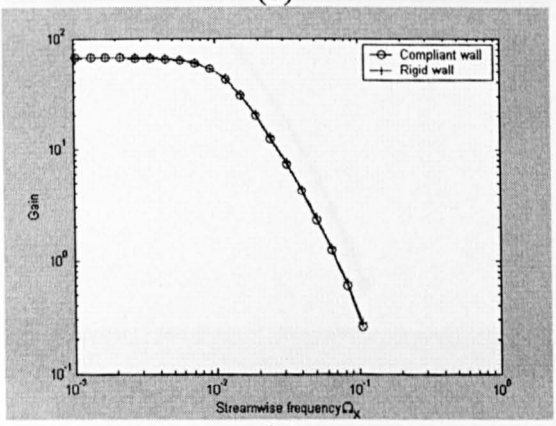

(c)

Figure5.14 Near wall gain spectra on a compliant surface with $\frac{\xi^2}{E\rho_{cs}L^2}=3.49$ (a) Re_θ=100 (b) Re_θ=200 (c) Re_θ=300

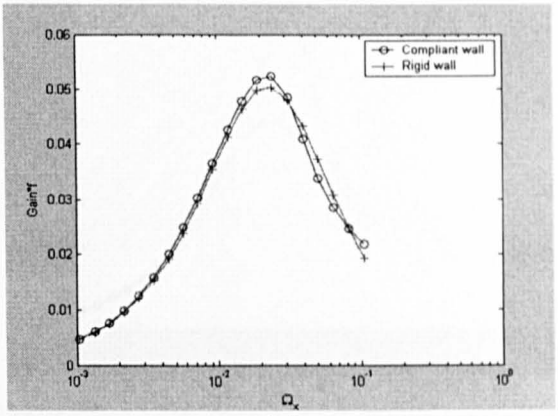

(a)

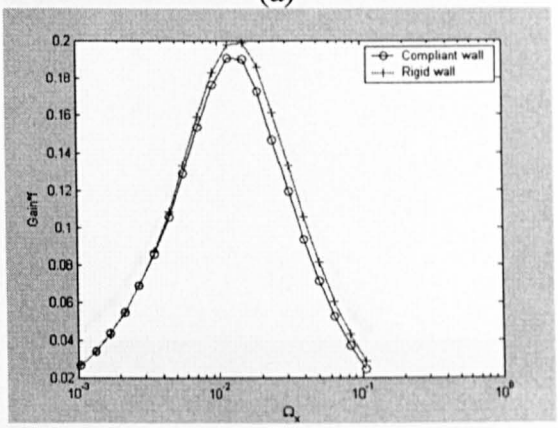

(b)

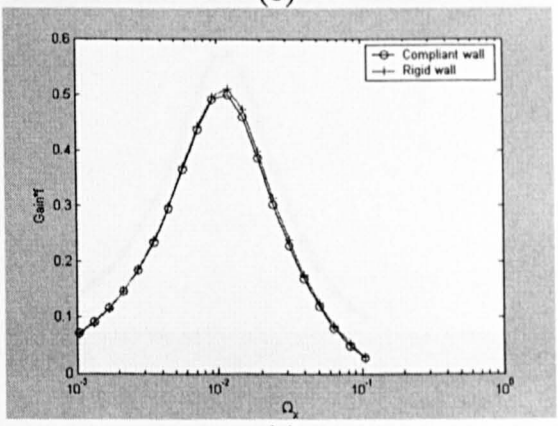

(c)

Figure5.15 Gain*frequency spectra on a compliant surface with $\frac{\xi^2}{E\rho_{cs}L^2}=3.49$ (a) Re_θ=100 (b) Re_θ=200 (c) Re_θ=300

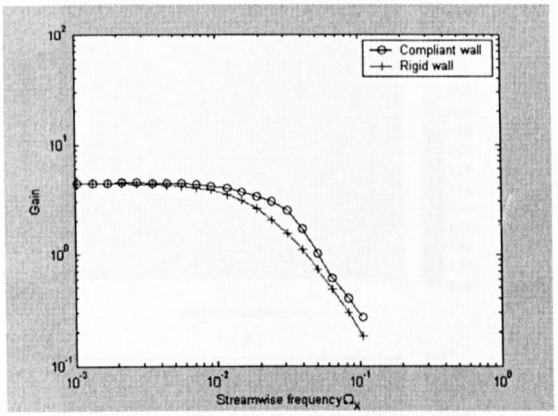

(a)

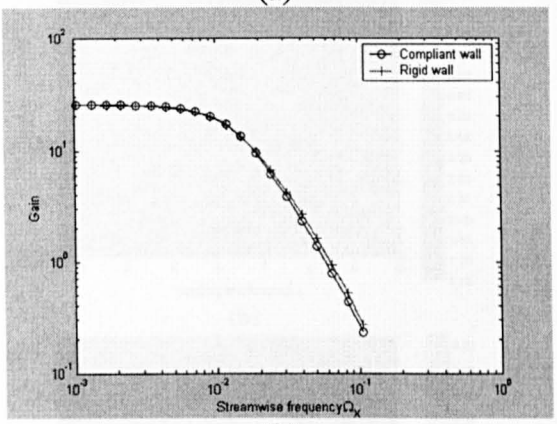

(b)

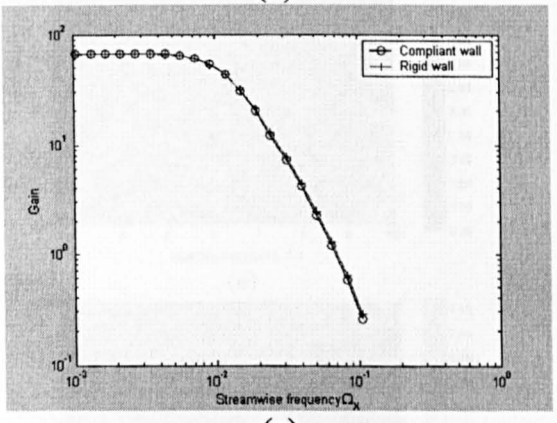

(c)

Figure5.16 Near wall gain spectra on a compliant surface with $\frac{\xi^2}{E\rho_{cs}L^2} = 6.13$ (a) Re_θ=100 (b) Re_θ=200 (c) Re_θ=300

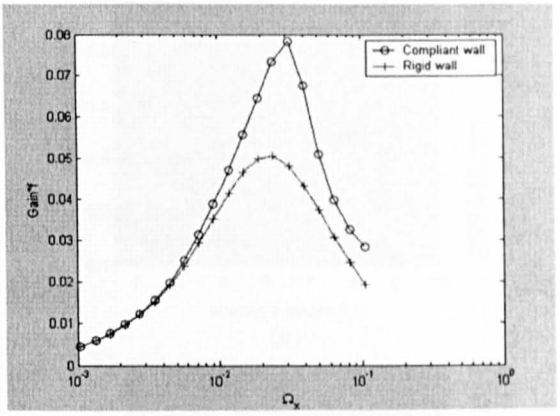

(a)

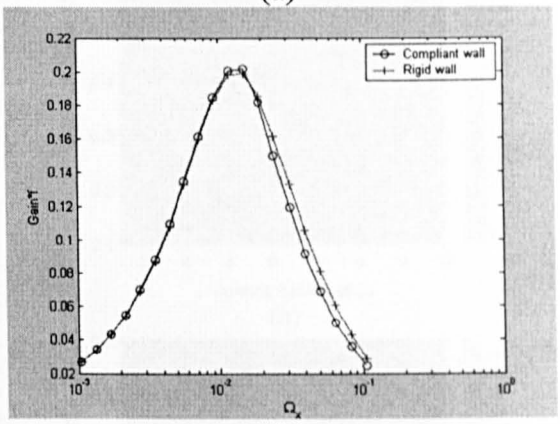

(b)

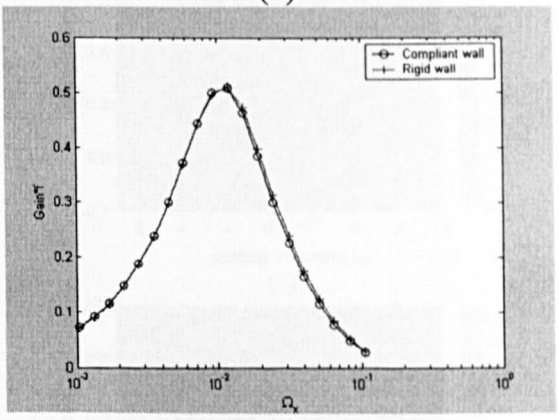

(c)

Figure5.17 Gain*frequency spectra on a compliant surface with $\frac{\xi^2}{E\rho_{cs}L^2} = 6.13$ (a) Re_θ=100 (b) Re_θ=200 (c) Re_θ=300

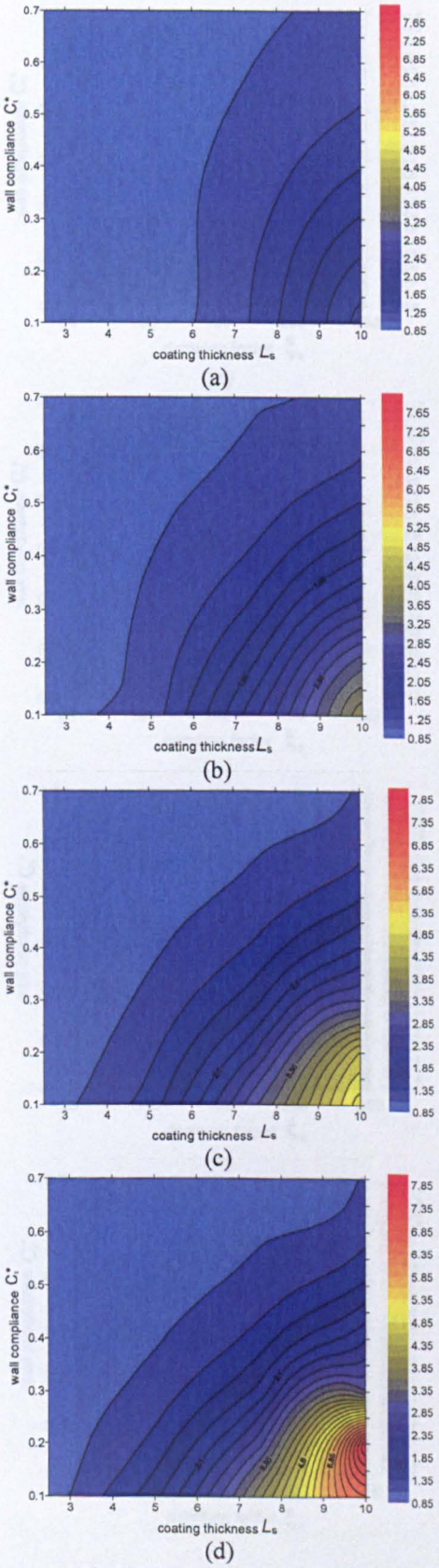

Figure 5.18 The effect of damping factor for different wall compliance and coating thickness at $\mathrm{Re}_\theta = 100$ (a) ξ_s=50 (b) ξ_s=100 (c) ξ_s=150 (d) ξ_s=200

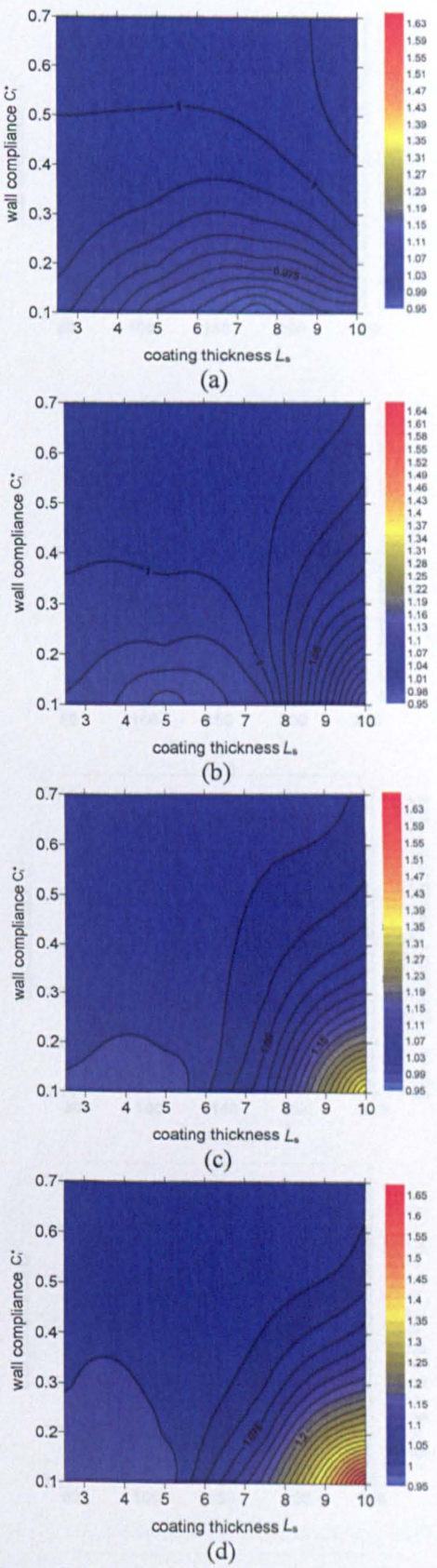

Figure 5.19 The effect of damping factor for different wall compliance and coating thickness at $\mathrm{Re}_\theta = 300$ (a) ξ_s=50 (b) ξ_s=100 (c) ξ_s=150 (d) ξ_s=200

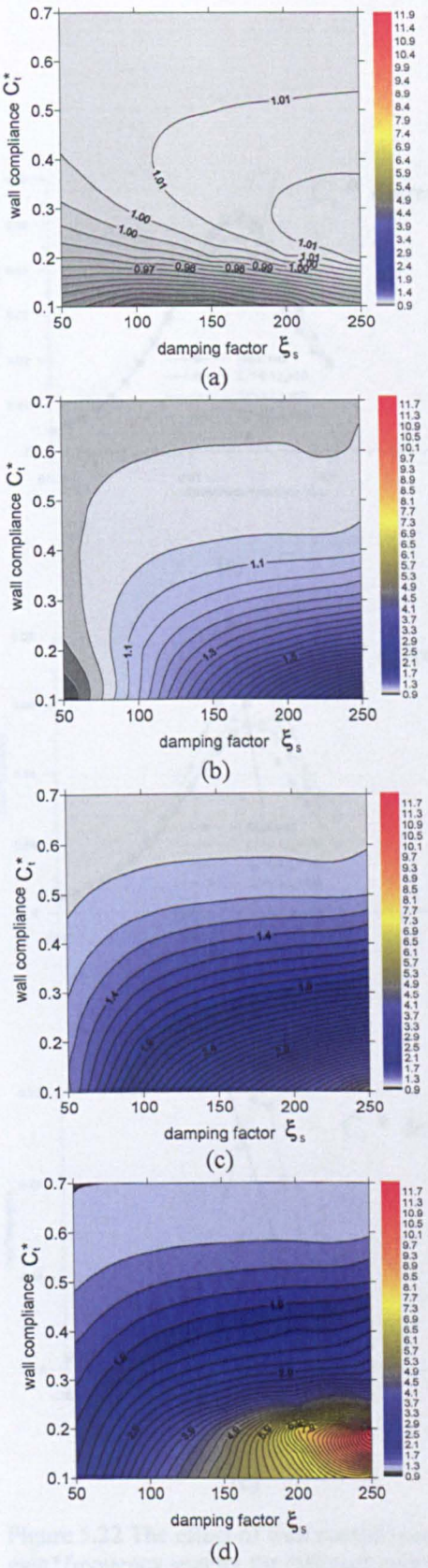

Figure 5.20 The effect of coating thickness for different wall compliance and damping factors at $\mathrm{Re}_\theta = 100$ (a) L_s=2.5 (b) L_s=5 (c) L_s=7.5 (d) L_s=10

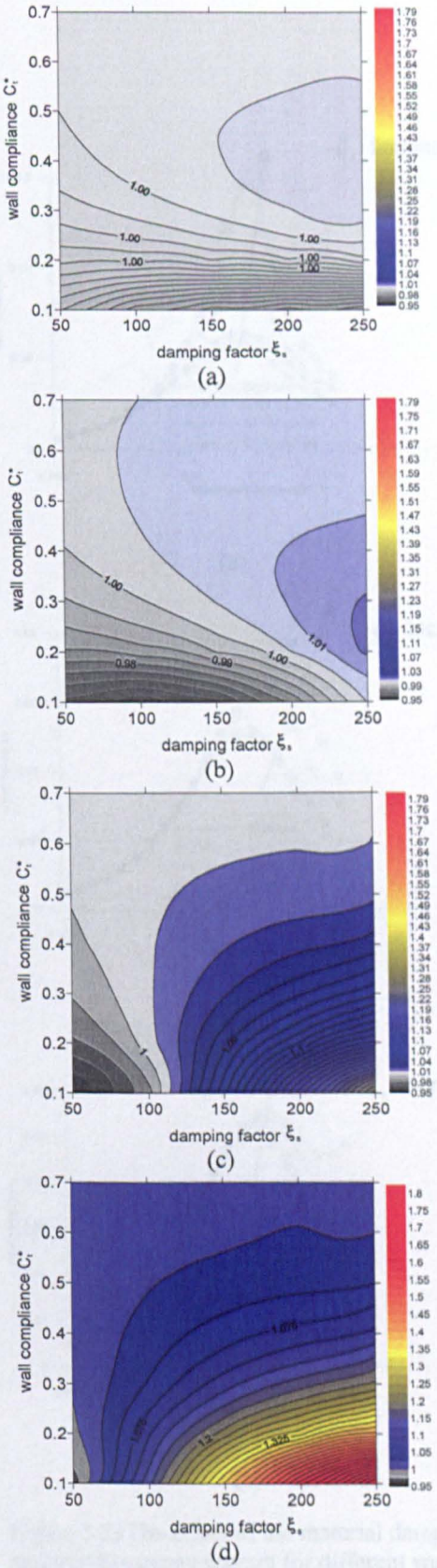

Figure 5.21 The effect of coating thickness for different wall compliance and damping factors at $\mathrm{Re}_\theta = 300$ (a) L_s=2.5 (b) L_s=5 (c) L_s=7.5 (d) L_s=10

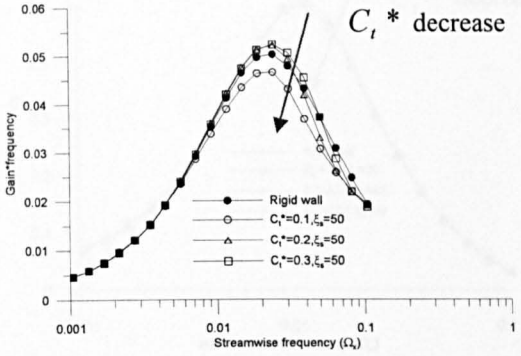

(a)

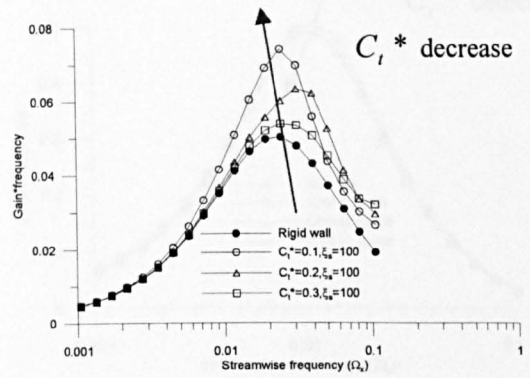

(b)

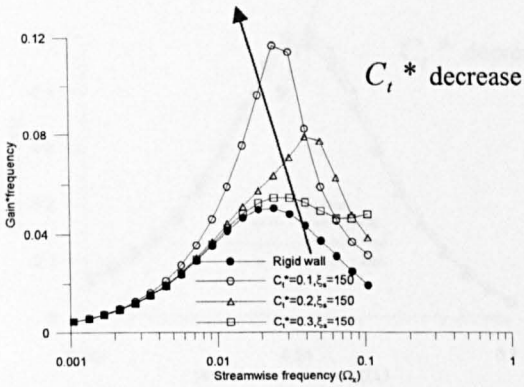

(c)

Figure 5.22 The effect of wall compliance on gain*frequency spectra for different material damping $\mathrm{Re}_\theta = 100$ (a) ξ_s=50 (b) ξ_s=100 (c) ξ_s=150

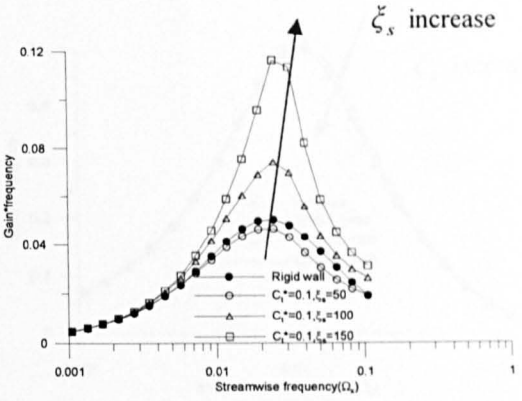

(a)

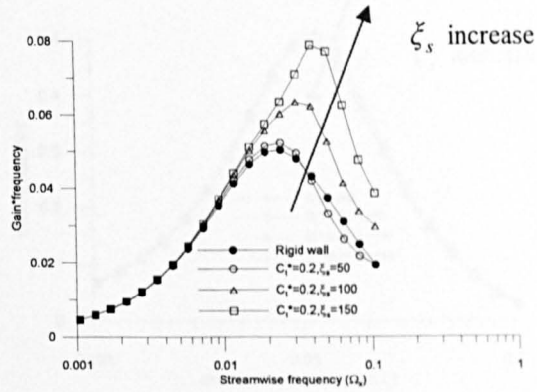

(b)

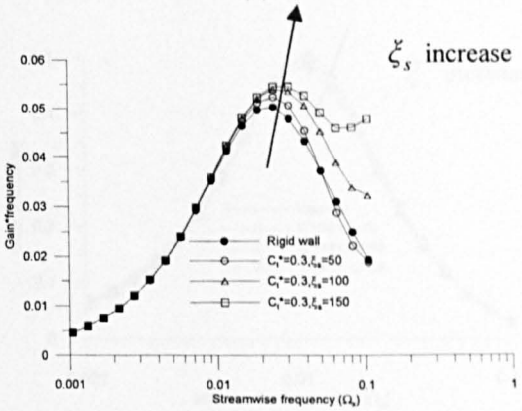

(c)

Figure 5.23The effect of the material damping on gain*frequency spectra for different wall compliance $\mathrm{Re}_\theta = 100$ (a) C_t * =0.1 (b) C_t * =0.2 (c) C_t * =0.3

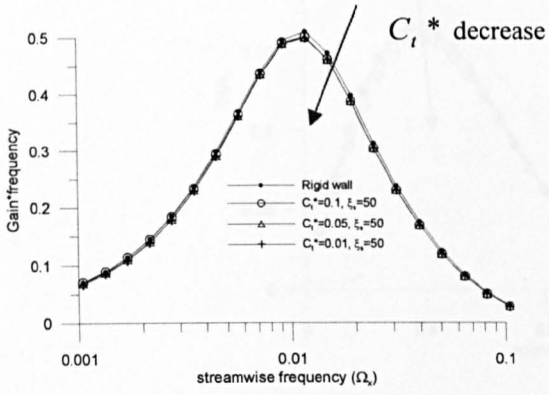

(a)

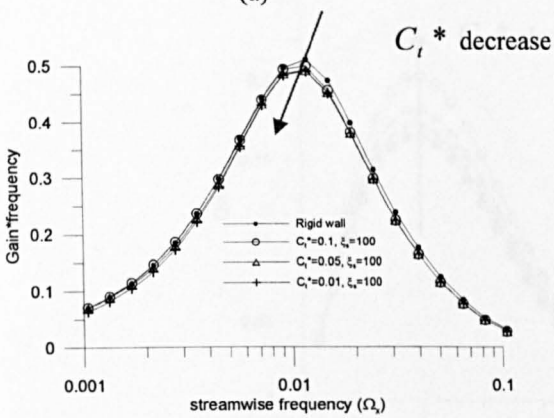

(b)

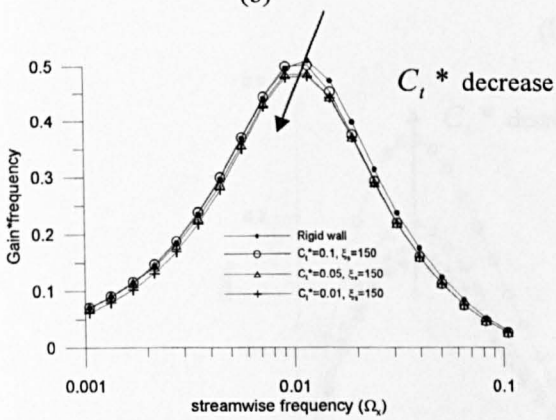

(c)

Figure 5.24 The effect of the material damping on gain*frequency spectra for different wall compliance $\mathrm{Re}_\theta = 300$ (a) ξ_s=50 (b) ξ_s=100 (c) ξ_s=150

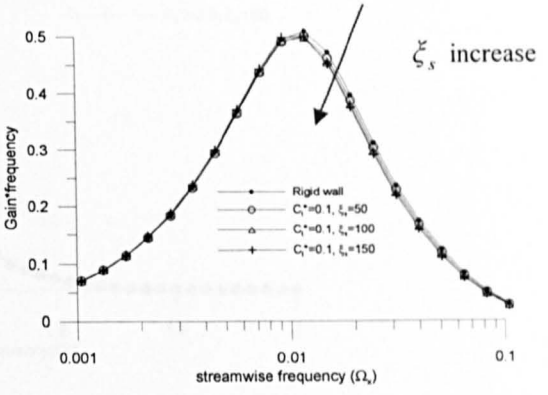

(a)

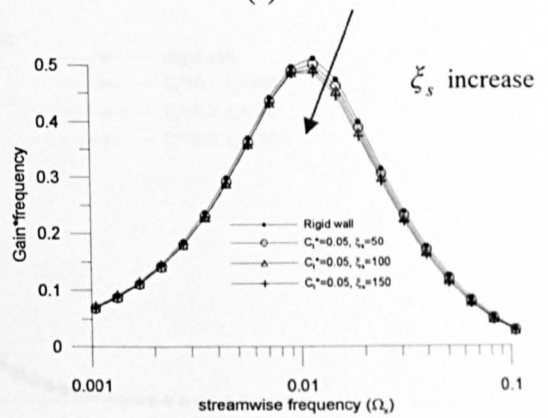

(b)

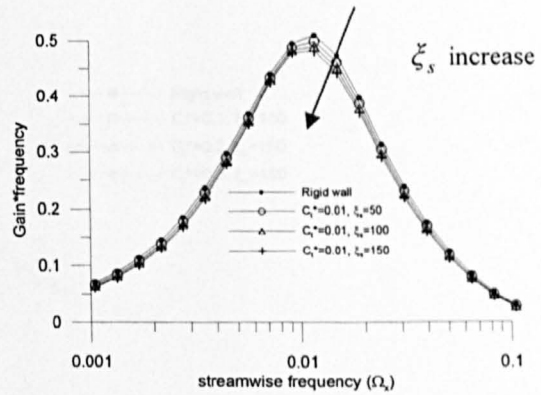

(c)

Figure 5.25 The effect of wall compliance on gain*frequency spectra for different material damping $\mathrm{Re}_\theta = 300$ (a) C_t * =0.1 (b) C_t * =0.05 (c) C_t * =0.01

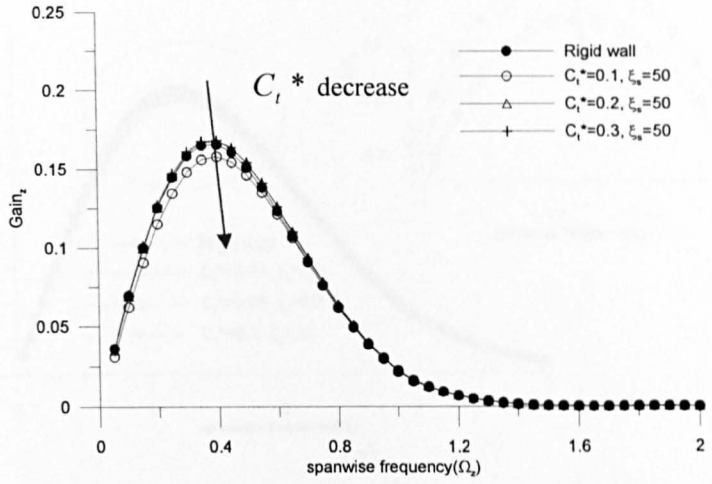

(a)

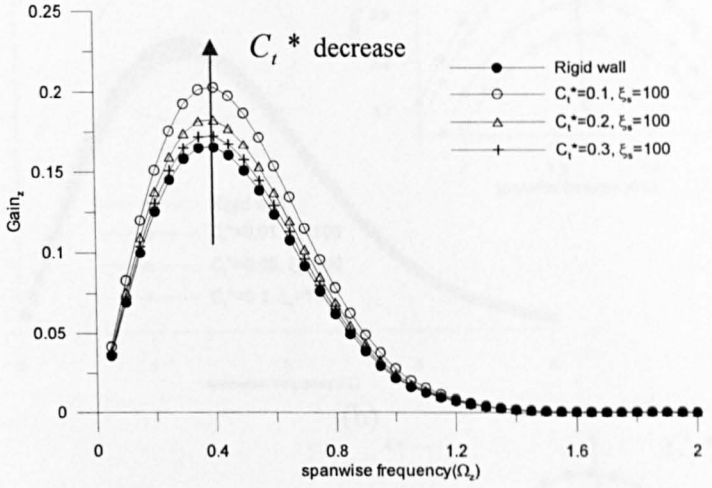

(b)

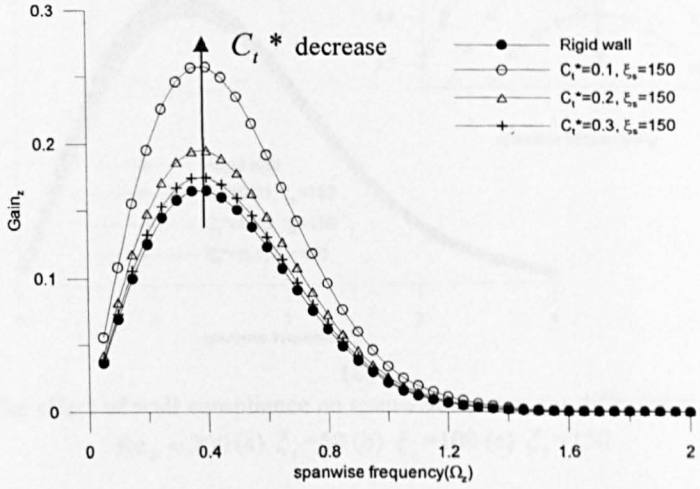

(c)

Figure 5.26 The effect of wall compliance on spanwise spectra for different material damping $\mathrm{Re}_\theta = 100$ (a) ξ_s=50 (b) ξ_s=100 (c) ξ_s=150

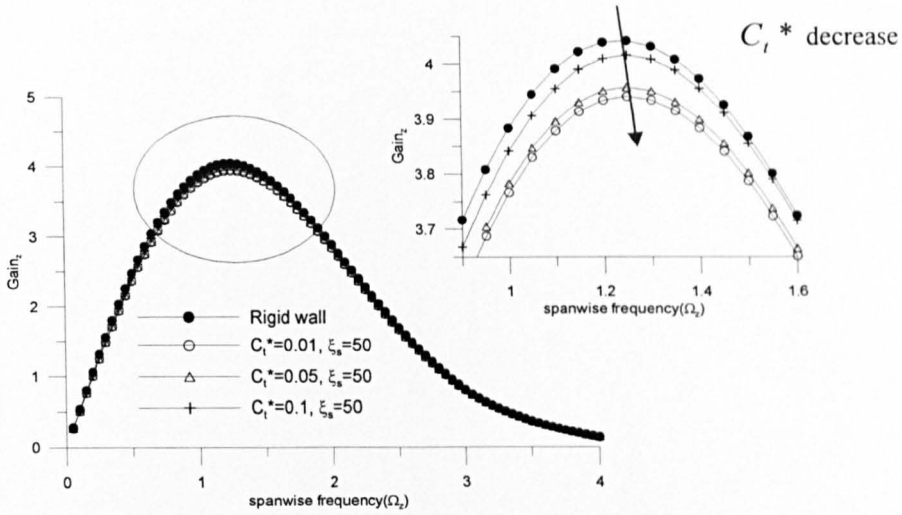

(a)

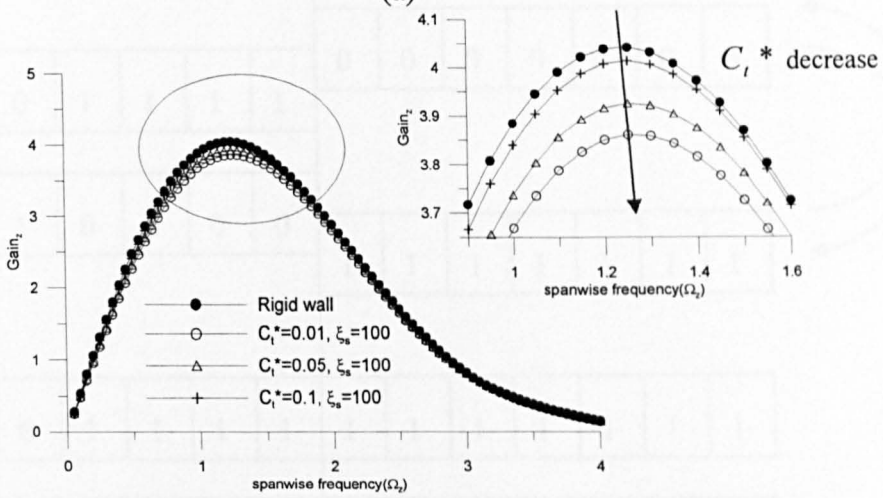

(b)

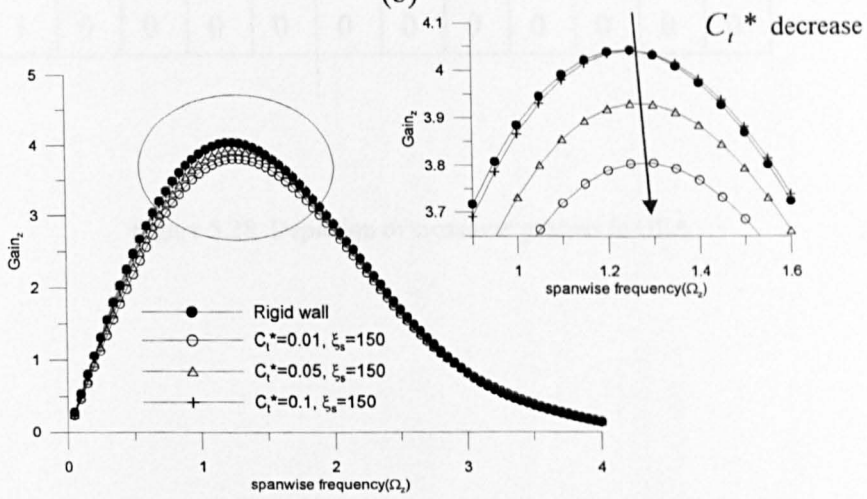

(c)

Figure 5.27 The effect of wall compliance on spanwise spectra for different material damping $\mathrm{Re}_\theta = 300$ (a) ξ_s=50 (b) ξ_s=100 (c) ξ_s=150

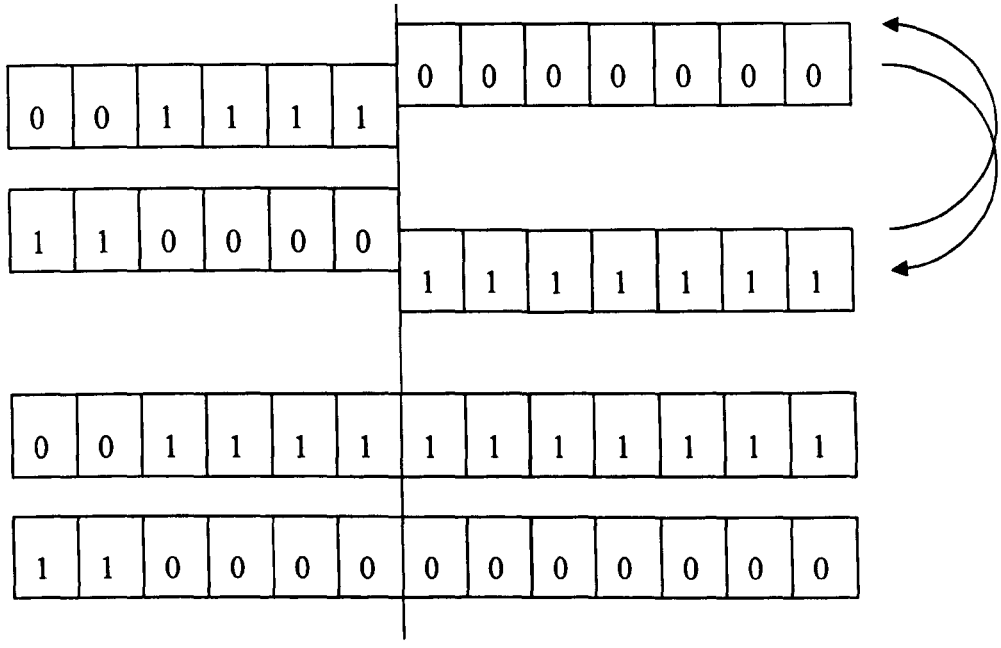

Figure 5.28 Depiction of crossover process in GEA

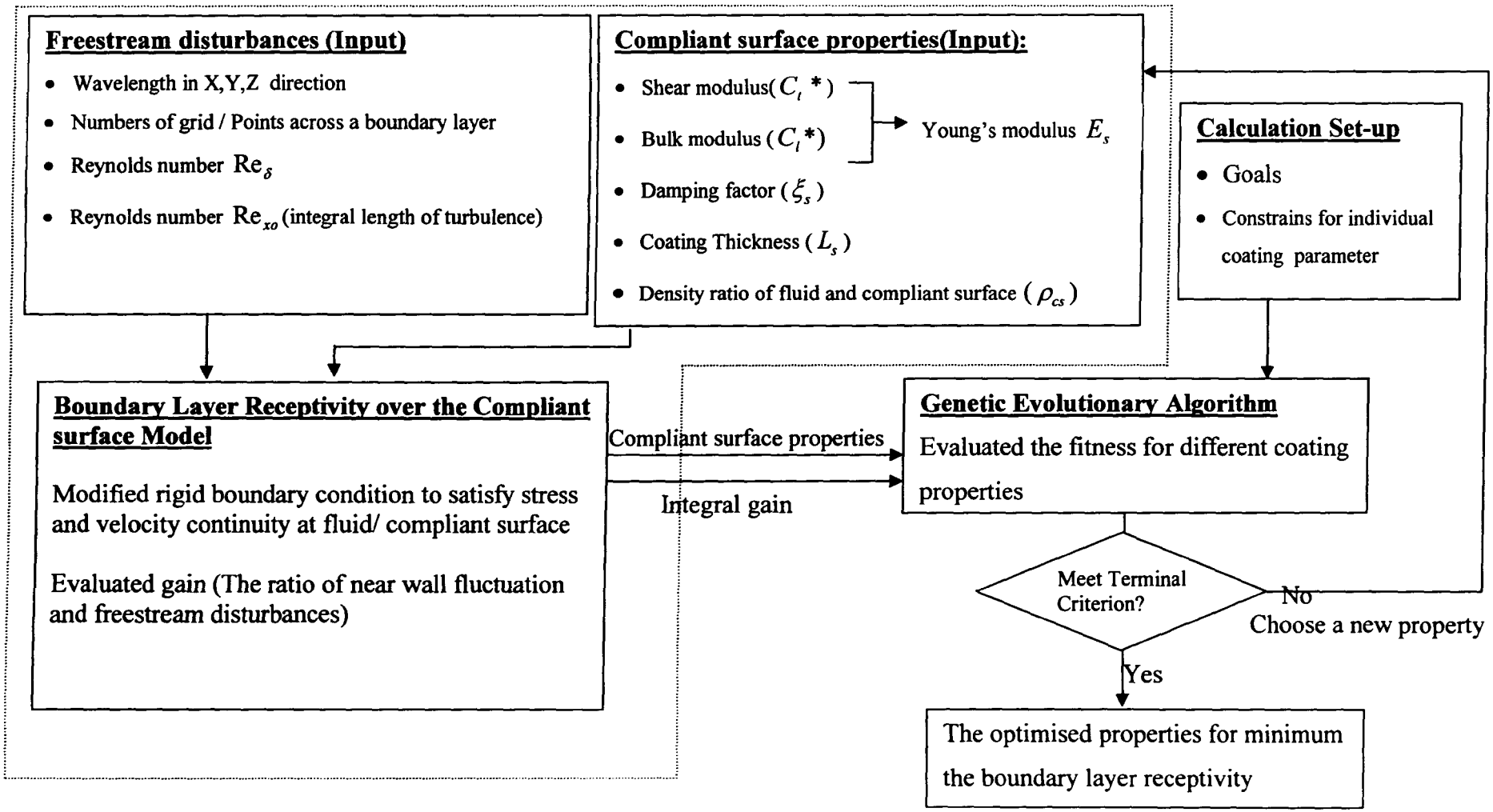

Figure 5.29 The adaptation of the compliant surface receptivity model and GEA

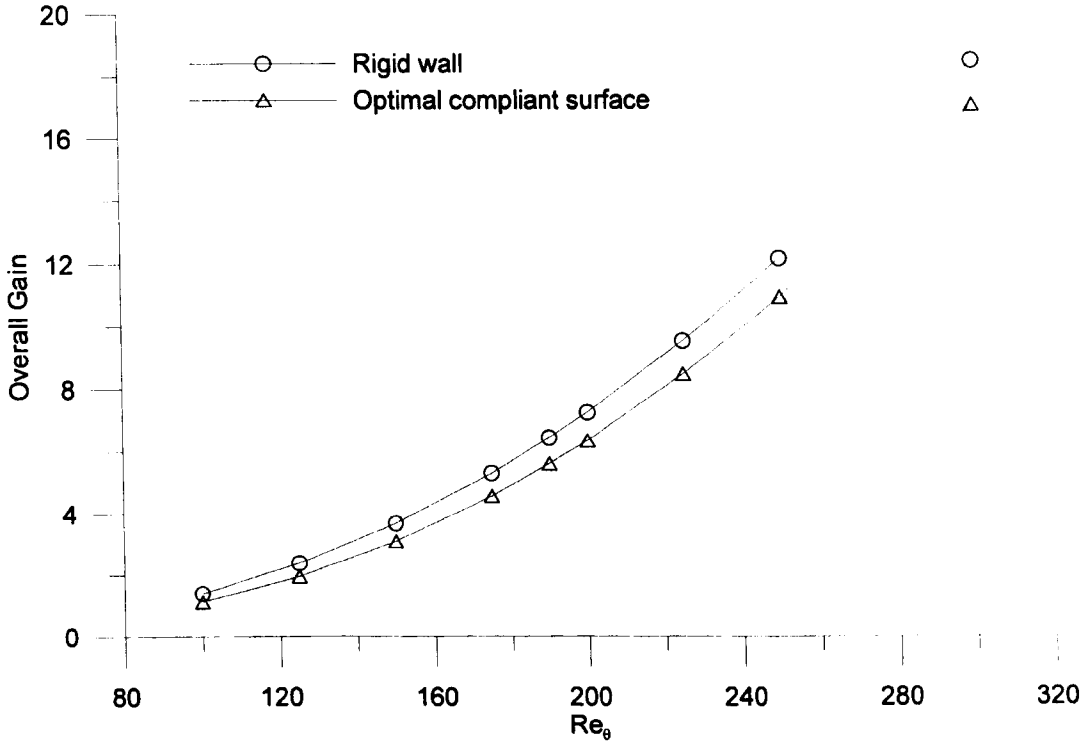

Figure 5.30 Overall gain comparisons for optimised compliant surface and rigid wall

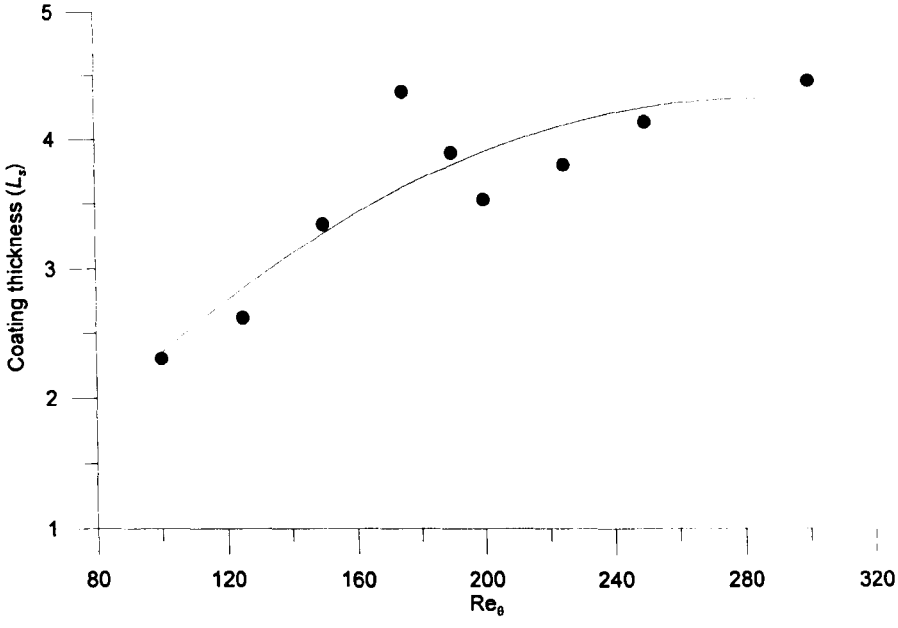

(a)

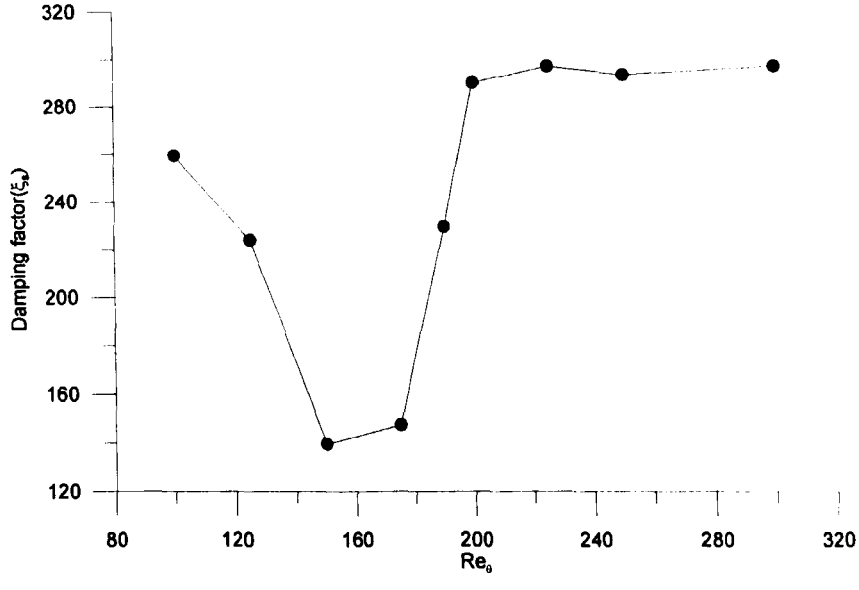

(b)

Figure 5.31 Optimised compliant surface properties (a) coating thickness L_s (b) damping factor ξ_s

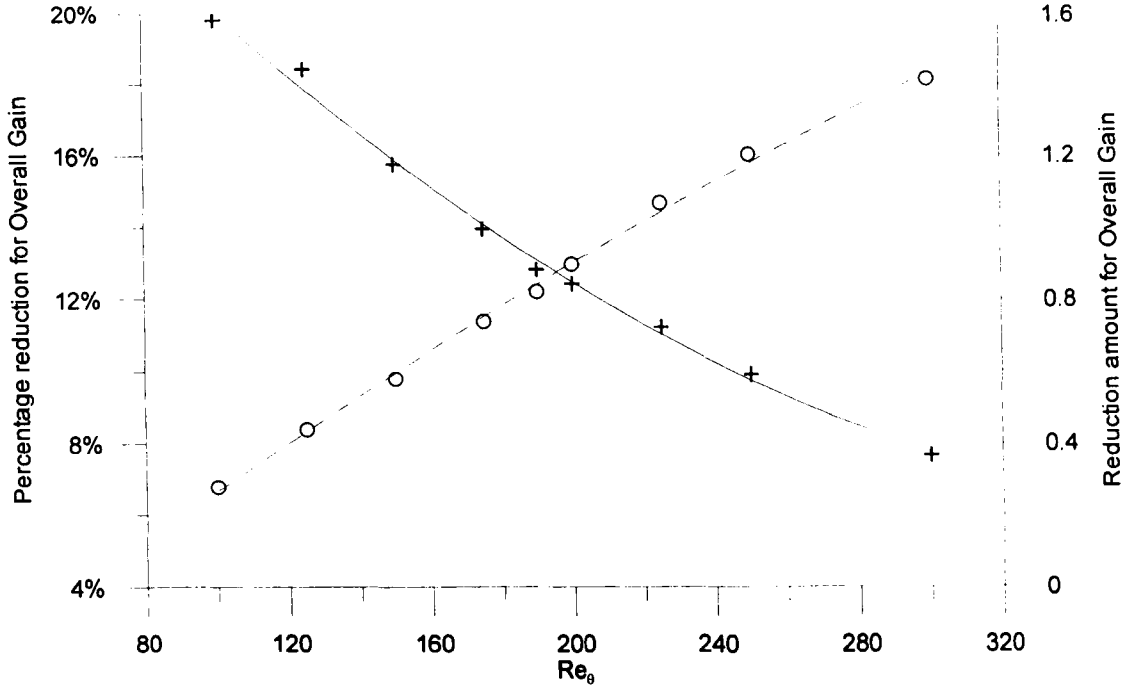

Figure 5.32 Overall gain reductions by an optimised compliant surface
(o: Percentage reduction for overall gain, right y-axis,
+: Reduction amount for overall gain , left y-axis)

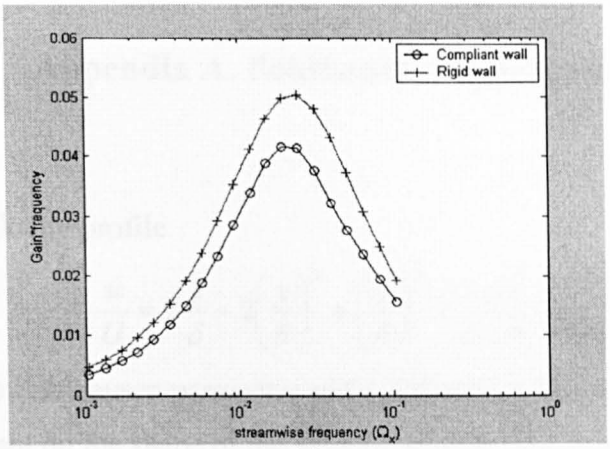

(a)

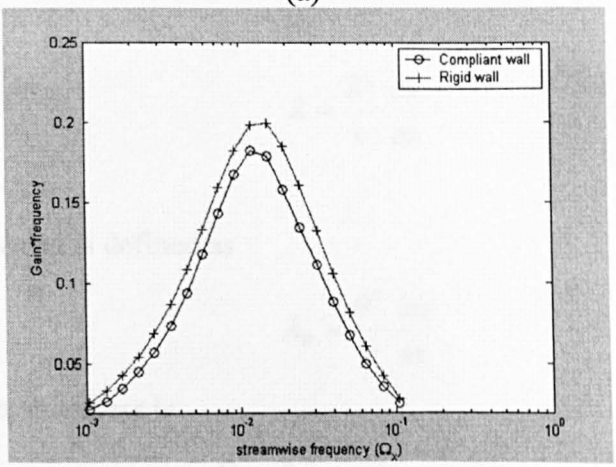

(b)

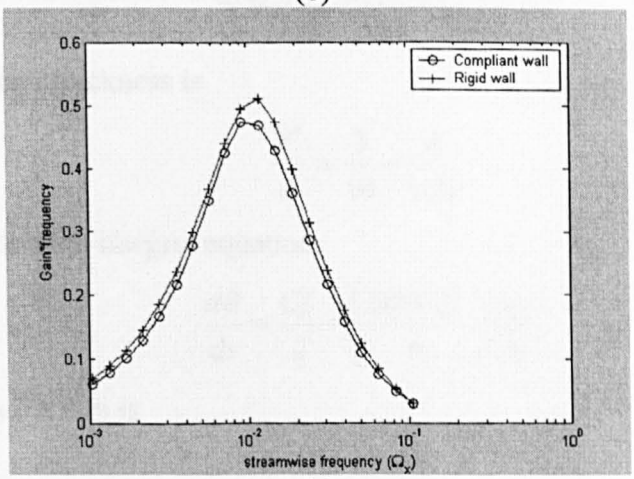

(c)

Figure 5.33 Streamwise spectra on optimised compliant surfaces
(a) $\mathrm{Re}_\theta = 100$ (b) $\mathrm{Re}_\theta = 200$ (c) $\mathrm{Re}_\theta = 300$

Appendix A. Pohlhausen Boundary layer

Pohlhausen velocity profile

$$\frac{u}{U} = 2\frac{y}{\delta} - 2\left(\frac{y}{\delta}\right)^3 + \left(\frac{y}{\delta}\right)^4 + \frac{\lambda}{6}\frac{y}{\delta}\left(1-\frac{y}{\delta}\right)^3 \tag{A.1}$$

where λ is the Pohlhausen parameter and it determines the effect of an external pressure gradient on the shape of the velocity profile. It is defined as

$$\lambda = \frac{\delta^2}{\nu}\frac{du}{dx} \tag{A.2}$$

Thwaites parameter is defined as

$$\lambda_\theta = \frac{\theta^2}{\nu}\frac{du}{sx} \tag{A.3}$$

The momentum thickness is

$$\frac{\theta}{\delta} = \frac{37}{315} - \frac{\lambda}{945} - \frac{\lambda^2}{9072} \tag{A.4}$$

The displacement thickness is

$$\frac{\delta^*}{\delta} = \frac{3}{10} - \frac{\lambda}{120} \tag{A.5}$$

From the momentum integral equation

$$\frac{d\theta}{dx} = \frac{Cf}{2} - \left(\frac{2\theta+\delta^*}{u}\right)\frac{du}{dx} \tag{A.6}$$

where the skin friction is

$$Cf = \frac{\nu\left.\frac{du}{dy}\right|_w}{\frac{1}{2}U^2} \tag{A.7}$$

$$\frac{\delta}{U}\left.\frac{du}{dy}\right|_w = 2 + \frac{\lambda}{6} \tag{A.8}$$

Combining (A.4)~(A.8) then

$$\therefore \frac{d\theta}{dx} = \frac{2\nu}{U^2}\frac{U}{\delta}\left(2+\frac{\lambda}{6}\right) - \frac{\delta}{U}\left\{2\left(\frac{37}{315} - \frac{\lambda}{945} - \frac{\lambda^2}{9072}\right) + \left(\frac{3}{10} - \frac{\lambda}{120}\right)\right\}\frac{du}{dx}$$

$$\therefore \frac{d\theta}{dx} = \frac{1}{\mathrm{Re}_\delta}\left(2+\frac{\lambda}{6}\right) - \frac{\lambda}{\mathrm{Re}_\delta}\left\{2\left(\frac{37}{315} - \frac{\lambda}{945} - \frac{\lambda^2}{9072}\right) + \left(\frac{3}{10} - \frac{\lambda}{120}\right)\right\}$$

$$= \frac{1}{\mathrm{Re}_\delta}\left\{\left(2+\frac{\lambda}{6}\right) - \left(\frac{74\lambda}{315} - \frac{2\lambda^2}{945} - \frac{2\lambda^3}{9072}\right) + \left(\frac{3\lambda}{10} - \frac{\lambda^2}{120}\right)\right\} \quad \text{(A.9)}$$

$$\frac{d\,\mathrm{Re}_\theta}{d\,\mathrm{Re}_x} = \frac{\nu}{U}\frac{d\,\mathrm{Re}_\theta}{dx} = \frac{\nu}{U\nu}\left(U\frac{d\theta}{dx} + \theta\frac{dU}{dx}\right)$$

$$\therefore \frac{d\theta}{dx} = \frac{d\,\mathrm{Re}_\theta}{d\,\mathrm{Re}_x} - \frac{\theta}{U}\frac{dU}{dx} = \frac{d\,\mathrm{Re}_\theta}{d\,\mathrm{Re}_x} - \frac{\theta}{U}\frac{\nu\lambda}{\delta^2} = \frac{d\,\mathrm{Re}_\theta}{d\,\mathrm{Re}_x} - \frac{\lambda\theta}{\delta}\frac{1}{\mathrm{Re}_\delta}$$

$$= \frac{d\,\mathrm{Re}_\theta}{d\,\mathrm{Re}_x} - \frac{1}{\mathrm{Re}_\delta}\left(\frac{\lambda\theta}{\delta}\right) \quad \text{(A.10)}$$

Substitute (A.9) into (A.10) then

$$\frac{d\,\mathrm{Re}_\theta}{d\,\mathrm{Re}_x} = \frac{1}{\mathrm{Re}_\delta}\left\{\left(2+\frac{\lambda}{6}\right) - \left(\frac{74\lambda}{315} - \frac{2\lambda^2}{945} - \frac{2\lambda^3}{9072}\right) + \left(\frac{3\lambda}{10} - \frac{\lambda^2}{120}\right) - \left(\frac{37\lambda}{315} - \frac{\lambda^2}{945} - \frac{\lambda^3}{9072}\right)\right\}$$

$$\frac{d\,\mathrm{Re}_\theta}{d\,\mathrm{Re}_x} = \frac{1}{\mathrm{Re}_\theta}\left(S(\lambda)\right) \quad \text{(A.11)}$$

Where

$$S(\lambda) = \left(\frac{37}{315} - \frac{\lambda}{945} - \frac{\lambda^2}{9072}\right)\left\{\left(2+\frac{\lambda}{6}\right) - \left(\frac{74\lambda}{315} - \frac{2\lambda^2}{945} - \frac{2\lambda^3}{9072}\right) + \left(\frac{3\lambda}{10} - \frac{\lambda^2}{120}\right) - \left(\frac{37\lambda}{315} - \frac{\lambda^2}{945} - \frac{\lambda^3}{9072}\right)\right\}$$

(A.11) can be rearranged into (A.12)

$$\mathrm{Re}_\theta\, d\,\mathrm{Re}_\theta = S(\lambda) d\,\mathrm{Re}_x \quad \text{(A.12)}$$

$$\frac{\mathrm{Re}_\theta{}^2}{\mathrm{Re}x} = \left(2S(\lambda)\right) \quad \text{(A.13)}$$

Therefore, the relationship between Re_x and Re_θ is

$$\frac{\mathrm{Re}_\theta{}^2}{\mathrm{Re}x} = 2\left(\frac{37}{315} - \frac{\lambda}{945} - \frac{\lambda^2}{9072}\right)\left\{\left(2 + \frac{\lambda}{6}\right) - \left(\frac{74\lambda}{315} - \frac{2\lambda^2}{945} - \frac{2\lambda^3}{9072}\right) + \left(\frac{3\lambda}{10} - \frac{\lambda^2}{120}\right) - \left(\frac{37\lambda}{315} - \frac{\lambda^2}{945} - \frac{\lambda^3}{9072}\right)\right\}$$

(A.14)

Appendix B. The dimensional analysis

Dimensional analysis is a method of reducing the number of variables in a process in order to simplify the establishment of a relationship between these variables.

In the current work, the *gain* for boundary layer over a compliant surface depends on the variables $U, \rho, \mu, \delta, f, E, \xi, \rho_{cs}, L$,

where U = Fluid free stream velocity, ρ = fluid density, μ =fluid viscosity, δ =boundary layer thickness, E=Young's modulus, ξ =damping factor for the compliant surface, L: coating thickness of the compliant surface and ρ_{cs}: density of compliant surface material.

According to the Buckingham $\prod$ theorem, if an equation involving m variables is dimensionally homogeneous, it can be reduced to a relationship among m - n independent dimensionless products, where n is the minimum number of reference dimensions required to describe the variables.

Here, $Gain = f(U, \rho, \mu, \delta, f, E, \xi, \rho_{cs}, L)$

The 9 variables involved so m=9, and there are three reference dimensions L, M, T, and so n=3. This will result in 6 independent dimensionless groups.

The dimensions of the 9 variables are

$$[U]=\frac{L}{T},[\rho]=\frac{M}{L^3},[\mu]=\frac{M}{LT},[\delta]=L,[f]=\frac{1}{T},[E]=\frac{M}{LT^2},[\xi]=\frac{M}{LT},[\rho_{cs}]=\frac{M}{L^3},$$

$$[L]=L$$

which leads to the 6 dimensionless groups

$$\left[\frac{\rho U\delta}{\mu}\right],\left[\frac{2\pi f\delta}{U}\right],\left[\frac{\xi^2}{E\rho_{cs}L^2}\right],\left[\frac{\rho_{cs}}{\rho}\right],\left[\frac{L}{\delta}\right], \text{ and}\left[\frac{E}{\rho U^2}\right]$$

Therefore, $Gain = f\left(\frac{\rho U\delta}{\mu}, \frac{2\pi f\delta}{U}, \frac{\xi^2}{E\rho_{cs}L^2}, \frac{\rho_{cs}}{\rho}, \frac{L}{\delta}, \frac{E}{\rho U^2}\right)$

The first two of these groups characterise the fluid flow. $\frac{\rho U\delta}{\mu}$ is the boundary layer thickness Reynolds number and $\frac{2\pi f\delta}{U}$ is the ratio of the frequency of the velocity fluctuations and the characteristic boundary layer frequency $\frac{U}{2\pi\delta}$. These groups are also used for boundary layers on rigid surfaces.

The third dimensionless group $\frac{\xi^2}{E\rho_{cs}L^2}$ characterises the material properties of the compliant surface. The remaining three dimensionless groups are concerned with the fluid-compliant surface interaction. $\frac{\rho_{cs}}{\rho}$ is the ratio of the densities, $\frac{L}{\delta}$ is the ratio of characteristic lengths and $\frac{E}{\rho U^2}$ relates the compliant surface material stiffness to the dynamic pressure for the fluid.